UNIVERSIDAD AUTÓNOMA DE MADRID

DOCTORAL THESIS

CLUES from The Three Hundred: A two-way approach to the influence of baryonic physics on galaxy formation

Author:
Robert MOSTOGHIU

Supervisor:
Dr. Alexander KNEBE

Co-supervisor:
Dr. Gustavo YEPES

A thesis submitted in partial fulfilment of the requirements for the degree of Doctor of Philosophy

in the

Department of Theoretical Physics

March 4, 2021

"Three, two, one... One, two, three... What the heck is bothering me?"

Carl Winslow

UNIVERSIDAD AUTÓNOMA DE MADRID

Abstract

CLUES from The Three Hundred: A two-way approach to the influence of baryonic physics on galaxy formation

by Robert MOSTOGHIU

Galaxy formation is one of the greatest challenges of modern astrophysics. Considering that approximately 95 per cent of the content of the Universe eludes us and that galaxies experience complex non-gravitational interactions during their evolution, finding an accurate model of galaxy formation is a difficult task. To examine this issue we use numerical simulations.

In this Thesis we present a compendium of results on baryonic processes in galaxy formation from two different approaches. The first approach uses numerically simulated galaxy clusters. Galaxy clusters are ideal laboratories for such analysis as they can be used for both cosmological and large scale structure studies, and for galaxy formation modelling. The second approach uses constrained simulations of the Local Universe. Instead of studying statistically-equivalent realisations of our local Universe, constrained simulations aim to (partially) reproduce it, which facilitates comparisons with observational data. Both approaches are complementary to each other, as the typical numerical resolution of each method naturally probes different scales.

The first part of this Thesis covers the analysis done using a galaxy cluster dataset, THE THREE HUNDRED project. We first describe how the dataset was built and some general properties of the galaxy clusters. 324 numerically modelled clusters have been simulated with various methods of capturing the sub-resolution (baryonic) physics, both full hydrodynamics and semi-analytic models, which allows us to understand how different hydrodynamical implementations influence cluster properties. Overall, we find they are in reasonable agreement with respect to baryonic fractions and scaling relations at redshift $z = 0$, and show some model-dependent differences for properties such as galaxy colours and central galaxies masses. We study the evolution of the mass density radial profiles of the clusters in the dataset to find how they accrete their mass across redshift. We show that the median total mass profile of the sample is already in place at $z \sim 2.5$ and that their degree of self-similarity is correlated with their (z=0) dynamical state and their time of formation, defined here as the redshift at which they accreted half of their $z = 0$ mass. The gas mass profiles qualitatively follow the same self-similar trends, with only a considerable deviation at $z \sim 2.5$. Thus, self-similarity is well preserved at high redshift even in the presence of baryonic interactions. Once we validated the mass accretion history of the clusters in the dataset, we explore the environmental effects of clusters on the stellar kinematics of infalling haloes. We show that both the mass and kinematics of their stellar component is well shielded from the tidal interactions inside cluster environments, despite being considerably stripped off of their dark matter and gas. However, for a small number of infalling objects we observe a spin-up of their stellar component as a result of mergers and remnant stellar cores inside the cluster. This suggests that the different kinematical mix between galaxies residing in cluster environments and field galaxies may not be caused by environmental effects transforming galaxies in clusters, as the kinematical disruption we observe in the infalling haloes in our sample only affects a small percentage of the total population.

The second part of this Thesis comprises the results obtained from constrained simulations from the CLUES project. For this part we investigate two observational open problems. In the first study we analyse the reversed radial stellar age gradient observed in the outskirts of the Triangulum (i.e. M33) galaxy. We use a simulated counterpart of the M33 galaxy to, first, show that it also shows such feature and, second, that its origin is compatible with an inside-out galactic disk growth scenario and accretion of old satellites at high galactocentric radii, with a lesser contribution from in-situ stellar migration. This population of old accreted stars can be identified by their high velocity dispersion, which future kinematical observations could detect at the outskirts of the galaxy. Finally, we study the star formation histories of satellite galaxies of the Local Group and compare them with the isolated ones. We find that, while in the majority of the cases the accretion onto the main host strips the infalling galaxy of its gas with a subsequent suppression in star formation, in about one third of the satellites we observe a clear enhancement of star formation after infall. We show that a suppressed star formation history can be discriminated from an enhanced one by the fraction of cold gas mass of their satellite at infall and their minimum pericentric distance to their central galaxy, and that peaks in their star formation correlate with the satellite-host interactions.

UNIVERSIDAD AUTÓNOMA DE MADRID

Resumen

CLUES from The Three Hundred: A two-way approach to the influence of baryonic physics on galaxy formation

por Robert MOSTOGHIU

La formación de galaxias es uno de los mayores retos de la astrofísica moderna. Teniendo en cuenta que aproximadamente el 95 por ciento del contenido del Universo nos elude y que las galaxias experimentan complejas interacciones no-gravitacionales durante su evolución, encontrar un modelo de formación de galaxias preciso es una tarea laboriosa. Para investigar este problema hacemos uso de simulaciones numéricas.

En esta Tesis presentamos un compendio de resultados sobre procesos bariónicos en la formación de galaxias desde dos puntos de vista distintos. El primer enfoque emplea cúmulos de galaxias numéricamente simulados. Los cúmulos de galaxias son los laboratorios ideales para este tipo de estudios, ya que pueden ser usados tanto para análisis cosmológicos y de estructuras de gran escala, como para modelizar la formación de galaxias. El segundo enfoque emplea simulaciones cosmológicas constreñidas del Universo Local. En lugar de estudiar realizaciones estadísticamente equivalentes de nuestro Universo local, las simulaciones constreñidas tienen como objetivo reproducirlo (de manera parcial), lo cual facilita comparaciones con resultados observacionales. Como la resolución numérica de cada método sondea de manera natural distintas escalas, los dos enfoques se complementan.

La primera parte de esta Tesis comprende el análisis realizado usando un conjunto de datos de cúmulos de galaxias, el proyecto THE THREE HUNDRED. Empezamos el análisis describiendo cómo este conjunto de datos fue construido y algunas propiedades generales de sus cúmulos de galaxias. Los 324 cúmulos de galaxias del proyecto han sido simulados empleando varios métodos que capturan la física (bariónica) a escalas por debajo de la resolución de las simulaciones, tanto con modelos hidrodinámicos completos como con modelos semianalíticos, que nos permiten entender cómo diferentes implementaciones hidrodinámicas influencian las propiedades de los cúmulos. En general, encontramos que los cúmulos de nuestras simulaciones se adecúan razonablemente bien a fracciones bariónicas y relaciones de escala a redshift $z = 0$; y que presentan algunas diferencias, ligadas a cada modelo empleado en su simulación, en los colores galácticos y las masas de las galaxias centrales. Estudiamos la evolución de los perfiles radiales de densidad de masa de los cúmulos del conjunto de datos para entender cómo éstos acretan su masa a lo largo de distintos redshift. Encontramos que el perfil mediano total de masa del conjunto de cúmulos de galaxias ya estaba establecido a $z \sim 2.5$ y que su grado de autosimilitud está correlacionado con su estado dinámico (a $z = 0$) y su tiempo de formación, que definimos como el redshift al cual han acretado la mitad de su masa a $z = 0$. Los perfiles de masa de gas siguen de manera cualitativa las mismas tendencias autosimilares, con solo una desviación considerable a $z \sim 2.5$. Por lo tanto, la autosimilitud de los cúmulos se conserva a redshift altos incluso en presencia de interacciones bariónicas. Una vez hemos validado la evolución de la acreción de masa del conjunto de cúmulos, exploramos sus efectos ambientales sobre la cinemática estelar de los halos que inciden en ellos. Mostramos que tanto la masa como la cinemática estelar de los halos se encuentran bien resguardadas de las interacciones de marea dentro de los entornos de los cúmulos de galaxias, a pesar de haber sido considerablemente despojados de su materia oscura y gas. No obstante, para un número pequeño de objectos que inciden en los cúmulos de galaxias, observamos que su componente estelar aumenta su grado de rotación como resultado de coalescencias y de interacciones con núcleos estelares remanentes dentro del cúmulo. Este resultado sugiere que las diferencias cinemáticas entre los galaxias que residen en los entornos de los cúmulos y las galaxias aisladas no se deben a los efectos ambientales que transforman las galaxias dentro de los cúmulos, ya que las alteraciones cinemáticas que observamos en los halos que inciden en los cúmulos de galaxias en nuestra muestra afectan solo a un porcentaje pequeño de la población total.

La segunda parte de esta Tesis comprende los resultados obtenidos a partir de simulaciones constreñidas del proyecto CLUES. Para esta parte investigamos dos problemas abiertos observacionales. En el primer estudio analizamos la inversión del gradiente radial de edad estelar que se observa en las afueras de la galaxia Triangulum ('M33'). Hacemos uso de una galaxia simulada homóloga a M33 para, primero mostrar que posee la misma característica peculiar, y segundo, que el origen de dicha característica es compatible con un crecimiento del disco galáctico desde dentro hacia afuera y una acreción de satélites antiguos a grandes distancias galactocéntricas, con una contribución menor debido a la migración estelar in-situ. Esta población de satélites antiguos puede ser identificada gracias a su alta dispersión de velocidades que futuras observaciones cinemáticas podrían detectar a las afueras de la galaxia. Finalmente, estudiamos la historia de formación estelar de las galaxias satélite del Grupo Local y las comparamos con galaxias aisladas. Encontramos que, aunque en la mayoría de casos su acreción en el halo anfitrión principal las despoja de su gas y posteriormente su formación estelar queda suprimida, en aproximadamente un tercio de las galaxias satélite identificamos un claro incremento de su formación estelar después de su caída en el anfitrión. Señalamos que una formación estelar inhibida puede ser distinguida de una incrementada mediante la fracción de masa gaseosa fría que tiene el satélite antes de su incidencia y su mínima distancia pericéntrica con respecto a su galaxia central, y en que los picos de su formación estelar están correlacionados con interacciones satélite-anfitrión.

Agradecimientos

Ahora que me encuentro al final de esta etapa me doy cuenta de que expresar en pocas palabras la importancia que han tenido las personas de mi alrededor en mi formación, tanto en el ámbito personal como en el académico, es una tarea prácticamente imposible. Son muchas las personas con las que he compartido este camino. Por ello siento que, de omitir a alguien, no sería justo. Pero, a pesar de lo difícil que me resulta elaborar una lista (y de lo probable que es que me deje a alguien), he de destacar a algunas personas.

En primer lugar, quiero darles las gracias a mis directores, Alexander y Gustavo, por el tiempo que me han dedicado, el apoyo que he recibido durante estos años, y por la confianza que han depositado en mí. Esta tesis no podría haberla realizado sin vuestra ayuda. Alexander, aún recuerdo cuando llegué a tu despacho tras acabar el máster y te pregunté por el doctorado. La pasión con la que me hablaste de tu investigación, la claridad con la que me transmitiste todos los detalles de lo que acabaría siendo mi doctorado, y el orden que sigue reflejándose en tu trabajo son cualidades que espero acabar adquiriendo. Gustavo, siempre he admirado la cantidad de detalles técnicos que conoces y la perspectiva práctica que adoptas ante los problemas. Las indicaciones que me has ofrecido me motivan a aprender más sobre las sutilezas de la computación. Los dos sois unas personas excepcionales, ha sido un placer trabajar junto a vosotros.

I would also want to highlight the support I had from the talented researchers throughout my PhD and the amazing collaborations I am happy to be part of, you made me feel welcomed and part of the team. I want to thank Noam, Arianna and Chris B for guiding me during my first research stay, for teaching me how to approach open problems, and for making sure everything went smoothly during my time there. Chris P, Claudia, Pascal, Adam, and Aaron R, thank you for taking hours from your own research time to talk about my projects, for providing resources that helped me learn much more about my research, and for including me in different activities. Frazer and Meghan, thanks for your thoughtful words and insightful ideas that greatly helped me organise and push forward the projects we were working on. Weiguang, thank you for always listening to my questions and for helping me in innumerable times despite having a lot on your plate already, even when your office was no longer close to mine. I want to thank all of you for the opportunities I was given, it has been an amazing experience.

Más allá del ámbito profesional, quiero dar las gracias a los amigos que me han ofrecido su apoyo incondicional en los momentos más exigentes. A Fran y Alex, por la cantidad de años que hemos recorrido juntos, disfrutando de los momentos buenos y afrontando los no tan buenos. Lo que empezó como una conversación de adolescentes que comparten los mismos intereses se convirtió en mucho más. Gracias por alegrar mi día a día con vuestro humor, por hacerme reflexionar tras nuestras conversaciones y, sobre todo, por ayudarme a mejorar como persona. A Laura, por contagiarme tu pasión por la naturaleza, la literatura y los cánidos, y por demostrarme que esa pasión excede cualquier maratón soporífero de entretenimiento electrónico o aventura fantástica inacabada. A Alex H y Andreea H, por las innumerables conversaciones interesantes que hemos tenido y porque, a pesar de que ya no llevamos la capucha puesta cuando nos sentamos al final del autobús, el espíritu rebelde sigue ahí, uniéndonos. A Alex T y Simón, porque desde que nos conocimos supe que nuestra amistad iba a ser única. Estoy sumamente agradecido de tener unos amigos como vosotros, que conocen mis fortalezas y mis debilidades, y que en incontables ocasiones han enriquecido mi visión de la vida gracias a las valiosas conversaciones que hemos tenido. A Claudia, por las veces en las que me has sorprendido con la cantidad de curiosidades que conoces y, ante todo, por las conversaciones terapéuticas que me ayudaron a seguir adelante. A Manu, Miguel y Adrián, por decidir romper el hielo y hablarle a ese estudiante nervioso de primero. Gracias por acompañarme durante todos estos años y por atender a nuestros encuentros anuales. A Doris y Sergio, por vuestra ayuda durante el doctorado, y por la paciencia que habéis tenido conmigo, porque sé que sin vosotros el doctorado habría sido más tedioso. A Ana, Matías, Daniel y Alejandro, por continuar la tradición del despacho y tener esos momentos de respiro entre tanto trabajo. Ha sido un placer trabajar (y hacer de todo menos trabajar) con vosotros, espero que sigáis adelante con éxito.

No puedo concluir estos agradecimientos sin antes dar las gracias a mi familia. A mi madre y a mi padre, por guiarme en este mundo, enseñarme a luchar por lo que me propongo, apoyarme en mis decisiones, empatizar con las dificulades por las que he pasado y por ofrecerme todo lo que he necesitado (y más). Lui bunica mea, pentru că ești ca o a doua mamă pentru mine. Îți mulțumesc pentru învățăturile pe care mi-ai dat, grija care mi-ai purtato, răbdarea care ai avuto atâția ani, și pentru că te-ai interesat de educația mea, chiar dacă era într-o limbă care nu vorbești. A mi hermano, mi orientador aeronáutico y ferroviario favorito, al que he visto crecer y convertirse en una persona determinada y responsable, capaz de todo lo que se proponga. Te deseo todo lo mejor para tu futuro. Gracias por todas las veces en las que me has animado y por aguantarme cada vez que me he explayado explicando algo. A mis tías Laura, Mia, Mona, y a mis tios Mitică y Viorel por todas las veces que os habéis acordado de mí y me habéis preparado algún detalle o ayudado con algún trabajo, aunque estuvieseis ocupados. A mi tía Larisa y a mi tío Liviu, porque, aunque estéis lejos de casa, cada vez que hablamos siento vuestro apoyo como si estuvieseis aquí. A mis primas Nicol, Jessica, Naomi y a mi primo Cristian, por vuestro espíritu alegre y por todas las palabras amables que siempre tenéis guardadas para mí.

A todos y cada uno de vosotros, que formáis parte de este recorrido, muchas gracias.

Contents

List of Figures

List of Tables

1 Introduction

One of the greatest challenges in modern astrophysics is the need of a complete theory of galaxy formation that is able to describe the intricate physical processes that shaped the galaxies we observe today. This is not entirely surprising considering that, on the one hand, the nature of approximately 95 per cent of the total content of the Universe, i.e. dark matter and dark energy, has yet to be determined (Planck Collaboration et al., 2018b); and on the other hand, galaxy formation goes beyond gravitational interactions and requires modelization of complex baryonic interactions (e.g. star formation, cooling processes, feedback, chemical enrichment, and radiative transfer) which often lead to degeneracy in the results.

Contrary to other scientific research areas, in cosmology and astrophysics we cannot arrange an experiment in which we change the initial conditions to study its outcome and, through repetition, determine which model describes the best the observational constrains. Observationally we only have one Universe, so what we see is what we get. Moreover, the median timescale of the processes we are interested in are far greater than human lifetime. Hence, we resort to numerical simulations to produce models based on our hypothesis, analyse the results, compare them with observational data, change our models accordingly in order to improve them, and ultimately predict features that could potentially be searched for in future observational analysis. Nevertheless, numerical simulations are not entirely safe from the aforementioned galaxy formation problems. The numerical implementation of gravitational interactions is relatively straightforward compared with the, effectively, endless combinations of implementations of the different baryonic interactions. This leads to situations in which, different underlying physical implementations result in similar outcomes (e.g. Neistein and Weinmann, 2010; Bower et al., 2010; Crain et al., 2015; Sembolini et al., 2016b).

In this Thesis we present a compendium of results on the influence of baryonic physics on galaxy formation from numerical simulations with the aim of understanding how non-gravitational interactions during the evolution of a galaxy influence its properties. These results were obtained from two different approaches to numerical simulations. One of the methods consists on statistically analysing numerically modelled galaxy clusters, while the other one uses constrained simulations that aim to reproduce the observed (local) Universe.

Galaxy clusters are the largest known gravitationally bound structures in the Universe. They contain up to tens of thousands of galaxies and have masses ranging from 10^{14} to 10^{15} solar masses (e.g. Comerford and Natarajan, 2007). However, despite the abundant number of galaxies residing in them, they are dark matter dominated structures: up to 90 per cent of their mass is dark matter, while the remaining mass is in the intra-cluster gas and the galaxies of the cluster (e.g. Gonzalez et al., 2013).

Our current understanding of structure formation describes the growth of structures such as cluster galaxies as the result of hierarchical mergers of smaller objects driven by the gravitational collapse of overdense regions that originated at the beginning of the Universe (White and Rees, 1978). However, a complete model of their evolution also requires a proper characterisation of the processes experienced by the galaxies in the cluster, beyond a description in terms of gravitational interactions, i.e. how gas cools and the forms stars, or feedback from supermassive black holes and supernovae (see Naab and Ostriker, 2017, for a recent review). Therefore, galaxy clusters are ideal laboratories for refining our models of structure formation since they provide clues at two different scales: at the cosmological scale, e.g. by studying the clustering of galaxies to derive cosmological parameters; and at the galactic scale, e.g. by analysing how cluster environments shape the galaxies we see today. Through the analysis of a statistical significant sample of galaxy clusters, we are able to obtain robust results for the galaxies in the cluster.

The second method used in this Thesis for studying galaxy formation is constrained simulations. The goal of constrained simulations is to obtain a large scale structure and cosmic web as close to the one found in our Universe as possible, rather than simulating one that is statistically equivalent. To produce constrained simulations a series of properties, e.g. mass distribution or observed velocities that are linked to the underlying potential, are imposed on the initial conditions of the simulations according to observational constraints which select from the (infinitely) pool of equivalently valid universe models the one which resembles the best our Universe. Thus, we can straightforwardly use the end results of a constrained simulation as a direct benchmark of their quality if we compare them with their observational counterparts. As it will be discussed in a later section, the fact that we can impose these conditions is a consequence our current cosmological model, in which the collapse of overdense regions that drives structure formation is thought to originate from primordial fluctuations at the very early stages of the Universe.

In this chapter we present the relevant background and literature for this Thesis. Sec. 1.1 introduces the principles and fundamental relations needed in cosmology. In Sec. 1.2 we characterise our current cosmological model. A general description of how structures form according to our current cosmological model is presented in Sec. 1.3. In Sec. 1.4 we follow that discussion by briefly reviewing some physical processes that are relevant to galaxy formation. Sec. 1.5 gives an overview of the different numerical techniques used for modelling it. At last, in Sec. 1.6 we detail the goals of this Thesis and its structure.

1.1 Cosmological framework

To understand how galaxies form, first we must ask a more general question: how do we understand the origin and evolution of the Universe? One of the aims of cosmology is to answer how the structures we observe today formed in an Universe that is currently under accelerated expansion (Riess et al., 1998; Perlmutter et al., 1999).

In an expanding Universe, electromagnetic radiation with a wavelength λ_E undergoes an increase in wavelength as it travels through the expanding space, and it is observed with a wavelength λ_0. The change in wavelength due to expansion of the Universe is called *redshift*, and it is defined by:

$$z = \frac{\lambda_0 - \lambda_E}{\lambda_E} \,. \tag{1.1}$$

Our current cosmological model is based upon a single assumption: that on a sufficiently large scale the Universe is homogeneous and isotropic in space[1] (Peebles, 1980; Yadav et al., 2005). This is commonly known as the *cosmological principle*. In terms of General Relativity, this is equivalent to requiring that the metric tensor of the Universe $g_{\mu\nu}$ is of the form of the Friedmann-Lemaître-Robertson-Walker (FLRW) metric:

$$\begin{aligned} ds^2 &= -(cdt)^2 + a(t)^2 \left[\frac{dr^2}{1-kr} + r^2 \left(d\theta^2 + \sin^2\theta d\phi^2 \right) \right] \\ &= g_{\mu\nu} dx^\mu dx^\nu \,, \end{aligned} \tag{1.2}$$

where c is the speed of light, t the cosmic time, $a(t)$ is the (dimensionless) cosmic expansion factor, and r, θ, and ϕ are 3-dimensional spherical coordinates. In this metric, k is a parameter that describes the curvature of space and can take the values $k = 0$ for flat, $k = -1$ for hyperbolic, or $k = +1$ for spherical spaces. Note that the scale factor $a(t)$ accounts for the spatial expansion of the Universe, and can be related with the cosmological redshift z via:

$$a = \frac{1}{1+z} \,. \tag{1.3}$$

[1] Note how the statement only concerns the spatial distribution of the objects in the Universe, and not its time evolution. The expansion of the Universe breaks the principle, i.e. the *strong* cosmological principle is violated in an expanding universe.

This relation allows us to describe a cosmological property (i.e. $a(t)$) in terms of an observational one (i.e. z). However, we have yet to find how the scale factor $a(t)$ evolves with time.

1.1.1 Friedmann equations

General Relativity allows us to determine the relation between the geometrical part of spacetime and its matter-energy content via the Einstein field equations:

$$R_{\mu\nu} - \frac{1}{2}Rg_{\mu\nu} + \Lambda g_{\mu\nu} = \frac{8\pi G}{c^4}T_{\mu\nu}\,, \tag{1.4}$$

where $R_{\mu\nu}$ is the Ricci tensor, which depends on the metric tensor $g_{\mu\nu}$, R is the Ricci scalar, which depends on the Ricci tensor, and Λ is Einstein's cosmological constant. On the right hand side we have G, Newton's gravitational constant, and $T_{\mu\nu}$, the energy-stress tensor. Considering the cosmological principle, the geometry of the Universe can be described by a FLRW metric, i.e. Eq. (1.2), and its matter-energy content by a perfect fluid, i.e. a fluid that is isotropic in its rest frame:

$$T_{\mu\nu} = \left(p + \frac{\rho}{c^2}\right)u_\mu u_\nu + pg_{\mu\nu}\,, \tag{1.5}$$

where p is the pressure of the fluid and ρ its density. Inserting these two conditions into the Einstein field equations, i.e. Eq. (1.4), we obtain the Friedmann equations, which describe the temporal evolution of the scale factor:

$$H^2(t) \equiv \left(\frac{\dot{a}}{a}\right)^2 = \frac{8\pi G}{3}\rho - \frac{kc^2}{a^2} + \frac{c^2\Lambda}{3}\,, \text{and} \tag{1.6}$$

$$\dot{H} - H^2 = \frac{\ddot{a}}{a} = -\frac{4\pi G}{3}\left(\rho + \frac{3p}{c^2}\right) + \frac{c^2\Lambda}{3}\,, \tag{1.7}$$

where $H(t)$ is the Hubble parameter. From Eq. (1.6) we can see that for a flat universe, i.e. k=0, with no cosmological constant term, there is a critical density ρ_c that can be written as

$$\rho_c(t) = \frac{3H^2(t)}{8\pi G}\,. \tag{1.8}$$

This threshold density determines the boundary between a spatially closed universe (i.e. positive curvature, $\rho > \rho_c$) and a spatially open one (i.e. negative curvature, $\rho < \rho_c$).

To solve the Friedmann equations and find the time evolution expression of the scale factor first we need to derive a couple of relations. Combining the first (Eq. 1.6) and the second (Eq. 1.7) Friedmann equations we can see that energy is conserved[2]:

$$\dot{\rho} + 3H\left(\rho + \frac{p}{c^2}\right) = 0\,. \tag{1.9}$$

On the other hand, if we recall the second law of thermodynamics and we use the energy conservation relation (i.e. Eq. 1.9), we find that the Universe expands adiabatically:

$$TdS = dU + pdV = 0\,, \tag{1.10}$$

where T is the temperature of the fluid, S its entropy, U represents its internal energy, p its pressure, and V its volume.

The last relation we need is an equation of state for the perfect fluid that describes the Universe, i.e. a relation between the pressure and the density of the fluid. We restrict ourselves to barotropic fluis, i.e. fluids with a linear relations between p and ρ, of the form

[2]This can also be derived from the $v = 0$ component of the energy-stress tensor conservation law, i.e. $\nabla_\mu T^{\mu 0} = 0$. The rest of the components, i.e. $\nabla_\mu T^{\mu i} = 0$ for $i = 1, 2, 3$, just yield $dp/dx^i = 0$, i.e. homogeneity.

$p = \omega(T)\rho c^2$, where $\omega(T)$ is an arbitrary function that in general depends on the temperature T of the fluid. Eq. (1.10) therefore implies that

$$\rho a^{3(1+\omega)} = \text{constant} . \tag{1.11}$$

However, the Universe is made of multiple components, i.e. $\rho = \Sigma\rho(a(t))$.

1.1.2 Density parameters

The components of the Universe have different equations of state. Thus, each of them evolves differently with the scale factor. We distinguish between three main components: radiation (i.e. relativistic particles) with $\omega = 1/3$, collisionless matter (i.e. non-relativistic matter) with $\omega = 0$, and vacuum energy (i.e. Einstein's cosmological constant) with $\omega = -1$.

The Friedmann equations can be expressed in a more convenient way in terms of the critical density ρ_c (i.e. Eq. 1.8) and separating the total density by its components.Taking into account the corresponding values of the ω parameter for each fluid component and scale factor evolution (i.e. Eq. 1.11), we find that the Friedmann equations Eq. (1.6) and Eq. (1.7) can be expressed as:

$$H^2(t) = H_0^2 \left(\Omega_{\mathrm{r},0}(1+z)^4 + \Omega_{\mathrm{m},0}(1+z)^3 + \Omega_{\mathrm{k},0}(1+z)^2 + \Omega_{\Lambda,0}\right) , \text{ and} \tag{1.12}$$

$$q \equiv -\frac{\ddot{a}a}{\dot{a}^2} = \frac{1}{2}\Omega_{\mathrm{m}}(z) + \Omega_{\mathrm{r}}(z) - \Omega_{\Lambda}(z) , \tag{1.13}$$

where

$$\begin{aligned}
\Omega_{\mathrm{m},0} &= \frac{\rho_{\mathrm{m},0}}{\rho_{\mathrm{c},0}} && \text{for collisionless matter,} \\
\Omega_{\mathrm{r},0} &= \frac{\rho_{\mathrm{r},0}}{\rho_{\mathrm{c},0}} && \text{for radiation ,} \\
\Omega_{\Lambda,0} &= \frac{c^2}{3H_0^2} && \text{for vacuum energy,} \\
\Omega_{\mathrm{k},0} &= -\frac{kc^2}{H_0^2} && \text{for curvature, and} \\
H_0 &= \left(\frac{\dot{a}}{a}\right)_0
\end{aligned} \tag{1.14}$$

are the dimensionless density parameters $\Omega_{\mathrm{i},0}$ (for $i = m, r, \Lambda, k$) defined at $z = 0$, and

$$\Omega_{\mathrm{i}}(z) = \frac{\Omega_{\mathrm{i},0}}{\left(\Omega_{\mathrm{r},0}(1+z)^4 + \Omega_{\mathrm{m},0}(1+z)^3 + \Omega_{\mathrm{k},0}(1+z)^2 + \Omega_{\Lambda,0}\right)}(1+z)^{3(1+\omega)} \tag{1.15}$$

are the density parameters at redshift z. From Eq. (1.12) we see that at for $z = 0$,

$$\Omega_0 = \Omega_{\mathrm{r},0} + \Omega_{\mathrm{m},0} + \Omega_{\mathrm{k},0} + \Omega_{\Lambda,0} = 1 , \tag{1.16}$$

which implies that there are only three independent density parameters. It is customary to define the curvature density as $\Omega_{\mathrm{k},0} = 1 - \Omega_0$. Thus, for a flat Universe, $\Omega_{\mathrm{k},0} = 0$.

1.1.3 Thermal history overview

The Friedmann equation Eq. (1.12) describes the evolution of the density components with the scale factor. Consequently, we identify three main epochs of the Universe, according to how fast each density component dissipates as the Universe expands. In Fig. 1.1 we show a diagram summarising the history of the Universe.

The first epoch is dominated by radiation (i.e. $\rho_r \propto a^{-4}$), as it was the most abundant component at early times. During this period the Universe was hot, baryonic matter was either still forming or ionised, and radiation pressure from photons prevented their collapse. As we will discuss in Sec. 1.2, it is during this time that dark matter was already able to

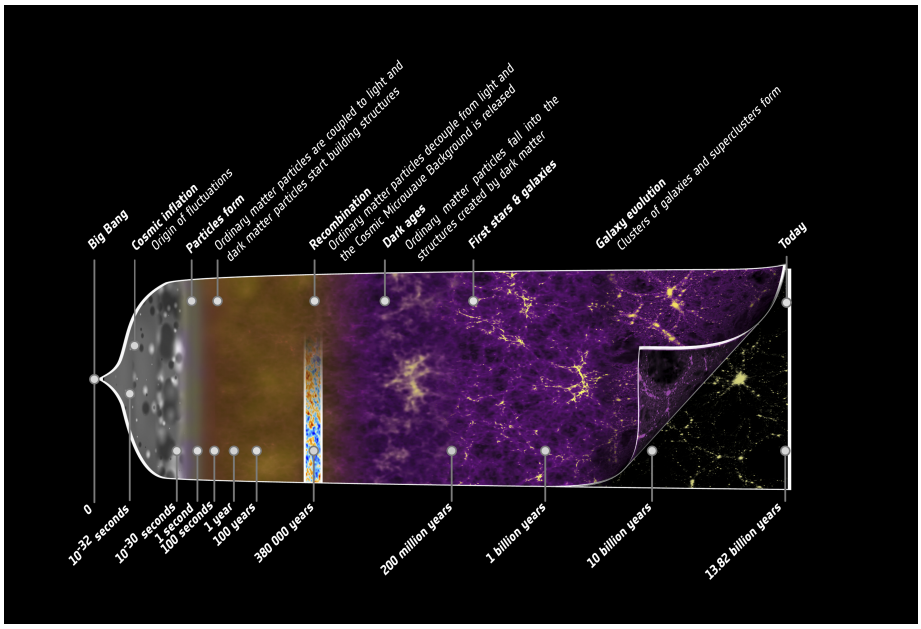

FIGURE 1.1: Timeline of the Universe, summarising the relevant epochs since the Big Bang. (Image credit: ESA – C. Carreau)

collapse (as it decoupled practically immediately after the Big Bang) and form the very first structures of the Universe. Radiation dissipates faster than the rest of the density components. Hence, at $z \sim 3500$ ($\sim 48 - 49$ thousand years since the Big Bang) the radiation and matter reached the same density values, defining the start of the following era, the matter dominated epoch (i.e. $\rho_m \propto a^{-3}$). As the Universe expanded, it also cooled, reducing the radiation pressure exerted on the baryonic material and allowing them to become neutral. Once the electrons and protons became bound to form neutral hydrogen atoms at $z \sim 1100$ (i.e. the *recombination* epoch, at around $\sim 370 - 380$ thousand years ago), baryonic matter was finally able to fall into the gravitational potential wells of the dark matter structures that collapsed during the previous epoch. At $z \sim 0.3$ (~ 10 billion years ago), the matter density in the Universe dropped to dark energy density values, which remained constant since the early Universe (i.e. $\rho_\Lambda = \text{constant}$). This started a new epoch in which dark energy dominates the evolution of the Universe, our current era.

1.2 The ΛCDM paradigm

In the previous section we discussed how the current cosmological model is founded upon the cosmological principle, i.e. that at sufficiently large scales the Universe is homogeneous and isotropic in space. Certainly, on smaller scales we see a different picture of the Universe.

The current cosmological paradigm describes the formation of the structures in the Universe with a model known as Λ *Cold Dark Matter*. Surprisingly enough, although the nature of some constituents of the model are still unknown in terms of particle physics, it successfully describes most of the observational results we know today and is compatible with cosmological observations such as distance determinations coming from supernovae, or the anisotropies statistics and primordial acoustic density waves, i.e. Baryonic Acoustic Oscillations (BAO), imprinted in the in the relic radiation from the early Universe, i.e. the Cosmic Microwave Background (CMB, see Fig. 1.2) (Penzias and Wilson, 1965; Peebles, 1970).

The ΛCDM model is characterised by three key assumptions. The first one is the existence of dark energy. Dark energy is the least understood component of our Universe, yet it is an essential part of cosmology as it accounts for the current accelerated expansion of the Universe (Riess et al., 1998; Perlmutter et al., 1999). As it seems to behave as some form of vacuum energy, the model contains a non-zero cosmological constant Λ term.

The second key assumption is the existance of dark matter. Dark matter amounts to approximately 25 per cent of the Universe, whereas the matter we know, observe, and are

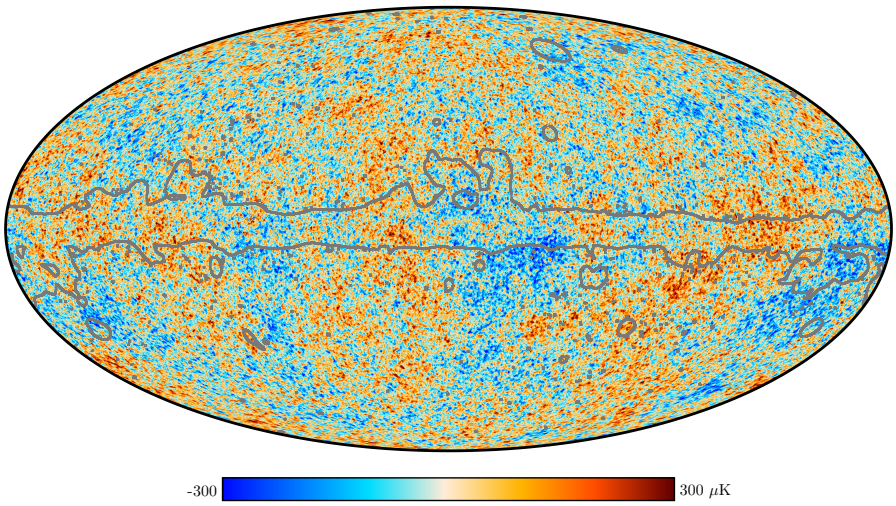

FIGURE 1.2: Cosmic Microwave Background temperature fluctuations from ESA's Planck satellite (Planck Collaboration et al., 2018a). The grey outline shows the extent of the confidence mask. The observed temperatures anisotropies can be translated into primordial fluctuations, which seeded the growth of the structures we find today. (Image credit: ESA and the Planck Collaboration)

able to classify according to the periodic table, i.e. baryonic matter, only constitutes 5 per cent. The remaining 70 per cent is in form of dark energy (Planck Collaboration et al., 2018b). Dark matter is introduced to understand the discrepancy between the inferred mass from luminous matter and from galaxy rotation curves (Zwicky, 1933; Rubin and Ford, 1970; Corbelli and Salucci, 2000; Sofue and Rubin, 2001), or in gravitational lensing studies (Wu et al., 1998; Refregier, 2003). Current observational constrains show that dark matter must be of non-baryonic nature (Feng, 2010; Lin, 2019).

The third aspect is the fact that in this model dark matter is non-relativistic, i.e. "cold". This distinguishes models in which smaller structures form from fragmentation of larger structures (i.e. "top-down" scenarios), as it occurs in relativistic (i.e. "hot") dark matter models, from schemes in which structures grow hierarchically, with smaller structures collapsing first and larger structures forming via mergers (i.e. "bottom-up" scenarios, Bond et al., 1984). Observational studies of structure formation at high redshift show that objects grow hierarchically, favouring non-relativistic dark matter models (Blumenthal et al., 1984).

A general ΛCDM model can describe universes with open, closed, and flat spatial curvatures. Recent observational results of the CMB support the fact that our Universe is compatible with a spatially flat Universe, i.e. $\Omega_{k,0} = 0$ (Planck Collaboration et al., 2018b). The observed spatial flatness, along with the required primordial fluctuations imprinted on the early Universe's space-time that trigger the formation of structures, are commonly thought to be achieved through some inflationary mechanism at first instants of the Universe (a review on different inflationary models can be found in Baumann, 2009; Wang, 2014). The spatially flat ΛCDM model used to describe our Universe is usually referred as the *concordance* model (or simply ΛCDM).

Summarising, the ΛCDM model describes a spatially flat Universe in which structures formed via the hierarchical collapse of cold dark matter clumps, induced by small primordial stochastic perturbations, assumed to follow a gaussian distribution, imprinted on the space-time of the first instants of Universe. As dark matter does not interact electromagnetically, they do not feel the radiation pressure of the early hot Universe and thus they can clump together to form bigger structures that act as the seeds for the eventual collapse of the rest of the matter content, once the Universe becomes sufficiently cold (i.e. after recombination) to allow their collapse. Dark matter clumps grow until they reach a virialised state, i.e. an equilibrium, to form "haloes" and host the baryonic matter we see today (White and Rees, 1978; Fall and Efstathiou, 1980).

TABLE 1.1: Cosmological parameters as obtained by the Planck Collaboration (Planck Collaboration et al., 2018b) with 68 per cent confidence limits for the ΛCDM model from Planck CMB data, in combination with lensing reconstruction and external data from baryonic acoustic oscillations. Note that the radiation density is estimated directly from the temperature of the CMB from Fixsen (2009).

Parameter	Present day value
Hubble constant	$h = 0.6766 \pm 0.0042$
radiation density	$\Omega_r = 2.47 \times 10^{-5} h^{-2}$
matter density	$\Omega_m = 0.3111 \pm 0.0056$
baryon density	$\Omega_b = 0.0489 \pm 0.0010$
curvature density	$\Omega_k \sim 0$
dark energy density	$\Omega_\Lambda = 0.6889 \pm 0.0056$
linear fluctuation amplitude	$\sigma_8 = 0.8102 \pm 0.0060$
spectral index	$n_s = 0.9665 \pm 0.0038$

Likewise, galaxies form in a similar way: via the collapse of baryonic material that radiates away its thermal energy in order to cool inside of haloes. The infalling gas is initially ionised due to shock heating from accretion (Benson, 2010; Bromm and Yoshida, 2011). Ionised gas is able to support itself in the potential of the halo thorough its own pressure. Thus, in order to collapse and form galaxies it needs to cool by radiating away its thermal energy. The collapse of baryonic material in the centre of the halo deepens its gravitational potential, inducing an adiabatic contraction of the halo which further concentrates the material in the centre of dark matter haloes (Blumenthal et al., 1986; Gnedin et al., 2004). While gas can radiate energy to cool and collapse to the centre, it cannot radiate its angular momentum. It is assumed that the torques from inhomogeneitis in the environment of haloes induce the same angular momentum to both the dark and the baryonic component of haloes. Consequently, the cooled gas that collapsed into the centre of the halo is able to eventually form a rotationally supported disk (Mo, Mao, and White, 1998; Agertz, Teyssier, and Moore, 2011). Once gas cools (while collapsing), it clumps together until it reaches a threshold density to form stars and, eventually, galaxies. Theoretical work has shown that baryonic mechanisms such as feedback from Active Galactic Nuclei (AGN) or supernovae regulate the cooling of the gas and that models which do not implement such mechanisms suffer from excessive star formation due to overcooling gas (Benson et al., 2003). A detailed discussion of such mechanisms is presented in Sec. 1.4.

1.2.1 Cosmological parameters

We finish this section by briefly discussing the cosmological parameters of the currently accepted concordance ΛCDM model. The model has 6 independent parameters needed to fit observations. These parameters are not predicted by the theory. Additionally, some parameters are fixed at "natural" values, e.g. $\omega_\Lambda = -1$. However, the model is allowed to vary some of these parameters when searching for beyond the standard model theories. The rest of the cosmological values are derived from the fit to cosmological observations. The current values of the main present day cosmological parameters of the ΛCDM are given in Tab. 1.1, as obtained by the Planck Collaboration (Planck Collaboration et al., 2018b) with 68 per cent confidence limits from Planck CMB data, in combination with lensing reconstruction and external data from baryonic acoustic oscillations.

The Hubble constant H_0 is usually expressed in terms of the reduced Hubble constant (sometimes colloquially called "little h") as $H_0 = 100h$ km s^{-1} Mpc^{-1}. This parameter is generally obtained from the expansion rate of the local Universe using type Ia supernovae or distant cepheids (Freedman and Madore, 2010; Weinberg et al., 2013).

The radiation density parameter Ω_r is directly derived from the CMB temperature, $T_{\text{CMB}} = 2.7255 \pm 0.0006$ K (Fixsen, 2009) and the Hubble constant. It is primarily determined by the energy density of the photons in the CMB, although neutrinos might also contribute to its value if they are currently considered as relativistic particles.

Measurements from clusters of galaxies (Allen, Evrard, and Mantz, 2011; Mantz et al., 2014) or the temperature distribution of the CMB (Efstathiou, 2001) determine the total matter density parameter, i.e. $\Omega_m = \Omega_c + \Omega_b$, where Ω_c is the cold dark matter density parameter.

The baryonic density parameter Ω_b can be estimated from the ratio of the peaks in the BAO found in the spectrum of the CMB (Weinberg et al., 2013; Addison et al., 2018). From the total matter and baryonic matter density parameters, we can derive the cold dark matter density.

The curvature density Ω_k in the concordance ΛCDM model is usually expressed in terms of the rest of parameters through the cosmic sum rule, i.e. $\Omega_0 = \Sigma_{i=r,m,k,\Lambda}\Omega_{0,i} = 1$. The latest observations show that it is compatible with 0. However, as we previously mentioned, this parameter is allowed to vary for some extended models (Planck Collaboration et al., 2018b; Efstathiou and Gratton, 2020).

Measurements from distant supernovae allow us to infer the rate of expansion of the Universe and determine the dark energy density parameter Ω_Λ (Weinberg et al., 2013; Abbott et al., 2019).

The linear fluctuation amplitude σ_8 is defined as the root-mean-square of matter fluctuations averaged over $8h^{-1}$ Mpc spheres and it allows us to determine the amplitude of the initial density perturbations (see Sec. 1.3). It can be estimated from the number density of cluster in the Universe (Schuecker et al., 2003).

Finally, the spectral index n_s is defined as the power of the initial power spectrum of the primordial fluctuations and its value is determined by the fit to the combined data of the model. As we will see in the following section, its value is critical for inflationary theories.

1.3 Structure formation

According to the standard model of cosmology, ΛCDM, structures form via the hierarchical growth of (gaussian) matter perturbations (see Sec. 1.2). In this section we present the formalism needed to describe this process.

Structure formation can be characterised by the following equations. The gravitational interaction experienced by a non-relativistic fluid of density ρ and pressure p can be described by the Poisson equation

$$\Delta\Psi = 4\pi G\left(\rho + \frac{3p}{c^2}\right) , \tag{1.17}$$

where Ψ is the gravitational potential. The fluid additionally must satisfy both the continuity equation

$$\frac{\partial\rho}{\partial t} + \nabla\cdot\left[\left(\rho + \frac{p}{c^2}\right)\mathbf{v}\right] = 0 , \tag{1.18}$$

where $\mathbf{v}$ is the (3-dimensional) velocity of the fluid; and the Euler equation

$$\left(\rho + \frac{p}{c^2}\right)\left(\frac{\partial\mathbf{v}}{\partial t} + (\mathbf{v}\cdot\nabla)\,\mathbf{v}\right) = -\left(\rho + \frac{p}{c^2}\right)\nabla\Psi - \nabla p . \tag{1.19}$$

These equations, along with an equation of state $p = p(\rho, S)$, where S is the entropy of the system, form a system of equations with seven unknown functions $\Psi, \rho, p, \mathbf{v}$, and S.

Finding the general solution of these equations is a non-trivial exercise, mostly due to the nonlinear nature of the equations. To approach the task at hand, we consider the following approximations. First, we note that we are interested in matter density perturbations, which in ΛCDM are induced by non-relativistic matter. Thus, we can neglect its pressure compared to its density, i.e. $p \ll \rho c^2$.

Next, we want to factor out the expansion of the Universe from our calculations. To achieve this, we express our equations in a reference frame in which the fluid is at rest with

respect to the expansion of the Universe. This frame of reference is called the *comoving* reference frame, and it is defined by the change of coordinates $\mathbf{r} = a\mathbf{x}$, where $\mathbf{r}, \mathbf{x}$ are the physical and the comoving coordinates, respectively.

Finally, motivated by the fact that in ΛCDM structures formed due to matter instabilities induced by small perturbations imprinted in the space-time of the early Universe, we consider small (adiabatic) perturbations about a homogeneous and isotropic background, i.e. $\rho = \bar{\rho}(1+\delta)$, where $\bar{\rho}$ denotes the background matter distribution and δ the small perturbations, i.e. $\delta \ll 1$.

Applying this constrains and combining the continuity equation Eq. (1.18) with the Euler equation Eq. (1.19) we obtain the equation that governs the density contrast evolution $\delta(\mathbf{x}, t)$[3]

$$\frac{\partial^2\delta}{\partial t^2} + 2H\frac{\partial\delta}{\partial t} - 4\pi G\bar{\rho}\delta - \frac{c_s^2}{a^2}\Delta\delta = 0\,, \tag{1.20}$$

where c_s is the speed of sound of the (adiabatic) perturbations.

Eq. (1.20) describes the evolution of matter perturbation, both collisional (i.e. baryons) and collisionless (i.e. dark matter). To solve it we look for solutions in terms of the wave expansion of the density contrast

$$\delta(\mathbf{x}, t) = \frac{1}{(2\pi)^3}\int \delta_k(t) e^{i\mathbf{k}\cdot\mathbf{x}} d^3k\,, \tag{1.21}$$

where $\mathbf{k}$ is the (reciprocal) wave vector. Working in reciprocal space has the advantage that Eq. (1.20) decomposes into separate equations for each value of $\mathbf{k}$. Thus, for simplicity, we analyse the case of a single wave, i.e. $\delta(\mathbf{x}, t) = \delta_k(t)\exp(i\mathbf{k}\cdot\mathbf{x})$. In $k-$space, Eq. (1.20) reduces to

$$\frac{\partial^2\delta_k}{\partial t^2} + 2H\frac{\partial\delta_k}{\partial t} + \left(\frac{c_s^2}{a^2}k^2 - 4\pi G\bar{\rho}\right)\delta_k = 0\,. \tag{1.22}$$

This form highlights the balance between gravity (i.e. $4\pi G\bar{\rho}$) and pressure (i.e. $c_s^2k^2/a^2$) in the dynamics of a perturbation of wave number k. Note how its functional form is similar to a damped harmonic oscillator in which the cosmological expansion term $2H(\partial\delta_k/\partial t)$ acts as the friction term. Eq. (1.22) has two simple analytic solution for each $k-$mode. If the term under parentheses is negative, we obtain exponential growing and decaying solutions[4], whereas if it is positive, we obtain (damped) oscillating solutions.

The interplay between gravity and pressure in Eq. (1.22) introduces a threshold scale that determines if gravitational collapse is possible for a particular perturbation mode. This is known as the *Jeans criterion*. Modes with a wavelength larger than the Jeans length λ_J are unstable to gravitational collapse and can grow, i.e.

$$\lambda = \frac{2\pi a}{k} > \lambda_J \equiv c_s\sqrt{\frac{\pi}{G\bar{\rho}}}\,. \tag{1.23}$$

The Jeans length naturally defines a mass scale, the *Jeans mass*, defined as the enclosed mass in a sphere of radius $R_\mathrm{J} = \lambda_J/2$. Hence, only perturbations more massive than the Jeans mass can collapse, i.e.

$$M_{\mathrm{J},\omega} = \frac{4\pi}{3}\left(\frac{\lambda_J}{2}\right)^3\bar{\rho}_\omega\,. \tag{1.24}$$

Note that the Jeans length depends on all gravitating components through $\bar{\rho}$, while the Jeans mass is defined for a certain component with an equation of state parameter ω.

1.3.1 Dark matter perturbations

We can now proceed to solve Eq. (1.22). As dark matter is the dominant non-relativistic matter component in matter perturbations, then we have that $c_s = 0$. Hence, Eq. (1.22)

[3] Note that now the spatial derivatives are taken in the comoving frame.
[4] We are only interested in the decaying modes, i.e. gravitational collapse.

TABLE 1.2: Growth scaling of matter density perturbations $\delta_{\mathrm{m,k}}$ and the background density $\bar{\rho}$ that sources them, for the three main epochs of the Universe.

	Radiation	Matter	Dark energy
$\delta_{\mathrm{m,k}} \propto$	$\ln a$	a	a^{-2}
$\bar{\rho} \approx$	$\rho_r \propto a^{-4}$	$\rho_m \propto a^{-3}$	$\rho_m \propto a^{-3}$

reduces to

$$\frac{\partial^2 \delta_k}{\partial t^2} + 2H\frac{\partial \delta_k}{\partial t} - 4\pi G\bar{\rho}\delta_k = 0\,. \tag{1.25}$$

Eq. (1.25) describes the evolution of dark matter perturbations across all the epochs of the Universe. As we have discussed in Sec. 1.1.3, the Universe can be described as a perfect fluid made of different components, each of them evolving differently with the scale factor according to Eq. (1.11). This determines three major epoch in the history of the Universe. Therefore, in order to find the time evolution of dark matter perturbations, we need to solve Eq. (1.25) for each epoch, substituting into the $4\pi G\bar{\rho}\delta_k$ term all the potential sources for the matter perturbations. In Tab. 1.2 we summarise the results for the growth scaling of matter density perturbations $\delta_{\mathrm{m,k}}$ and the background density $\bar{\rho}$ that sources them. We can see that dark matter perturbations $\delta_{\mathrm{m,k}}$ can essentially grow only during the matter domination epoch, where they grow proportional to the scale factor, as the growth during the radiation epoch is negligible (as a consequence of the expansion rate of the Universe at that time). During the dark energy epoch, despite matter being the only component abundant enough to collapse, they are suppressed.

1.3.2 Statistics of the perturbations

We conclude this section by discussing the statistical analysis of perturbations, which allows us to infer their properties from observations (for a review, see Tong, 2019). Density perturbations can be expanded into waves as shown in Eq. (1.21). Since we are interested in small perturbations about a background density, Eq. (1.25) ends up being linear in the perturbations, thus each mode of the perturbation evolves independently. In ΛCDM perturbations are thought to be stochastic. Thus, by construction, the spatial average of δ at a given time vanishes, i.e. $\langle \delta(\mathbf{x}, t)\rangle = 0$. The first non-trivial statistic we can construct from a stochastic perturbation is the two-point correlation function ξ_2, i.e.

$$\xi_2 \equiv \langle \delta(\mathbf{x}, t)\delta(\mathbf{y}, t)\rangle = \xi_2(|\mathbf{x}-\mathbf{y}|, t)\,, \tag{1.26}$$

where we used the fact that the Universe is homogeneous and isotropic in the last step. We can interpret the two-point correlation function as the excess probability with respect to a random distribution that two galaxies are separated by a distance $|\mathbf{x}-\mathbf{y}|$ at a given time t. Once again, it is convenient to express the two point correlation ξ_2 in $\mathbf{k}-$space, i.e.

$$\begin{aligned}\langle \delta(\mathbf{k}, t)\delta(\mathbf{k}', t)\rangle &= \int e^{-i\mathbf{k}\cdot\mathbf{x} - i\mathbf{k}'\cdot\mathbf{y}}\langle \delta(\mathbf{x}, t)\delta(\mathbf{y}, t)\rangle d^3x\, d^3y \\ &= \int e^{-i\mathbf{k}\cdot\mathbf{r} - i(\mathbf{k}'+\mathbf{k})\cdot\mathbf{y}}\xi_2(r, t) d^3r\, d^3y \\ &= (2\pi)^3\delta_D^3(\mathbf{k}+\mathbf{k}')\int e^{-i\mathbf{k}\cdot\mathbf{r}}\xi_2(r, t) d^3r\,,\end{aligned} \tag{1.27}$$

where we defined $\mathbf{r} = \mathbf{x}-\mathbf{y}$. The Dirac delta function $\delta_D^3(\mathbf{k}+\mathbf{k}')$ [5] explicitly shows the the two-point correlation function is invariant under translations. In $k-$space, the two-point

[5] The subscript "D" is added to the Dirac delta function δ_D in order to distinguish it from the density contrast $\delta_k(t)$.

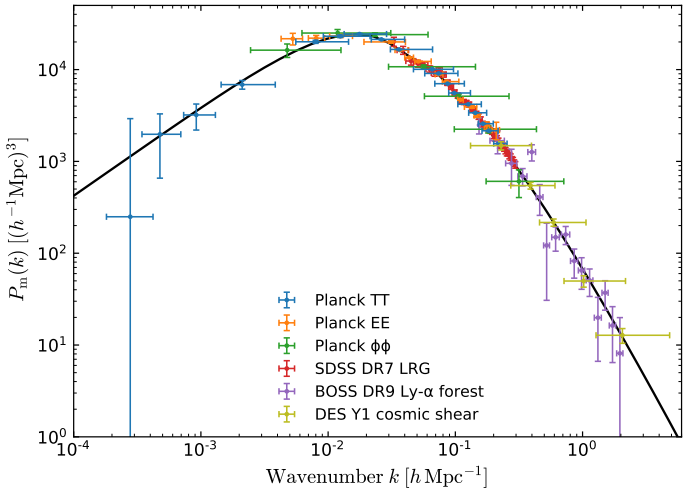

FIGURE 1.3: Linear theory power spectrum $P(k)$ as obtained from different cosmological probes from Planck Collaboration et al. (2018a). There is a remarkable agreement between observational results with the ΛCDM prediction (black line) over scales that span more than three orders of magnitude. Note how at large scales (i.e. low k modes) the power spectrum follows a power law with slope $n_s \sim 1$. (Image credit: ESA and the Planck Collaboration)

correlation function of a perturbation is commonly known as the *power spectrum* $P(k,t)$, i.e.

$$P(k,t) = \int e^{-i\mathbf{k}\cdot\mathbf{r}} \xi_2(r,t) d^3r \,, \tag{1.28}$$

or in spherical coordinates, such that $\mathbf{k}\cdot\mathbf{r} = kr\cos\theta$:

$$P(k,t) = \frac{4\pi}{k} \int_0^\infty r \sin kr\ \xi_2(r,t) dr \,. \tag{1.29}$$

Each mode of the primordial perturbation spectrum is assumed to follow a gaussian distribution and to evolve independently. Thus, providing that the linear theory analysis holds at a time t_i, the power spectrum $P(k)$ time evolution up to a time t_0 can be described in terms of a (scale dependent) transfer function $T(k)$, i.e. $P(k,t_0) = T(k)^2 P(k,t_i)$. The fluctuation evolution of a k mode is determined by the era of the Universe at which it entered the Universe's particle horizon. Note that, as we discussed in Sec. 1.3.1, perturbations can only grow during the matter dominated era. Hence, modes that entered the horizon during the radiation era are effectively "frozen" (i.e. the Meszaros effect, Meszaros, 1974) until the Universe reaches the matter-radiation equality, i.e. $z \sim 3500$. The transfer function $T(k)$ reflects this entry time difference between the modes, which induces a scale at which perturbations deviate from the (quasi) scale-invariant primordial power spectrum, determined by the maximum mode that entered the horizon at matter-radiation equality.

Fits to observational constrains at large scales (i.e. low k perturbation modes) favour power spectra that behave as power laws, i.e. $P(k) \propto k^n$ (Fig. 1.3). In Sec. 1.2.1 we saw that one of the parameters of the ΛCDM model is the spectral index n_s, i.e. the power of the initial power spectrum, which the observational constrains put close to 1. A power spectrum close to $n_s = 1$ (i.e. a Harrison-Zeldovich spectrum) has the property that is (almost) scale-invariant, i.e. the density perturbations have the same amplitude regardless of the scale. In the previous section we anticipated that the value of the spectral index is crucial to inflationary models, since they generate scale-free power spectra. For this reason, they are the favoured mechanisms to explain the origin of the primordial fluctuations in the early Universe and its spatial flatness.

Throughout this section we have exclusively analysed perturbations in the linear regime. However, to understand galaxy formation we need to go well beyond linear perturbation

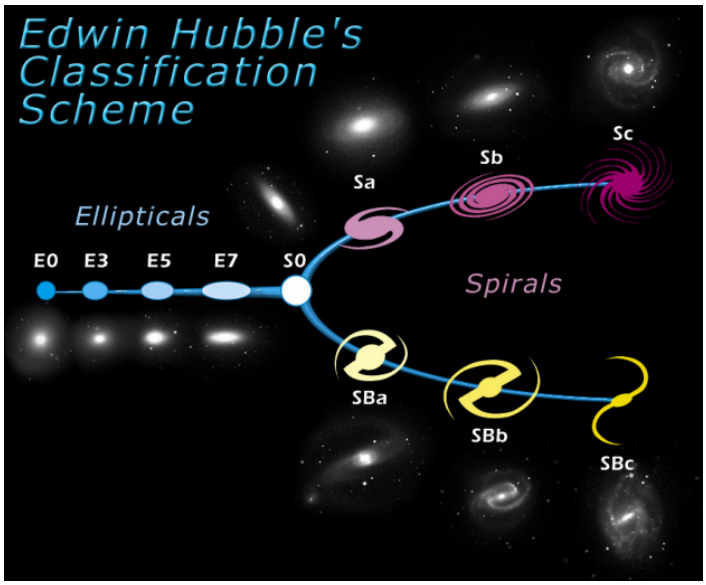

FIGURE 1.4: Hubble's morphological classification of galaxies. (Image credit: Hubble Space Telescope, NASA & ESA)

theory. In the non-linear regime, Eq. (1.17) to Eq. (1.19), plus equations that describe the (magneto)hydrodynamical interaction of baryons, crucial for galaxy formation, must be solved explicitly.

One of the possible ways to describe these processes is via analytical (quasi-linear) formalisms, such as the Zel'dovich approximation (Zel'dovich, 1970; White, 2014), an analytical description of the perturbations in 1st order Lagrangian perturbation theory. Another possible choice is numerical simulations.

1.4 Galaxy evolution

Before we move to the non-linear description of perturbations, we briefly describe some of the key baryonic mechanisms needed for an accurate galaxy formation model.

Observations have shown that colour-magnitude diagrams of galaxies define two populations known as the "blue cloud" and the "red sequence" (Strateva et al., 2001; Bell et al., 2004). These populations can be characterised according to their amount of star formation, their morphology, or their colours (see Baldry et al., 2004, for an in-depth analysis of the galaxy bimodality). In terms of star formation, galaxies in the blue cloud predominantly contain bright, young stars that are blue (i.e. their surface temperature corresponds to a peak emission wavelength at blue frequencies). On the other hand, galaxies in the red sequence tend to be have dimmer, older and redder stars. Following the traditional Hubble tuning fork diagram (Hubble, 1926) for galaxy morphology classification (Fig. 1.4), galaxies in the blue cloud tend to be disc-dominated (i.e. "late-type") galaxies, while the ones in the red sequence are mostly elliptical (i.e. "early-type") galaxies[6]. Colour classifications also reflect this bimodality, as implied by their classification names: galaxies in the red sequence have predominantly red colours, whereas in the blue cloud dominate bluer ones (Fig. 1.5). It is thought that galaxies start their evolution in the blue sequence and, as their star formation decreases, they end up in the red sequence. The study of mechanisms that turn off star formation in a galaxy is known as galaxy *quenching*.

In ΛCDM, galaxies form from the accreted baryonic material in the centres of a dark matter haloes (see the discussion in Sec. 1.2). As haloes grow via hierarchical mergers with other haloes, they are potentially able to gain more baryonic material. Thus, a sensible assumption is that the mass of a galaxy is determined by all the baryonic material that the halo was able

[6]This is an unfortunate nomenclature, as the Hubble turning fork does not represent a *time* evolution of galaxies, i.e. from "early" to "late type" galaxies, but rather the complexity of their appearance, as the names where borrowed from spectral classifications of stars (see Baldry, Glazebrook, and Driver, 2008, for a detailed discussion).

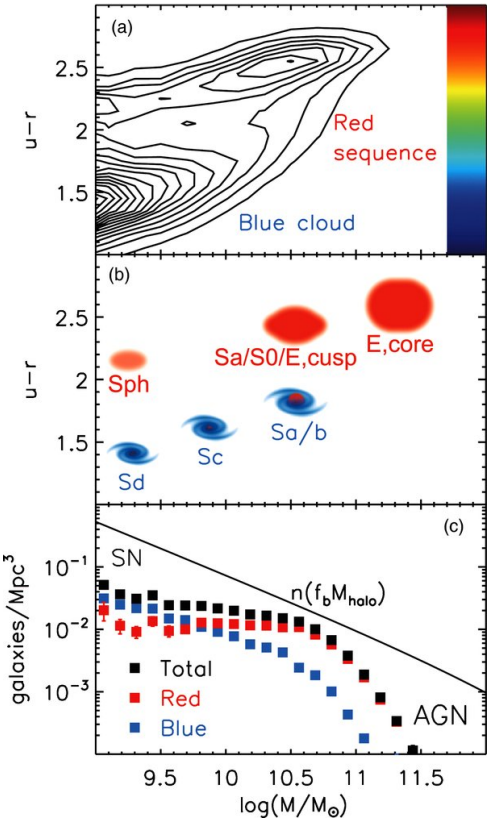

FIGURE 1.5: Galaxy colour (a) and morphology (b) bimodality relation, and baryonic mass function (c). Galaxies are distributed following a bimodal distribution once they are classified by their colours, morphology, and star formation. The baryonic mass function shows how galaxies do not simply follow the cosmological baryonic fraction prediction. Supernova and AGN feedback regulate the amount of star formation at the low and high end of the mass spectrum. (Image credit: Kormendy and Bender, 2012)

to capture during its formation, i.e. $M_{\rm galaxy} = (\Omega_b/\Omega_m)M_{\rm halo}$. Nevertheless, observational results show that this is not the case and that both at low halo masses (i.e. $M_{\rm halo} < 10^10$ $M_\odot$) and at high halo masses (i.e. $M_{\rm halo} > 10^{11}$ $M_\odot$) the mass of a galaxy deviates from this expected behaviour (Fig. 1.5).

In Sec. 1.2 we anticipated that there are primarily two mechanisms which prevent gas from cooling and, consequently, form stars. The first process is supernova feedback. Supernovae are energetic explosive events that happen at the end of the evolutionary stages of massive stars or when white dwarfs are able to trigger a nuclear runaway, i.e. an uncontrollable fusion reaction that eventually detonates the star. These energetic events have three main effects on the evolution of a galaxy. The first one is the ejection of gas. Supernovae are able to drive out the gas out of the galaxy's halo, which reduces the reservoir of gas that can potentially be used to form stars. A second consequence is that it reheats the surrounding cold gas in the halo. As only cold gas is able to collapse to form stars, the reheating of the cold gas contributes to the quenching of the galaxy. Finally, the ejection of the gas in the halo contributes to the chemical enrichment of the environment, which influence the "metal" abundance, i.e. elements heavier than hydrogen and helium, of next generation of stars. Overall, supernova feedback dominates in low mass haloes, as they do not have enough gravitational pull that allows them to recycle the ejected gas through its halo.

The second mechanism is feedback from Active Galactic Nuclei (AGN). AGNs are supermassive black holes that reside in the centre of massive galaxies and emit a characteristic luminosity from the accreted material into them. Similar to supernova feedback, the energetic radiation emitted by AGNs can both heat up and eject the gas in the halo. However, AGN feedback only dominates in massive haloes, where supermassive black holes are able

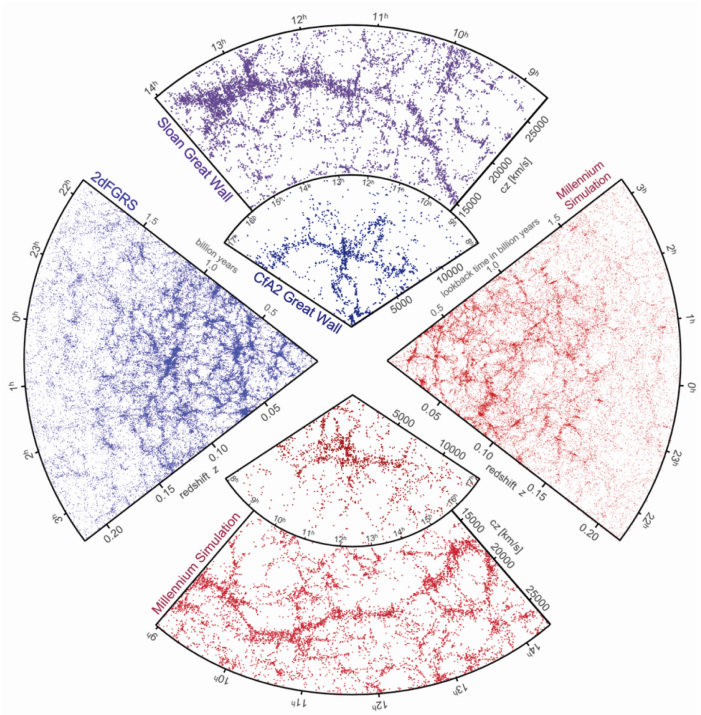

FIGURE 1.6: Large scale structure comparison with mock catalogues from N-body simulations. The top and left wedges show the results from the CfA2, SDSS, and 2dFGRS surveys. On the bottom and right wedges we can see a mock catalogue of the large scale structure obtained from a semi-analytic techniques and N-body cold dark matter simulations. The mock catalogue contains a "Great Wall" structure similar to the observational one, as seen in the small bottom and top wedges, respectively. (Image credit: Springel, Frenk, and White, 2006)

to form.

So far we have discussed processes that are driven by internal properties of the halo, known as *secular* or *mass* quenching mechanisms, i.e. that depend on the stellar mass of the galaxy. However, there are also external or *environmental* processes that are able to quench galaxies, such as mergers between haloes that disrupt the galaxy residing inside them, and depending on the amount of gas involved in the interactions it can result in a further star formation (i.e. "wet" mergers) or it can quench it (i.e. "dry" mergers) (Lin et al., 2008); tidal stripping, i.e. the removal of material from the halo from environmental tidal forces (Moore et al., 2006; Knebe et al., 2006; Park et al., 2007); or ram pressure stripping, the removal of the interstellar medium in infalling galaxies due to the pressure exerted by the host environment (Gunn and Gott, 1972; Arthur et al., 2019; Mostoghiu et al., 2020b).

To properly model galaxy formation, all these physical processes have to be considered (to some extent) in our non-linear description of structure formation.

1.5 Numerical simulations

Numerical simulations provide a description of the non-linear evolution of the total matter, i.e. dark matter and baryons, density perturbations that originated in the early (linear) epoch of Universe (see Sec. 1.3). As a first order approximation, we can model the matter density evolution solely with its dark matter component. In such simulations, we define N bodies to sample the phase space evolution of the matter density of the Universe, where one particle in the simulation generally represents billions of physical particles.

While dark-matter-only simulations cannot fully describe the non-linear evolution of the primordial perturbations, considering that dark matter dominates the gravitational collapse

of perturbations, they are nevertheless useful for understanding processes such as the hierarchical structure formation of ΛCDM (e.g. Fakhouri, Ma, and Boylan-Kolchin, 2010), the density profiles of haloes (e.g. Navarro, Frenk, and White, 1996; Klypin et al., 2016), or the large scale structure of the Universe (e.g. Fig. 1.6 from Springel, Frenk, and White, 2006). Even so, to understand galaxy formation, baryons must be added to numerical simulations. Numerical simulations that include baryonic physics in their modelling by solving their governing equations are denominated (full) hydrodynamical simulations [7].

It is important to remark here that the full set of equations that describe the relevant baryonic processes in a cosmological hydrodynamical simulation cannot be fully solved self-consistently due to the massive computational power required to track the baryon evolution across the typical time-scales of such processes. To overcome this limitation, we only follow the hydrodynamical evolution of the gas component, while mechanism such as star formation, feedback processes, or black-hole evolution are added via numerical prescriptions (i.e. subgrid physics, more on this in Sec. 1.5.2). Thus, the term "full hydrodynamics" refers only to the numerical analysis of the gaseous component in the simulation. Note that, whereas dark-matter-only simulations solve their governing equations using N body methods, full hydrodynamical simulations employ additional techniques to accommodate the complexity of both the dark matter and baryonic components, either by using particle-based methods (similar to the dark-matter component) or grid-based methods (more on these methods in Sec. 1.5.2).

Running a full numerical simulation can be thought as a three step procedure in which we first generate the appropriate initial conditions, then we evolve them in time, and finally we analyse the end product. For a recent review, see Vogelsberger et al. (2020).

1.5.1 Initial conditions

The initial conditions are required to reflect the properties of the primordial matter density field of the early Universe. To achieve this, the dark matter and gas density components are set up to represent a homogeneous and isotropic distribution and to follow the expected baryonic fraction of our Universe. We recall that the early (linear) regime of the Universe described by such initial conditions does not contain stars, as stars form from the primordial (neutral) gas much later on in the simulation, according to the star formation recipe of each hydrodynamical model. Once we define the homogeneous and isotropic distribution, we perturb it according to the cosmological density fluctuations obtained from observational data. The fluctuations can be conveniently described in terms of their wave expansion (see Eq. 1.21). However, observations only constrain its power spectrum $P(k,t)$, i.e. the spatial-averaged squared amplitude of a complex-valued function that characterise the perturbations. Since phases remain unconstrained, we can obtain an infinite number of statistically equivalent realisations of the same power spectrum, i.e. an infinite number of universes statistically equivalent to our own. This uncertainty in the phases of the initial density perturbations in the simulations induce a sample variance in the results as large as 20 per cent for properties of individual objects (Knebe and Domínguez, 2003).

In practice, the numerically generated initial conditions face a series of limitations. First, we can only simulate a finite volume of the Universe, usually chosen to be a box of side length B, with a finite number of dark matter particles N, each with a mass m that is adjusted such that it agrees with the matter density of the Universe Ω_m[8]. To account for the fact that the Universe is infinite[9], i.e. with no physical boundary, we use periodic boundary conditions. Second, whereas the primordial density perturbations are described by an infinite number of wavenumbers, simulations can only probe a limited number of scales, determined by the largest wavelength perturbation that fits the box side-length, and the minimum dark matter inter-particle distance. Ideally, we would want large volumes with large number of particles, i.e. a high resolution simulation that resolves both small and

[7] We make the distinction between full hydrodynamical simulations and semi-analytical models, in which the relevant baryonic physics equations are not solved self-consistently but added as recipes for the interactions.

[8] The limitations in the gas component depend on the approach used to describe it.

[9] The observable Universe is certainly finite. There are multiple definitions for its size. In particular, we can define its radius in terms of the *cosmological* horizon (also known as the *particle* horizon), defined as the maximum distance from which light from particles could have travelled to the observer since the beginning of the Universe.

large scale structures; however, due to their computational requirements, a trade-off must be made between the parameters. Consequently, we have simulations designed for different target scales.

A particularly interesting method for generating initial conditions that alleviates this issue are zoom simulations (Katz and White, 1993; Navarro and White, 1994). In such simulations we first produce a low resolution instance of our simulation. From that low resolution simulation we identify the structure(s) we want with higher resolution. Once selected, we trace back the particles to their initial conditions and re-sample the necessary perturbation modes with more particles. Finally, we re-run the simulation with the increased number of particles. Following this procedure we are able to produce high resolution regions for target objects without substantially increasing the computational time of the simulation (e.g. `NIHAO`, Wang et al. 2015; `Cluster-EAGLE`, Barnes et al. 2017a). In the following chapters, Ch. 2 and Ch. 3, we analyse simulations that use this technique, THE THREE HUNDRED and the CLUES projects, respectively.

Finally, we discuss a method for generating initial conditions that addresses the degeneracy in standard initial conditions, namely, the fact that the phases of the primordial perturbations cannot be determined from observations. Instead of choosing random phases, we constrain them using observational data in such a way that the output of the simulation resembles the actual structure we aim to simulate. This type of simulations are called *constrained* simulations (e.g. Kolatt and Dekel, 1997; Mathis et al., 2002; Martinez-Vaquero, Yepes, and Hoffman, 2007; Lavaux, 2010; Gottlöber, Hoffman, and Yepes, 2010), and will be the main focus of Ch. 3, where we use data from the CLUES project.

1.5.2 Time evolution

Once we generated the initial conditions, the next step is to evolve them according to the equations that describe their interactions. Like in every numerical computation, the equations must be discretised so that they can be integrated. Note that, due to memory limitations, generally only a few number discretised outputs or "snapshots" that show the time evolution of the system after some time-step interval that is chosen in the simulation are saved during the time evolution.

The evolution of the system is described by the generalised Boltzmann equation, which governs the time evolution of the phase-space distribution function of a particle $f(\mathbf{r}, \mathbf{v}, t)$, i.e.

$$\hat{\mathbf{L}}[f] = \mathbf{C}[f] \,, \tag{1.30}$$

where $\hat{\mathbf{L}}$ is the Liouville operator and $\mathbf{C}$ is the collision operator.

Eq. (1.30) determines the probability that a particle will be found in an infinitesimal interval $[\mathbf{r} - d^3r/2, \mathbf{r} + d^3r/2]$, $[\mathbf{v} - d^3v/2, \mathbf{v} + d^3v/2]$. In the Hamiltonian mechanics formalism this can be re-written as

$$\frac{df}{dt} = \frac{\partial f}{\partial t} + \{f, H\} = \mathbf{C}[f] \,, \tag{1.31}$$

where H is the Hamiltonian of the system and $\{\cdot, \cdot\}$ denotes the Poisson bracket. Given two functions of the canonical coordinates q_i, p_i, e.g. $A(q_i, p_i, t)$ and $B(q_i, p_i, t)$, the Poisson bracket is defined as

$$\{A, B\} = \sum_{\mathrm{i}=1}^{N} \left(\frac{\partial A}{\partial q_i} \frac{\partial B}{\partial p_i} - \frac{\partial A}{\partial p_i} \frac{\partial B}{\partial q_i} \right) . \tag{1.32}$$

The total matter density can be classified according to its dynamics into a collisionless component (e.g. dark-matter) and a collisional component (e.g. gas). For the non-relatistic *collisionless* component, Eq. (1.31) reduces to

$$\frac{df}{dt} = \frac{\partial f}{\partial t} + \mathbf{v} \cdot \nabla f - \nabla \Psi \cdot \frac{\partial f}{\partial \mathbf{v}} = 0 \,, \tag{1.33}$$

where Ψ is the gravitational potential. Thus, the Boltzmann equation is coupled with the Poisson equation Eq. (1.17).

To solve this equation we note that Eq. (1.33) tells us that the phase-space distribution function f is *constant* along trajectories $[\mathbf{r}(t), \mathbf{v}(t)]$ that satisfy the equation, i.e. $f(\mathbf{r}, \mathbf{v}, t) =$

$f(\mathbf{r}_0, \mathbf{v}_0, 0)$, Liouville's theorem. From Hamilton's equation of motion for the system, i.e.

$$\begin{aligned} \{\mathbf{r}, H\} &= \frac{\partial H}{\partial \mathbf{v}} \,, \\ \{\mathbf{v}, H\} &= -\frac{\partial H}{\partial \mathbf{r}} \,, \text{with} \\ H &= \frac{1}{2}\mathbf{v}^2 + \Psi(\mathbf{r}) \,, \end{aligned} \tag{1.34}$$

we obtain the equations

$$\begin{aligned} \frac{d\mathbf{r}_{\rm nc}}{dt} &= \mathbf{v}_{\rm nc} \,, \\ \frac{d\mathbf{v}_{\rm nc}}{dt} &= -\nabla\Psi \,, \text{with} \\ \Delta\Psi &= 4\pi G\rho_{\rm tot} \,, \end{aligned} \tag{1.35}$$

where we use the "nc" subscript to indicate that they apply only to the collisionless component of the total matter density $\rho_{\rm tot}$. Note that the Poisson equation is sourced by the total matter density of the Universe, which manifests that dark matter interacts with the other components only through gravity.

The dynamics of collisionless systems are driven by a background interaction with long-range forces. On the other hand, the collisional component, e.g. gas, is driven by local (i.e. short-range) interactions. Thus, Eq. (1.30) now reads

$$\frac{df}{dt} = \frac{\partial f}{\partial t} + \mathbf{v}\cdot\nabla f - \nabla\Psi\cdot\frac{\partial f}{\partial \mathbf{v}} = \left(\frac{\delta f}{\delta t}\right)_{\rm coll} \,, \tag{1.36}$$

where $(\delta f/\delta t)_{\rm coll}$ is the collision integral. If we assume that collisions are entirely described in terms of two-body scattering, i.e. ignoring long-range interactions, the collision term can be expressed as

$$\left(\frac{\delta f}{\delta t}\right)_{\rm coll} = \int |\mathbf{v}_1 - \mathbf{v}_2|\sigma\left(|\mathbf{v}_1 - \mathbf{v}_2|, \Omega\right)\left[f(\mathbf{p}_2')f(\mathbf{p}_1') - f(\mathbf{p}_2)f(\mathbf{p}_1)\right] d\Omega d^3p_2 \,, \tag{1.37}$$

where the primed quantities represent the momenta after the collision, $\sigma\left(|\mathbf{v}_1 - \mathbf{v}_2|, \Omega\right)$ is the differential cross-section of the collision, and Ω the solid angle spanned by the collision.

To obtain the equations of motion, we take the moments of Eq. (1.36) for the mass, momentum and energy of the gas:

$$\begin{aligned} \frac{\partial\rho_c}{\partial t} + \nabla\cdot(\rho_c\mathbf{v}_c) &= 0 \,, \\ \frac{\partial(\rho_c\mathbf{v}_c)}{\partial t} + \nabla\cdot(\rho_c\mathbf{v}_c\otimes\mathbf{v}_c + p\mathbb{1}) &= -\rho_c\nabla\Psi \,, \\ \frac{\partial(\rho_c E)}{\partial t} + \nabla\cdot\left[\mathbf{v}_c\left(\rho_c E + p\right)\right] &= -\rho_c\mathbf{v}_c\cdot(\nabla\Psi) - (\Gamma - L) \,, \text{with} \\ \Delta\Psi &= 4\pi G\rho_{\rm tot} \,. \end{aligned} \tag{1.38}$$

Here ρ_c is now the mass density of the gas component, p its pressure, E its energy, $\otimes$ is the dyadic product, $\mathbb{1}$ the identity vector, and Γ and L the rate of cooling and heating of the gas, respectively (more on this in the following section). We use the "c" subscript to remark that these quantities apply only to the collisional component. Additionally, the gas component is treated as an ideal gas following the closure relations:

$$\begin{aligned} p &= \rho_c(\gamma - 1)\rho_c\epsilon \,, \\ \rho_c\epsilon &= \rho_c E - \frac{1}{2}\rho_c v_c^2 \,, \end{aligned} \tag{1.39}$$

where γ is the adiabatic index of the gas and ϵ the internal energy per unit mass[10]. These set of equations describe the evolution of an ideal gas. However, we might be interested in characterising the evolution of the gas in the presence of magnetic fields, e.g. in galaxies with accreting black holes (i.e. AGNs). Thus, for such cases we need to consider interactions beyond the ideal hydrodynamical equations. To achieve this, hydrodynamical simulations treat the gas component as a quasineutral plasma, i.e. an ionised gas with no net charge density, for the reason that we are interested in its behaviour on time scales longer than the plasma's own oscillations, and on length scales longer than the distances at which electric fields produced by its ions propagate inside the plasma. Under these assumption, Eq. (1.38) are replaced by the (ideal) magnetohydrodynamics equations.

The total matter density evolution is determined by solving the coupled dark matter (i.e. Eq. 1.35) and gas (i.e. Eq. 1.38) equations. Note that the equations of motion describe the temporal evolution of the dark matter and gas component, whereas the Poisson equation couples all the components at a *fixed time*. Thus, first we solve Poisson's equation at a given time to find the gravitational potential that enters the equations of motion. Once the potential is found, it is used to update the phase space configuration of the matter components. After expressing the equations in comoving coordinates to eliminate the expansion of the Universe, we proceed to solve them.

The dark matter equations can be solved by numerically integrating the equations of motion of the N "pseudo-particles" that trace the phase space of the dark matter component. The gas and the Poisson equations, on the other hand, can be approached from two different viewpoints. We can adopt a Lagrangian point of view in which we introduce, in principle, new particles to that trace the phase space of the gravitational positions and velocities along their trajectories to solve the Poisson equation (likewise for the gas component), i.e. a *particle* approach; or we can use an Eulerian point of view and instead describe the evolution at fixed positions in the volume, i.e. a *grid* approach. Both viewpoints have their advantages and disadvantages, and the choosing between them it is typically a matter of convenience for the problem at hand. A review of these methods can be found in Yepes et al. (1997), Dolag et al. (2008), Dolag, Bykov, and Diaferio (2008), and Vogelsberger et al. (2020). Here we highlight a couple of popular techniques for each component.

Gravitational interaction

We start with the gravitational interaction. Particle-based approaches tend to be the favoured approach for solving the Poisson equation, as we can use the *same* particles that we used for tracing the phase space evolution of the matter component. A straightforward particle implementation is the particle-particle method (PP) (e.g. Aarseth, Gott, and Turner, 1979; Sugimoto et al., 1990), in which we just compute the Newtonian force between all particles in the volume. Once the total force is calculated, the equations of motion Eq. (1.35) can be numerically integrated. The PP method is simple to implement but extremely time consuming as the force computation involves N^2 operations. We can reduce this computational load by organising particles intro a "tree structure" according to their relative distances (TREE) (Appel, 1985; Barnes and Hut, 1986). Particles far away from a given contribution are less important for the determination of its total force than near neighbours, thus we can combine distant particles (according to a distance criterion) into a single contribution of their centre-of-mass. This procedure considerably reduces the computational load to $N \log N$, while keeping the advantages of the PP method.

We recall that the gravitational interaction is a long-range force, so particles should only feel the average potential of the rest of the particles. Solving the equations of motions with (particle-based) N-body methods might, nevertheless, introduce unwanted (local) particle collisions in the system from numerical problems. This can be addressed by increasing the number of particles, which also increases the computational cost of the simulation, or by "softening" the gravitational interaction at low distance scales according to some model, e.g. Plummer softening (Plummer, 1911; Athanassoula et al., 2000). However, the issue can be completely avoided if instead we use grid-based methods.

[10]Note that the Hamiltonian used to derive the equations of motion only includes the kinetic and gravitational energy, i.e. we use the same one as in the collisionless case (see Eq. (1.34)). Instead of including the internal energy of the gas in the Hamiltonian, it is taken into account in the closure relations.

Grid-based approaches calculate the gravitational force in the nodes a homogeneous grid defined in the volume, improving the speed of the force calculation but with less accuracy of over particle-based methods. The simplest grid implementation is the particle-mesh method (PM) (Klypin and Shandarin, 1983; White, Frenk, and Davis, 1983). In this approach, particles interact with a background gravitational potential obtained from solving the Poisson equation in the grid instead with each other like in PP methods. The main advantage is that is a computationally fast algorithm (i.e. $N \log N$) that can simulate a large amount of particles. Another advantage is that, as we mentioned earlier, interactions are naturally softened at small scales, but this implies that high density regions below the mesh separation, remained unresolved. A solution to this problem comes in the form of Adaptive Mesh Refinement (AMR) methods (Berger and Colella, 1989; Gnedin, 1995; Kravtsov, Klypin, and Khokhlov, 1997), in which grids are modified adaptively when higher resolution is needed. The mesh can be refined either by changing the grid spacing, creating a finer mesh ("h" refinement); by moving or stretching the grid, e.g. making it non-uniform or adapting it to the fluid ("r" refinement); or by changing the order of accuracy on local grids ("p" refinement). The greatest challenge for grid-based methods are resolving the complicated structure that appear in structure formation, such sheets or filaments from the large scale structure, where regular grids cannot fully adapt to their shape.

To overcome the limitations of the particle and grid-based algorithms, a third approach was developed that combines parts from particle and grid methods to create hybrid methods. Here we highlight some of the available methods. The particle-particle-particle-mesh (P^3M) hybrid (Hockney, Goel, and Eastwood, 1974) approach separates the force calculation into a short range force contribution, calculated with a PP algorithm, with a long range contribution, obtained from a PM method. The transition between the forces is determined by a cut-off in the PP force. Note that the P^3M will behave as a PP method in high density regions, which limits the number of particles that is able to simulate, unlike a pure PM approach. Another hybrid approach is to combine the advantages of the tree hierarchy of TREE codes for short-range force calculations with the long-range force contribution covered by a PM approach, i.e. a Tree-PM scheme (Xu, 1995). This algorithm is similar to the P^3M method in the sense that splits the force calculations in two terms, but instead of calculating the force in high density regions with a PP method it uses a tree algorithm. Particles in low-density regions are evolved according to the PM force contribution, regardless of their distance.

Hydrodynamical interaction

As for the hydrodynamical component (i.e. the gas), once again, we can adopt a particle (i.e. Lagrangian) or grid (i.e. Eulerian) point of view to solve the governing equations. Most particle approaches solve the (magneto)hydrodynamical equations governing the gas using an algorithm called Smoothed Particle Hydrodynamics (SPH, e.g. Gingold and Monaghan, 1977; Springel, 2010; Price, 2012). In the SPH approach, the gas density is sampled by particles which carry the usual N-body information (e.g. position, velocity, or mass[11]) with additional baryon-specific properties such as temperature, pressure, metallicity. SPH consist on performing an interpolation that allows to find the hydrodynamical variables from individual values sampled by N subvolumes, i.e. particles. This can be achieved by substituting continuous fields (i.e. density, temperature) by smoothed estimates over a scale using a normalised interpolation kernel. The smoothed estimates are then replaced in the hydrodynamical equations, and then discretised in terms of particles. One of the drawbacks of traditional SPH methods is their treatment of shocks and discontinues. To alleviate this, a series of terms (e.g. artificial viscosity) are added to the formulation to influence the dynamics of the particles and alleviate the underlying issue (Read and Hayfield, 2012; Hopkins, 2013).

Grid-based methods solve the equations in a, either fixed or adaptive, mesh. The most popular grid-based approach to (magneto)hydrodynamics is the Godunov algorithm (Godunov, 1959; Colella and Woodward, 1984). In the Godunov-approach, the time evolution of gas properties is determined as fluxes through grid zones in a small time interval. Assuming that quantities are constant within cells, where the constant is chosen to give the correct

[11] Gas particles in the initial conditions are set to have a masses that corresponds to the density of baryons in the Universe Ω_b.

cell average of the quantity, the problem reduces to solving 1-dimensional discontinuities between contiguous cells that have different constant values, i.e. the Riemann shock tube problem (e.g. LeVeque, 1992; Saad, 1993). Once the fluxes are determined, the averages of each cell are updated accordingly. The main advantage of this method is that there is no need for introducing artificial viscosity terms to deal with shock (as in traditional SPH algorithms). However, for multidimensional problems (e.g. in the presence of magnetic fields), a 1-dimensional Riemann solver cannot treat each dimension independently: in such situations, the components of the magnetic field might jump across cells and, consequently, induce a non-zero divergence on the field (which violates the Maxwell equations, see e.g. Brackbill and Barnes, 1980).

Subgrid models

We have shown how the dark matter and gas properties can be obtained from solving their respective equations that describe their evolution across the simulation. However, to form galaxies we need stars and a model for the complex baryonic process involved in galaxy formation (see Sec. 1.4). These processes cover a wide dynamic and temporal range and are often unresolved in the large volumes needed by cosmological simulations. To incorporate them, we add analytical (effective) prescriptions, known as *subgrid physics*, that couple the resolved matter with the unresolved scales.

Subgrid physics covers processes such as when clumped cold gas will turn into stars, how gas is ejected in the presence of a supernova, the mass loss of stars due to stellar winds, or how gas behaves in the presence of an AGN. In this section we briefly describe some common prescriptions for the aforementioned processes. To form stars first we need to describe how gas is able to dissipate its energy. Gas mainly cools through collisions, e.g. inverse Compton, Bremsstrahlung, or excitation and ionisation processes, and it is generally assumed that gas collisions beyond two-body interactions are negligible. Such interactions are considered in the gas evolution via the energy equation as sink and source terms in terms of the gas cooling Γ and heating L functions, respectively (see Eq. 1.38), that encode complex cooling channels. The cooling rate of the gas (initially comprised mainly of hydrogen and helium) depends on its abundance of heavier elements, i.e "metals", due to the fact that each metal has its own cooling rate. Metals are mainly formed from the nucleosynthesis processes occurring inside stars and supernovae explosions. As galactic winds from supernovae expel their metals in their environment, the new generation of stars form with a different chemical abundance than their predecessors. Thus, cooling rates change with time and environment.

Once gas cools to a threshold (model-dependent) temperature and density, it collapses and part of its mass is converted to form collisionless star particles. Similar to dark matter and gas, stars cannot be individually resolved. Hence, a single star particle is taken to represent a population of stars with a single age and metallicity, known as as a simple stellar population (SSP), from an assigned stellar initial mass function (IMF) that describes the mass range of the formed stellar populations. Generally, the star formation rate is modelled using a probabilistic sample scheme in which the conversion of gas to stars is proportional to a power law the gas density (gas particle or cell mass), i.e. a Kennicutt-Schmidt law (Schmidt, 1959; Kennicutt, 1998). The phase space of the formed star particles evolves according to the collisionless equations of motion. Additional baryonic processes, e.g. the amount of star mass loss due to galactic winds or stellar evolution, depend on to the details of the subgrid model.

However, if we only account for gas cooling, we overproduce stars, i.e. the commonly known the *overcooling* problem. Realistic star formation models require the addition of processes which regulate the conversion of gas into stars. One of such mechanism is stellar feedback. Stars are able to inject energy and momentum into their environment primarily via supernovae feedback. In order to reach sufficiently effective outflows that eject the gas from galaxies, subgrid models either regulate the thermal energy of the gas, e.g. by temporarily disabling radiative cooling (Stinson et al., 2006) or by artificially heating the affected gas in a probabilistic manner (Dalla Vecchia and Schaye, 2012); or by using a gas wind component decoupled from the governing hydrodynamical equations (Springel and Hernquist, 2003). The overcooling problem is especially predominant in low resolution cosmological simulations. The thermal energy emitted by supernovae explosions is expected to

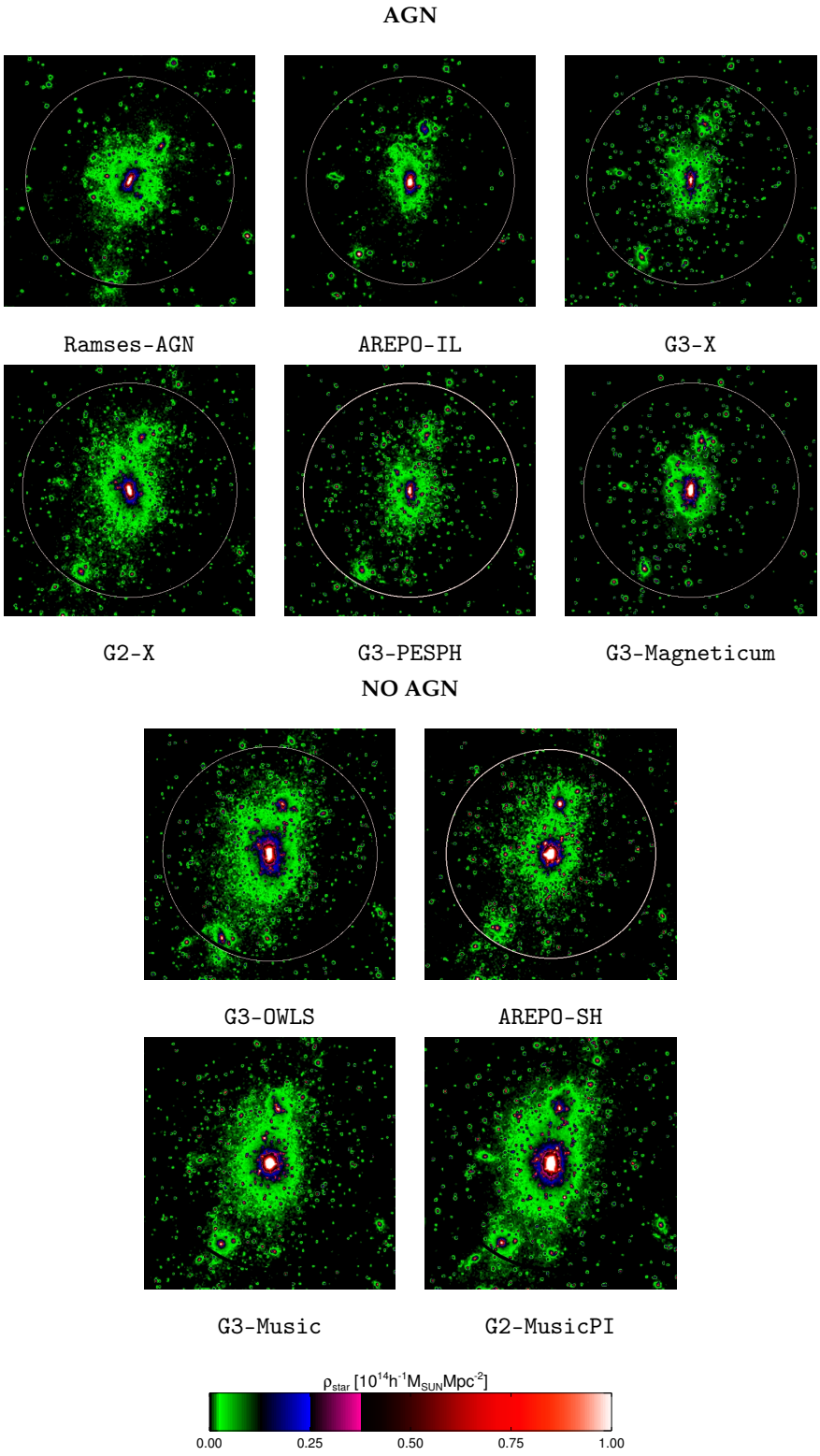

FIGURE 1.9: Projected stellar density of the same halo simulated with different codes. The white circle indicates the obtained halo radius (i.e. $M_{200\rho_{\rm crit}}$, more in Sec. 1.5.3) in each simulation; the black one, the corresponding radius in `G3-Music`. While all the simulations share the same initial conditions, different gravitational and hydrodynamical solvers with distinct subgrid recipes, grouped here by their AGN implementation (or lack thereof), produce diverse stellar distributions. (Image credit: Sembolini et al., 2016b)

expand as a hot bubble and be converted into the kinetic energy of the ejecta. Nevertheless, in such simulations, the spatial scales at which this process occurs is poorly resolved and, consequently, the thermal energy is instead deposited in high-density regions, making the supernova feedback inefficient.

The second process required to control star formation originates from supermassive black holes at the centre of galaxies. The origin of such black holes is not yet understood. Moreover, cosmological simulations cannot resolve them. These limitations are typically addressed by numerically populating dark matter haloes with black holes that accrete the nearby material following a Bondi-Hoyle-like accretion capped at Eddington rates, i.e. an accretion rate proportional to the gas mass density of the medium, the gas speed sound, and the mass of the black hole (Springel, Di Matteo, and Hernquist, 2005). The accretion rate is resolution-dependent. Thus, it is usually artificially increased to compensate for the unresolved phases of the nearby gas. General relativity effects are neglected, and as a consequence, the black holes from two merging galaxies instantly form one single black hole once they encounter each other near their accretion radius. Moreover, accreting supermassive black holes emit radiation and induce outflows in the galactic gas. Their feedback is typically classified into two modes: a radiative one that occurs when the black hole accretion rate is very efficient, typical in galaxies at high redshift, i.e. the "quasar" mode; and a kinetic one when the accretion rate is lower, in massive galaxies at low redshift, i.e. the "radio" mode. Nevertheless, these modes are currently unresolved in cosmological simulations. Hence, AGN feedback is usually calibrated to match observational data, without distinguishing between the mechanisms.

As each numerical simulation has its own collection of subgrid models to characterise the complex interactions during galaxy formation, a N-body approach for the dark-matter and stellar component, and a (magneto)hydrodynamical solver for the gas, their output must be analysed and calibrated according to observational constrains (see Fig. 1.9 for a qualitative analysis of different simulation outputs). However, the inherent degeneracy in the parameters of subgrid physics makes them the largest unknown in galaxy formation simulations. Regardless of the approach, the goal is to obtain a total matter density distribution evolved up to the target time step. What remains is to analyse the end results.

1.5.3 Output analysis

Once we obtained the matter density distribution at the target time, we extract information from the distribution in order to compare it with observational results. To this end, we use object "finders" that allow us to extract the clustering information of the structures that formed in the simulation.

Like with gravity solvers, there are multiple approaches to halo finding. They can be classified by two properties: first, by how much particle phase-space information they require to find the candidate structures, i.e. if they use positions and subsequently they refine their results velocity information, e.g. `SUBFIND` (Springel et al., 2001) or `AHF` (Gill et al., 2004; Knollmann and Knebe, 2009), or if they start with the complete phase-space information, e.g. `6DFOF` (Diemand, Kuhlen, and Madau, 2006), `ROCKSTAR` (Behroozi, Wechsler, and Wu, 2013), or `VELOCIraptor` (Elahi et al., 2019); and second, by the algorithm employed to determine the grouping of particles. The two main algorithms are the spherical-overdensity method (e.g. Lacey and Cole, 1994) and the friends-of-friends method (e.g. Davis et al., 1985). A spherical-overdensity method searches for peaks in the density distribution and grows spherical shells about those peaks until they reach a density cut set by the algorithm. The candidate halo is considered to contain all the particles up to the outermost shell. The friends-of-friends algorithm instead creates links between particles that are closer than some threshold and those that are large enough are considered to be haloes. Both algorithms will remove the particles that are not found to be gravitationally bound to the candidate halo, until the remaining structure is considered gravitationally bound.

Haloes do not have a natural definition for their boundary, hence multiple definitions can be used for determining their spatial extent. We highlight two of them here. Assuming a spherical-shaped halo[12], the first one defines a halo radius r_Δ (and its corresponding

[12]Deviation from a spherical halo are typically estimated in terms of the principal axis of the inertia tensor of the enclosed mass distribution

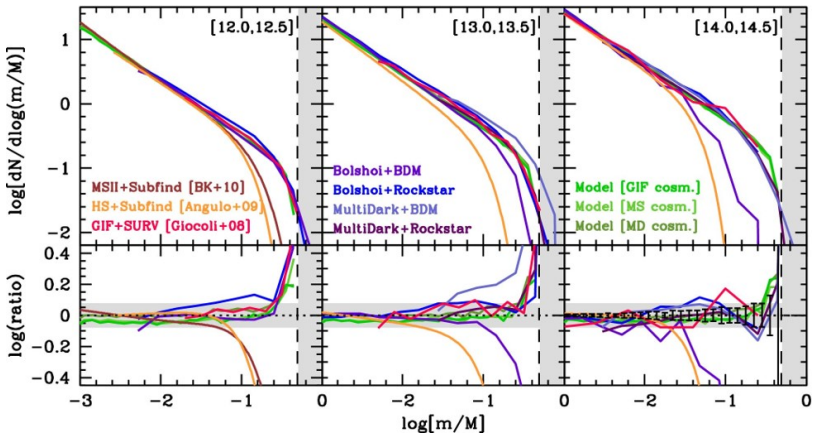

FIGURE 1.10: Subhalo mass functions from different simulations and halo finders (top) as a function of subhalo mass m, normalised by the host mass M. The results are shown for three host mass bins, as indicated by the brackets in the upper-right corner. Green curves represent different model predictions, whereas curves of other colours are the different simulations results. The bottom panels show the ratio between the upper subhalo mass function and a fidual analytical subhalo mass function introduced to fit a semi-analytical model in the analysis. The grey horizontal shaded region represents deviations with respect to the fidual model of ± 20 per cent. Additionally, a grey shaded region is added to indicate the $m/M > 0.5$ region, the forbidden region of the semi-analytical model used in the analysis (but not for the simulations). The error bars in the lower right panel indicate the underlying uncertainties of the simulation. Note how at the massive end models can differ by an order of magnitude. Comparing the deviations with the uncertainties of the simulation we can see this is not a consequence of sample variance but a halo finder effect. (Image credit: van den Bosch and Jiang, 2016)

enclosed mass M_Δ) as the radius at which the total mass density $\rho(r) = M(< r)/(4\pi r^3/3)$ drops below Δ times a reference density, e.g. the critical density $\rho_{\rm crit}$ or the background matter density $\rho_{\rm bg} = \Omega_m \rho_{\rm crit}$ of the Universe, where $M(< r)$ is the enclosed mass up to a radius r and Ω_m is the dimensionless matter density parameter. Typical values for Δ in the literature, motivated by the collapse of a spherical top-hat density profile, are $\Delta = 200, 500$, and 2500. Another popular choice for the radius of a halo is $r_{\rm vir}$, determined by calculating the virial radius of a halo from the collapse of an overdensity in a ΛCDM Universe. An approximate formula to the general problem was presented in Bryan and Norman (1998), where the virial radius $r_{\rm vir}$ can be found from the virial density $\rho(r) = (18\pi^2 - 82q - 39q^2)\rho_{\rm crit}$, with $q = \Omega_{\Lambda,0}/(\Omega_{m,0}a^{-3} + \Omega_{\Lambda,0})$. Note that both r_Δ and $r_{\rm vir}$ can be related by choosing the appropriate Δ parameter and reference density, i.e. $200\rho_{crit} \sim 99\rho_{bg}$. Thus, while the naming convention of halo properties might differ depending on our choice, their sizes (and derived properties) are the same.

Comparisons between halo finders (e.g. Onions et al., 2012; Knebe et al., 2013b; van den Bosch and Jiang, 2016) show that many are in good agreement when determining the positions and integral properties of the haloes. The situation worsens when comparing how they find substructure in haloes and their properties (e.g. Fig. 1.10), as there is no clear definition of "boundness" for subhaloes. These differences arise primarily due to the distinct particle collection methods in object finders and – to a minor extent – the procedure they implement to remove unbound particles in haloes. However, the diversity of subgrid models introduces greater variations in the final results, more than the choice of the object finder used to analyse it.

Once we obtain a catalogue of properties for the haloes in the simulation, the last step consist in comparing the results with observations and, if applicable, re-tuning the model to improve the results.

1.6 Thesis outlook

In this Thesis we aim to extend the current knowledge of galaxy formation by studying how baryonic processes influence properties of galaxies during their evolution. The study is done by using two different approaches to numerical simulations that, since they naturally probe different scales of the Universe, provide results that are complementary to each other. The first approach consists on analysing a set of 324 numerically modelled zoomed galaxy clusters from THE THREE HUNDRED project. The second approach uses zoomed galaxies obtained from constrained simulations of the Local Group from the CLUES project. The description of each dataset, procedure, and results from each method is presented in their own (self-contained) chapters.

The results derived from the analysis of zoom simulations of clusters of galaxies can be found in Ch. 2. The chapter studies how cluster environments influence the evolution of infalling galaxies. We start by describing how the zoom simulations were constructed and we present some general properties of the sample. Next we study the evolution of the total mass density profiles of the main galaxy clusters in the dataset to find how stable is their mass distribution across their formation. Additionally, we analyse their gas mass density profiles and a dark-matter only counterpart to find if gas is a good tracer of the dark matter density profile. Finally, we conclude the chapter by studying the angular momentum of the star component of infalling haloes in the cluster regions. The results from this chapter were published in Cui et al. (2018), Mostoghiu et al. (2019), and Mostoghiu et al. (2020a) (In prep.).

In Ch. 3 we present the results from the second approach, where we use galaxies obtained from (zoomed) constrained simulations. This chapter focuses on star formation-related processes on realistic galaxies. We start by briefly describing the methods in which the constrained simulations were obtained. The first study consist of an in-depth analysis of the radial stellar age gradient of M33. In this analysis we use a numerical counterpart of the Triangulum galaxy (M33) to propose a mechanism that explains the peculiar age profile observed in the real galaxy. The final part of this chapter presents an analysis on the star formation histories of infalling satellite galaxies and proposes a scenario in which star formation can be enhanced after their infall. The results presented in this chapter were published in Mostoghiu et al. (2018), and Di Cintio et al. (2020) (In prep.).

In Ch. 4 we summarise the main findings of this Thesis and provide a discussion on future projects that can be further investigated. A Spanish version of the chapter can be found in Ch. 5.

2 Numerically modelled galaxy clusters: THE THREE HUNDRED project

In this chapter we introduce the THE THREE HUNDRED[1] dataset, a project that aims to model 324 large galaxy clusters with full-physics hydrodynamical zoomed re-simulations.

The chapter is organised as follows. First we briefly describe the process of creating a zoom simulation in Sec. 2.1. In Sec. 2.2 we present in detail the properties of the dataset used for this chapter and we compare some general of its general properties with observations. We follow the general analysis by studying the evolution of their total mass density profiles during their formation in Sec. 2.3. Additionally, we study the gas mass density profiles of the galaxy clusters haloes in the sample and their dark-matter-only counterparts to asses how important are baryonic effects for their radial mass growth. Finally, in Sec. 2.4 we focus on the environmental effects on the (specific) stellar angular momentum of infalling objects in cluster regions. Each section is based on the published work shown at the beginning of each section.

2.1 Zoom simulations

The computational cost of running a hydrodynamical simulation greatly increases when we want to simulate large volumes (i.e. cosmological scales) and at the same time have a reasonable resolution to describe galaxies in the volume (see Sec. 1.5.1 for an overview of the strengths and limitations of the different numerical approaches). As the computational power in our hands is limited, to alleviate this we generate zoom simulations (for a review see Oñorbe et al., 2014).

Zoom simulations are based on the idea that, generally, we are interested in obtaining high resolution descriptions of only certain regions of the simulation, while the rest of the volume remains at the nominal (lower) resolution (e.g. Katz and White, 1993; Navarro and White, 1994). To achieve this (and not disturbing the primordial perturbations applied in the initial conditions in the process), a region (i.e. a Lagrangian volume) is selected from a (collisionless) low-resolution simulation, tracked back to their initial conditions, and re-simulated with an increased resolution. Thus, we can use our the computational power to resolve the interesting regions while the gravitational long range forces are still captured by the low-resolution regions (Navarro and White, 1994; Klypin et al., 2001; Power et al., 2003).

The initial conditions are generated to reflect this: the selected regions have a higher (mass and spatial) resolution, whereas everywhere else the resolution is the same as in the original simulation. As we impose periodic boundary conditions that reflect the infinite nature of the Universe (see Sec. 1.5.1), a series of boundaries of intermediate resolution are initialised around the volumes of interest to capture low frequency perturbation modes (Power and Knebe, 2006). However, certain technical aspects have to be taken into account when introducing different resolutions in the simulation, such as how many boundaries have to be included or how to avoid contamination of low-resolution particles into high-resolution regions. As these questions depend on the details of each code, their treatment is model-dependent (for a study of these issues see Oñorbe et al., 2014).

Finally, once the collisionless component (i.e. dark matter) is properly initialised following this multi-mass technique, the collisional part (i.e. gas) is generally added only to

[1] https://the300-project.org

the high resolution regions in the usual way (i.e. using either particle or grid approach and constrained by the baryonic fraction of the Universe), since on large scales dark-matter dominates the evolution of the large scale structure of the Universe.

2.2 THE THREE HUNDRED dataset

Section based on Cui et al. (2018)

This section describes the dataset and study the differences to observations for fundamental galaxy cluster properties and scaling relations. We find that the modelled galaxy clusters from the dataset are generally in reasonable agreement with observations with respect to baryonic fractions and gas scaling relations at redshift $z = 0$. However, there are still some (model-dependent) differences, such as central galaxies being too massive, and galaxy colours (g-r) being bluer (about 0.2 dex lower at the peak position) than in observations. The agreement in gas scaling relations down to $10^{13}h^{-1}\mathrm{M}_{\odot}$ between the simulations indicates that details of the sub-grid modelling of the baryonic physics only has a weak influence on these relations. We also include — where appropriate — a comparison to three semi-analytical galaxy formation models in the dataset as applied to the same underlying dark-matter-only simulation. We remark that all simulations and derived data products are publicly available.

2.2.1 Introduction

Galaxy clusters are the largest gravitationally bound objects in the Universe and as such they provide a host environment for testing both cosmology models and theories of galaxy evolution. Their formation depends both on the underlying cosmological framework and the details of the baryonic physics that is responsible for powerful feedback processes. Amongst others, these mechanisms regulate the observed properties of the Intra-Cluster Medium (ICM), the size of the central brightest cluster galaxy and the number and properties of the satellite galaxies orbiting within a common dark matter halo. Thus, clusters of galaxies can be considered to be large cosmological laboratories that are useful for pinning down both cosmological parameters and empirical models of astrophysical processes of galaxy formation acting across a range of coupled scales.

Observational and theoretical effort has been devoted to improve our understanding of the formation and evolution of galaxy clusters. On the observational side, multi-wavelength telescopes are designed to observe different properties of galaxy clusters: radio and far infrared data provide information on the cold gas; optical data focuses attention on the stellar properties and provides input to gravitational lensing analyses which target the dark-matter (DM) component; millimetre and X-ray observations target the ICM. Aiding these observations, hydrodynamical simulations of the formation and evolution of galaxy clusters have been a very powerful tool to interpret and guide observations for more than 20 years (Evrard, Metzler, and Navarro, 1996; Bryan and Norman, 1998). However, these extremely large objects with masses $M \geq 10^{15}h^{-1}\mathrm{M}_{\odot}$ are very rare and can only be found in large volumes $V \gg (100h^{-1}\mathrm{Mpc})^3$, and modelling such volumes with all the relevant dark matter *and* baryonic physics, while obtaining sufficient mass and spatial resolution at the same time, is challenging. Therefore, the most commonly used approach is to perform so-called "zoom" simulations, i.e. selecting an object of interest from a parent dark matter simulation and only adding baryonic physics (at a much higher resolution) in a region about that object (see Sec. 2.1). This strategy has led to valuable results, but in order to be of statistical significance one would need to run hundreds – if not thousands – of such zoom simulations, which is what workers in the field are striving for at the moment.

The generation of substantial samples of highly resolved galaxy cluster simulations that include all the relevant baryonic processes has seen great advances in the last years, e.g. the 500 MUSIC clusters (Sembolini et al., 2013), the sample of 29 clusters of Planelles et al. (2013), the 10 RHAPSODY-G clusters (Wu et al., 2015), the 390 MACSIS clusters (Barnes et al., 2017b), the 30 CLUSTER-EAGLE (Barnes et al., 2017a) and 24 related HYDRANGEA clusters (Bahé et al., 2017). The mass resolution of these zoom simulations varies with each sample, covering the range of dark matter particle masses $m_{\mathrm{DM}} = 9.7 \times 10^6 h^{-1}\mathrm{M}_{\odot}$ for HYDRANGEA

and CLUSTER-EAGLE up to $4.4 \times 10^9 h^{-1}\mathrm{M}_\odot$ for the large MACSIS sample. There are additionally cluster samples extracted from full box simulations, e.g. COSMO-OWLS (Le Brun et al., 2014) and its follow-up BAHAMAS (McCarthy et al., 2017) featuring hundreds of galaxy clusters, but the majority with masses lower than $10^{14.5} h^{-1}\mathrm{M}_\odot$ and at a mass resolution of $m_{\mathrm{DM}} \sim 4 \times 10^9 h^{-1}\mathrm{M}_\odot$.

In a series of precursor papers (i.e. the NIFTY cluster comparison project introduced in Sembolini et al., 2016a; Sembolini et al., 2016b) the authors investigated the differences in cluster properties arising from simulating *one* individual galaxy cluster with a variety of different numerical techniques including standard SPH, modern[2] SPH, and (moving) mesh codes. The results obtained there led them to the choice of using the modern SPH code `GADGET-X` which includes an improved SPH scheme and the implementation of black hole (BH) and active galactic nuclei (AGN) feedback compared to the fiducial `GADGET-MUSIC` code.

The primary goal of this section is to introduce THE THREE HUNDRED[3] project and its associated dataset that maximises the ratio between number of objects and mass resolution: 324 regions of radius $15 h^{-1}$Mpc – having a cluster with mass $M_{200} > 6.42 \times 10^{14} h^{-1}\mathrm{M}_\odot$ at its centre – have been modelled with a combined mass resolution of $m_{\mathrm{DM}} + m_{\mathrm{gas}} = 1.5 \times 10^9 h^{-1}\mathrm{M}_\odot$. This is, in fact, the same resolution as used for the previous MUSIC clusters, but the difference here lies in an improved modelling of subgrid physics and an application of a modern numerical SPH scheme[4]. We detail the hydrodynamical simulations, and the procedures for producing the cluster catalogue. We also present generic results, such as the dynamical state, baryon fraction, and optical/gas scaling relations. In addition, we add to the plots – where possible – the results from three semi-analytical galaxy formation models `GALACTICUS` , `SAG` , and `SAGE` , noting that they have been applied to the same dark-matter-only simulation that formed the basis for the selection of the clusters presented here (see Knebe et al., 2018, for the public release of the corresponding catalogues). Although this is not the first time that a joint analysis of hydrodynamical simulations with SAMs has been performed (for example, Saro et al., 2010; Cui et al., 2011; Monaco et al., 2014; Guo et al., 2016), it is, to our knowledge, the first time such an approach has been applied to a large number of galaxy clusters. Detailed comparisons between the models and further investigation into different aspects of the cluster properties have been presented in companion papers (Wang et al., 2018; Mostoghiu et al., 2019; Arthur et al., 2019; Ansarifard et al., 2020; Haggar et al., 2020; Kuchner et al., 2020; Li et al., 2020; Knebe et al., 2020; Mostoghiu et al., 2020a; Mostoghiu et al., 2020b)

This section is structured as follows: we begin by describing the properties of the cluster sample in Sec. 2.2.2, which also includes a description of the hydrodynamical methods and of the semi-analytic models. We briefly present our results for cluster bulk properties and for the relevant relations in different wavebands in Sec. 2.2.3. We conclude our results in Sec. 2.2.4.

2.2.2 Sample overview

Our dataset originates from extracting 324 spherical regions centred on each of the most massive clusters identified at $z = 0$ by the friends-of-friends (FoF) phase-space halo finder `ROCKSTAR` [5] (Behroozi, Wechsler, and Wu, 2013) within the dark-matter-only MDPL2, MultiDark simulation (Klypin et al., 2016)[6]. In Tab. 2.1 we show the cosmological parameters of the MDPL2 simulation, which are those of the 2015 *Planck* mission (Planck Collaboration et al., 2016). The MDPL2 is a periodic cube of comoving length $1 h^{-1}$Gpc containing 3840^3 dark matter particles, each of mass $1.5 \times 10^9 h^{-1}\mathrm{M}_\odot$.

[2] We define "modern" as those SPH implementations that adopt an improved treatment of discontinuities. See Sec. 1.5.2.

[3] `https://the300-project.org`

[4] Technically speaking, these are *not* zoom simulations in the traditional sense, as we do not increase the mass resolution in a region of interest. We instead decrease the resolution in outside the regions of interest (while simultaneously adding gas to the region of interest) in order to enable the comparison with our semi-analytical models, which need single-mass dark-matter-only simulations.

[5] `https://bitbucket.org/gfcstanford/rockstar`

[6] The MultiDark simulations are publicly available at the `https://www.cosmosim.org` database.

TABLE 2.1: Parameters of THE THREE HUNDRED simulations.

	Value	Description
$\Omega_{\rm m}$	0.307	Total matter density parameter
$\Omega_{\rm b}$	0.048	Baryon density parameter
Ω_Λ	0.693	Cosmological constant density parameter
h	0.678	Hubble constant in units of 100 km s^{-1} Mpc^{-1}
σ_8	0.823	Power spectrum normalisation
$n_{\rm s}$	0.96	Power index
$z_{\rm init}$	120	Initial redshift
$\epsilon_{\rm phys}$	6.5	Plummer equivalent softening in h^{-1}kpc
L	1	Size of the MDPL2 simulation box in h^{-1}Gpc
$R_{\rm resim}$	15	Radius for each re-simulation region in h^{-1}Mpc
$m_{\rm DM}$	12.7	dark matter particle mass in $10^8 h^{-1}{\rm M}_\odot$
$m_{\rm gas}$	2.36	gas particle mass in $10^8 h^{-1}{\rm M}_\odot$

The full-physics hydrodynamical simulations

The 324 clusters at the centre of each re-simulation region were selected initially as those with the largest halo virial mass[7] at $z = 0$ with $M_{\rm vir} \gtrsim 8 \times 10^{14} h^{-1}{\rm M}_\odot$. The centres of their dark matter haloes serve as the centre of a spherical region with radius $15h^{-1}$Mpc, for which initial conditions with multiple levels of mass refinement have been generated using the fully parallel GINNUNGAGAP[8] code. Dark matter particles within the highest resolution Lagrangian regions are split into dark matter and gas particles, according to the assumed cosmological baryon fraction Ω_b/Ω_m listed in Tab. 2.1. The dark matter particles outside this region are successively degraded in multiple layers (with a shell thickness of $\sim 4h^{-1}$Mpc) with lower mass resolution particles (increased by 8 times for each layer) that eventually provide the same tidal fields yet at a much lower computational costs than in the original simulation[9]. As the size of the re-simulated region is much larger than the virial radius of the cluster it surrounds, each region also contains many additional groups and filamentary structure which could be physically associated with the cluster they surround.

The initial conditions – also publicly available – were run with the "modern" SPH code GADGET-X . A total of 128 different snapshots have been stored for each simulation from redshift $z = 17$ to 0. We also run the same simulations with our fiducial GADGET-MUSIC code (Sembolini et al., 2013). Both codes are based on the gravity solver of the GADGET3 Tree-PM code (an updated version of the GADGET2 code; Springel, 2005). However, even though both use Smoothed-Particle Hydrodynamics (SPH) to follow the evolution of the gas component, they apply different SPH techniques as well as rather distinct subgrid prescriptions. GADGET-X includes an improved SPH scheme (Beck et al., 2016) with artificial thermal diffusion, time-dependent artificial viscosity, high-order Wendland C4 interpolating kernel and wake-up scheme. These features improve the SPH capability of tracking gas-dynamical instabilities and mixing processes by better describing the discontinuities and reducing the clumpiness instability of gas. They also minimise the viscosity away from shock regions and especially in rotating shears. On the other hand, GADGET-MUSIC uses the classic entropy-conserving SPH formulation with a 40 neighbour M3 interpolation kernel. The differences

[7] The halo virial mass is defined as the mass enclosed inside an overdensity of ∼98 times the critical density of the Universe (Bryan and Norman, 1998). See Sec. 1.5.3 for an approximate analytical form of this definition.

[8] https://github.com/ginnungagapgroup/ginnungagap

[9] The initial conditions for these clusters are publicly available in GADGET format and can be downloaded from http://music.ft.uam.es upon request. We have also produced higher resolution initial conditions corresponding to an equivalent resolution of 7680^3 particles, for a sub-sample of the cluster catalogue.

TABLE 2.2: Summary of the baryonic models for the two full-hydrodynamics simulation codes in `The Three Hundred` project.

Baryon physics	`GADGET-MUSIC`	`GADGET-X`
Gas treatment		
homogeneous UV background	Haardt and Madau (2001)	Haardt and Madau (1996)
Cooling	metal independent	metal dependent (Wiersma et al., 2009)
Star formation and stellar feedback		
Stellar model	Springel and Hernquist (2003)	Tornatore et al. (2007)
Threshold for star forming	0.1 cm^{-3}	0.1 cm^{-3}
Initial Mass Function	Salpeter (1955)	Chabrier (2003)
Kinetic feedback	Springel and Hernquist (2003)	Springel and Hernquist (2003)
Wind velocity	400 km s^{-1}	350 km s^{-1}
Thermal feedback	2-phase model (Yepes et al., 1997)	only set the hot phase temperature
Gas mass loss	via galactic winds	no
BH and AGN feedback		
BH seeding	no	$M_{bh} = 5 \times 10^6 h^{-1} M_\odot$ for $M_{FoF} \geq 2.5 \times 10^{11} h^{-1} M_\odot$
BH growth	no	Individual accretion of hot and cold gas
AGN feedback	no	Steinborn et al. (2015)

in baryon treatment have been summarised in Tab. 2.2. For more details and the implications of the code differences see the previous comparison papers (Sembolini et al., 2016a; Sembolini et al., 2016b).

All data was then analysed with a standardised pipeline that includes the spherical-overdensity halo finder `AHF` [10] (Gill et al., 2004; Knollmann and Knebe, 2009) which self-consistently includes both gas and stars in the halo finding process and automatically identifies haloes and substructure (subhaloes, subsubhaloes, etc.). For each halo, we compute the radius R_{200}, i.e. the radius r at which the density $M(< r)/(4\pi r^3/3)$ drops below $200\rho_{crit}$ [11] (see Sec. 1.5.3). Here ρ_{crit} is the critical density of the Universe at the respective redshift. Subhaloes are defined as haloes which lie within the R_{200} region of a more massive halo, the so-called host halo. As subhaloes are embedded within the density of their respective host halo, their own density profile usually shows a characteristic upturn at a radius $R_t \lesssim R_{200}$, where R_{200} would be their actual radius if they were found in isolation. We use this "truncation radius" R_t as the outer edge of the subhalo. Hence, subhalo properties (i.e. mass, density profile, velocity dispersion, rotation curve) are calculated using the gravitationally bound particles inside the truncation radius R_t. For a host halo, which contains the mass of their subhaloes, we calculate properties using the radius R_{200}. Halo merger trees, that link objects between different redshifts (i.e. snapshots), were constructed using `MergerTree` which forms part of the `AHF` package.

We also calculate luminosities in different spectral bands from the stars within the haloes by applying the stellar population synthesis code `STARDUST` (see Devriendt, Guiderdoni, and Sadat, 1999, and references therein for more details). This code computes the spectral energy distribution from far-UV to radio, for an instantaneous starburst of a given mass, age and metallicity. The stellar contribution to the total flux is calculated assuming a Kennicutt initial mass function (Kennicutt, 1998).

The full dataset consists of 324 re-simulated regions, which cover a much larger volume (out to 15 h^{-1}Mpc in radius) than the central halo's virial radius and hence our sample includes many other objects outside that sphere. These objects are composed of haloes, groups and filaments, which allow us to investigate the pre-processing of the galaxy cluster as well as its large-scale environment. As some of the objects close to the boundary could be contaminated by low resolution particles in the hydrodynamic simulations, we explicitly checked that all the objects included in the comprehensive catalogue do not contain any low

[10] `http://popia.ft.uam.es/AHF`

[11] Similarly, the subscript 500 used in this paper later are for haloes defined with enclosed overdensities of 500 times the critical density of the Universe.

TABLE 2.3: Summary of the main properties of the semi-analytical models in `The Three Hundred` project.. We only list here whether or not the model has been re-calibrated to the MDPL2 simulation, how it treats orphan galaxies (i.e. galaxies devoid of a dark matter halo), whether it features intra-cluster stars, and how luminosities are available. There are certainly many more differences in the exact implementation of the baryonic physics, but we refer the reader to the model presentation for those details.

SAM	Re-calibration	Orphan galaxies	Intra-cluster stars	Luminosities
`GALACTICUS`	no	yes, but without positions/velocities	no	yes
`SAG`	yes	yes, with full orbit integration	yes	yes
`SAGE`	yes	no	yes	only for a sub-volume via TAO

resolution particles. In what follows we refer to this dataset, which consists of all the uncontaminated haloes from all the simulations as the "comprehensive" sample (see App. A for details).

The semi-analytical models

The aforementioned MDPL2 dark-matter-only simulation has been populated with galaxies by three distinct SAMs, i.e. `GALACTICUS` (Benson, 2012), `SAG` (Cora et al., 2018), and `SAGE` (Croton et al., 2016). The public release of the resulting catalogues can de found in Knebe et al. (2018). The same 324 regions (using the same radius cut) have also been extracted from the SAMs' halo and galaxy catalogue that covers the entire $1h^{-1}\mathrm{Gpc}^3$ volume of the parent MDPL2 simulation. This data set constitutes the counterpart sample of the hydrodynamical catalogue, which will be referred as the comprehensive sample as well. This allows for a direct comparison of the same galaxy clusters as modelled by our cosmological simulation codes detailed above. We briefly summarise the salient differences between these SAMs in Tab. 2.3, for a more detailed presentations of the three models we refer to Knebe et al. (2018) . Note that `SAGE` calculates luminosities in post-processing via the Theoretical Astrophysical Observatory (TAO[12], Bernyk et al., 2016), which is currently only possible for a sub-volume of the full $1h^{-1}$Gpc box. Therefore, `SAGE` will not enter any luminosity-related plots.

2.2.3 Results and discussion

Before quantifying the differences in various cluster properties, we first illustrate in Fig. 2.1 the distributions of simulated galaxies and dark matter within a cluster ($r \leq R_{200}$) from one of our re-simulated regions, from both hydrodynamical simulations (upper row) and from SAMs (lower row). Each galaxy is represented by a sphere with size proportional to stellar mass that includes halo stars for the two hydrodynamical simulation, but only uses the stellar mass of the central galaxy for the SAMs. Their colours are based on their SDSS r, g, and u band luminosities. The background colour map indicates the dark matter density field, which is produced by the `Py-SPHViewer` code (Benitez-Llambay, 2015). The two circles mark the R_{200} (outer) and R_{500} (inner) radii.

It is apparent that the galaxies marked in the different panels are neither exactly in the same position nor do they have the same size for the hydrodynamical simulations. This is not surprising given that the dynamics within the virialised region is non-linear and so small differences in orbit become rapidly amplified. That said, the underlying dark matter density field is visually similar with a large infalling group to the south-east. Both R_{200} and R_{500} are recovered well by the re-simulation. The galaxies also differ due to the varying treatment of baryonic processes, as seen in e.g. Sembolini et al. (2016a), Sembolini et al. (2016b), Elahi et al. (2016), Cui et al. (2016b), and Arthur et al. (2017). Note that the galaxy positions are identical for the two SAMs as they reflect the positions of the dark matter haloes in the underlying dark-matter-only simulation which are the same. The apparent larger sizes for the hydrodynamical galaxies can be related back to the inclusion of halo stars. In agreement with previous studies (for example Ragone-Figueroa et al., 2013; Cui et al., 2014; Cui et al.,

[12] http://tao.asvo.org.au

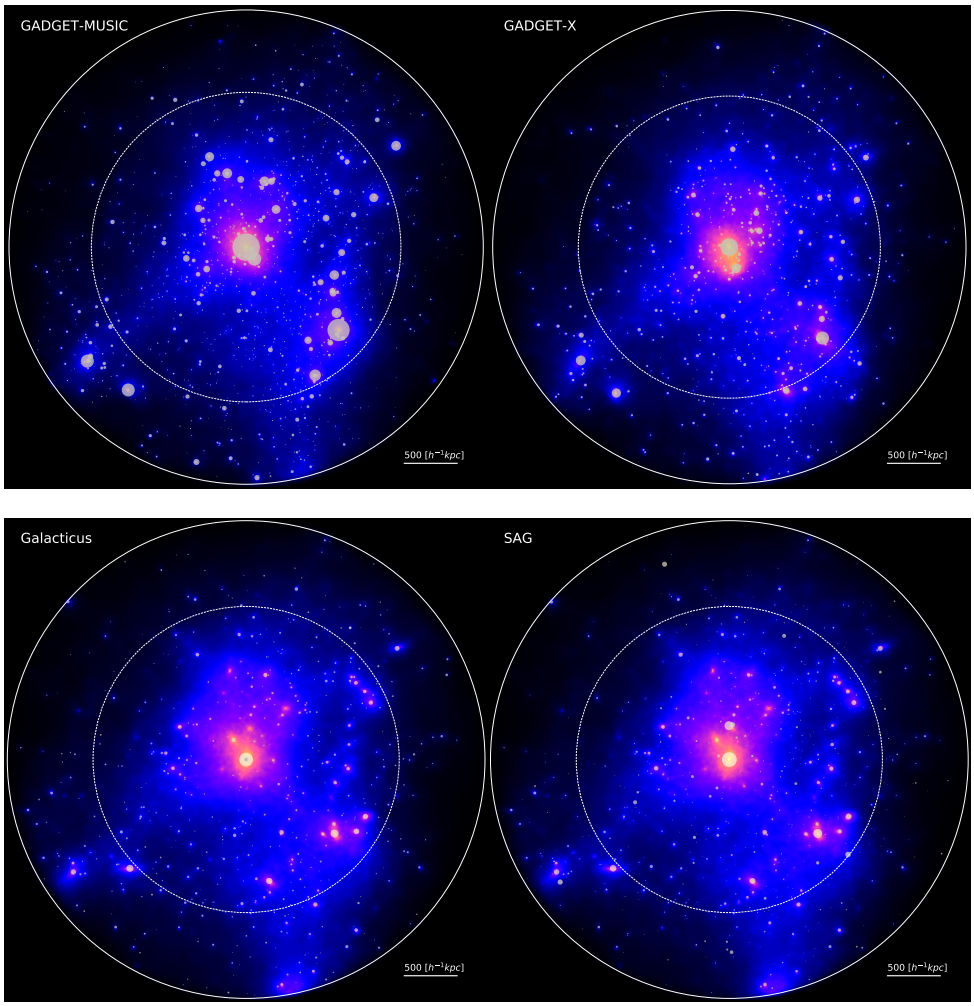

FIGURE 2.1: The distribution of galaxies within R_{200} of the most massive cluster within one re-simulated region from the dataset (region 1). The upper row shows the results from `GADGET-MUSIC` (left) and `GADGET-X` (right). The lower row shows the results from the SAMs `GALACTICUS` (left) and `SAG` (right). The projected dark matter density is shown in the background with a blue-red colour map. Galaxy colour is taken from their SDSS r, g, and u band magnitude and the symbol size is proportional to stellar mass. The two circles mark the radii R_{200} (outer circle) and R_{500} (inner circle).

2016b), the galaxy stellar masses are significantly larger for GADGET-MUSIC , which does not include a model for AGN feedback.

Halo properties

In this section, we focus on the results from the hydro simulations, noting that the properties of the haloes of the SAM galaxies are identical to the MDPL2 halo properties presented elsewhere (Klypin et al., 2016; Knebe et al., 2018).

Baryon effects on halo mass In order to compare individual clusters between the original MDPL2 simulation and the 324 re-simulated regions the haloes need to be matched. There is generally a direct 1-to-1 alignment between the largest object within the original simulation and the re-simulated region, as illustrated in Fig. 2.1. Both the original MDPL2 region and the resimulated region have been (re)processed using AHF . This ensures exact consistency between the halo finder definitions, i.e. it avoids effects introduced by using results from different halo finders (Knebe et al., 2011a; Knebe et al., 2013a). Further, AHF can extract haloes self-consistently from simulations including gas and stars as well as dark matter. We use the halo centre position as the primary criteria for matching the clusters and select the one with the nearest mass when there are multiple matches. As previously mentioned the exact halo positions will have moved slightly from those in the original dark-matter only simulation but these changes are generally small (at the level of a few percent of the virial radius in most cases, Cui et al., 2016b). Occasionally the differences are larger, typically due to the presence of an ongoing merger. It has been shown that halo finders struggle to uniquely track the main halo through a merger and rather treat the two participating objects as a host-subhalo system (Behroozi et al., 2015). Furthermore, the cluster centre can flip between different density peaks (subhaloes) due to baryonic processes (Cui et al., 2016a). That said, in our worst-case scenario, we have two matched haloes with ~ 40 per cent mass difference caused by a massive merging subhalo. In general cases, these different kinds of mismatching only happen for the dynamically un-relaxed clusters, not for the relaxed ones.

Accurate estimates of cluster masses are very important for constraining cosmological parameters and models (i.e., Bocquet et al., 2016; Sartoris et al., 2016). Thus, we present here a quantitative comparison of the halo masses as found in the hydrodynamical simulations with their respective counterparts from the dark-matter-only MDPL2 simulation (see Cui and Zhang, 2017, for a review of the baryon effect). Fig. 2.2 shows the mass ratio of clusters in GADGET-MUSIC (red circle and lines) and GADGET-X (blue star and lines) to their MDPL2 counterparts; M_{200} is shown in the left-hand side panel and M_{500} in the right-hand side panel[13]. In order to reduce any issues due to mismatching, we select a sample of dynamically relaxed clusters (see below for details) from the complete sample and repeat the comparison.

The mass ratio for M_{200} from both hydrodynamical simulations is very close to unity (with the median difference lying basically within 1 per cent), with a scatter less than ~ 5 per cent (~ 2.5 per cent for the dynamically relaxed sub-sample). At the low mass end, GADGET-X (for both samples) tends to have about 1 per cent higher mass than its MDPL2 counterpart. However, the M_{500} mass in both sets of hydrodynamical simulations tends to be several (up to 6) per cent higher than its dark-matter only counterpart below $\sim 9 \times 10^{14} h^{-1}\mathrm{M}_{\odot}$. Above this halo mass the ratio drops to around 1 again. It is worth noting that for M_{500} there is a larger scatter of ~ 8 per cent for the complete sample and ~ 4 per cent for the relaxed sub-sample. We ascribe this larger mass change for M_{500} to baryonic processes which have a larger effect closer to the cluster's centre and for the less massive haloes. The two simulation codes show similar results for $M \gtrsim 10^{15} h^{-1}\mathrm{M}_{\odot}$ at both overdensities, which means that the baryon physics has little influence on both M_{500} and M_{200} at this cluster mass range. For the M_{200} mass changes, this is in agreement with previous similar comparisons (e.g. Cui et al., 2012; Cui, Borgani, and Murante, 2014; Cui et al., 2016b). For M_{500}, Cui, Borgani, and Murante, 2014 reported a slight mass decrease when AGN feedback is included and a slight mass increase without AGN feedback. At this halo mass range, $M_{500} > 10^{14.5} h^{-1}\mathrm{M}_{\odot}$, the difference between GADGET-X and Cui, Borgani, and Murante (2014) could be caused by

[13] The M_{500} sample was constructed by using AHF to find the largest halo contained within each of the 324 clusters of the mass-complete sample (and matching these as before).

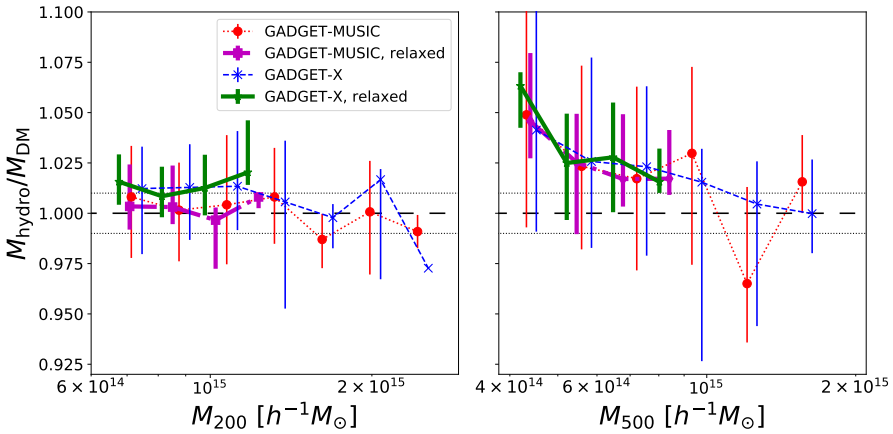

FIGURE 2.2: The mass ratio between matched clusters at $z = 0$ identified in the hydrodynamical simulations ($M_{\rm hydro}$) and in the corresponding cosmological dark-matter-only run MDPL2 ($M_{\rm DM}$) for M_{200} (left panel) and M_{500} (right panel) as a function of $M_{\rm DM}$. The complete sample used here is represented by thin lines, while the dynamically relaxed sub-sample is in thick lines. The median value for each mass-bin is shown via the symbols (red dots for `GADGET-MUSIC` and blue stellar symbols for `GADGET-X`) with error-bars indicating the 16$^{\rm th}$ and 84$^{\rm th}$ percentiles. The black horizontal long-dashed and dotted lines indicate equivalent mass and 1 per cent variation respectively.

either a sample effect (Cui, Borgani, and Murante, 2014, studied very few clusters) or due to the details of the baryonic model implemented in the simulation.

Dynamical Relaxation To determine the dynamical state of the cluster sample we study three indicators, following Cui et al. (2017), specifically:

- the virial ratio $\eta = (2T - E_{\rm s})/|W|$, where T is the total kinetic energy, $E_{\rm s}$ is the energy from surface pressure and W is the total potential energy,
- the centre-of-mass offset $\Delta_{\rm r} = |R_{\rm cm} - R_{\rm c}|/R_{200}$, where $R_{\rm cm}$ is the centre-of-mass within a cluster radius of R_{200}, $R_{\rm c}$ is the centre of the cluster corresponding to the maximum density peak of the halo. Using the position of the minimum of the gravitational potential would give a similar result as investigated by Cui et al. (2016a).
- the fraction of mass in subhaloes $f_{\rm s} = \sum M_{\rm sub}/M_{200}$ where $M_{\rm sub}$ is the mass of each subhalo.

We adopt the following criteria to select dynamically relaxed clusters: $0.85 < \eta < 1.15$, $\Delta_{\rm r} < 0.04$ and $f_{\rm s} < 0.1$, which need to be satisfied at the same time (see, for instance, Neto et al., 2007; Knebe et al., 2008; Power, Knebe, and Knollmann, 2012). Note that we use here a slightly larger limit for $f_{\rm s}$ than in Cui et al. (2017). This is because (1) R_{200} is used instead of the virial radius[14], and (2) this threshold for $f_{\rm s}$ gives a relaxation fraction ($\sim$ 20 per cent for both hydrodynamical simulations) comparable to observations (for example, Mantz et al., 2015; Biffi et al., 2016).

In Fig. 2.3, we show the relations between these three parameters for the mass-complete sample: $\Delta_{\rm r}$ versus η in the left-hand panel and $f_{\rm s}$ versus η in the right-hand panel. The two hydro-runs show a similar distribution of relaxed clusters (shown for convenience at the top and to the right of the figure panels), in agreement with Cui et al. (2017). The histogram peak of the η parameter from `GADGET-X` has a slightly higher value than the peak from `GADGET-MUSIC` . This could be due to the AGN feedback, which releases additional energy into the kinetic component.

[14]Note that for the given cosmology $R_{200} < R_{\rm vir}$ and hence the M_{200} masses of the host haloes considered here will be about 25 per cent smaller than $M_{\rm vir}$.

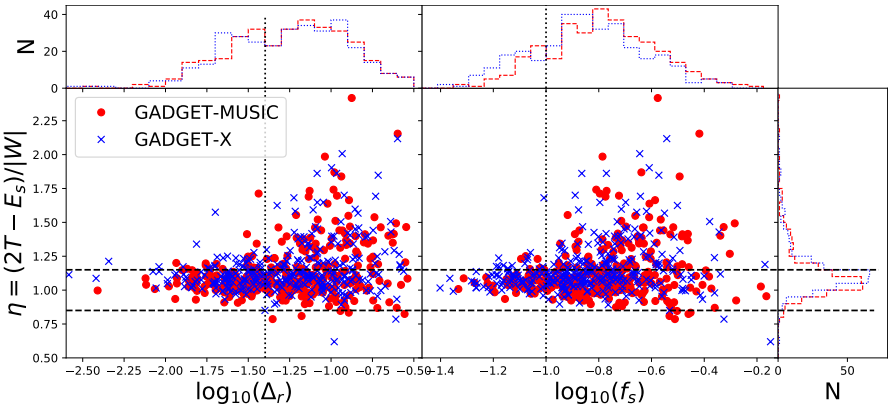

FIGURE 2.3: For the mass-complete sample, the left hand panel shows the relation between the virial ratio (η) and the centre-of-mass offset (Δ_r). The right-hand side panel shows the relation between η and the subhalo mass fraction (f_s). The top and right-hand sub-panels show their corresponding histograms. Red filled circles (red dashed line for the histogram) show the clusters from the GADGET-MUSIC run, while the blue crosses (blue dotted line for the histogram) show the GADGET-X results. The two horizontal dashed lines show the selection limits for the η parameter, while the vertical dotted lines show the selection limits for Δ_r and f_s (see text).

TABLE 2.4: The fraction of relaxed clusters. The first column shows the mass range. The second to fourth columns show the relaxation fractions from all three methods combined, Δ_r plus f_s, and only f_s criterion, respectively. Each cell shows two values, of which the first one is the relaxation fraction for GADGET-MUSIC and the second value is for GADGET-X . Clusters with $M_{200} < 6.42 \times 10^{14}\ h^{-1}\mathrm{M}_\odot$ (mass bins above the dashed line) are taken from the comprehensive sample.

$M_{200}\ [10^{14}h^{-1}\mathrm{M}_\odot]$	η, Δ_r & f_s	Δ_r & f_s	f_s
$0.10 - 0.50$	0.44 / 0.36	0.56 / 0.48	0.70 / 0.65
$0.50 - 1.00$	0.36 / 0.34	0.45 / 0.46	0.56 / 0.57
$1.00 - 6.42$	0.27 / 0.29	0.30 / 0.35	0.43 / 0.48
> 6.42	0.15 / 0.17	0.16 / 0.21	0.17 / 0.23

A quantitative analysis of the relaxation fraction within our comprehensive halo catalogue, for different mass bins and with different combinations of relaxation parameters is given in Tab. 2.4. The fraction of relaxed clusters shows a clear decreasing trend as halo mass increases. This is simply because the more massive the object is, the less likely it is to have reached dynamical relaxation by redshift $z = 0$. This can be traced back to the relation between formation time and halo mass (see Fig. 2 in Power, Knebe, and Knollmann, 2012, for instance). There is very little change in relaxation fraction for the complete sample when different criteria are applied. However, there is a noticeable difference in the relaxed cluster fraction for the smallest mass bin, with the fraction for GADGET-X being significantly lower ($\sim$ 8 per cent) than that for GADGET-MUSIC when all three criteria are applied. This is due to the AGN feedback in GADGET-X efficiently ceasing star formation in small objects and creating gas turbulence. The relaxation fractions for the mass-complete sample from both GADGET-MUSIC and GADGET-X show an obvious decrease. On the contrary to the smallest mass bin, the relaxation fraction from GADGET-MUSIC seems lower than from GADGET-X . This overturn can be understood from the fact that the mass fraction of substructures in GADGET-MUSIC is higher than GADGET-X , which dominates the relaxation fraction.

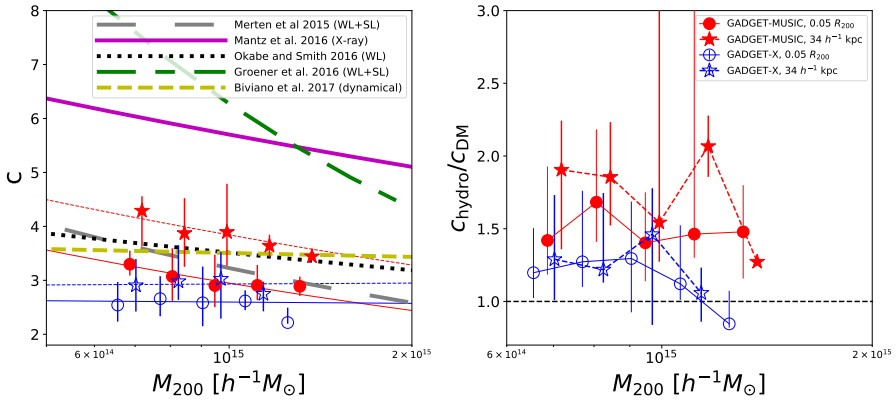

FIGURE 2.4: Left panel: The concentration–halo mass relation for the relaxed galaxy clusters from the two hydrodynamical simulation runs compared with various observational results. As indicated in the legend, thick lines with different styles show the best fit results from recent observational data obtained with different methods (Merten et al., 2015; Mantz, Allen, and Morris, 2016; Okabe and Smith, 2016; Groener, Goldberg, and Sereno, 2016; Biviano et al., 2017). Symbols show the median values with the 16^{th} - 84^{th} percentile error-bars from the hydro simulations: circles and stars (red filled symbols for `GADGET-MUSIC` and blue open symbols for `GADGET-X`) for the concentration derived by fitting the density profile up to two inner radii ($34h^{-1}$kpc and 0.05 R_{200}, see text for details). The red (blue), thin solid and dashed lines are the best fit result to the concentration mass relation of `GADGET-MUSIC` (`GADGET-X`) clusters. In the right panel of this figure, we represent the ratio of the concentration between the hydrodynamical simulation clusters and their match in the original MDPL2 dark-matter-only simulation. Again, the symbols show the median values with the 16^{th} - 84^{th} percentile error-bars.

Concentration-mass relation Knowledge of the halo concentration, c, and mass, M, would specify the full evolution of a halo in the spherical collapse model (Bullock et al., 2001). The relation $c - M$ between these two fundamental properties, alongside its standard deviation, are related to the variance in the assembly histories of dark matter haloes (e.g. Zhao et al., 2003b; Zhao et al., 2003a). Furthermore, the normalization and evolution of this relation also depend on the cosmological model (e.g. Dolag et al., 2004; Carlesi et al., 2012). However, there exists some tension between the observationally estimated relation and the theoretical prediction. This could result from not comparing the same properties when contrasting baryonic simulations and observational results with carefully imposed selection criteria (see Rasia et al., 2013; Biviano et al., 2017, for example). Here, we only use our relaxed galaxy clusters from the mass-complete sample to investigate and compare this relation with the observational results.

The halo density profiles can be analytically described by an NFW profile (Navarro, Frenk, and White, 1997),

$$\frac{\rho(r)}{\rho_{\rm crit}} = \frac{\delta_{\rm c}}{(r/r_{\rm s})(1+r/r_{\rm s})^2}\,, \tag{2.1}$$

which is characterised by the two parameters, $r_{\rm s}$ and $\delta_{\rm c}$. The concentration c_{200} is then given by $R_{200}/r_{\rm s}$. We fit our simulated cluster density profiles, defined by equally spaced log-bins, to this functional form with both parameters free, but exclude the very central region in this process. Due to the presence of the BCG, the mass profile in the centre is much steeper than the total mass profile (Schaller et al., 2015b). As the edge of the BCG is not clearly defined, we adopt two different inner "exclusion" radii during the fitting: 0.05 R_{200}, as suggested by for example Schaller et al. (2015b) and Cui et al. (2016b), and $\sim 34h^{-1}$kpc following Biviano et al. (2017). We have verified that the NFW profile provides a good fit regardless of the adopted inner radii ($34h^{-1}$kpc or 0.05 R_{200}). In both cases the difference between the fit and the original density profile is within 20 per cent at all radii. In the left

TABLE 2.5: The fitting parameters for the concentration-mass relation with fitting function: $\log_{10} c_{200} = \alpha - \beta \log_{10} M_{200}/M_{\odot}$. The first row shows the results with the inner radius set to 0.05 R_{200}, while the second row is for a $34h^{-1}$kpc inner radius. Each cell shows two values, of which the first one is for the fitting parameter α and the second value is β.

Inner radius	GADGET-MUSIC	GADGET-X
	α / β	α / β
0.05 R_{200}	4.60 / 0.27	0.62 / 0.013
$34h^{-1}$kpc	4.02 / 0.23	0.34 / -0.01

panel of Fig. 2.4 we show the $c - M$ relation for our relaxed galaxy clusters and compare the relation with observational results coming from both X-ray and optical data obtained with different techniques (please refer to the figure caption and legend, respectively). For each of the two hydrodynamical simulation codes, we show results stemming from either truncation approach: circles for using the range $[0.05\ R_{200}, R_{200}]$ and stars for a fixed inner radius of $34h^{-1}$kpc. We fit our $c - M$ relation using the following analytical function

$$\log_{10} c_{200} = \alpha - \beta \log_{10}(M_{200}/M_{\odot}) \, . \tag{2.2}$$

The fitting parameters α and β are listed in Tab. 2.5.

It is evident that the $c - M$ relation from our hydro-simulated clusters is closer to the observational results from Merten et al., 2015; Okabe and Smith, 2016; Biviano et al., 2017 than those from Mantz, Allen, and Morris, 2016; Groener, Goldberg, and Sereno, 2016. The $c - M$ relation from the GADGET-MUSIC run is slightly higher than from the GADGET-X run and it is in better agreement with observational results which have lower concentrations. We can see that the concentrations with a $34h^{-1}$kpc inner cut-off are systematically higher than the ones with a 0.05 R_{200} cut-off (see also Rasia et al., 2013, for similar results with different inner radii). Our fitted $c - M$ relation from the GADGET-X clusters is much flatter than Schaller et al. (2015a), simply because their fit covers a much larger mass range, which is dominated by the lower mass objects. Furthermore, GADGET-X shows an increasing slope with $\beta = -0.01$ when a fixed inner radius of $34h^{-1}$kpc is taken. This can be understood because $34h^{-1}$kpc corresponds to a smaller fraction of R_{200} for a massive cluster than for a less massive halo. Therefore it is not surprising to see a relatively high concentration for the most massive haloes when a fixed physical cut-off radius is applied.

In the right panel of Fig. 2.4, we investigate the baryon effects on the $c - M$ relation by showing the relative change in concentration from dark-matter-only simulated clusters to their equivalent in the two hydro-runs. The change on $c - M$ relation due to baryons varies from $\sim$ 25 per cent (for both radii) for GADGET-X to about 1.5 - 2 times (0.05 R_{200} - $34h^{-1}$kpc) for GADGET-MUSIC . However, this ratio is much lower for the highest mass bin for GADGET-X with both inner radii (also for GADGET-MUSIC with the inner radius of $34h^{-1}$kpc). The influence of baryons on the concentration is a little higher than in Rasia et al. (2013), which may be the result of both the different radius range used for profile fitting and differences in the baryonic model employed.

Baryon fractions

The formation of a galaxy cluster depends not only on gravity acting on cosmic scales but also on sub-resolution phenomena such as star formation and various feedback mechanisms returning energy back to the intra-cluster gas. It is a process that involves interplay between dark and baryonic matter. One of the most important quantities to quantify the relation between dark matter and baryons is the baryonic mass fraction. It has therefore been intensively studied: on the theoretical side, mostly by means of hydrodynamical simulations (e.g. Sembolini et al., 2016a; Planelles et al., 2013; Wu et al., 2015; Barnes et al., 2017a); and on the observational side via multi-wavelength observations (e.g. Laganá et al., 2013; Eckert et al., 2016; Chiu et al., 2018).

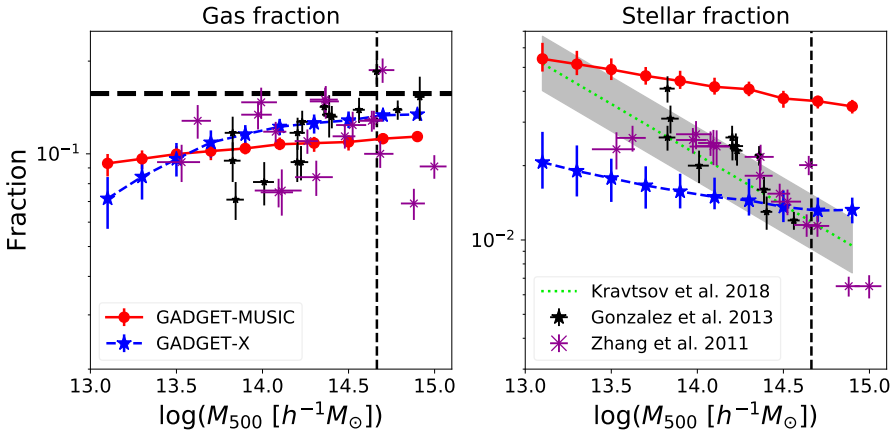

FIGURE 2.5: The baryonic fractions from the two hydrodynamical simulations within R_{500}. Gas fractions are shown on the left-hand side panels, while stellar fractions are shown on the right-hand side panels. As shown in the legend on the top-left panel, hydrodynamical simulations are shown with red filled symbols (median value) with error-bars ($16^{\text{th}} - 84^{\text{th}}$ percentiles) for `GADGET-MUSIC` and blue stars with error-bars for `GADGET-X` . Observational data points from Gonzalez et al. (2013) and Zhang et al. (2011) are shown as black stars and magenta cross symbols respectively, while the lime dotted line shows the fitting result from Kravtsov, Vikhlinin, and Meshcheryakov (2018) with the grey shaded scatter. The thick black horizon dashed lines on the left-hand side panels indicate the cosmic baryon fraction (Ω_b/Ω_m). The vertical dashed lines in the upper row shows the mass limit for the complete sample.

In Fig. 2.5, we show the gas and stellar mass fractions for the comprehensive sample from hydrodynamical simulations within R_{500}. The gas fraction for `GADGET-X` is larger than for `GADGET-MUSIC` at the massive end, and drops more quickly towards lower mass haloes. The gas fraction from `GADGET-X` shows a better agreement with the data of Gonzalez et al. (2013) at the massive end; both simulations are in line with the results from Zhang et al. (2011) due to its large scatter. The offset between the two hydro-runs is much larger (a factor of $2-3$) for the stellar fraction. Again, `GADGET-X` shows a better agreement with the observational data points at the massive end. However, it has a flatter slope than the observational results, which is close to the `GADGET-MUSIC` result at $M_{500} \lesssim 10^{13.5} h^{-1}\mathrm{M}_\odot$. This is possibly caused by the strong AGN feedback in `GADGET-X` . Essentially both hydrodynamic models have a stellar fraction versus mass slope that is inconsistent with the observational data.

Previous comparisons of the stellar and gas mass fractions from full-physics hydrodynamical simulations with observations have shown that models without AGN feedback consistently have too low a gas fraction and too high a stellar fraction due to the over-cooling problem (for example Planelles et al., 2013). This is also seen in Fig. 2.5 comparing the `GADGET-MUSIC` and the `GADGET-X` results. Although `GADGET-X` tends to have a better agreement with the observational results, the AGN feedback implementation featured by this code is still not perfect: the most massive clusters at $M_{500} \gtrsim 10^{15} h^{-1}\mathrm{M}_\odot$ still have a stellar fraction that is a little too high; while intermediate and low mass haloes ($M_{500} \lesssim 10^{14} h^{-1}\mathrm{M}_\odot$) have stellar fractions that are too low. Nevertheless, we note that the stellar mass fraction estimated from observations is not without issues: there is relative uncertainty about the contribution of the intra-cluster light (for example Zibetti et al., 2005; Gonzalez, Zaritsky, and Zabludoff, 2007; Puchwein et al., 2010; Cui et al., 2014), which is included in Gonzalez et al. (2013) and Kravtsov, Vikhlinin, and Meshcheryakov (2018), but not in Zhang et al. (2011); another problem is the influence of the different initial mass functions adopted in observations to derive stellar mass from luminosities (see e.g. Chiu et al., 2018, for detailed discussions).

The difference in the stellar mass fractions shows the importance of the detailed prescription for baryon processes. The connection between the encapsulated physics and the

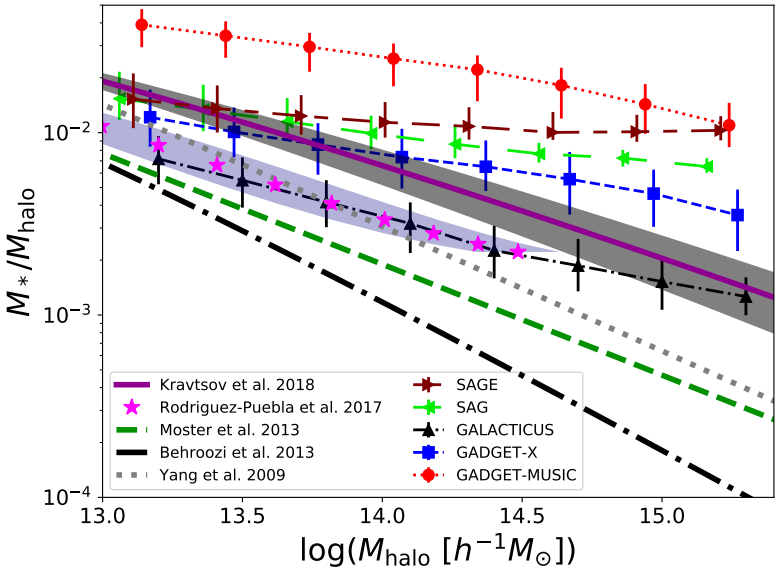

FIGURE 2.6: The stellar-to-halo mass relation for central galaxies in the complete sample. As indicated in the legend, observational results are shown as thick lines (Yang, Mo, and van den Bosch (2009), grey dotted line, Behroozi, Wechsler, and Wu (2013), dot-dashed black line and Moster, Naab, and White (2013), green dashed line) with the latest results from Rodríguez-Puebla et al. (2017) shown as magenta stars with the light shaded area and Kravtsov, Vikhlinin, and Meshcheryakov (2018) as a solid purple line with the dark shaded region. Our hydrodynamical simulation and SAM results are shown in different symbols (median value) with error-bars ($16^{\rm th} - 84^{\rm th}$ percentile): `GADGET-MUSIC` with red solid circles and dotted line; `GADGET-X` with blue solid squares and dashed line; `GALACTICUS` with black filled triangles and dash-dotted line, `SAG` with lime triangles and long dashed line and `SAGE` with maroon triangles and long-short dashed line.

resultant baryonic fractions, examining the difference between relaxed and un-relaxed clusters, between cool core and non-cool core clusters, as well as the redshift evolution of these fractions is presented in Ansarifard et al. (2020).

Stellar and gas relations of clusters

Stellar-to-halo mass relation Scaling relations between the total cluster mass and observational quantities are derived in several multi-wavelength studies. Commonly used observational probes include stellar luminosity, X-ray temperature or the Comptonization parameter (e.g. Reiprich and Böhringer, 2002; Lin, Mohr, and Stanford, 2004; Andersson et al., 2011), which normally show a self-similar relation to cluster mass. They are very powerful tools to derive total cluster masses from different observations. However, before the mass can be estimated, they need to be accurately calibrated and their dispersion properly estimated. It is worth noting that the scaling relations derived from observations could be biased by sample selection which should have no influence on our mass-complete sample. In this section, we investigate the scaling relations found in our hydrodynamical simulations, and compare them with those from SAMs and observations.

How galaxy properties relate to their host dark matter halo is an open question in astronomy. Therefore, a substantial effort has focused on establishing robust determinations of the galaxy-halo connection, commonly reported in the form of the stellar-to-halo mass relation, SHMR (Guo et al., 2010; Yang et al., 2012; Moster, Naab, and White, 2013; Behroozi, Wechsler, and Wu, 2013, and references therein). In Fig. 2.6, we compare our SHMR with results from the literature. It is worth noting here that the haloes from the comprehensive sample with mass below the completeness limit constitute a biased sample, which are lying in a dense environment compared to observations. We only include central galaxies in the

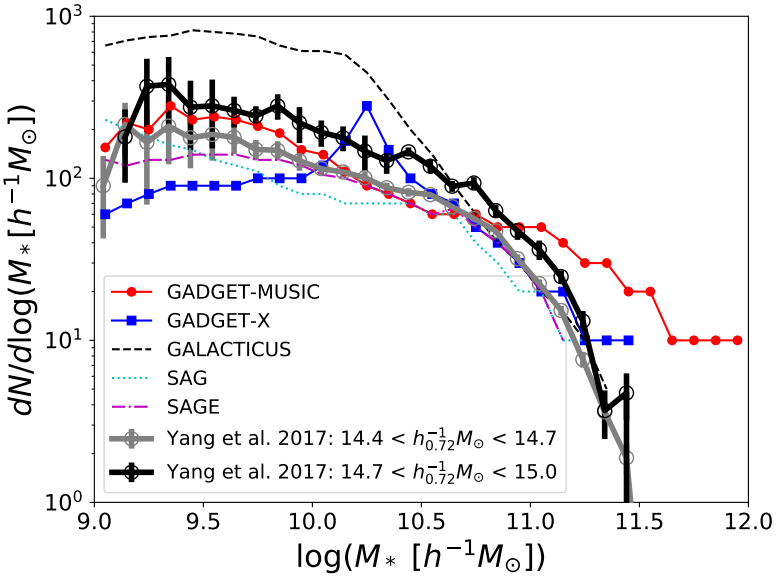

FIGURE 2.7: The median stellar mass function of satellite galaxies within the mass-complete cluster sample. `GADGET-MUSIC` is shown with a red line with circle symbols and `GADGET-X` with a blue line with square symbols. The three SAMs are presented by different lines: `GALACTICUS` as a black dashed line, `SAG` as a cyan dotted line and `SAGE` as a magenta dot-dashed line. They are compared with observational results from Yang et al. (2018), which are shown in thick black for halo mass range $[10^{14.7} - 10^{15}\ h_{0.72}^{-1}M_\odot]$ and thick grey for halo mass range $[10^{14.4} - 10^{14.7}\ h_{0.72}^{-1}M_\odot]$, both lines include error-bars.

calculation as the haloes of satellites galaxies will have suffered tidal disruption. However, as the hydrodynamical simulations feature stars in the halo (which can be treated as ICL), we also include the mass of the ICL in the calculation for the SAMs `SAG` and `SAGE` . Therefore, the central galaxy here is BCG+ICL.

In agreement with our previous findings in Fig. 2.1 and Fig. 2.5, `GADGET-MUSIC` has the highest stellar-to-halo-mass fraction. `SAGE` , `SAG` and `GADGET-X` are in the second family, which tend to agree with the observational result at the lower mass end, but deviate from them at the massive end. `GALACTICUS` , which does not have ICL included, is in better agreement with Rodríguez-Puebla et al. (2017) and Yang, Mo, and van den Bosch (2009). Moreover, we confirm that `SAGE` also presents a better agreement with the observations if the ICL is excluded. We further note here that the BCG mass from Ragone-Figueroa et al. (2018) (a similar cluster simulation based on `GADGET-X`) is in a good agreement with observational results after applying a cut in radius. In addition, Pillepich et al. (2018) also reported that the exact functional form and magnitude of the stellar mass to halo mass relation strongly depend on the definition of a central galaxy's stellar mass.

Therefore, the differences shown in this plot could be simply caused by the definition of the central galaxy. We further include the fitting result from Kravtsov, Vikhlinin, and Meshcheryakov (2018), who claim to account for the stellar mass in the same way as the model results here, i.e. BCG mass plus ICL mass. It is interesting to see that their $M_{\rm BCG}$ - $M_{\rm halo}$ relation is much closer to the results from our models (except `GADGET-MUSIC` which is far from any observation results and `GALACTICUS` which does not include ICL), especially at $M_{\rm halo} \lesssim 10^{14}h^{-1}{\rm M}_\odot$. However, the offsets between the solid purple line and our model results (including `GALACTICUS` when compared with the observational results that do not include ICL) are still large for the most massive haloes. This means that the quenching of star formation in these massive clusters is still problematic for the models investigated here.

Stellar mass function for satellite galaxies Though the satellite galaxy stellar-mass function is not a scaling relation, we briefly switch focus from central galaxies to satellite galaxies

and present the result in this subsection. We only use the mass-complete sample for this investigation and limit our satellite galaxies to objects within R_{200} as per the observational sample. We show the stellar mass function – median averaged over all clusters – in Fig. 2.7.

As indicated in the legend, different style thin lines represent different versions of the simulations and SAMs, while observational results from Yang et al. (2018) at two different cluster mass bins are highlighted as thick lines. Note that the complete cluster sample is used here without further binning in halo mass, because its mass limit is basically comparable with the Yang et al. (2018) most massive mass bin. The lower mass bin from Yang et al. (2018) catalogue is presented here to aid the comparison. The horizontal extensions to the red and blue curves are artefacts of the median values.

Compared to the observational results, `GADGET-MUSIC` has more massive satellite galaxies with masses $M_* > 10^{11.5} h^{-1}\mathrm{M}_\odot$. `GADGET-X` shows a slightly reduced number of satellite galaxies towards the low mass end. `GALACTICUS` features the opposite trend. These deviations from the actual observations can be understood as an overabundance of massive satellite galaxies in `GADGET-MUSIC` due to the lack of AGN feedback; too few low mass satellite galaxies in `GADGET-X` can be caused by either a resolution issue (note that galaxies of $M_* \sim 10^{10} h^{-1}\mathrm{M}_\odot$ only contain a few hundreds of stellar particles due to the poor simulation resolution) or the stripped/heated gas due to the Wendland kernel and feedback; and too many low mass satellite galaxies in `GALACTICUS` is because of a surplus of orphan galaxies (see Table 2 in Knebe et al., 2018). `SAG` and `SAGE` seem not to suffer from this problem due to their different treatment of the orphan galaxy population. We refer to Pujol et al. (2017) for a detailed comparison of the orphan galaxies between different SAMs. However, we note that the scatter across models seen here is at the level found in previous comparisons of theoretically modelled galaxy stellar mass functions of galaxies (Knebe et al., 2015; Knebe et al., 2018).

Optical scaling relations We continue to investigate the correlations between luminosity/magnitude, stellar mass, and colours by comparing our modelled galaxies to the observational results from Yang et al. (2018). We again only use the galaxies from our mass-complete sample here. For a fair comparison to our theoretical data, we apply the same mass cut ($M_{200} \geq 6.42 \times 10^{14} h^{-1}\mathrm{M}_\odot$) to the group catalogue of Yang et al. (2018) and use all the satellites and central galaxies with $M_* > 10^9 h^{-1}\mathrm{M}_\odot$ in these selected groups (the same criteria also applied to our complete sample). The results can be viewed in Fig. 2.8 where the top panel shows the luminosity-stellar mass relation (based upon the SDSS-r band), the middle panel presents the $g-r$ colour – magnitude (at SDSS-r band) relation and the bottom panel shows the colour-colour relation with $u-r$ versus $r-i$. Note that the `SAGE` model does not provide luminosities *ab initio* and has hence been excluded from this plot.

Similar to Fig. 2.5, the contours are drawn at the same percentile density levels (16^{th}, 50^{th} and 84^{th}) after a normalised 2D binning with the observational results shown as different colour-filled areas. In the top panel, we recover a very tight correlation between luminosity and stellar mass with little variation between observation and the models (excluding `SAG`). `GADGET-MUSIC` , `GADGET-X` , `GALACTICUS` and Yang et al. (2018) observational results are binned only in stellar mass and presented by symbols with error-bars indicating the $16^{\mathrm{th}} - 84^{\mathrm{th}}$ percentile. While `SAG` , which tends to have a larger spread in luminosity, is shown with cyan contours. Moreover, we fit the M_* - luminosity relation for the models (excluding `SAG`) and the observational result with a linear function $f(x) = ax$.

We find that all the models give a consistent result with a slope of 0.895, which is shown by the solid black line shifted up by 0.5 dex in the top panel. In the colour-magnitude relation, both hydrodynamical simulations and SAMs show values $\sim 0.1 - 0.2$ below the $g-r$ colour of the observations. There are very few galaxies with a $g-r$ colour less than 0.7 in the observational results compared to the SAMs. This indicates that the SAMs – as applied to a full cosmological simulation here – fail to reduce their star-forming galaxies sufficiently in the cluster environment. The hydrodynamical simulations also have problems in ceasing star formation, especially for the brightest galaxies. For the colour-colour plot presented in the bottom panel, the results from the two hydrodynamical simulations are in agreement with the two SAMs. Although they all show a noticeable overlap with the observational results, the peaks for the four models are slightly shifted to smaller values in both colours compared to the observations.

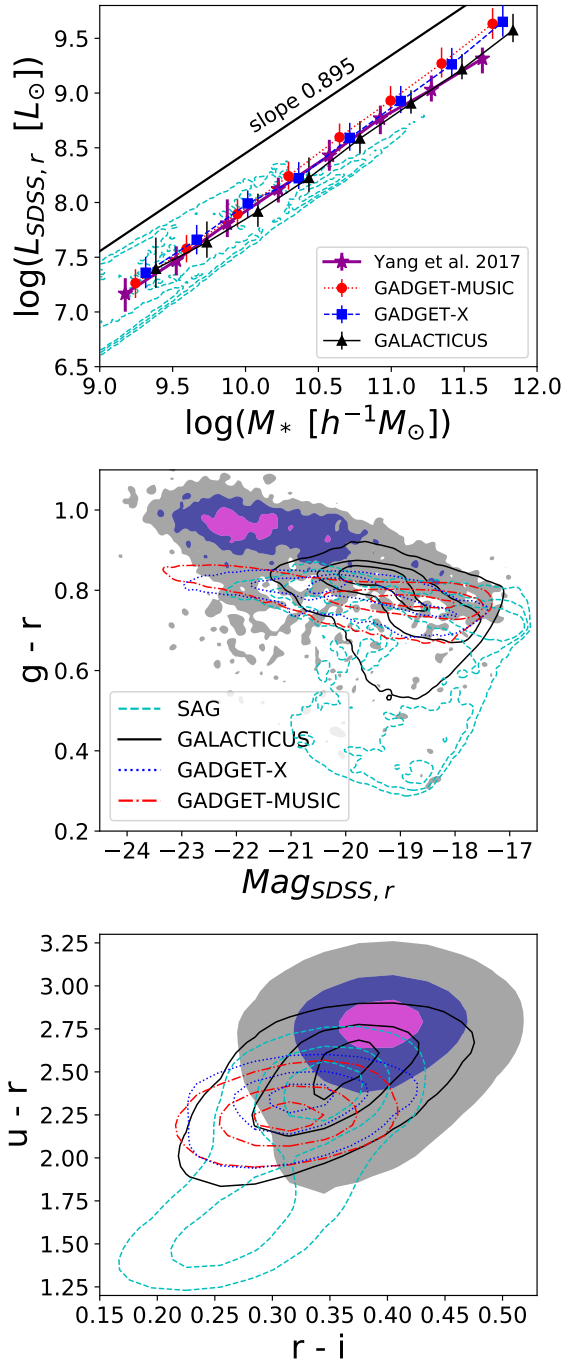

FIGURE 2.8: Top panel: the luminosity-stellar mass relation for all the galaxies inside the clusters (using the SDSS-*r* band). As indicated in the legend, different symbols (median value) with error-bars ($16^{th} - 84^{th}$ percentile) are for different models and for the observational result from Yang et al. (2018), while the result from `SAG` is presented in cyan contours. The top sloping black line (shifted up by 0.5 dex) shows the slope 0.895 which fits both the models and the observational result. Middle panel: the colour-magnitude relation for the galaxies inside the clusters. Bottom panel: the colour-colour relation for galaxies inside the clusters. The legend in the middle panel distinguishes the colours for the models with different line styles for both middle and bottom panels with the colour map is again from Yang et al. (2018).

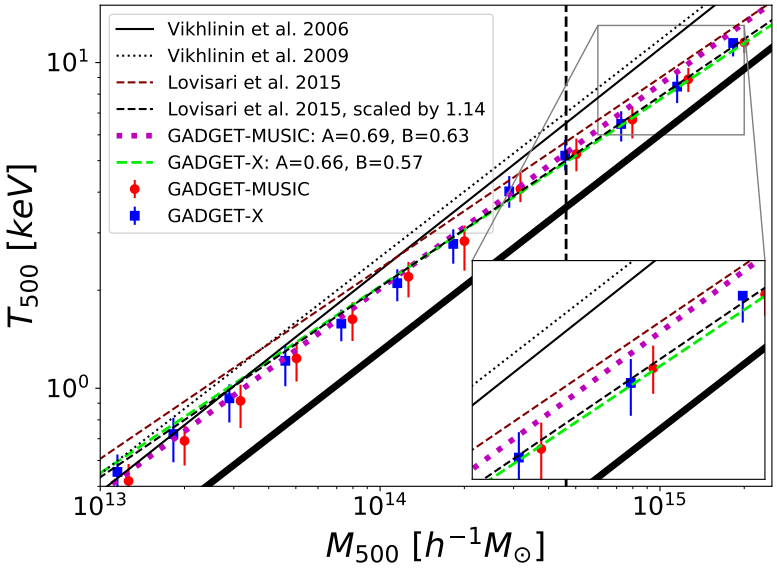

FIGURE 2.9: The temperature-mass relation for the clusters from the two hydrodynamical simulations. Red filled circles (blue filled squares) with errorbars ($16^{\text{th}} - 84^{\text{th}}$ percentile) are for `GADGET-MUSIC` (for `GADGET-X`). The solid and dotted black lines show the observational results from Vikhlinin et al. (2006) and Vikhlinin et al. (2009), respectively. The maroon dashed line shows the fitting result from Lovisari, Reiprich, and Schellenberger (2015) (scaled by 1.14 as a black dashed line). Our fitting results from `GADGET-MUSIC` and `GADGET-X` are presented by magenta dotted and lime dashed lines respectively. The thick solid black line shows the self-similar relation $T_{500} \propto M_{500}^{2/3}$ predicted from non-radiative simulations.

Gas scaling relations

For the gas scaling relations, we now use our comprehensive sample of objects, but restrict our analysis to the hydrodynamical simulations for which we have immediate access to multiple gas properties. We confine the analysis to M_{500} by re-selecting all gas particles within R_{500} to facilitate direct comparison to the observational results. We first investigate the temperature-mass ($T - M$) relation. The gas temperature is computed using the mass weighted temperature formula $T = \sum_i T_i m_i / \sum_i m_i$, where T_i and m_i are the temperature and mass of a gas particle, respectively. In Fig. 2.9, we show the relation between the mass-weighted gas temperature and M_{500}. Moreover, we apply a simple linear fitting function in logarithm space to fit the data from all the samples:

$$T_{500} = 10^{\mathrm{A}} \left(\frac{M_{500}}{6 \times 10^{14}\ M_\odot} \right)^{\mathrm{B}} . \tag{2.3}$$

Note that we exclude the h in the normalisation mass of the fitting equation (i.e. Eq. 2.3).

Since, as discussed above, our comprehensive cluster sample is not complete at the low mass end, data points below our completeness threshold are weighted according to their completeness during the fitting. As the comprehensive sample forms a mass-incomplete set of haloes they may conceivably be a biased dataset. Such a bias could in principle arise due to their physical proximity to a larger halo but how to accurately quantify such a bias, if it exists, is unclear. Best-fit curves are shown as a magenta dotted line for `GADGET-MUSIC` and a green dashed line for `GADGET-X` ; the parameters are summarised both in the legend and Tab. 2.6. Since the low mass data has less weight and there are few clusters in the high mass range, it is not surprising to see that the fitting lines are offset from the symbols which show the median values in each mass bin.

The best fitting parameters are slightly different between the two hydrodynamical simulations: `GADGET-MUSIC` has a steeper slope close to the self-similar relation with B = 2/3

TABLE 2.6: The fitted parameters for the $T_{500} - M_{500}$ relation with fitting function: $T_{500} = 10^{A}(M_{500}/6 \times 10^{14}\ M_{\odot})^{B}$, see Eq. (2.3) for details.

Simulation	A	B
GADGET-MUSIC	0.688±0.011	0.627±0.007
GADGET-X	0.663±0.012	0.574±0.008

(Kaiser 1986, also predicted by the non-radiative simulations, see Bryan and Norman 1998; Thomas et al. 2001 for example) compared to GADGET-X . This is mainly caused by the low temperature of the clusters with small halo mass. Compared to the results from (Vikhlinin et al., 2006; Vikhlinin et al., 2009), there is a good agreement at low halo mass with our simulations. However, there is a clear offset between our simulation result and their results for massive haloes. This could be caused by the hydrostatic method used in observations which can underestimate the total mass due to a non-thermal pressure component. This bias has been corrected in (Lovisari, Reiprich, and Schellenberger, 2015), which, although it is still above our best fit lines, is closer to our data for the most massive haloes (closer to GADGET-MUSIC than to GADGET-X). In addition, their result is also slightly higher than our simulation results at low halo mass. This is because of the spectrum-weighted temperature adopted in (Lovisari, Reiprich, and Schellenberger, 2015), which is about 14 per cent higher than the mass weighted temperature (Vikhlinin et al., 2006; Sembolini et al., 2016b). We follow (Sembolini et al., 2016b) by correcting for this difference by scaling down the fitting function from (Lovisari, Reiprich, and Schellenberger, 2015) by a factor of 1.14 (black dashed line in Fig. 2.9). This produces a very good match to the fitting result from GADGET-X . It is worth noting that the self-similar relation does not provide a good fit to our data (see also Truong et al., 2018). Lastly, Truong et al., 2018 reported lower temperatures than observed resulting in a normalisation shift of about 10 per cent for the $T - M$ relation for their AGN model. Similarly, (Henden et al., 2018) also found such a difference with zoomed-in cluster simulations. However, they claimed this is most likely caused by the underestimated total mass due to the biased X-ray hydrostatic mass than a lower temperature in their simulation.

Finally, we present the analysis on the Sunyaev-Zel'dovich (SZ) effect (Sunyaev and Zeldovich, 1970), i.e. the diffusion of cosmic microwave background photons within a hot plasma (normally inside galaxy clusters) due to inverse Compton scattering. The SZ effect provides a unique view of a galaxy cluster. Therefore, it has become one of the most powerful cosmological tools used to study the ICM, as well as the nature of the dark matter and dark energy components of the Universe. Numerous works have been devoted to investigate and understand this effect, both observationally (e.g. Staniszewski et al., 2009; Marriage et al., 2011; Planck Collaboration et al., 2016) and theoretically by means of cosmological simulations (e.g. da Silva et al., 2000; Sembolini et al., 2016a; Le Brun, McCarthy, and Melin, 2015; Dolag, Komatsu, and Sunyaev, 2016).

The thermal SZ signal is characterised by the dimensionless Compton y-parameter, which is defined as

$$y = \frac{\sigma_T k_B}{m_e c^2} \int n_e T_e dl \ , \tag{2.4}$$

where σ_T is the Thomson cross-section, k_B the Boltzmann constant, c the speed of light, m_e the electron rest-mass, n_e the electron number density and T_e the electron temperature. The integration is done along the observer's line of sight. In the hydrodynamical simulations, the electron number density, n_e for one gas particle can be represented as $n_e = N_e/dV = N_e/(dAdl)$, here N_e is the number of electrons in the gas particle, dV is its spatial volume which is broken down into dA (the projected area) and dl (the line of sight distance). Therefore, the integration can be represented by the summation (Sembolini et al., 2016a; Le Brun, McCarthy, and Melin, 2015):

$$y = \frac{\sigma_T k_B}{m_e c^2 dA} \sum_i T_i N_{e,i} W(r, h_i) \ , \tag{2.5}$$

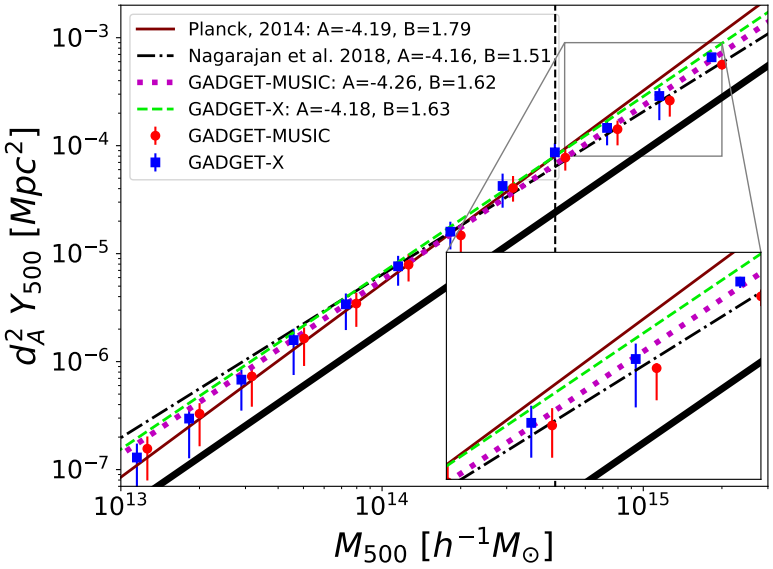

FIGURE 2.10: The $Y_{500} - M_{500}$ relation. Similar to Fig. 2.9, red circles (median value) with error-bars ($16^{\text{th}} - 84^{\text{th}}$ percentile) are for `GADGET-MUSIC` while blue squares with error-bars are for `GADGET-X` . The thin maroon line comes from the *Planck* observation (Planck Collaboration et al., 2014) and the dash-dotted line is the fitted result from Nagarajan et al. (2019) with cluster mass estimated by the weak-lensing method. While the black dotted and lime dashed lines show our fitting results for `GADGET-MUSIC` and `GADGET-X` respectively. The lower thick black line shows the self-similar relation $Y_{500} \propto M_{500}^{5/3}$.

where we applied the same SPH smoothing kernel $W(r, h_\mathrm{i})$ as the hydrodynamical simulation to smear the y signal from each gas particle to the projected image pixels, and h_i is the gas smoothing length from the simulations. It is worth noting that the number of electrons per gas particle is metallicity dependent: $N_\mathrm{i} = [N_\mathrm{e} m_\mathrm{i}(1 - Z - Y_\mathrm{He})] / (\mu m_\mathrm{p})$, where N_e is the number of ionised electrons per hydrogen particle, m_i the mass of the gas particle, Z the metallicity of the gas particle, Y_He the helium mass fraction of the gas particle, μ the mean molecular weight and m_p the proton mass[15].

The integrated Comptonization parameter Y over an aperture inside R is given by

$$Y = \int y d\Omega = \sum_{\mathrm{i}}^{i \in R} y_\mathrm{i} \,, \tag{2.6}$$

where Ω is a solid angle, which can be expressed as an aperture of radius R. In observations, this Y parameter is normally re-expressed as $d_A(z)^2 E(z) Y$, where $d_A(z)$ is the angular diameter distance and $E(z) = H(z)/H0 = \sqrt{\Omega_\mathrm{m}(1+z)^3 + \Omega_\Lambda}$ gives the redshift evolution of the Hubble parameter, $H(z)$, in a flat ΛCDM Universe. Here we are only presenting clusters at redshift $z = 0$, for which $E(z) = 1$. In the subsequent analysis, we focus on Y_{500} within an aperture of R_{500}. Moreover, we only present projected results in the x-y plane here. Since we have a large number of samples, the projection effect should have a negligible impact on our results.

In Fig. 2.10, we show the scaling between Y_{500} and M_{500}. Similar to Fig. 2.9, symbols with error-bars are calculated from our comprehensive sample by binning in mass. We refer to the legend in Fig. 2.10 for further details. Here, we adopt a similar functional form as used

[15]The analysis pipeline for this calculation is publicly available as a python package from https://github.com/weiguangcui/pymsz.

TABLE 2.7: The fitted parameters for the $Y_{500} - M_{500}$ relation. See equation Eq. (2.7) for details.

Simulation	A	B
GADGET-MUSIC	-4.26±0.07	1.62±0.31
GADGET-X	-4.18±0.07	1.63±0.29

for the $T - M$ relation to fit the data from our comprehensive sample:

$$d_A^2 Y_{500} = 10^{\mathrm{A}} \left(\frac{M_{500}}{6 \times 10^{14}\ M_\odot} \right)^{\mathrm{B}} . \tag{2.7}$$

The best-fitting parameters from Planck Collaboration et al. (2014) are A = -4.19 and B = 1.79, which relies on mass estimates from a mass-proxy relation due to Kravtsov, Vikhlinin, and Nagai (2006). The fitting result from Nagarajan et al. (2019) which used the weak lensing mass of the APEX-SZ clusters, is shown as a purple dash-dotted line with A = -4.16 and B = 1.51. We fit our simulation data to the same function and present the results in Fig. 2.10 for GADGET-MUSIC as a black dotted line and for GADGET-X as a green dashed line. The value of the best-fitting parameters are shown in both the figure legend and Tab. 2.7. Compared to the best-fit Planck relation, our simulation results have a slightly flatter slope. However, comparing to the result from Nagarajan et al. (2019) who used a more precise mass estimation method, both GADGET-X and GADGET-MUSIC are slightly above (similar offsets as comparing with the Planck result) the purple line at the high mass end. On the contrary, the Planck (APEX-SZ) fitting line is under (above) the simulation results at the low mass end ($M_{500} < 10^{13.5} h^{-1}\mathrm{M}_\odot$). In addition, GADGET-X only shows a marginally higher amplitude than GADGET-MUSIC , especially at the high-mass end of the relation. Both are also in agreement with the self-similar relation with B = 5/3 (e.g. Bonamente et al., 2008). This means that the scaling between M_{500} and Y_{500} is almost independent of the gas physics and is the more robust relation, which is in agreement with Planelles et al. (2017) and Truong et al. (2018), for example. It is worth noting that neither observations used mass $M_{500} < 10^{14} h^{-1}\mathrm{M}_\odot$ to do the fitting. It is interesting to see that this scaling relation extends down to mass $M_{500} = 10^{13} h^{-1}\mathrm{M}_\odot$ for our models.

2.2.4 Conclusions

We introduced THE THREE HUNDRED project, i.e. a database of more than 300 synthetic galaxy clusters with mass $M_{200} > 6 \times 10^{14} h^{-1}\mathrm{M}_\odot$. The clusters have been individually modelled in a cosmological volume of side length $1 h^{-1}$Gpc with all the relevant baryonic physics (including AGN feedback) using the "modern" SPH code GADGET-X (Beck et al., 2016). The large re-simulation regions of radius $15 h^{-1}$Mpc – centred on the 324 most massive galaxy clusters as found in the parent dark matter only MDPL2 simulation – contain many additional objects, in total about 5500 objects with a mass $M_{200} > 10^{13} h^{-1}\mathrm{M}_\odot$. This suite of massive galaxy clusters therefore not only allows to study the formation and evolution of a mass-complete sample, but also carefully investigate their environments and the pre-processing of material entering the galaxy cluster.

This section focuses on presenting the galaxy clusters in the sample by primarily studying their redshift $z = 0$ properties and comparing them to observational data. This serves as a validation of the public data. Additionally, we do have at our disposal the same suite of clusters, but simulated with a "classical" SPH technique and without AGN feedback (i.e. the GADGET-MUSIC code, Sembolini et al., 2016a). This forms a comparison benchmark, demonstrating the differences that choices surrounding physical prescriptions can make. We further presented – where appropriate – the results as obtained via three distinct SAMs (GALACTICUS , SAG , and SAGE) that were applied to the underlying dark matter only MDPL2 simulation. A comparison between full physics simulations and semi-analytic models of galaxy formation on this scale or with this number of objects adds to existing efforts

of gauging the relevance of various physical processes and its numerical modelling. In subsequent studies we will apply a more elaborate analysis including redshift evolution and formation processes.

We find that our clusters are in reasonable agreement with observations and summarise our main findings as follows:

- The cluster mass difference between the hydrodynamical simulations and their dark-matter-only counterpart is very small for M_{200}, with about 5 per cent scatter. However, M_{500} is about 2-6 percent higher in the hydrodynamical simulation than their MDPL2 counterparts at $4 \times 10^{14} \lesssim M_{500} \lesssim 10^{15}$, with a large scatter of about 10 per cent. Using the dynamically relaxed sample reduces the scatter in half, but does not change the systematic differences.

- The dynamically relaxed cluster sample has a $c - M$ relation which appears to be flat for `GADGET-X` across the considered mass range. The concentrations for `GADGET-MUSIC` are generally larger (factor of $\sim$1.3) and in better agreement with observations. In both models the concentrations of the hydrodynamically modelled clusters are larger than those of their dark-matter-only counterparts; for `GADGET-MUSIC` this applies to the full mass range whereas for `GADGET-X` concentrations appear unaffected by the inclusion of baryon physics beyond $10^{15}h^{-1}\mathrm{M}_{\odot}$.

- `GADGET-X` shows baryonic fractions at $M_{500} \gtrsim 10^{14}h^{-1}\mathrm{M}_{\odot}$ that are generally in agreement with observations, while `GADGET-MUSIC` forms too many stars due to the lack of AGN feedback. `SAG` has the highest gas fraction and the lowest stellar fraction in haloes. `SAGE` and `GALACTICUS` share similar gas fractions and stellar fractions (slightly higher in `SAGE` than `GALACTICUS`).

- Besides `GALACTICUS` , all the models included in this study do not produce a stellar halo mass relation that is consistent with observations. This could be caused by the inclusion of the ICL. Even comparing with the observational result from Kravtsov, Vikhlinin, and Meshcheryakov, 2018, which has ICL included, the BCGs in our modelled clusters ($M_{\mathrm{halo}} \gtrsim 10^{14.5}$) are still massive.

- For the stellar mass function of the satellite galaxies, `GADGET-MUSIC` over produces the number of massive satellites. At lower stellar mass, `GALACTICUS` (`GADGET-X`) has more (less) satellites than the observations.

- The hydro runs and `GALACTICUS` show a linear luminosity-mass relation (with a slope of 0.895) which is very consistent with the observational result. All the models fail to represent the peak position from observations for the colour-magnitude and colour-colour contour.

- For the gas scaling relations, both `GADGET-X` and `GADGET-MUSIC` are generally in agreement with the observational temperature-mass and Y_{500}-mass relations. The fitting for the hydrodynamical simulations extends to $10^{13}h^{-1}\mathrm{M}_{\odot}$, which shows the power of the scaling relation. The small difference between the two simulations indicates that baryonic processes only have a weak influence on these relations (see also Hahn et al., 2017).

Our theoretically modelled galaxies and galaxy clusters generally present similar results and matches to observations - at least on certain scales of interest. However, we do see deviations in multiple aspects between these models and the observations, especially for the massive central galaxy (BCG+ICL). To understand the disagreements and to connect them with the input sub-grid baryonic models, we need to a) extend the comparisons to even smaller scales than the ones presented here, b) consistently derive quantities by mimicking observations more quantitatively, and c) track the impact of these baryonic models over a wider range of redshifts. Eventually, as our cluster sample contains different physical implementations of various baryonic processes from both hydrodynamic and SAM modelling, this will allow us to investigate, understand, and pin down the differences between our results and connect them back with the underlying physics.

2.3 Self-similarity in galaxy cluster density profiles

Section based on Mostoghiu et al. (2019)

Once the dataset has been validated, we study how massive galaxy clusters accrete their mass during their their evolution, and how this influences their internal mass distribution.

Recent numerical studies of the dark matter density profiles of massive galaxy clusters ($M_{\rm halo} > 10^{15} M_{\odot}$) show that their median radial mass density profile remains unchanged up to $z > 1$, displaying a highly self-similar evolution. In this section we verify this scenario by using the data set of the THE THREE HUNDRED project, i.e. 324 cluster-sized haloes as found in full physics hydrodynamical simulations. We track the progenitors of a mass-complete sample of clusters at $z = 0$, and find that their median shape is already in place by $z = 2.5$. However, selecting a dynamically relaxed subsample ($\sim$ 16 per cent of the clusters), we observe a shift of the scale radius r_s towards larger values at earlier times. Classifying the whole sample by formation time, this evolution is understood as a result of a two-phase halo mass accretion process. Early-forming clusters – identified as relaxed today – have already entered their slow accretion phase, hence their mass growth occurs mostly at the outskirts. Late-forming clusters – which are still unrelaxed today – are in their fast accretion phase, thus the central region of the clusters is still growing. We conclude that the density profile of galaxy clusters shows a profound self-similarity out to redshifts $z \sim 2.5$. This result holds for both gas and total density profiles when including baryonic physics, as reported here for two rather distinct sub-grid models.

2.3.1 Introduction

In the hierarchical growth paradigm of a Λ cold dark matter (ΛCDM) Universe, where the continuous merging of lower mass systems into haloes yields more massive systems, galaxy clusters are the biggest gravitationally bound systems. Although they are dark-matter dominated, and thus their growth is driven by gravitational interaction, at the same time their properties are also determined by the interaction with the baryonic component of clusters. For this reason, galaxy clusters form ideal laboratories for understanding the underlying cosmology of our Universe and the physical processes driving galaxy evolution.

It has been shown that for a flat Universe with scale-free initial density fluctuations, and at scales where baryonic physics can be neglected, dark matter haloes evolve self-similarly (e.g. Kaiser, 1986). And while the general shape of their density profiles is well defined by the two-parameter family of Navarro-Frenk-White (NFW) profiles (Navarro, Frenk, and White, 1996), individually there can be great deviations –especially in the outer parts (Diemer and Kravtsov, 2014). Observationally, scaling relations between directly measurable cluster properties, such as the X-ray luminosity ($L_{\rm X}$) or temperature (kT), can often be approximated by power laws. Hence, once the clusters are normalised by their mass, self-similar models can predict the slope of such relations (Bower, 1997). However, non-gravitational processes (e.g. Pearce et al., 2000; Voit and Ponman, 2003; Kravtsov, Vikhlinin, and Nagai, 2006; Maughan et al., 2012) are known to disrupt self-similarity and thus deviations are observed from such theoretical predictions, albeit observational results suggest that the influence of these processes is confined within the innermost regions of the clusters (e.g. Bartalucci et al., 2017b; McDonald et al., 2017; Ghirardini et al., 2018). Moreover, defining cluster masses and scales in terms of a characteristic density of the Universe (e.g. the background or critical density) induces an apparent evolution or "pseudo-evolution" on the cluster (Bryan and Norman, 1998; Diemer, More, and Kravtsov, 2013): the halo grows not only through dynamical processes, such as the merger of haloes, but also due to the change in the redshift-dependent reference density, which changes the normalisation of the observed scaling relation. This needs to be borne in mind when interpreting results, especially from numerical simulations where various mass definitions are being used throughout the literature (see Knebe et al., 2013b, for a discussion about possible halo mass definitions in simulations).

The growth of the universal dark matter halo density profile (as found in simulations of cosmic structure formation, Navarro, Frenk, and White, 1997) is often described in terms of a two-phase process: an early fast accretion phase where mass builds up in the central region

of the cluster, and a later slow accretion phase, where the mass builds in the outer region of the cluster while the mass density in the inner region remains approximately constant (Gott and Rees, 1975; Gunn, 1977; Łokas and Hoffman, 2000; Ascasibar et al., 2004; Ascasibar, Hoffman, and Gottlöber, 2007; Lithwick and Dalal, 2011). These accretion modes are also observed in numerical simulations (e.g. Bullock et al., 2001; Wechsler et al., 2002; Zhao et al., 2003b; Diemer and Kravtsov, 2014). Nevertheless, the numerical study of galaxy clusters at high redshift is a computationally-demanding task. In order to compare the results with observations, the profiles obtained from simulations are required to achieve spatial resolution down to the kpc scale (e.g. Bartalucci et al., 2017b; Bartalucci et al., 2017a; Ruppin et al., 2017) in order to resolve the inner regions of the clusters where complex baryonic processes, like feedback from stars or active galactic nuclei (AGN), take place. At the same time, the simulations need to correctly reproduce the influence of the large-scale structure on the outer – gravity-dominated – regions of the profile.

In a recent article, Le Brun et al. 2018, (from now on, LB+18) have shown that the 25 most massive galaxy clusters, as found in their dark matter only simulations and when scaled appropriately, have density profiles that are already in place at redshifts $z > 1$ and hence remarkably robust to mergers and any other evolutionary effects. To this extent they have studied the median density profile of the most massive systems identified at redshifts $z = 0, 0.6, 0.8$, and 1.0. Note that as they did not track the progenitors of their $z = 0$ sample, they always had a mass complete set at every redshift studied. They found that the median density profiles of their sample of objects exhibits very little evolution with only a mild scatter of 0.15 dex.

In order to study the evolution of density profiles we have taken a different approach and followed the merging history of our sample at redshift $z = 0$ backwards in time. Our dataset stems from THE THREE HUNDRED[16] project, i.e. a sample of over 300 galaxy clusters simulated with full-physics hydrodynamics (see Cui et al., 2018, for more details). This sample includes within it a set of objects similar in mass and selection to that presented by LB+18, but all our clusters are simulated with the relevant baryonic physics as modeled by two different hydrodynamics solvers and full-physics sub-grid models alongside the same gravity solver (i.e. `GADGET-MUSIC` and `GADGET-X` , as described below). While we also have at our disposal the corresponding dark matter only simulations, here we only present results from the full-physics runs (see App. C for a more direct comparison to the work of LB+18, and App. D for the dark matter only results).

This section is structured as follows: In Sec. 2.3.2 we describe the properties of the selected sample in detail. The results for the progenitors of the redshift $z = 0$ sample are presented in Sec. 2.3.3, classified either by their dynamical state or by their formation time. In Sec. 2.3.3 we also focus on the observational predictions from the redshift evolution of the (total) mass density profiles of the clusters by analysing their corresponding gas mass density profiles from the complete sample, the present day cluster scales in terms of their dynamical state and formation time. Finally, we conclude our analysis in Sec. 2.3.4.

2.3.2 Sample selection

In this section we use clusters within the THE THREE HUNDRED dataset, which were created by extracting 324 spherical regions of $15h^{-1}$ Mpc radius centred on each of the most massive clusters identified at $z = 0$ within the dark-matter-only MDPL2, MultiDark simulation (Klypin et al., 2016). Here we review the features of the dataset. For a detailed description of the dataset we refer to Sec. 2.2.

The cosmological parameters of THE THREE HUNDRED are based on the *Planck* 2015 cosmology (Planck Collaboration et al., 2016), with $\Omega_m = 0.307$, $\Omega_b = 0.048$, $\Omega_\Lambda = 0.693$, $h = 0.678$, $\sigma_8 = 0.823$, and $n_s = 0.96$. The cluster in the dataset were run with multiple codes, e.g. `GADGET-MUSIC` (Springel, 2005; Sembolini et al., 2016a) and `GADGET-X` (Beck et al., 2016), in a box of $1h^{-1}$ Gpc side-length.

For the analysis of the haloes we used the `AHF` [17] halo finder (Gill, Knebe, and Gibson, 2004; Knollmann and Knebe, 2009), which locates local overdensities in an adaptively

[16] https://the300-project.org
[17] http://popia.ft.uam.es/AHF

smoothed density field as potential halo centres and automatically identifies haloes and substructure (subhaloes, subsubhaloes, etc.). To trace haloes through the snapshots we build merger trees with `MergerTree`, a tool that comes with `AHF` .

The study of the fundamental galaxy cluster properties and scaling relations of the sample is discussed in Sec. 2.2. To summarise, overall, the modelled galaxy clusters in both codes are in reasonable agreement with observations with respect to baryonic fractions and gas scaling relations at redshift $z = 0$, with some (mode-dependent) differences, such as the existence of too massive central galaxies, or bluer galaxy colours (about 0.2 dex lower at the peak position) compared with observations.

With a simulated volume of radius $15h^{-1}$ Mpc each of our regions contains many more objects than the large cluster located at the centre. However, in this paper we confine ourselves solely to considering the evolution of the central object, i.e. the object on which the spherical region is centred and that was originally chosen to be modeled. By construction, these objects form, at redshift $z = 0$, a mass-complete sample of the largest objects in the full MDPL2 box (see App. A). But their progenitors will *not* form a mass-complete sample at higher redshifts.

To quantify the dynamical state of our objects, we adopt the same estimators as presented in Sec. 2.2. This means, that for each of our 324 large haloes we calculate three proxy indicators for virialisation. The first parameter is the fraction of mass in subhaloes $f_s = \sum M_{\rm sub}/M_{200}$, where $M_{\rm sub}$ is the mass of each subhalo. The second parameter is the virial equilibrium parameter $\eta = (2T - E_{\rm s})/|W|$, where T is the total kinetic energy, $E_{\rm s}$ the energy associated to the surface pressure exerted on the halo at r_{200} due to in-falling material, and W is the total potential energy. Finally, the last parameter is the centre-of-mass offset $\Delta_{\rm r} = |r_{\rm cm} - r_{\rm c}|/r_{200}$, where $r_{\rm cm}$ is the centre-of-mass within a cluster radius r_{200}, and $r_{\rm c}$ is the centre of the cluster corresponding to the maximum density peak of the halo. As described in Sec. 2.2, the criteria for selecting dynamically relaxed clusters are: $0.85 < \eta < 1.15$, $\Delta_{\rm r} < 0.04$, and $f_{\rm s} < 0.1$, which need to be satisfied simultaneously (see Neto et al., 2007; Power, Knebe, and Knollmann, 2012; Cui et al., 2017, for similar definitions). With these parameters, ~ 16 per cent (~ 17 per cent for `GADGET-X` ; and ~ 15 per cent for `GADGET-MUSIC`) of the mass-complete sample are relaxed at $z = 0$.

For the analysis of the density profiles we restrict our data to radii selected according to the following method. We first analyse the radial profiles of the MDPL2 clusters, avoiding inner bins where two-body collisions dominate the interaction between particles by requiring an estimate for the local collisional relaxation time to be larger than the age of the universe (Power et al., 2003). As this convergence criterion is based upon dark matter only simulations, we have used the counterpart MDPL2 clusters to determine their maximum innermost converged radius $r_{\rm conv}^{\rm MDPL2}$ (usually determined by the least massive object in the sample), and guided by this radius, we selected the radial values from the hydrodynamical runs entering our analysis. We refer to this inner limit as the "validation'" radius $r_{\rm valid}$: this turns out to be $r_{\rm valid} = r_{\rm conv}^{\rm MDPL2} \sim 28\ h^{-1}$kpc (approximately 4 times the softening of the simulation) at $z = 0$, and $\sim 37\ h^{-1}$kpc, $\sim 44\ h^{-1}$kpc, and $\sim 55\ h^{-1}$kpc (in comoving coordinates) at redshifts $z = 0.5, 1$, and 2.5, respectively. For each halo we focused our study on the mass density profile. While we mainly analysed the total (dark and baryonic matter) mass density profiles, we also studied the dark-matter-only and gas profiles from the hydrodynamical simulations (and the dark-matter-only profiles from the underlying dark-matter-only simulation, see App. D); none of that has an effect on the results and conclusions drawn from them, respectively, and hence we decided to only show the total mass results here.

By using two hydrodynamical codes with the same gravitational treatment but different SPH recipes and subgrid physics, we are able to study the influence – if any – of these changes on the evolution of the density profiles investigated in detail in the following section. However, we expect the influence of different baryonic processes to be (mostly) reflected in the innermost regions of the clusters, where we find pronounced deviations from a Navarro-Frenk-White (NFW) profile (Navarro, Frenk, and White, 1996) that otherwise describes our cluster profiles remarkably well.

TABLE 2.8: Minimum, median, and maximum mass values of the 324 cluster mass-complete sample at $z = 0$ sample and their progenitors at each redshift (see text for further details). In each row, the left value corresponds to the `GADGET-X` simulation, the right one to `GADGET-MUSIC` . All values are in units of $10^{14}h^{-1}\mathrm{M}_{\odot}$.

Redshift	min(M_{200})		med(M_{200})		max(M_{200})	
	G-X	G-MUSIC	G-X	G-MUSIC	G-X	G-MUSIC
$z = 0$	5.22	5.18	8.22	8.27	26.21	26.22
$z = 0.5$	0.58	0.31	3.90	3.80	18.93	18.95
$z = 1$	0.23	0.21	1.64	1.73	6.90	6.89
$z = 2.5$	0.0071	0.0065	0.16	0.17	1.77	1.80

2.3.3 Results and discussion

From the mass density profiles obtained for each galaxy cluster in the sample, we calculated the median profile at each redshift. We first defined 35 radial bins between the minimum and the maximum radial bin of the whole sample. We then interpolate each individual profile to those radii. If –for a given cluster– the profile would require extrapolation to one of our predefined radial bins, we instead flag that radial bin indicating that not all clusters can contribute to it. The resulting median values at our 35 radii are calculated using (non-flagged) interpolated values requiring contribution from at least 50 per cent of the sample. This criterion reduces the number of bins of the median profiles to ~ 30 bins, with inner and outer limits of $\sim 6h^{-1}$kpc and $\sim 1274h^{-1}$kpc at $z = 0$, respectively. Although we are not interested in the innermost region of the profile for this study, we also mark the unvalidated values (i.e. $r < 28, 37, 44$, or $55h^{-1}$kpc depending on the redshift) calculated from at least 50 per cent of the clusters, i.e. inner profile values which pass the first criterion but fail the second (for more details about the median profiles, see App. B).

Following the work of LB+18, the density profiles have been normalised by the critical density of the Universe at the corresponding redshift, and the radii have been scaled by r_{500}. When plotting the density profiles we further multiplied them by $(r/r_{500})^2$ to reduce the dynamical range. This also allows us to determine the scale radius r_s via the peak position $x_{\rm peak}$ of the resulting curve[18]

$$r_s = x_{\rm peak}\, r_{500}\,, \tag{2.8}$$

where the median r_{500} value will be used. The peak position of a median profile is found by first selecting the values found in the region $r/r_{500} > 0.2$ and $r/r_{500} < 1.1$ at our 4 target redshift. The median profile values in the selected region are then interpolated at 1000 points on this interval using 3rd order splines. From the interpolated profiles we then find the (scaled) radii at which the profiles reach their maximum. To obtain the uncertainty of the peak we started from the $30 - 70^{\rm th}$ percentiles of the median profile at a redshift value. We then applied the same procedure we used for the median profile to both percentiles curves and obtained an uncertainty interval for each peak's position (i.e. selecting a region, interpolating the original data, and finding the maximum's position). Next, we apply a Savitzky-Golay filter (Savitzky and Golay, 1964) with a 5-point window and a 3rd order spline to the interpolated data. Note that we use a relatively small window for the smoothing. This is done in order to ensure that the high redshift median profiles are being smoothed[19]. Using the smoothed interpolated data, we find the maximum's position.

According to LB+18, we should not expect to find any evolution out to redshift $z \sim 1$. We note that results from LB+18 were obtained for mass-complete samples at the corresponding

[18] Formally speaking, by multiplying the density profile with r^2, the peak position is characterised by r_{-2}, i.e. the position where the logarithmic slope is -2. But for a NFW profile $r_s = r_{-2}$ and hence we refer to it as the scale radius.

[19] After removing the innermost bins $r < r_{\rm valid}$ (see explanation in Sec. 2.3.2), ensuring that at least half the sample enters the median calculation, and selecting the region for the interpolation, we might end up with as few as ~ 7 points at the interpolation stage.

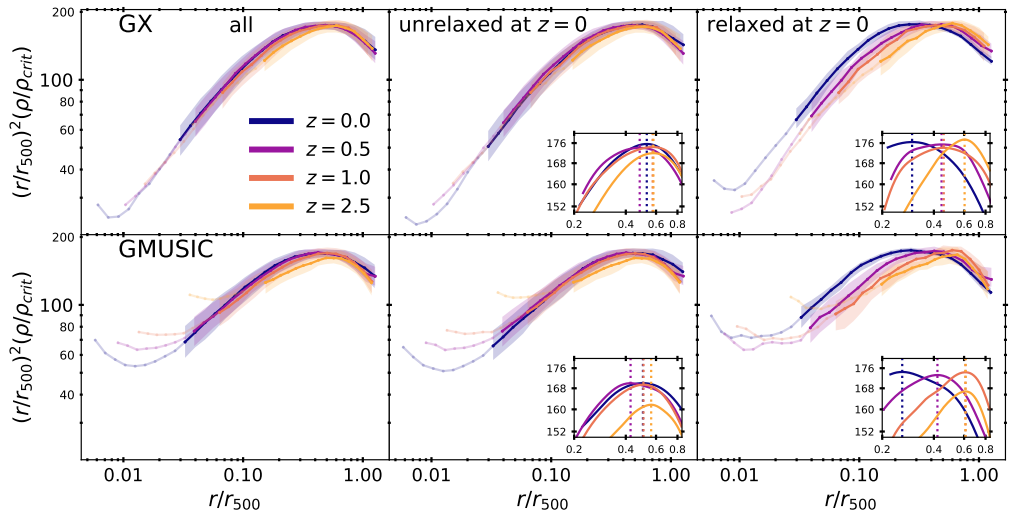

FIGURE 2.11: Median scaled mass density profiles of the central haloes at $z = 0$ and their main progenitors at $z = 0.5$, 1, and 2.5. The top row shows the results from `GADGET-X` , the bottom row from `GADGET-MUSIC` . The first column shows the results for the whole mass-complete sample (324 clusters), while the unrelaxed ($\sim$ 84 per cent of the total sample) and the results from the relaxed ($\sim$ 16 per cent) subsamples are presented in the second and third columns, respectively. The shadowed regions represent the $30-70$ percentiles. Unvalidated values are shown in lighter colors. In the insets we show the peak's position, r_s/r_{500}, for every curve.

redshifts. However, we are following the central haloes found at redshift $z = 0$ backwards in time. We therefore consider it relevant to summarise in Tab. 2.8 the minimum, median, and maximum masses of our objects at all redshifts of relevance. It is worth mentioning that the central halo from region "0047" is undergoing merger event at $z = 0$. During such events, halo finders are known to present some problems (see, for instance, Fig.4 in Behroozi et al. 2015). We found that for `GADGET-X`'s central halo "0047" `AHF` assigned the other cluster participating in the merger as the host halo; hence obtaining $\sim$ 20 per cent less mass than in its `GADGET-MUSIC` counterpart. Thus, we removed this central halo from the results in Tab. 2.8.

Dependence on dynamical state

Besides showing the evolution of the density profile in the left column of Fig. 2.11, we also split our sample of objects according to their dynamical state at redshift $z = 0$. The results are shown in the middle column for the unrelaxed clusters ($\sim$ 84 per cent of the total sample), and in the right column for the relaxed clusters ($\sim$ 16 per cent). The two different rows correspond to `GADGET-X` (top) and `GADGET-MUSIC` (bottom). The $30-70$ percentiles are represented by the shadowed regions. Unvalidated values calculated from at least 50 per cent of the clusters are shown in lighter colours. Besides deviations attributed to baryonic physics in the inner regions of the profiles and the expected influence from different environments at the outermost regions, the profiles present a strikingly self-similar evolution within $0.1 < r/r_{500} < 1$, with only a slight deviation in the maximum position at different redshifts. This is in agreement with previous results found by LB+18: after rescaling the density we find that the density profiles of the massive haloes of galaxy clusters evolve self-similarly.

However, when classified by their dynamical state, we observe some remarkable differences: unlike the complete sample, for the relaxed clusters there is a clear shift in the position of the maximum r_s/r_{500} with redshift, decreasing as we move to smaller redshift. To better identify the shift, we added insets for the subsamples of the total 324 central haloes sample. In the insets of Fig. 2.11 we can see that, while the whole sample presented a maximum at $r_s/r_{500} \sim 0.6$, once we select relaxed objects we see that they display a shift in the maximum position from redshift $z = 2.5$ onwards, reaching $r_s/r_{500} \sim 0.3$ at $z = 0$. While we

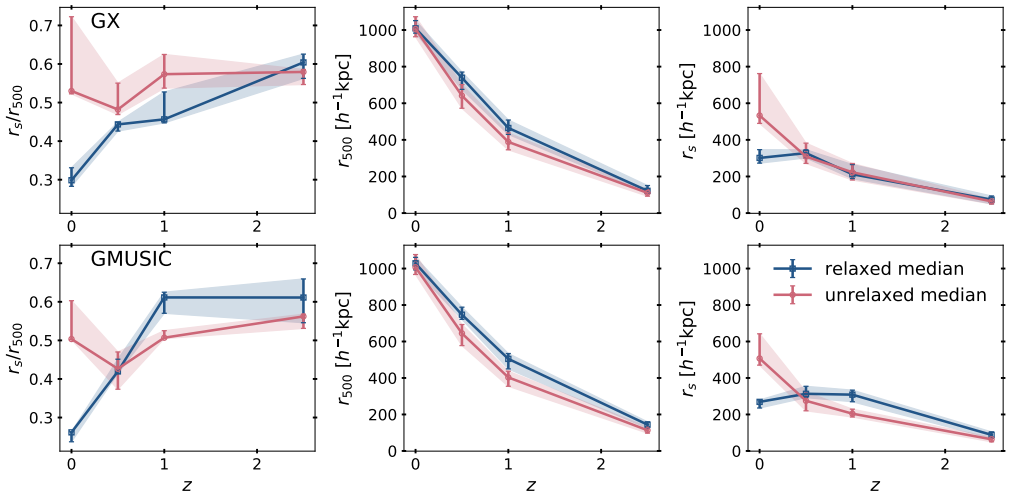

FIGURE 2.12: Redshift evolution of the density peak's position r_s/r_{500} (first column), r_{500} (second column) and the scale radius, r_s (third column), all in physical units, for the central cluster haloes at redshift $z = 0$ and their main progenitors at redshift $z = 0.5, 1$, and 2.5, classified by their dynamical state at redshift $z = 0$ (~ 84 per cent unrelaxed, ~ 16 per cent relaxed). In the top row, we show the results from `GADGET-X`; in the bottom row, for `GADGET-MUSIC`.

primarily studied the density peak's position shift, note that, qualitatively, the peak value $(r_s/r_{500})^2(\rho_s/\rho_{crit})$ is approximately constant (within the errors), where ρ_s is the density of the halo at $r = r_s$.

As we observe a shift in the ratio r_s/r_{500}, we now explore in more detail whether this is caused by a decrease in r_s, an increase in r_{500}, or a combination of both. To this extent we determine the peak positions as seen in Fig. 2.11 via spline-interpolation and the median r_{500} for the respective sample. This allows us to calculate the corresponding r_s via Eq. (2.8). Another approach to retrieve these numbers would be to use r_s and r_{500} values obtained from individual fits of the density profile to the functional form of an NFW profile. We confirm that this does not alter or affect our results.

The redshift evolution of the ratio r_s/r_{500} is presented in Fig. 2.12 (left column), alongside the individual evolution of r_{500} (middle column) and r_s (right column) – all in physical units. The upper row shows results for `GADGET-X` whereas the lower row shows `GADGET-MUSIC` . The relaxed and unrelaxed samples are colour-coded according to the legend. As we can see, r_{500} grows monotonically down to $z = 0$ for both the relaxed and unrelaxed subsamples, with a slightly steeper slope in the unrelaxed subsample. The growth of r_{500} is a result of the combined effect of accretion and pseudo-evolution, however, pseudo-evolution affects both subsamples equally. On the other hand, we see that r_s undergoes a different evolution depending on the dynamical state of the clusters. For unrelaxed clusters, r_s grows monotonically down to $z = 0$ with a similar slope to the observed growth in the physical r_{500}, thus the overall evolution of the density peak is not seen in the median trend. For the relaxed clusters, we see an initial period of growth, similar to the one in the unrelaxed subsample, until at $z \sim 0.5$ the growth slows down and remains close to a constant value. We can understand this difference as a result of the different accretion phases each subsample experiences close to $z = 0$, something expected from the secondary infall model (e.g. Ascasibar et al., 2004; Ascasibar, Hoffman, and Gottlöber, 2007).

Dependence on formation time

As the dynamical state of a galaxy cluster is linked to its formation time (i.e. earlier formed systems have had more time to relax and eventually pass from the phase of early, fast accretion to the stage of late, slow accretion), we now sub-divide our mass-complete sample at redshift $z = 0$ into several formation redshift bins as follows: to determine the formation time we fit the mass accretion history (MAH) of each cluster to the functional form proposed

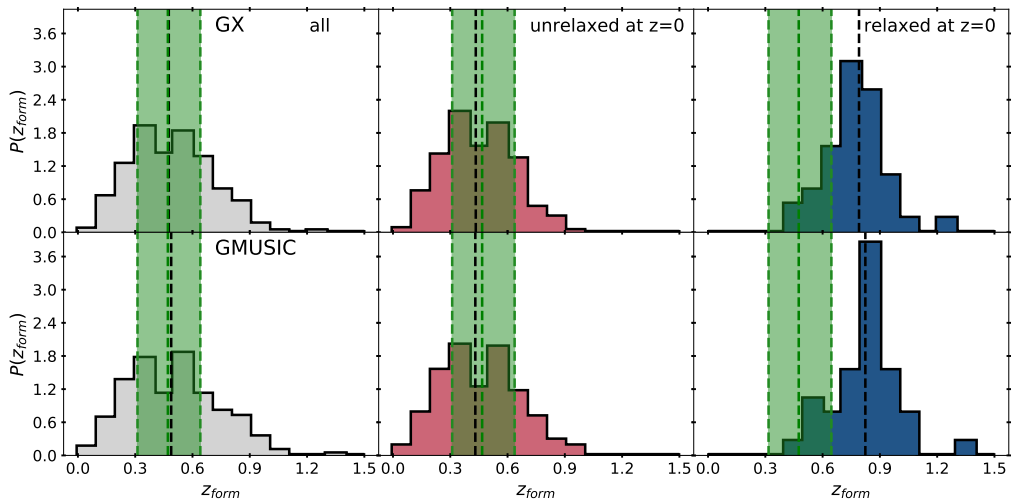

FIGURE 2.13: Formation time distribution of the whole mass-complete sample (left column), the unrelaxed (middle column) and the relaxed (right column) at $z = 0$ subsamples, as obtained from GADGET-X (top row) and GADGET-MUSIC (bottom row). The black dashed line represents the median formation time of each sample. The middle green dashed line and green shaded regions show the expected formation time and 1σ errors, respectively, from the extended Press-Schechter calculation of Power, Knebe, and Knollmann (2012), for the median halo mass of each sample.

.

in Wechsler et al. (2002).

$$M_{200}(z) = M_{200}^{z=0} \ \exp\left(-\alpha z\right), \tag{2.9}$$

where α is a characteristic parameter for each cluster which describes the (assumed constant) mass accretion rate of the halo. The formation redshift $z_{\rm form}$ is now defined as the redshift where $M_{200}(z_{\rm form})/M_{200}^{z=0} = 0.5$ or equivalently

$$z_{\rm form} = -\ln(0.5)/\alpha\,. \tag{2.10}$$

With this definition, in Fig. 2.13 we show the distribution of formation redshift of the whole mass-complete sample (first column), the unrelaxed subsample (second column), and the relaxed subsample (third column) for the two hydrodynamical simulations in our database, G-X (top row), and G-MUSIC (bottom row). The dashed black line shows the median formation time of each sample, and the green dashed line and green shaded region show the expected median formation time and 1σ errors from the extended Press-Schechter theory calculation of Power, Knebe, and Knollmann (2012). The median formation time of the mass-complete sample is in good agreement with the expected value for haloes of the same median mass. However, although there is an overlap in the formation time distributions of the unrelaxed and relaxed subsamples, i.e. we find both unrelaxed and relaxed clusters within $0.4 \leq z_{\rm form} \leq 1$, the relaxed clusters formed well before the expected value. This confirms the correlation between formation time and dynamical state (e.g. Power, Knebe, and Knollmann, 2012; Wong and Taylor, 2012). Note that – according to the results presented in the previous relaxation analysis – the total mass density profile of the clusters is found to be already in place at $z = 2.5$, long before their formation time.

To confirm the link between the formation time of our clusters and the shift observed in the peak position for r_s/r_{500} for dynamically relaxed clusters at $z = 0$, we present in Fig. 2.14 the evolution of the median density profile again, but this time for three distinct formation time bins chosen to minimise overlap in formation times and also to give roughly equal numbers of clusters at the two extremes in both simulations (more on this later), i.e. $z_{\rm form} < 0.3$ (~ 21 per cent of the total sample, left column), $0.3 < z_{\rm form} < 0.6$ (~ 49 per cent, middle column), and $z_{\rm form} > 0.6$ (~ 30 per cent, right column); the two rows are again for GADGET-X (upper row) and GADGET-MUSIC (lower row).

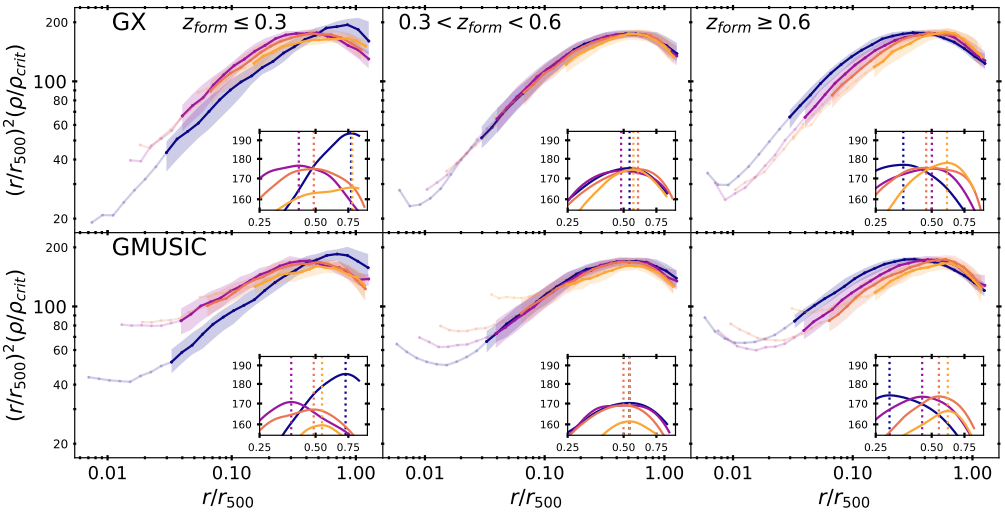

FIGURE 2.14: Same as Fig. 2.11 but now the sample is separated into late-formed ($z_{\rm form} \leq 0.3$, $\sim$ 21 per cent of the total sample, left column), intermediate-formed ($0.3 < z_{\rm form} < 0.6$, $\sim$ 49 per cent, middle column), and early-formed ($z_{\rm form} \geq 0.6$, $\sim$ 30 per cent, right-column) clusters, as found in both simulations.

The plot confirms that early formed system show a shift, but also that there is substantial scatter for late formed objects. Fig. 2.15 further quantifies the shift in r_s, r_{500}, and its ratio. This plot is analogous to Fig. 2.12, but now there are three lines in each panel, one for each redshift of formation bin.

We obtain a similar shift once we turn to the early formed ($z \geq 0.6$) subsample. Comparing the early-formed (green) and late-formed (pink) subsamples within each code, we find that the r_{500} and $r_{\rm s}$ growth is similar to what we observed in the evolution of the dynamically relaxed and unrelaxed clusters in Fig. 2.12. Between $z = 2.5$ and $z = 1$, the early-formed clusters grow faster than the late-formed ones; however, between $z = 1$ and $z = 0.5$, both cluster subsamples appear to have approximately the same r_{500} growth rates in both codes. Although the $r_{\rm s}$ growth rate of GADGET-X's early-formed clusters is steeper than GADGET-MUSIC's, there are no major differences in terms of $r_{\rm s}/r_{500}$. It is not until redshift $z < 0.5$ that we observe a considerable difference in the peak's position evolution. At $z = 0$ we end up with a difference of $\Delta(r_{\rm s}/r_{500}) \sim 0.5$ between the early and late-formed clusters. Similar to the trends observed in Fig. 2.12, the r_{500} growth rate at $z < 0.5$ of the late-formed clusters becomes much steeper than the rate of the early-formed, such that both subs-samples end up with a similar size at $z = 0$. The r_s evolution, however, differs. Unlike the late-formed clusters, the median $r_{\rm s}$ of the early-formed clusters remains constant from $z = 0.5$. This result confirms that the formation time of the clusters drives the shift observed in the relaxed subsample and that the dynamical state is not the primary driver of it, even though there is a correlation between early-formed clusters and relaxed clusters, as seen from the formation time distribution presented in Fig. 2.13.

We now seek a better understanding of the shift in the median density profiles, as seen for the relaxed subsample. Overall, relaxed clusters formed earlier ($z_{\rm form} \sim 0.8$) than the unrelaxed ones ($z_{\rm form} \sim 0.4$). This implies that at $z = 0$, as seen from the growth rates of both the physical $r_{\rm s}$ and r_{500}, most of the unrelaxed clusters are still in the fast accretion phase whereas the majority of the relaxed clusters have entered the slow accretion phase: contrary to the mass buildup of the unrelaxed subsample, infalling material no longer accumulates in the central region but rather in the outskirts of the clusters. Consequently, for the relaxed sample, $r_{\rm s}$ no longer grows while, along with pseudo-evolution, the infalling material induces a growth in r_{500}. This is in agreement with the secondary infall model (e.g. Łokas and Hoffman, 2000; Ascasibar et al., 2004; Ascasibar, Hoffman, and Gottlöber, 2007) and previous numerical results (e.g. Bullock et al., 2001; Wechsler et al., 2002; Zhao et al., 2003b).

While this trend is observed in the median results for the relaxed subsample, we argue

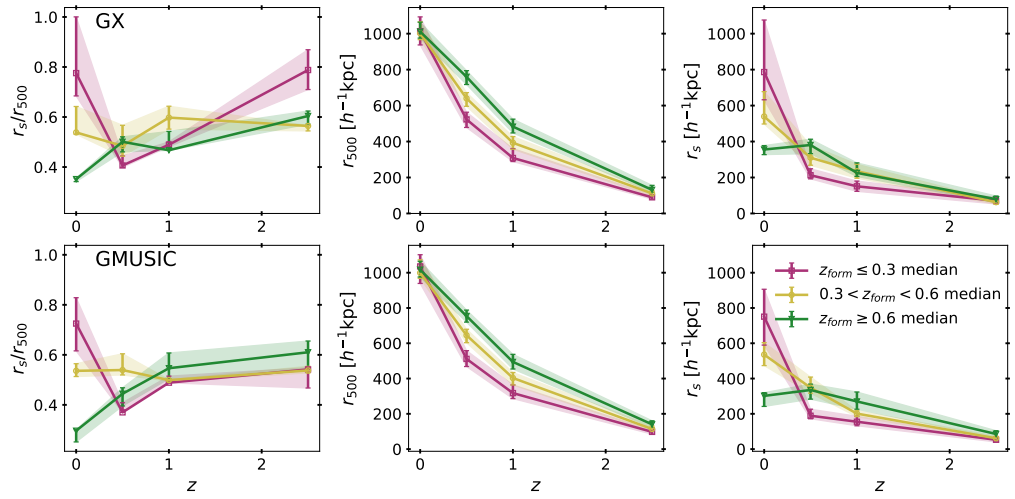

FIGURE 2.15: Same as Fig. 2.12 but now the sample is separated into late-formed, intermediate-formed , and early-formed clusters as in Fig. 2.14.

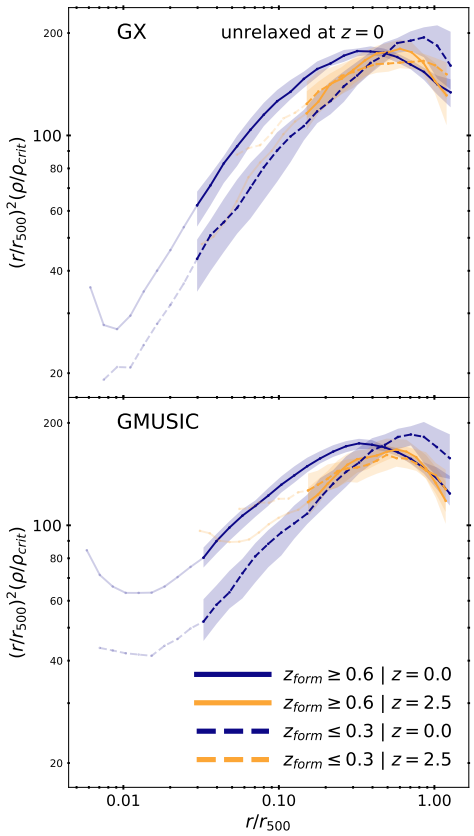

FIGURE 2.16: The redshift evolution of the median scaled density profiles ($z = 0$ and $z = 2.5$) for unrelaxed early-formed ($\sim$ 24 per cent of the unrelaxed clusters, with $z_{\rm form} \geq 0.6$) and unrelaxed late-formed ($\sim$ 25 per cent, with $z_{\rm form} \leq 0.3$) clusters, from `GADGET-X` (top) and `GADGET-MUSIC` (bottom).

that the main reason why the shift is not visible in the median profiles of the whole sample (Fig. 2.11) is the scatter associated with the diversity of density profiles in the unrelaxed clusters. Since the sample is mostly dominated by unrelaxed (as classified at $z = 0$), relatively late-formed ($z_{\rm form} \sim 0.5$) clusters, studying the median profile evolution washes out such a shift. This can be verified in Fig. 2.16, where we show the evolution of the median density profile of only unrelaxed clusters ($\sim$ 272 clusters) that formed early ($\sim$ 24 per cent of the unrelaxed sample, with $z \geq 0.6$, solid lines) and late ($\sim$ 25 per cent, with $z \leq 0.3$, dashed lines) in GADGET-X (upper panel) and GADGET-MUSIC (lower panel).

We see that unrelaxed, early-formed systems also show a marginal trend for evolution of the peak position, albeit still within the respective percentiles of the unrelaxed late-formed ones. In regards to the formation time selection criteria used in the analysis, while the chosen boundary values, i.e. $z_{\rm form} = 0.3$ and $z_{\rm form} = 0.6$, are somewhat arbitrary, it is worth noting that picking different values, besides changing the sample sizes and the relaxed/unrelaxed fractions of clusters in each bin, will not induce drastically different results, as we can infer from Fig. 2.16. As previously stated, the correlation between dynamical state and formation time in Fig. 2.13 leads to the shift in the relaxed subsample, but as we showed in Fig. 2.16, formation time dictates the shift.

Influence on gas mass profiles

We now raise the question of how these results relate to observations. As reported by McDonald et al. (2017), the mean (hot) gas profile of massive clusters shows a pronounced self-similar evolution out to a redshift of $z \sim 1.9$. Having performed full physics hydrodynamical simulations, we also have access to the gas density profile and hence show its evolution in the same manner as before in Fig. 2.17 and with a focus on relaxed and unrelaxed systems. We confirm that the gas density profile follows qualitatively the self-similar evolution observed in the total mass density profile seen in Fig. 2.11: out to $z = 1$, the mass-complete sample and the unrelaxed subsample evolve self-similarly, whereas the relaxed subsample shows a shift in the peak's position. Focusing in the relaxed subsample we can see that both codes evolve in a similar fashion, and that the main difference resides in the scatter in the profiles. GADGET-X's median profiles show more diversity due to the influence of AGN feedback (specially in the inner $r/r_{500} < 0.1$ region), while GADGET-MUSIC's median profiles have overall less scatter at those scales. In order to present a clearer picture of the evolution of the gas profiles, we added insets for the two subsamples. As we can see in the insets, there is a broadening of the median profiles at $z = 0$ compared with the profile at $z = 2.5$. However, despite this broadening, there is indeed a shift in the peak's position of the relaxed subsample as the scatter at the peak's position is negligible compared with the shift between $z = 0$ and $z = 2.5$ (i.e. $\Delta(r/r_{500}) \sim 0.2 - 0.4$).

By redshift $z = 2.5$ the profiles deviate slightly from the rest of the distribution, which might be caused by several processes. At high redshift mergers are the main source of halo mass build-up, as they are in their early-phase accretion mode (e.g. Wechsler et al., 2002; Burke and Collins, 2013). Hence, processes like ram-pressure stripping could remove the gas of the infalling satellites (e.g. Fujita, 2001; Fujita, 2004; Wang et al., 2018; Arthur et al., 2019; Mostoghiu et al., 2020b). The deficit could also be attributed to the high star formation rate in our simulated clusters, which peaks around $z = 2.5$ (as seen in Figure 4 of Wang et al., 2018). Both the central galaxy and the infalling satellite galaxies from mergers produce a gas deficit at different scales. Finally, the clumpiness of gas particles due to the SPH treatment of hydrodynamics in numerical simulations (e.g. Hobbs et al., 2013) may also be a cause, at least for GADGET-MUSIC . This numerical issue causes the gas to clump rapidly into the halo centre –contrary to the smooth accretion of gas– and leave a lower gas density at outer halo radius.

Nevertheless, the fact that we observe a self-similar evolution of the gas density profile does not come as a surprise as the scales we are probing here are dominated by gravity and hence the gas is a biased tracer (note the different scales on the y-axis as compared to the previous total matter density plots). We observe that the gas profiles show inherently larger scatter, especially at small scales ($r/r_{500} < 0.02$) and for GADGET-X (i.e. the code that features AGN feedback affecting the central regions). However, we can constrain the influence of the

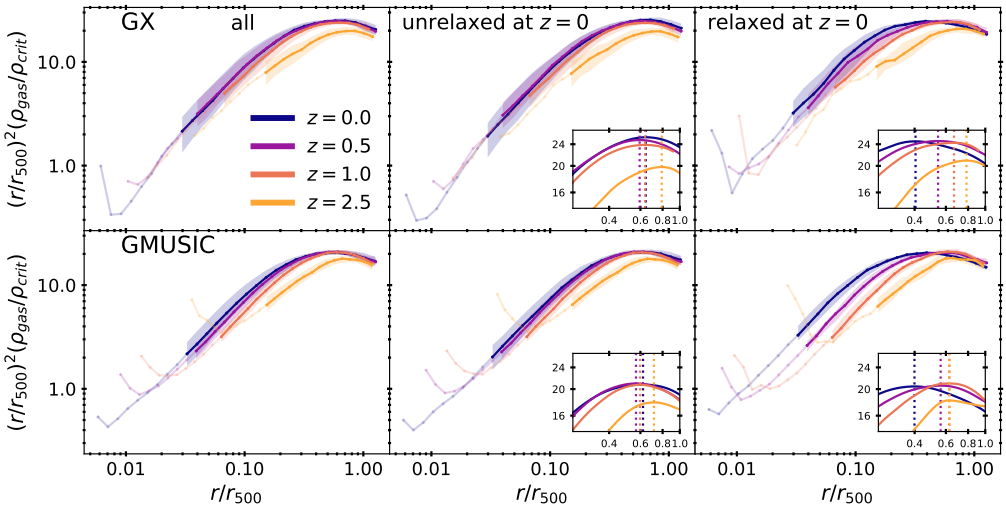

FIGURE 2.17: Median scaled gas mass density profiles of the central haloes at $z = 0$ and their main progenitors at $z = 0.5$, 1, and 2.5, classified by their dynamical state at $z = 0$, as in Fig. 2.11. The top row shows the results from `GADGET-X` , the bottom row from `GADGET-MUSIC` .

baryons to lie within $r/r_{500} < 0.01 - 0.1$, depending on the redshift. Compared with observations, recent results of high redshift massive galaxy clusters show that beyond the core of the clusters ($r/r_{500} > 0.3$) the level of self-similarity in gas density profiles is particular remarkable and that non-gravitational effects, such as AGN feedback, can be confined in the $r/r_{500} < 0.2$ region (McDonald et al., 2017). Moreover, in Ghirardini et al. (2018), the authors analysed 12 massive ($M_{500} = 3 - 9 \times 10^{14} M_{\odot}$) high-quality local ($z < 1$) galaxy clusters and determined the *intrinsic* scatter of thermodynamic quantities as a function of radius. The amount of scatter is minimised in the $0.2 < r/r_{500} < 0.8$ range, the region where the gas is highly vitalised and baryonic effects are negligible. In the inner region ($r/r_{500} < 0.3$) baryonic effects induce large scatter within the population, while in the outer region ($r/r_{500} \geq 1$) the scatter is driven by the different accretion rates from one cluster to another (see Eckert et al., 2012; Reiprich et al., 2013, and references therein, for more determinations of intrinsic scatter). Looking at Fig. 2.17 we can see similar trends: up to $z = 1$, the least amount of scatter, as described by the shaded region corresponding to the $30 - 70$ percentiles, is achieved for $0.3 < r/r_{500} < 1$. The median gas profiles from `GADGET-X` follow the self-similar evolution down to $r/r_{500} \sim 0.02$. However, the scatter induced by non-gravitational processes dominates in the region. On the other hand, in `GADGET-MUSIC` , although deviations from the self-similar trend are visible at the same radial range, the scatter is systematically lower.

Present day halo scales

The main finding from the previous sub-sections (notwithstanding the dark matter-gas connection) can be summarised by Fig. 2.18. In Fig. 2.18 we present the scale radius r_s and r_{500} at redshift $z = 0$ for every cluster in the sample as a function of its formation redshift $z_{\rm form}$, where we additionally colour-code the clusters by their dynamical state at $z = 0$.

For this plot we now require individual r_s values for each cluster. These are obtained by fitting the enclosed[20] radial mass distribution $M(< r)$ to the functional form of a NFW profile (e.g. Łokas and Mamon, 2001)

$$\frac{M(s)}{M_{200}} = g(c) \left(\ln(1 + cs) - \frac{cs}{1 + cs} \right), \tag{2.11}$$

[20]The enclosed mass $M(< r)$ is a cumulative – and generally smooth – profile, hence it is easier to obtain a good fit.

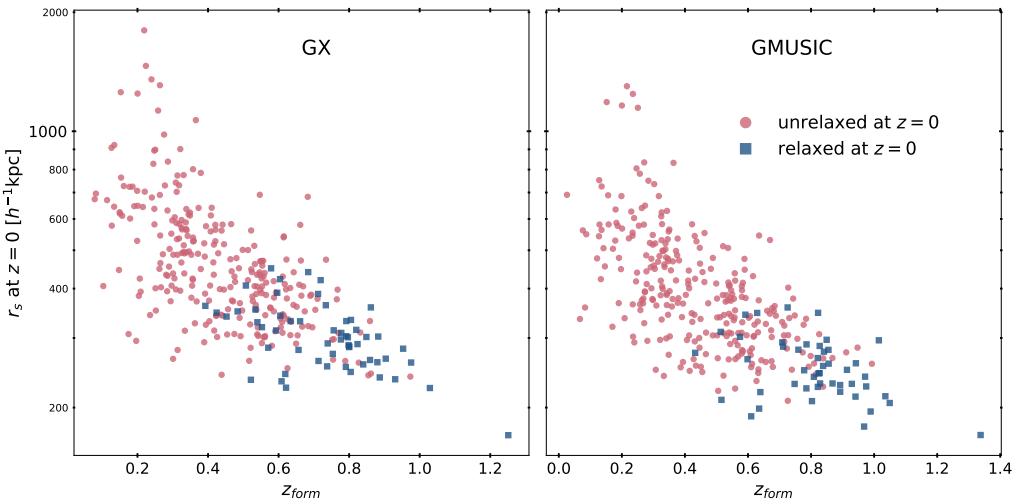

FIGURE 2.18: Scale radius r_s at redshift $z = 0$ correlation with formation redshift $z_{\rm form}$ for relaxed clusters (blue) and unrelaxed clusters (orange). The left panel shows the results for `GADGET-X` and the panel for `GADGET-MUSIC` .

with

$$s = \frac{r}{r_{200}}\,, \tag{2.12}$$

$$c = \frac{r_{200}}{r_s}\,, \text{ and} \tag{2.13}$$

$$g(c) = \frac{1}{\ln(1+cs) - cs/(1+cs)}\,, \tag{2.14}$$

where c, the only free parameter, is the concentration of the cluster; r_s is now simply calculated as

$$r_s = \frac{r_{200}}{c}\,. \tag{2.15}$$

The overall trend shows that relaxed clusters end up with smaller values of r_s at $z = 0$ than the unrelaxed ones. It is worth noting that, as discussed in previous sections, there are unrelaxed clusters which formed at similar redshift as relaxed ones. Morever, the early-formed unrelaxed haloes show a considerable amount of scatter in their scale radius r_s at $z = 0$, there are unrelaxed haloes with comparable r_s values to the relaxed ones that formed earlier. These effects are mainly due to two issues. First, the classification of the mass-complete sample by its dynamical state is done at redshift $z = 0$ and it is kept up to $z = 2.5$, i.e. we do not track information about the dynamical state of the progenitors of the haloes. A cluster classified as relaxed at $z = 0$ might not pass our relaxation criteria at higher redshifts; and vice versa, an unrelaxed cluster at $z = 0$ might have been a relaxed cluster at some point in its past and only recently being disturbed again. If an initially relaxed cluster becomes unrelaxed without undergoing a significant change in its formation time determination, e.g. a change in its subhalo fraction f_s due to minor mergers, it would show as an unrelaxed halo with similar formation times and r_s values at $z = 0$ to the relaxed haloes. Second, a recent (major) merger might induce a steep mass accretion close to $z = 0$, which –given our formation time definition– consequently translates into a lower than expected value for $z_{\rm form}$. Thus, we can understand the unrelaxed haloes with comparable r_s values to the relaxed ones as haloes that in fact formed earlier (i.e. $z > 0.3$) and have been disturbed recently by a major merger and, as such, they have a lower r_s value than the rest of the haloes in the early-formed bin.

2.3.4 Conclusions

In this section we used the mass-complete sample of the THE THREE HUNDRED dataset (described in Sec. 2.2), consisting of 324 galaxy cluster haloes with median mass $M_{200} =$

$8.2 \times h^{-1}10^{14}\mathrm{M}_{\odot}$. For cluster-sized haloes, self-similarity is expected to dominate the redshift evolution of their mass density profiles, although baryonic non-gravitational interactions are known to disrupt the effect. We have used our data set to verify this. By tracking the evolution of the central haloes found at $z = 0$ back to $z = 2.5$ we investigated the self-similarity of their density profiles. We summarise our main results here:

- The density profiles of the whole sample is consistent with a self-similar evolution, suggesting that the density profile is stable and already in place even at $z \geq 2$, long before their formation time and as found in dark matter only simulations by other workers in the field (e.g. LB+18). However, when separating the sample according to their dynamical state at $z = 0$, the relaxed clusters ($\sim$ 16 per cent of the total sample) show a shift in where their scaled median density profile peaks.

- The shift in the scaled the median density profiles of relaxed clusters is a result of a different evolution of r_s, the scale radius of a NFW density profile, and r_{500} between the unrelaxed and relaxed subsamples. This is understood within the context of a two-phase accretion model for halo mass growth, as theoretically argued (e.g. Gunn and Gott, 1972; Gunn, 1977; Ascasibar et al., 2004) and found in numerical simulations (e.g. Wechsler et al., 2002; Zhao et al., 2003b). While unrelaxed clusters are still in their fast accretion mode at $z < 0.5$, in which infalling material is accreted to the cluster centre inducing rapid growth in both $r_{\rm s}$ and r_{500}; relaxed clusters reached the slow accretion phase at $z < 0.5$ and thus infalling material remains in the outer region of the cluster while the inner region evolves almost unperturbed. Therefore, $r_{\rm s}$ slows its growth at the later stages of the cluster's evolution while r_{500} keeps growing due to the effects of infalling material (and also pseudo-evolution) at the outskirts of the halo.

- We classified the sample by their formation time, defined here as the redshift at which the fitted mass growth curve of the cluster reaches 50 per cent of its total mass M_{200} at $z = 0$, regardless of their dynamical state. We find that once binned by their formation time, the same trend is observed. Early formed ($z_{\rm form} \geq 0.6$) clusters end up with lower values of $r_{\rm s}/r_{500}$ than late-forming clusters ($z_{\rm form} \leq 0.3$).

- This shift, although potentially visible also for unrelaxed haloes due to the overlap between unrelaxed early-formed haloes and relaxed late-formed ones, is not visible in the median profiles of unrelaxed profiles due to the scatter associated with their diversity of density profiles. Relaxed clusters, on the other hand, have stable density profiles, i.e. less scatter, and consequently the shift is visible in this subsample.

- The gas profiles also follow qualitatively the self-similar evolution of the total density profile with only a considerable deviation at $z = 2.5$ which can be attributed to the combined effect of the merger activity and star formation rate at that redshift, and numerical effects from SPH. This follows naturally from the fact that gravity is the main driving force at the scales studied here and thus gas is a biased tracer of the underlying dark-matter distribution of the cluster. Even the powerful AGN in the centre of the clusters in the `GADGET-X` simulations does not affect the density profile at distances $r \gtrsim 0.1 r_{500}$, although it increases the scatter in the inner regions of the cluster. The influence of the baryons on the total (dark matter and baryons) density profile can be conservatively constrained within the innermost part of the cluster, at $r/r_{500} < 0.01 - 0.1$, depending on the redshift. We note that our results are in agreement with observations (e.g. McDonald et al., 2017; Ghirardini et al., 2018), although the shift observed in our dynamically relaxed/early-formed subsample is not detected in observational studies due to the implicit selection of the sample in every observation.

The implications of this work form something of a warning to those seeking to use massive galaxy clusters as cosmological probes. The significant shuffling of the rank order in mass of massive clusters should not be a surprise: at the very massive end the mass function is steep and small changes in mass can make a large difference. In the era of league tables those close to the top know full well that the likely direction of travel can only be down. This fact of life as a giant galaxy cluster makes it very easy to select a biased sample and both theorists and observers need to be aware of the consequences of this.

The most massive clusters today are not the same clusters as those most massive at $z = 1$. Selecting a mass-limited sample, such as that used by LB+18 is one way out of this conundrum, but such a choice may obscure certain theoretical ideas about cluster growth. Certainly great care needs to be expressed in sample selection as it is clear that without a detailed knowledge of completeness bias may be introduced into any measure of evolution. We have also demonstrated that care should be taken when selecting a relaxed sample of objects: these are the set where is it easiest to see evolution and growth along theoretical lines because this set have lower scatter in their properties. As such, they may not actually evolve self-similarly.

2.4 Stellar angular momentum evolution of cluster galaxies

Section based on Mostoghiu et al. (2020a) (In prep.)

In the previous section we studied how the most massive clusters in the dataset accrete their mass during their growth, and found how similar their density profile evolution is, both for the total and gas mass. Even though individual density profiles are diverse, statistically-speaking, the accreted material is radially deposited following similar trends. On the other hand, their environments are quite varied and shape the properties of the infalling objects into the main cluster. In this section, we focus on the kinematic properties of such haloes.

We use the 324 numerically modelled galaxy clusters as provided by THE THREE HUNDRED project to study the evolution of the kinematic properties of the stellar component of haloes on first infall. We select objects with $M_{\rm star} > 5 \times 10^{10} h^{-1} {\rm M}_{\odot}$ within $3R_{200}$ of the main cluster halo at $z = 0$ and follow their progenitors. We find that although haloes are stripped of their dark matter and gas after entering the main cluster halo, the stellar kinematics are unaffected by the change of environment. For the vast majority of our 'galaxies' – defined as the central stellar component found within the haloes that form our sample – their position in the specific stellar angular momentum−stellar mass plane $j_{\rm star}$ – $M_{\rm star}$, and their kinematic properties, as described by the fraction of ordered rotation, are mostly unchanged by the influence of the central host cluster. For a small number of infalling slow rotators, stellar mergers and encounters with remnant stellar cores close to the centre of the main cluster, particularly during pericentre passage, are able to spin-up their stellar component such that they appear as fast rotators at $z = 0$.

2.4.1 Introduction

In a hierarchical model of structure formation, the structures observed today are a result of the merging of dark matter clumps at high redshift via gravitational collapse. As the clumped dark matter grows into larger objects to form haloes, they experience tidal torques from neighbouring objects. At the same time, baryons condense in the centre of such structures to form galaxies (Peebles, 1969; Doroshkevich, 1970; White and Rees, 1978; White, 1984). During their mutual formation both the dark matter and baryonic component experience the same tidal fields, and hence it is expected that they gain the same amount of specific angular momentum. Furthermore, considering that baryons evolve inside dark matter haloes, it is also expected that the kinematic evolution of galaxies is influenced by the halo in which they reside.

However, galaxies and their haloes also feel the influence of the environment. Haloes falling towards and eventually orbiting within galaxy clusters are disrupted by a series of processes predominant in the cluster environment, e.g. ram-pressure stripping (Gunn and Gott, 1972; Abadi, Moore, and Bower, 1999; Bahé and McCarthy, 2015; Arthur et al., 2019) that removes the gas in haloes and quenches the star formation of galaxies; galaxy harassment (Moore et al., 1996; Moore, Lake, and Katz, 1998; Smith, Davies, and Nelson, 2010; Smith et al., 2015), mergers (Dressler, 1980; Hashimoto and Oemler, 2000; Behroozi et al., 2014), tidal torques (Fujita, 1998; Balogh, Navarro, and Morris, 2000; Park et al., 2007), and interactions in general (Knebe et al., 2006; Recchi, 2014) that can disrupt the haloes' components; and dynamical friction (Valtonen et al., 1990; Jiang and Binney, 2000; Fujii, Funato, and Makino, 2006; van den Bosch, 2017; Miller et al., 2020) which slows down infalling haloes

and, over time, causes them to fall to the centre of the cluster. While the stars residing deep inside the potential well of the halo are shielded from tidal effects, they might nevertheless feel and react to the change of its own halo caused by the aforementioned processes. Or put differently, if the kinematic evolution of galaxies is indeed tied to its halo, the cluster environment affecting the halo could eventually also disrupt the kinematics of galaxies at its centre. This question now lies at the heart of the present study.

Previous numerical studies have shown how tidal interactions can disrupt infalling haloes in different environments. The seminal work of Hayashi et al. (2003) studied how tides influence substructure in dark matter-only simulations. Their analysis showed that, although tides preferentially strip the outer regions of haloes, they also decrease the halo's central density after each pericentric passage. Subsequent studies improved the tidal disruption estimation by including a stellar component to their analysis (e.g. Bullock and Johnston, 2005; Peñarrubia, Navarro, and McConnachie, 2008). The stellar component was found to be exceptionally resilient to tides, preserving its density profile shape even after losing a considerable amount of stars. Nevertheless, the stellar dynamics of such calculations were modelled by analytic profiles, which simplify processes such as the mass loss from dynamical friction, the halo phase-space evolution after merger interactions, or the stellar mass fractions determined by star formation. More recent studies overcame these limitation by introducing a stellar component modelled by full-physics hydrodynamics (e.g. Smith et al., 2016; Łokas, 2020; Errani and Peñarrubia, 2020; Mazzarini et al., 2020). However, these studies primarily focus on mass-loss processes, hence the question of how environmental effects influence the kinematic properties of the stellar component of infalling haloes remains to be addressed.

One of the fundamental kinematic properties of galaxies is the relation between their specific angular momentum and their stellar mass, first presented in Fall (1983). It was shown that galaxies follow parallel sequences in the specific angular momentum $j_{\rm star}$ – stellar mass $M_{\rm star}$ plane, where $j_{\rm star} \equiv {\rm J}_{\rm star}/M_{\rm star}$, and $\rm J_{star}$ is the galactic angular momentum. Their trend can be described by a power-law of the form $j_{\rm star} \propto M_{\rm star}^{\alpha}$, where $\alpha \approx 0.7$. Such a relation has been extensively studied since the seminal work of Fall (1983): recent observational results presented the possible dependence between the galactic component trends (e.g. Romanowsky and Fall, 2012; Obreschkow and Glazebrook, 2014; Fall and Romanowsky, 2018), the distribution of galaxies in the $j - M$ plane and their correlation with kinematic properties (e.g. Cortese et al., 2016), or the relation at high-redshift (e.g. Burkert et al., 2016; Harrison et al., 2017). On the other hand, simulations showed the existence of a smooth transition between different galactic components (Teklu et al., 2015), the evolution of the angular momentum and the quenching of star formation (e.g. Lagos et al., 2017), the type of rotational support galaxies acquire during their evolution (e.g. Lagos et al., 2018a), or the angular momentum retained by the different baryonic components during halo formation (e.g. Dutton and van den Bosch, 2012; Stevens, Croton, and Mutch, 2016; Obreja et al., 2019). Given the fundamental nature of $j - M$ plane, if the cluster environment plays a decisive role in the kinematic evolution of infalling galaxies, it should be reflected on the trends of the relation.

These recent studies also revealed the need for a more accurate and robust galaxy classification (e.g. Cappellari et al., 2011; Krajnović et al., 2013; Tacchella et al., 2015; Bluck et al., 2019). Emsellem et al. (2007), for instance, proposed one that classifies galaxies according to their kinematics. Recent observational results show that the fraction of slowly rotating galaxies show a strong dependence on the stellar mass, a weaker one on local environment, and no correlation with host cluster mass. Nevertheless, at high stellar masses (i.e. $M_{\rm star} > 10^{11}{\rm M}_{\odot}$), slow rotating galaxies comprise less than half of the galaxy population (Emsellem et al., 2007; Cappellari et al., 2011; Brough et al., 2017). Lagos et al. (2018b) confirmed these results in simulations and found that environmental effects do not need to strongly modify the kinematics of galaxies, suggesting that the difference between field and cluster galaxies today may instead be due to so-called 'progenitor bias', i.e. that galaxies at the moment of infall onto clusters are kinematically different to the galaxies that are in the field at $z = 0$ (see van Dokkum and Franx, 2001; Cortese et al., 2019, for a detailed discussion). However, the small sample of simulated clusters analysed in the simulation work mentioned above cannot fully probe environmental effects in a statistical manner. A large sample of simulated clusters is therefore required to pinpoint the effect environment has on the specific angular momentum of infalling galaxies – something to be addressed in the present work.

We approach these issues by analysing simulations from THE THREE HUNDRED project[21], i.e. a sample of over 300 galaxy clusters simulated with full-physics hydrodynamics (Cui et al., 2018). In this work we extend the previous stellar angular momentum analysis to this set of massive simulated galaxy clusters to study the influence of the cluster environment on the stellar kinematics of infalling galaxies.

This section is organised as follows. In Sec. 2.4.2 we present the data used for the analysis, how we selected the sample of galaxies used for the analysis and the classification of our objects. Sec. 2.4.3 describes our results, where we focus on the kinematic evolution of the sample and their angular momentum-stellar mass relation. Finally, we conclude the study in Sec. 2.4.4.

2.4.2 Sample selection

'The Three Hundred' Central Galaxy Clusters

The Simulations The simulated clusters in THE THREE HUNDRED dataset were created by extracting 324 spherical regions of $15h^{-1}$ Mpc radius centred on each of the most massive haloes identified at $z = 0$ within the dark-matter-only MDPL2 simulation (Klypin et al., 2016)[22]. MDPL2 was simulated with a *Planck* 2015 cosmology (Planck Collaboration et al., 2016), with $\Omega_{\rm M} = 0.307$, $\Omega_{\rm b} = 0.048$, $\Omega_\Lambda = 0.693$, $h = 0.678$, $\sigma_8 = 0.823$, and $n_s = 0.96$ and consists of a box of $1h^{-1}$ Gpc side-length which contains 3840^3 dark matter particles each of mass $1.5 \times 10^9 h^{-1}$ $\mathrm{M}_\odot$. In order to model the galaxy clusters with all the relevant baryonic physics, those $15h^{-1}$ Mpc regions were traced back to the initial conditions and there populated with gas particles by leading to a mass resolution of $m_{\rm DM} = 1.27 \times 10^9 h^{-1}\mathrm{M}_\odot$ and $m_{\rm gas} = 2.36 \times 10^8 h^{-1}\mathrm{M}_\odot$, respectively. Outside the re-simulated region, to reduce the computational cost of the original MDPL2 simulation, dark matter particles are degraded with lower mass resolution particles to maintain the same large scale tidal field. Using a Plummer equivalent softening of $6.5h^{-1}$ kpc for both the dark matter and baryonic component, the new initial conditions were now moved forward in time using `GADGET-X` (Beck et al., 2016). `GADGET-X` is a modified version of `GADGET3` with a modern Smooth Particle Hydrodynamics (SPH) scheme which improves the treatment of gas particles (Beck et al., 2016; Sembolini et al., 2016b). Results of simulations of galaxy clusters based on `GADGET-X` have been presented in several previous papers (e.g. Rasia et al., 2015; Planelles et al., 2017) and in the *nIFTy cluster comparison* project (Sembolini et al., 2016a; Elahi et al., 2016; Cui et al., 2016b; Arthur et al., 2017). A total of 129 snapshots are saved from $z = 16.98$ to $z = 0$.

The Halo Finding The halo analysis was done using the `AHF`[23] halo finder (Gill, Knebe, and Gibson, 2004; Knollmann and Knebe, 2009). `AHF` locates local overdensities in an adaptively smoothed density field as potential halo centres and automatically identifies haloes and substructure (subhaloes, subsubhaloes, etc.). The radius of a halo R_{200} and the corresponding enclosed mass M_{200} are calculated as the radius r at which the cumulative density $\rho(< r) = M(< r)/(4\pi r^3/3)$ drops below $200\rho_{\rm crit}(z)$, where $\rho_{\rm crit}(z)$ is the critical density of the Universe at a given redshift z.

The Merger Trees The progenitors of the haloes are tracked across the snapshots with `MergerTree`, a tool that comes with `AHF`. Each halo identified at redshift $z = 0$ is tracked backwards in time, identifying as the main progenitor at some previous redshift the halo that maximises the merit function $\mathcal{M} = N^2_{A\cap B}/(N_A N_B)$, where N_A and N_B are the number of particles in haloes H_A and H_B, respectively, and $N_{A\cap B}$ is the number of particles that are in both H_A and H_B. The code further has the ability to skip snapshots, i.e. progenitors of haloes that are not found in the previous snapshot are still searched for in earlier snapshots, recovering an otherwise truncated branch of the merger tree (see Wang et al., 2016). However, to reduce errors during the tracking of the stellar kinematic evolution of our objects we consider an object 'lost' if it cannot be found for 5 consecutive snapshots.

[21] https://the300-project.org
[22] The MultiDark simulations – incl. the MDPL2 used here – are publicly available at https://www.cosmosim.org
[23] http://popia.ft.uam.es/AHF

In summary, we have 324 numerically modelled central galaxy clusters and all the haloes orbiting in and about them out to a distance of $15h^{-1}$ Mpc available for our analysis. The details of this full data set are presented in Sec. 2.2. Here we are though applying a few selection criteria to both the central clusters and the field and subhaloes to be described now.

Cluster Selection

As we aim at tracing back all the objects in and about the central galaxy cluster, our analysis requires that we can always define a main progenitor for each of the 324 central haloes. As shown in Behroozi et al. (2015), major mergers during the formation of those central objects pose a challenge to this. Following the discussion in Haggar et al. (2020), we therefore identified and removed central cluster haloes whose main progenitor's position changes by more than half their radius $R_{200}(z)$ between two consecutive snapshots $[z, z + \Delta z]$. We further require the main branch to at least extend to redshift $z = 2$. This reduces the number of regions entering the analysis from 324 down to 236. This is approximately 8 times more cluster regions than used in other state-of-the-art cluster simulation studies (e.g. Bahé et al., 2017; Barnes et al., 2017a).

Halo Selection

Each of our 236 selected central galaxy clusters is surrounded by a multitude of haloes out to the $15h^{-1}$ Mpc edge of the region that was modelled including all the relevant baryonic physics. But as we are interested in studying the angular momentum of the stellar component of these haloes, we are limiting our analysis to haloes with at least $M_{\rm star} > 5 \times 10^{10} h^{-1} {\rm M}_{\odot}$. This corresponds to at least 1000 star particles. Additionally, only those haloes that lie within $3R_{200}$ of the central galaxy cluster at redshift $z = 0$ are traced backwards in time. For these haloes we then define their infall redshift $z_{\rm inf}$ as the redshift at which the halo crosses central galaxy cluster's $2R_{200}(z)$ for the first time: recent numerical studies show that around $\sim 1.5R_{200} - 2R_{200}$, haloes experience a sharp cut-off in their gas content which could indicate the presence of an accretion shock (Power et al., 2018; Arthur et al., 2019; Mostoghiu et al., 2020b) and hence we decided to use $2R_{200}$ (instead of R_{200}) as our reference crossing radius. Haloes that cannot be assigned an infall redshift will be removed from the analysis.

Stellar Component

To select the stellar component of our haloes – that one might identify with its galaxy – we opted for a spherical region enclosing 15 per cent of the haloes' physical radius (e.g. Bailin and Steinmetz, 2005). However, as tidal interactions with the central galaxy cluster impact on the size of subhaloes (Muldrew, Pearce, and Power, 2011; Onions et al., 2012) we used the radius as found right before crossing $2R_{200}$ of the central galaxy cluster. This aperture is now interpreted as the 'size of the galaxy' and kept fixed in physical coordinates across the snapshots. We performed a series of tests using different criteria (e.g. an aperture not depending on the halo's physical radius but rather fixing it to 30kpc) that showed that even though haloes suffer an overall mass loss while orbiting within their host halo, the central stellar mass in the aperture is mostly unaffected. This agrees with other simulations, which show that stellar stripping is rare, and happens only after the dark matter has suffered significant stripping (> 80 per cent, e..g Smith et al., 2016; Bahé et al., 2017). It is important to point out again that even though the stellar mass of our galaxy does not change (something we also quantify below), we cannot rule out any back-reaction of the stars to the change in potential caused by tidal stripping of the halo. Finally, to take into account the spatial resolution of our simulations we restrict our objects to have a 'galaxy size' of at least $2\epsilon = 13h^{-1}$kpc ~ 20 kpc. We remark that this additional condition removes only the smallest galaxies in the sample, which is less than 5 per cent of the objects selected so far. Moreover, practically all of the star particles reside within our aperture and hence we are not considerably reducing the number of star particles by cutting out the 'galaxy' as defined here. The remaining 6509

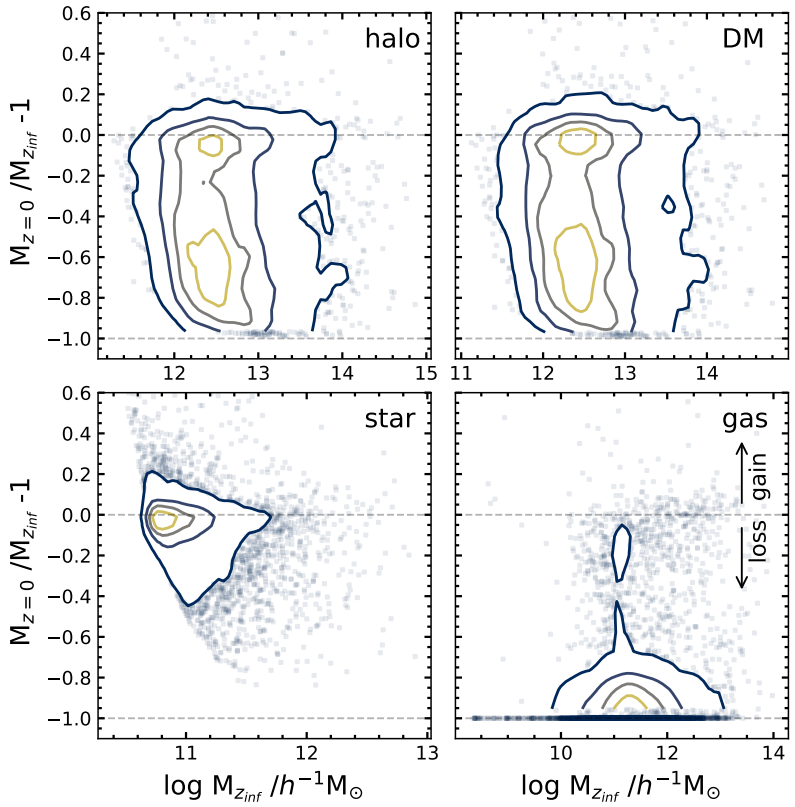

FIGURE 2.19: Evolution of the different mass components of the haloes in the sample from their infall redshift $z_{\rm inf}$ to their $z = 0$ values. Contour levels show the 75, 50, 25 and 5 per cent of the maximum counts of the distributions. The horizontal lines at 0 and -1 correspond to no change and maximum mass loss, respectively. The position in the plane of objects beyond the 5 per cent contour are shown as square markers.

objects, with halo masses from $9.2 \times 10^{10} h^{-1}\mathrm{M}_\odot$ to $5.3 \times 10^{14} h^{-1}\mathrm{M}_\odot$, constitute the analysis sample, built by combining all the objects that satisfy the aforementioned criteria from the 236 cluster regions considered here.

2.4.3 Results and discussion

In what follows we are comparing the properties of our selected haloes orbiting in and about the central galaxy clusters at infall redshift $z_{\rm inf}$ (i.e. when crossing $2R_{200}$) and present day time $z = 0$.

Mass Evolution

To understand the processes that shape the haloes after their first infall we show in Fig. 2.19 the fractional change in mass since their infall redshift and as a function of infall mass. Contour levels show 75, 50, 25, and 5 per cent of the maximum counts of the distributions. The horizontal lines at 0 and -1 correspond to no change and maximum mass loss, respectively. Objects beyond the 5 per cent contour are shown as square markers. As expected, haloes crossing the denser regions of the central galaxy cluster lose a considerable amount of mass (e.g. Klimentowski et al., 2010). Haloes that only entered the central halo once and did not leave, in general, conserve more of their initial mass than the ones that experienced multiple infalls into the denser regions of the galaxy cluster. In terms of the stellar mass in the haloes, the loss is significantly lower due to the fact that most of the stellar component resides in the central region of the halo mainly shielded from tidal forces. We nevertheless observe an

increase in stellar mass loss at the 5 per cent level as we move to the massive end of the stellar mass distribution. Such haloes present substructure residing in the halo component (i.e. outside the central aperture) and thus they are prone to suffering mass loss from processes that strip the halo at its outskirts. The gas component, on the other hand, is mostly gone regardless of their mass as gas is affected by an entirely different set of processes as they fall into the central halo, i.e. ram-pressure stripping (Arthur et al., 2019; Mostoghiu et al., 2020b). Studying the radial distribution of the gas inside infalling haloes (not shown here), we find that haloes that never reached the denser regions of the cluster halo are still considerably stripped of their gas component, in agreement with Power et al. (2018) and Arthur et al. (2019).

In summary, Fig. 2.19 clearly shows that the stellar component of our haloes is the least affected by the environment of the central galaxy cluster. The question nevertheless remains if we will find changes in the kinematical properties. But the haloes of our 'galaxies' (as defined by the star particles in the aperture) certainly undergo some changes as manifested by the mass loss. It is therefore not yet clear that even though the galactic stellar mass more or less remains constant that there will be no reaction of its internal dynamics to the varying influence of the central galaxy cluster.

Fraction of co-rotational energy

We study the influence of the central galaxy cluster on the internal dynamics of our galaxy sample after their first infall by following the evolution of their specific stellar angular momentum j_*.

The galaxies in our sample can be classified by the fraction of stellar kinetic energy that is invested in co-rotation $\kappa_{\rm corot}$, as presented in Sales et al. (2010) and Correa et al. (2017):

$$\kappa_{\rm corot} = \frac{E_{\rm corot}}{E_{\rm kin}} \, , \, E_{\rm corot} = \sum_{j_{z,i}>0} \frac{1}{2} m_i \left(\frac{j_{z,i}}{r_{2d,i}} \right)^2 \, , \tag{2.16}$$

where $E_{\rm kin}$ is the kinetic energy of the star particles in the aperture, $E_{\rm corot}$ is the rotational energy of the corotating star particles contributing to the rotation of the galaxy, m_i the mass of the star particle;

$$\begin{aligned} j_{z,i} &= \boldsymbol{j}_i \cdot \hat{\boldsymbol{J}}_{\rm tot} \, , \\ \boldsymbol{j}_i &= (\boldsymbol{r}_i - \boldsymbol{r}_{\rm halo}) \times (\boldsymbol{v}_i - \boldsymbol{v}_{\rm halo}) \, , \text{ and} \\ \hat{\boldsymbol{J}}_{\rm tot} &= \frac{1}{J_{\rm tot}} \frac{\sum m_i \boldsymbol{j}_i}{\sum m_i} \, , \end{aligned} \tag{2.17}$$

the specific angular momentum along the direction of the total angular momentum, the specific angular momentum of a star particle in the rest frame of its halo, and the direction of the total specific angular momentum of the galaxy, respectively; and $r_{2d,i} = (|\boldsymbol{r}_i - \boldsymbol{r}_{\rm halo}|^2 - ((\boldsymbol{r}_i - \boldsymbol{r}_{\rm halo}) \cdot \hat{\boldsymbol{J}}_{\rm tot})^2)^{1/2}$ the cylindrical radius of star particles. As we exclusively use the definition based on co-rotating star particles, we drop the subscript from the parameter κ from now on.

With this definition, Correa et al. (2017) found that a threshold value in κ successfully separated the slow-rotating, passive galaxies ($\kappa < 0.4$); from the fast-rotating, star-forming galaxies ($\kappa > 0.4$). Using this threshold value, only 4 per cent of our galaxies present fast rotation at $z = 0$. Note that our sample is kinematically dominated by slow rotators, whereas compared with observations at similar halo mass ranges, the fraction of fast rotators is close to 80–85 per cent (Brough et al., 2017). Such disparity is expected considering the mass resolution of our simulations, which favours the modelling of a large number of galaxy clusters and their environments. In order to properly resolve rotating disks a significantly better mass resolution is required (see, e.g. Scannapieco et al., 2012, for a detailed study of numerical resolution and galaxy formation), hence the specific stellar angular momentum distribution of our sample is highly-skewed towards slow rotators.

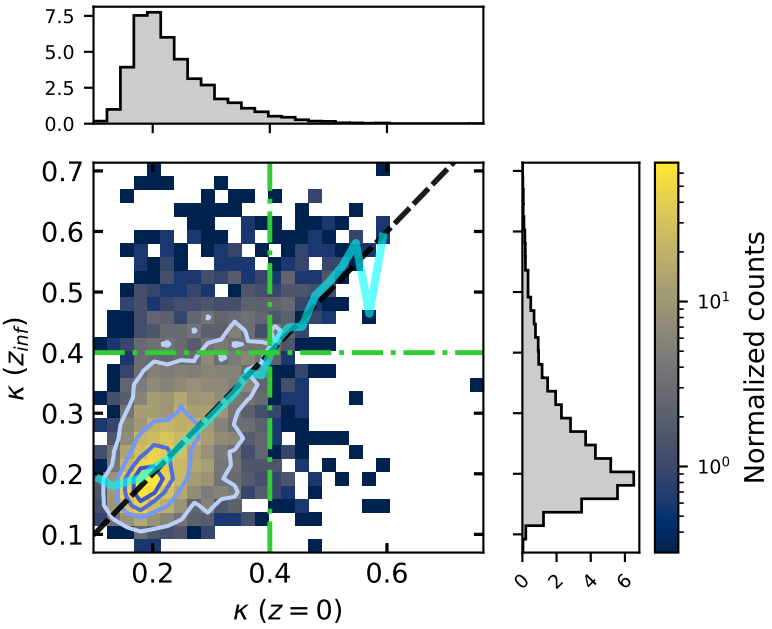

FIGURE 2.20: Fraction of ordered rotation κ at $z = 0$ and at their infall redshift $z_{\rm inf}$. The diagonal dashed line shows the $1:1$ relation. The horizontal and vertical green dash-dotted lines mark the κ threshold value. Median values in bins of $\kappa(z = 0)$ for the sample are represented by the solid cyan line. Bins are coloured by their corresponding normalised counts. The contour lines show where 75, 50, 25, and 5 per cent of the maximum counts lie.

Changes in κ since infall We compared the fraction of ordered rotation at two different times in the evolution of the galaxies to find if the $z = 0$ values are a consequence of the influence of the central galaxy cluster during their infall. In Fig. 2.20 we show the κ values of the sample at $z = 0$ compared to their values at infall $z_{\rm inf}$, before experiencing the central cluster's influence. The black dashed diagonal line shows the $1:1$ relation. The horizontal and vertical green dash-dotted lines mark the Correa et al. (2017) κ threshold value. The median values in bins of κ at $z = 0$ are represented by the solid cyan line. Bins are coloured by their corresponding number of counts and contours show where 75, 50, 25, and 5 per cent of the maximum counts lie.

We find that for most of the haloes in the sample the fraction of stellar ordered rotation is unaffected by their infall (Pearson coefficient of 0.56), with a median value at $z = 0$ and at $z_{\rm inf}$ of $\kappa \sim 0.22$. However, beyond the 5 per cent contour, i.e. close to the κ threshold value, we identify two populations: galaxies which were fast rotators at their infall redshift and became slow rotators at $z = 0$, and a smaller group of galaxies which were slow rotators at their infall redshift and became fast rotators by the time they reached $z = 0$. To identify which processes are responsible for the changes observed in the evolution of κ we separate slow rotators from fast rotators at $z = 0$ and study each sub-sample separately. In the previous section we found that the haloes in the sample are mostly stripped of their gas by the time they fall into the denser regions of the central galaxy cluster. Nevertheless, the removal of gas does not affect the rotational properties of the galaxies, as seen from their κ parameter. Cortese et al. (2019) reported a similar result using EAGLE galaxies: satellite galaxies go through significant changes in their specific star formation rate, but those are not accompanied by changes in their stellar spin parameter, i.e. the degree of stellar rotation of satellite galaxies does not drastically change after their infall. Thus, we conclude that the fraction of ordered rotation is hardly affected by the (potentially violent) stripping processes that disrupt the dark matter halo.

Temporal evolution of κ for fast and slow rotators Recent numerical results show that galaxies which continue to accrete gas and form stars are very efficient at spinning up (Lagos

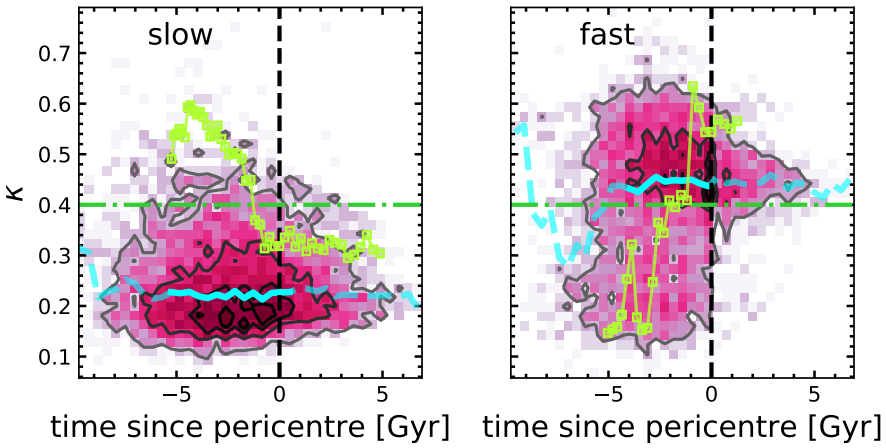

FIGURE 2.21: Evolution of the fraction of co-rotational energy as a function of the time since the pericentre passage for slow (left) and fast (right) rotators as classified by their $z = 0$ κ value. Contours show 75, 50, 25, and 5 per cent of the distribution. The cyan solid line shows the median value at each time bin. For bins in which less than 50 per cent of the sample entered the median calculation, we instead use a dashed line. The green horizontal dash-dotted line shows the κ threshold value for fast rotators. The pericentre is marked with a vertical dashed line. In each panel we additionally show the evolution of a galaxy from the corresponding sub-sample using green square markers.

et al., 2017). However, this is unlikely to be the cause here as gas accretion is expected to be hampered in clusters. Lagos et al. (2018a) found that galaxies can be spun up or down by mergers depending on their orbital orientation and gas content (see Schulze et al., 2018, for similar results). To investigate the origin of the change in the fraction of co-rotation after infall found in Fig. 2.20, in Fig. 2.21 we study the κ evolution of fast and slow rotators found at $z = 0$ as a function of the time since their pericentre passage, defined as the closest approach of an infalling halo to the central galaxy cluster[24]. Contours show 75, 50, 25, and 5 per cent of the maximum counts in the distribution. We show the median value at each time bin with a cyan solid line, and when the number of haloes in a bin is less than 50 per cent of the maximum count we use a dashed line instead. The κ threshold value is represented by the green horizontal dash-dotted line and the pericentre time is marked with a vertical dashed line. In each panel we additionally show the κ evolution of a galaxy from the respective sub-sample with green square markers, and we downsampled the number of slow rotators to match the number of fast rotators at $z = 0$.

As already anticipated by the κ evolution in Fig. 2.20, most of the galaxies in each sub-sample maintain their fraction of co-rotational energy κ after their infall. However, over the course of 5 Gyrs after the pericentre passage we observe a decrease of ~ 0.2 in κ in both sub-samples (~ 0.04/Gyr) at the 5 per cent countour. Moreover, the κ evolution of the sample slow rotator galaxy shows that it was considered a fast rotator at some point, but became a slow rotator after ~ 4 Gyr. Such slow decrease can be attributed to the two-body heating of the stellar component: as galaxies infall into the central galaxy cluster, the background (more massive) dark matter particles residing inside the cluster that fly by these galaxies tend to increase the stellar mean interparticle distance due to the softening scale used for the stellar particles, heating up the stellar component and effectively puffing up the stellar distribution while spinning them down. As these galaxies fall further into the cluster, the density of dark matter particles increases and consequently the amount of fly-bys is boosted. Along with this slow decrease, we also identify processes which can spin-up galaxies on a faster scale. But these changes – as observed for the fast rotator sample galaxy – are happening close to pericentre passage and are investigated in more detail now.

[24]Our definition of 'pericentre' does not necessarily imply they are within R_{200} of the central galaxy cluster.

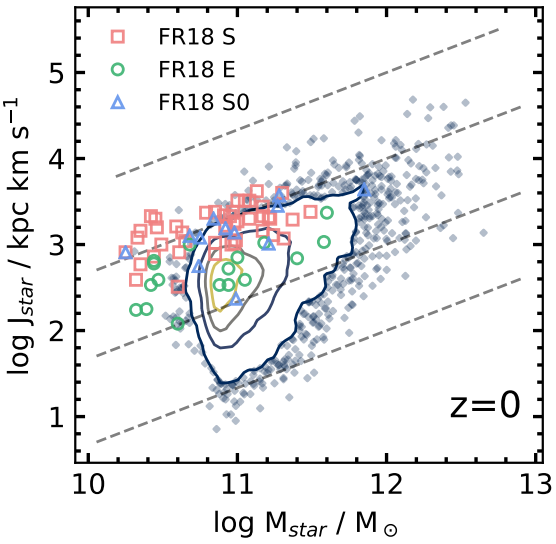

FIGURE 2.22: Specific angular momentum and stellar mass relation of the sample of galaxies at $z = 0$ along the Fall and Romanowsky (2018) galaxies with $M_{\rm star} \gtrsim 1.6 \times 10^{10} {\rm M}_\odot$, with their morphological classification as represented by the different coloured markers.The diagonal dashed lines show the $M^{2/3}$ relation for zero-points -3 (top line) to -6 (bottom line). The contours show 75, 50, 25, and 5 per cent of the sample. The position in the plane of objects beyond the 5 per cent contour are shown as filled markers.

Spinning-up slow rotators As most of our sample is dominated by slow rotators, we focus on processes which are able to spin-up slow rotators and eventually convert them to fast rotators at $z = 0$. To isolate the galaxies which cross the threshold κ value to become fast rotators from the ones that conserve their classification up to $z = 0$, i.e. the ones that remained fast rotators after their infall into the cluster environment, we select galaxies from the fast rotators sub-sample which experience a rapid κ increase (i.e. $\Delta\kappa > 0.2$) within 1 Gyr since their pericentre passage. These galaxies form only 13 per cent of the fast rotators at $z = 0$ (34 objects, 0.5 per cent of the total number of haloes in the galaxies sample). Within this sub-sample, we identify galaxies for which a sudden change in their star particle count was accompanied by a sudden spin-up of their specific angular momentum (and consequently an increase in their κ parameter) near their pericentre, and galaxies for which the number of stars close to the pericentre does not seem to play a crucial role in their κ evolution.

Following the star particle distribution of these galaxies, we find that the fast increase in κ and in the number of stars is a consequence of two processes: mergers with other haloes, and fly-bys of stellar remnants within the central aperture used to define the galaxies residing in each halo. In agreement with Lagos et al. (2018a) and Schulze et al. (2018), we find that the co-rotating (counter-rotating) infalling stars from mergers are able to spin-up (spin-down) our galaxies. On the other hand, acting on shorter timescales and without a significant stellar gain, we find that stellar remnants are able to temporarily disrupt the spin of our objects. These haloes are the residual cores of infalling haloes, where the original dark matter component of the halo has become lost and subsumed by the main halo. Considering that the stellar component of the remnant haloes is smaller than the central galaxy extension of the haloes in the sample ($\sim 1/3$ of the aperture size), and that the amount of remnant stellar cores increases close to the centre of the galaxy cluster, these objects contribute transiently to the co-rotational energy in the aperture and, as such, κ increases near the pericentre of our objects.

Summary We conclude that for most of the galaxies in our sample entering massive galaxy clusters their kinematic properties (as captured by the fraction of ordered rotation κ) do not change in a significant manner – even though we have seen that their haloes undergo substantial changes. Slow rotators were slow rotators before entering the cluster halo and the

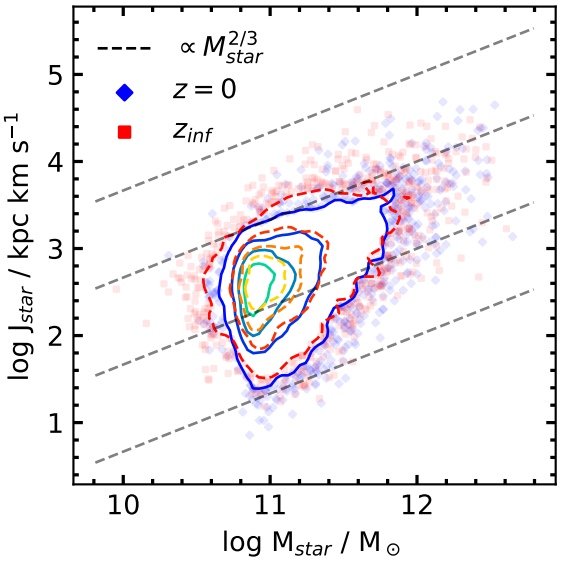

FIGURE 2.23: Specific angular momentum and stellar mass relation of the sample of galaxies at $z = 0$ along the Fall and Romanowsky (2018) galaxies with $M_{\rm star} \gtrsim 1.6 \times 10^{10} {\rm M}_\odot$, with their morphological classification as represented by the different coloured markers. The diagonal dashed lines show the $M^{2/3}$ relation for zero-points -3 (top line) to -6 (bottom line). The contours show 75, 50, 25, and 5 per cent of the sample. The position in the plane of the simulated objects beyond the 5 per cent contour are shown as filled markers.

(few) fast rotators in the sample were fast rotators prior to entering the cluster environment. The two-body heating of the stellar component of infalling haloes induced by the more massive dark matter particles in the cluster environment affects equally both samples, slowly reducing their stellar specific angular momentum as they orbit the cluster region. Thus, we find within the fast rotators galaxy sample, objects that became slow rotators by the time they reached $z = 0$. On the other hand, from the fast rotators sample at $z = 0$, which is an already small percentage of the overall population (i.e. ~ 4 per cent), we identify ~ 13 per cent of them which were previously classified as slow rotators. We find that these two processes acting on different timescales, i.e. mergers with other infalling haloes and stellar remnants transiting the aperture used for defining the galaxies of the haloes in the sample, are able to spin-up the galaxies.

Stellar angular momentum and stellar mass relation

In the previous section we identified processes which are able to change specific angular momentum of infalling galaxies. Nevertheless, most of the objects remain unaffected by such interactions. In this section we study the influence of the central galaxy cluster on the internal dynamics of our galaxies by following their evolution in the specific angular momentum-stellar mass plane.

In Fig. 2.22 we show the relation for the stellar mass at $z = 0$ alongside the galaxies with $M_{\rm star} \gtrsim 1.6 \times 10^{10} {\rm M}_\odot$, classified by their morphology with different coloured markers from Fall and Romanowsky (2018). The contours represent 75, 50, 25, and 5 per cent of the sample. The position in the plane of galaxies beyond the 5 per cent contour are shown as filled markers. The dashed lines indicate the $j_{\rm star} = \lambda M_{\rm star}^{2/3}$ relation for different zero-points (log $\lambda = -3$ to -6), as presented in Teklu et al. (2015). Most of the sample lies between the -4 and -5 line. Comparing galaxies in the sample with the Fall and Romanowsky (2018) ones, most of the simulated galaxies have similar stellar angular momentum values to the observed elliptical galaxies (green circles), whereas compared to the spiral galaxies (coral squares) they have up to 10 times lower stellar angular momentum. This difference is

expected from our stellar mass selection and the highly-skewed stellar angular momentum distribution of our sample towards slow rotators.

As some of our galaxies experienced great changes in their fraction of ordered rotation during their evolution since their infall we aim to find if these changes are also visible in the specific stellar angular momentum-stellar mass plane. We show their position in the $j - M$ plane after their infall redshift in Fig. 2.23. Once again, we find that the distribution is mostly unchanged after entering the cluster halo. However, galaxies positioned furthest from the average position in the $j - M$ plane at their infall redshift move towards lower specific angular momentum and stellar mass values after infalling, as seen in the 5 per cent contours and points below that level.

These results show that the internal dynamics of infalling galaxies into massive galaxy clusters, as quantified by either the fraction of ordered rotation κ or the evolution of their location in the specific angular momentum-stellar mass plane, are mostly unaffected by the processes in such environments even after their halos have been considerably stripped of their mass, and consequently, disrupted the halo potential in which these galaxies reside.

2.4.4 Conclusions

We analysed the central stellar component of haloes from THE THREE HUNDRED project, a suite of 324 galaxy cluster regions simulated with full-physics hydrodynamics, to study of the influence of galaxy clusters on the internal dynamics of infalling galaxies. We selected objects with $M_{\rm star} > 5 \times 10^{10}\, h^{-1}{\rm M}_{\odot}$ within $3R_{200}$ from the galaxy cluster halo at $z = 0$. After applying different selection criteria that ensure the correct tracking of the stellar component of each halo we obtain a sample of 6509 galaxies from 236 cluster regions, i.e. approximately 8 times more cluster regions than used in other state-of-the-art cluster simulation studies (e.g. Bahé et al., 2017; Barnes et al., 2017a). Here we summarise our main results:

- Using the fraction of stellar co-rotational energy κ to track the internal dynamics of the infalling galaxies in our sample we find that it remains mostly unchanged for most of the galaxies after they enter the galaxy cluster environment.
- Although infalling haloes are mostly depleted of all their gas and stripped off their dark matter halo by the time they reach $z = 0$, their stellar kinematics are unaffected by this change, in agreement with Cortese et al. (2019).
- We studied the time evolution of the κ parameter. Even though most galaxies do not experience great κ changes during their evolution, we identify an overall slow decrease in the fraction of ordered rotation close to their pericentre passage (~ 0.04/Gyr) which we attribute to numerical effects. Along with this effect we found that $\sim$ 13 per cent of the fast rotators at $z = 0$, an already small population in our sample, were slow rotators that experienced a faster change in their κ parameter within the past few Gyrs (~ 0.2/Gyr) due to two different processes: stellar mergers of infalling haloes (in agreement with Lagos et al., 2018b; Schulze et al., 2018), and transient encounters with the stellar remnants of haloes that have lost their dark matter component during their own passage through the cluster, entering within the aperture we used for defining the properties of our galaxies.
- We found that similar to the κ evolution of our galaxies, the specific angular momentum-stellar mass relation for the galaxies in the sample showed no substantial change in their location on the $j - M$ plane from their infall redshift until $z = 0$.

Recent analysis of galaxy properties show that moving to a kinematical classification scheme helps in disentangling some challenges in galaxy evolution (Cappellari et al., 2011; Bluck et al., 2014; Tacchella et al., 2015). As we move to these kinematic classifications we need to understand how stable the classification is during the evolution of the galaxies. In this work we studied how the internal dynamics of a sample comprised of mostly slow rotator galaxies evolve after infalling into massive galaxy cluster haloes, and found that their $z = 0$ classification holds even from before the time they entered the cluster environment, were processes such as ram-pressure stripping (Gunn and Gott, 1972; Abadi, Moore, and Bower, 1999; Bahé and McCarthy, 2015; Arthur et al., 2019), mergers (Dressler, 1980;

Hashimoto and Oemler, 2000; Behroozi et al., 2014; Lagos et al., 2018a), and other physical processes could potentially disrupt their kinematic properties. Moreover, we find that in terms of their position in the fundamental specific stellar angular momentum-stellar mass plane (Fall and Romanowsky, 2018) they remained mostly unaffected by such processes.

Our results point to a scenario in which the different kinematical mix between cluster environments and field galaxies may not be caused by environmental effects transforming galaxies in clusters, as the stellar specific angular momentum disruption we observe in the infalling haloes in our sample – either by spinning up or down of the stellar component of the galaxies – only affects a small percentage of the total population. Therefore, any comparison of cluster population properties in which it is assumed that the $z = 0$ central and satellite galaxies are completely representative of the galaxy formation nurture experienced by the infalling progenitors of such galaxies should take into account this caveat. Other simulations are starting to show similar results (e.g. Cortese et al., 2019), which means that the well known 'progenitor bias' may be extremely important when investigating trends in galaxy properties and their environment. Nevertheless, our sample contains a limited number of fast rotators. Future simulations, where the stellar mass resolution is increased and a smaller softening scale is used to better resolve the stellar component, for similar cosmological volumes, would help us extend the analysis to a bigger sample of fast rotators to determine the fate of such objects with a greater statistical significance.

3 *Constrained Local UniversE Simulations*: CLUES project

In this chapter we move from zoomed cosmological simulations of clusters of galaxies (see Ch. 2), which represent statistically equivalent *realisations* of our Universe, to (zoomed) constrained simulations from the CLUES[1] project that aim to instead *reproduce* the environment within a few tens of megaparsecs around the Milky Way, i.e. the Local Group.

We start this chapter by summarising how we can produce constrained simulations of the local Universe (Sec. 3.1). Then, we present our first study that uses such type of simulations in Sec. 3.2, in which we study the peculiar stellar age gradient of the Triangulum Galaxy (M33) by comparing its simulated counterpart with the observational results. Finally, in Sec. 3.3 we use constrained simulations to analyse the star formation of infalling satellites into Milky Way, Andromeda (M31), and Triangulum (M33)-like counterparts. The published work from which each study is based on is shown at the beginning of each section.

3.1 Constrained simulations

Galaxy formation models are best constrained by data coming from our nearby environment, i.e. the Local Group. Thus, the better we understand how the observed structures in the Local Group formed from the initial conditions we use in cosmological simulations, the better we can refine our models of galaxy formation.

The initial matter density perturbations used to set the initial conditions of cosmological numerical simulations are only defined in terms of their power spectrum, i.e. the amplitude squared of complex-valued functions, as current observational data from the CMB cannot provide more information. Their phases are, in principle, unknown (see discussion in Sec. 1.5.1). Therefore, setting a particular configuration of phases (one for each perturbation mode) produces a statistically equivalent realisation of our Universe. In order to reproduce *our* Universe (or, due to computational limits, a part of its volume) we need to find the correct combination of phases. The *Constrained Local UniversE Simulations* (Gottlöber, Hoffman, and Yepes, 2010, CLUES) project aims to achieve this: using observational data from the nearby environment as constraints imposed on the initial conditions of the simulations, we can obtained simulations that reproduce the local large scale structure and cosmic web of our Universe.

In order to create constrained simulations of the Local Group (LG), the first iterations of the initial conditions of CLUES simulations were tuned using as observational constraints peculiar velocities obtained from the MARK III catalog (Willick et al., 1997), surface brightness fluctuations (Tonry et al., 2001), local volume galaxy catalogues (Karachentsev et al., 2004), and the position and virial properties of nearby X-ray selected clusters of galaxies (Reiprich and Böhringer, 2002) (see Sec. 3.1). The more recent CLUES simulations, however, instead use the observational constrains from the galaxy distance database COSMICFLOWS3 (Tully, Courtois, and Sorce, 2016). By using peculiar velocities, we have a direct link to the underlying dark matter distribution of the nearby Universe, avoiding the clustering bias present in constrains obtained from matter density estimations[2].

In a ΛCDM Universe, the small perturbations that collapsed and evolved to form the current day structures are assumed to be Gaussian random fields. Therefore, using the Hoffman-Ribak algorithm (Hoffman and Ribak, 1991) for generating *constrained* Gaussian

[1] https://www.clues-project.org/

[2] We do need to consider the intrinsic bias due to the fact that we are only able to detect the most luminous objects, i.e. the Malmquist bias (Malmquist, 1922; Malmquist, 1925).

fields and the aforementioned observational data as constraints, the initial conditions are generated to produce a Universe with the correct large scale structure (a full description of the procedure can be found in Kravtsov, Klypin, and Hoffman, 2002; Klypin et al., 2003). Note that only large, linear scales are constrained: random (unconstrained) waves dominate on small scales which induce random displacements in the density distribution from realisation to realisation. Since properties of the LG such as mass, relative positions and velocities, are non-linear, they are unconstrainable. Therefore, low resolution initial conditions are run to $z = 0$, and those simulations which reproduce a structure resembling the LG are selected for high resolution resimulation. Finally, the resolution of the simulation is increased following a zoom-in technique (Katz et al., 1994; Navarro and White, 1994) (see Sec. 2.1). The end result is a local group, selected in a frequentist manner, embedded in the proper constrained large scale structure.

3.2 M33 and its reversed radial stellar age gradient

Section based on Mostoghiu et al. (2018)

HST/ACS observations along the major axis of M33 show that the mean age of its stars decreases with increasing distance from the galaxy centre. Such a behaviour is consistent with an inside-out growth of the disc. However, in the outermost observed field, at $r \simeq 11.6$ kpc, a reversal of this gradient is detected, with old stars found in high percentages beyond this radius. In this section we investigate the origin of such a reversal in stellar age gradient by using a simulated M33 analogue from the Constrained Local UniversE Simulations (CLUES). The simulated M33 is similar to the observed one in terms of mass, rotation velocity, surface brightness and, likewise to what has been reported in observations, shows a stellar age turnaround at large radii. We demonstrate that this reversal is mostly a result of stellar accretion from old satellite galaxies and, to a lesser extent, of stellar migration of in-situ stars. The old accreted stars, with formation times $t_f < 4$ Gyrs, are kinematically hot and can be differentiated from the in-situ stars by their high velocity dispersion and the fact that they do not have rotationally-supported orbits. In the future, obtaining kinematic information of the stars in the outskirt of M33 will help to verify this scenario.

3.2.1 Introduction

In a ΛCDM universe, spiral galaxies consist of a disc component made of stars, cold gas and dust, a central bulge and a stellar halo, all embedded in a dark matter halo (White and Rees, 1978). The disc component can be separated into two different parts: the thin disc, and the thick disc (Burstein, 1979; Gilmore and Reid, 1983). These two components are defined by examining the vertical scale height of stars when separated by age (e.g. Haywood et al., 2013; Bensby, Feltzing, and Oey, 2014) or metallicity (e.g. Fuhrmann, 2008; Bensby, Feltzing, and Oey, 2014). The stars in the thin disc component are formed by gas accretion at the later stages of galaxy formation and they have a wide range of ages (Yoachim and Dalcanton, 2006). The stars in the thick disc, however, are older and their origin is still debated (e.g. Brook et al., 2004; Villalobos and Helmi, 2008; Minchev et al., 2015).

The distribution of stars in galactic discs is also an ongoing research area. One of the favoured modes for the mass assembly of a galaxy is the "inside-out" scenario (Chiappini, Matteucci, and Gratton, 1997; Mo, Mao, and White, 1998; Brook et al., 2012; Pilkington et al., 2012; Bird et al., 2013). In the inside-out growth proposal, the inner disc is thought to assemble first as a consequence of the high density of accreted gas residing in the centre of the galaxy's potential well. Thus, the fraction of young stars is expected to increase with galactocentric radius. Several galaxies have been found to be compatible with such a growth model (Pérez et al., 2013; Sánchez-Blázquez et al., 2014; Tacchella et al., 2015).

Recent observations regarding the ages of stars in the neighbouring galaxy M33 indicate that this galaxy is compatible with an inside-out disc growth scenario, in which old stars are detected in the inner region of the galaxy, while young, disc stars tend to naturally be found in the outskirts of the disc (Williams et al., 2009; Barker et al., 2011). Specifically, these observations made use of the *Hubble Space Telescope Advance Camera for Surveys* (HST/ACS),

to derive the cumulative star formation history (SFH) along M33's major axis and for different radii. The SFH was derived using the synthetic colour-magnitude diagram (CMD) fitting method. CMDs were obtained by measuring resolved stellar photometry using the ACS module of the DOLPHOT software package (Dolphin, 2000). Assuming an initial mass function and stellar evolution isochrones, a fitting is performed on the CMD to obtain the star formation rate at their respective ages and metallicities. Williams et al. (2009) and Barker et al. (2011) showed that within $\sim$ 9 kpc from M33's center, the mean age of stars decreases as one moves further out from the galactic centre. Additionally, they found that at radii greater than $\sim$ 9 kpc, however, this *age gradient* reverses, such that the mean age of stars increases as one approaches the outer region of M33. The age gradient thus reverses from decreasing mean stellar age with radius (within 9kpc) to increasing mean stellar age with radius (beyond 9 kpc). Note that the age gradient reversal is accompanied by a surface brightness and stellar mass surface density break beyond 8 kpc (Ferguson et al., 2007; Barker et al., 2011), whose physics remains contentious (see Ruiz-Lara et al., 2017, for a recent review of the subject using simulations).

Similar age profiles have been identified in both simulations (Roškar et al., 2008a; Roškar et al., 2008b; Sánchez-Blázquez et al., 2009; Martínez-Serrano et al., 2009; Ruiz-Lara et al., 2016b, e.g.) and observations of disc galaxies (e.g. Bakos, Trujillo, and Pohlen, 2008; Yoachim, Roškar, and Debattista, 2012; Zheng et al., 2015; Ruiz-Lara et al., 2016a), yet the origin of the reversal is not clear. Several explanations for the reversal have been proposed: stellar migration, in which the inner disc forms inside-out and the region beyond the upturn radius is populated with stars that migrated from the inner disc (Roškar et al., 2008a; Roškar et al., 2008b; Ruiz-Lara et al., 2016b); projection effects, that cause a contamination and overlap of stars from different galactic components (Barker et al., 2011); a decrease in the gas volume density in the disc, which induces a break in the star formation density which itself coincides with the radius where the gas disc begins to warp (Sánchez-Blázquez et al., 2009); or old stars coming from mergers that, due to their significant energy, remain in orbits at large, outer radii (Gill, Knebe, and Gibson, 2005; Sales et al., 2007; Brook et al., 2012; Ruiz-Lara et al., 2016b).

In this paper we explore the age gradient of a simulated M33 analogue galaxy, formed in a constrained Local Group environment as part of the CLUES[3] project (Gottlöber, Hoffman, and Yepes, 2010; Carlesi et al., 2016). The initial conditions have been constrained by observational data such that the $z = 0$ cosmography is forced to reproduce the real local environment (Libeskind et al., 2015; Sorce et al., 2016). The simulated M33 analogue shares many properties with the observed M33 and was formed in a similar environment. This means that our analysis of the origin of the M33 analogue may provide insights into the mechanisms driving the age gradient, in the real M33, in particular the reversal of the age gradient that is observed.

This section is organised as follows. In Sec. 3.2.2 we present the simulated M33, the simulation's properties, and the features of our candidate galaxy. The reversal of the age gradient in the SFH of M33 is presented in Sec. 3.2.3, along with the adopted methods to analyse the age reversal, the implications of our study, and some observational predictions. Finally, in Sec. 3.2.4 we summarise our results.

3.2.2 A simulated counterpart of M33

In this section we describe the properties of the M33 candidate found within one of the hydrodynamical numerical simulations performed as part of the *Constrained Local UniversE Simulations* (CLUES) project (Gottlöber, Hoffman, and Yepes, 2010).

Constructing the numerical M33

In this work we use a simulated LG obtained from following the same procedure described in Sec. 3.1. The simulated LG includes a third galaxy which resembles M33 in terms of mass and placement, being at $\simeq$ 800 kpc from the other two main halos.

The simulation was run using the standard ΛCDM *Wilkinson Microwave Anisotropy Probe* 3 (WMAP3) cosmology (Spergel et al., 2007), with $\Omega_M = 0.24$, $\Omega_b = 0.042$, $\Omega_\Lambda = 0.76$, $\sigma_8 =$

[3] www.clues-project.org

0.75, $h = 0.732$, and an $n = 0.95$ slope of the power spectrum. We used the parallel Tree-SPH code GASOLINE (for further details see Wadsley, Stadel, and Quinn (2004) and references therein) to simulate a cosmological box with side length $L_{\rm box} = 64h^{-1}$ Mpc, and effective particle resolution of $m_{\rm DM} = 2.1 \times 10^5 h^{-1}{\rm M}_\odot$ and $m_{\rm gas} = 4.4 \times 10^4 h^{-1}{\rm M}_\odot$.

These hydrodynamical simulations have been presented and used to explore dwarf galaxies in the Local Volume (see Santos-Santos et al., 2016; Santos-Santos et al., 2017, where full details are found). In particular, the simulated galaxies were shown to match a range of scaling relations, including the relations between stellar and halos mass, stellar and HI gas mass, size and stellar mass, and the Tully-Fisher relation. The simulations include an ionising UV background, gas cooling, and star formation, with the stars feeding energy back into the interstellar medium (ISM) gas. Gas is eligible to form stars when it reaches temperatures below 15000K in a dense environment, with minimum density threshold of 10 amu/cm^3. Blastwave supernova feedback is included following the Stinson et al. (2006) model, allowing an efficient regulation of star formation within galaxies. The stellar particles are formed with an initial mass of $m_\star = 1.5 \times 10^4 h^{-1}{\rm M}_\odot$.

To identify halos in the simulation we used the MPI+OpenMP hybrid halo finder *AMIGA Halo Finder* (AHF [4], Gill, Knebe, and Gibson, 2004; Knollmann and Knebe, 2009), which locates local overdensities in an adaptively smoothed density field as potential halo centers and automatically identifies halos, subhalos, subsubhalos, etc. For every found halo, AHF calculates its virial radius $r_{\rm vir}$ as the radius r at which the density $\rho(r) = M(< r)/(4\pi r^3/3)$ drops below $\Delta_{\rm vir}\rho_{\rm bg}$, where $\Delta_{\rm vir}$ is a cosmological model and time dependent threshold parameter, and $\rho_{\rm bg}$ is the cosmological background matter density. The threshold $\Delta_{\rm vir}$ is computed using the spherical top-hat collapse model. For the cosmology that we are using, $\Delta_{\rm vir}$ = 355 at $z = 0$ (Bryan and Norman, 1998) (a discussion of these models is presented in Sec. 1.5.3).

To trace halos through the snapshots we build merger trees with MergerTree, a tool that comes with AHF . MergerTree identifies counterpart objects in the same simulation at different redshifts. MergerTree follows each halo identified at redshift $z = 0$ backwards in time, identifying as the main progenitor at some other redshift the halo that both shares the most particles with the present halo and is closest in mass. More details can be found in Srisawat et al. (2013).

Finally, for the analysis of the identified halos we used the Python-based package PYNBODY[5] (Pontzen et al., 2013).

Validating the numerical M33

In this section we focus our attention on the M33 candidate found in the Local Group simulation, examining how the properties of the candidate compare to the observed one. We start by showing, in Fig. 3.1, a visualisation of the simulated galaxy at $z = 0$, with the face-on and side-on views of the stellar and gas density of our M33 candidate. A warped disc component can be seen in the edge-on view, similarly to the warped disc reported in observations of M33 (e.g. Corbelli and Schneider, 1997; Kam et al., 2017). Moreover, similar to the observed M33, our simulated counterpart shows well defined spiral features, clearly visible in the face-on gas density plot.

In order to compare more quantitatively with observational results, we present in Tab. 3.1 the virial and stellar mass of the M33 candidate, and we compare these values with the observational M33 data reported in Corbelli et al. (2014) and Kam et al. (2017). For the simulation, the virial mass is computed as the total mass within the virial radius at $z = 0$, while the stellar mass is the sum of all the star particles found within the galaxy and its halo. We note that with a value of $M_{\rm vir} = 2.7 \times 10^{11} M_\odot$ and $M_\star = 5.1 \times 10^9 M_\odot$, our simulated M33 lies on the expected $M_\star$-$M_{\rm halo}$ relation, or abundance matching relation (e.g. Moster et al., 2010).

For the observed Triangulum galaxy, the virial mass and the stellar mass, together with the concentration of dark matter halo, are obtained by considering the composite probability of three events: the dynamical fit to the measured rotation curve of M33, the stellar mass

[4] http://popia.ft.uam.es/AHF
[5] https://github.com/pynbody/pynbody

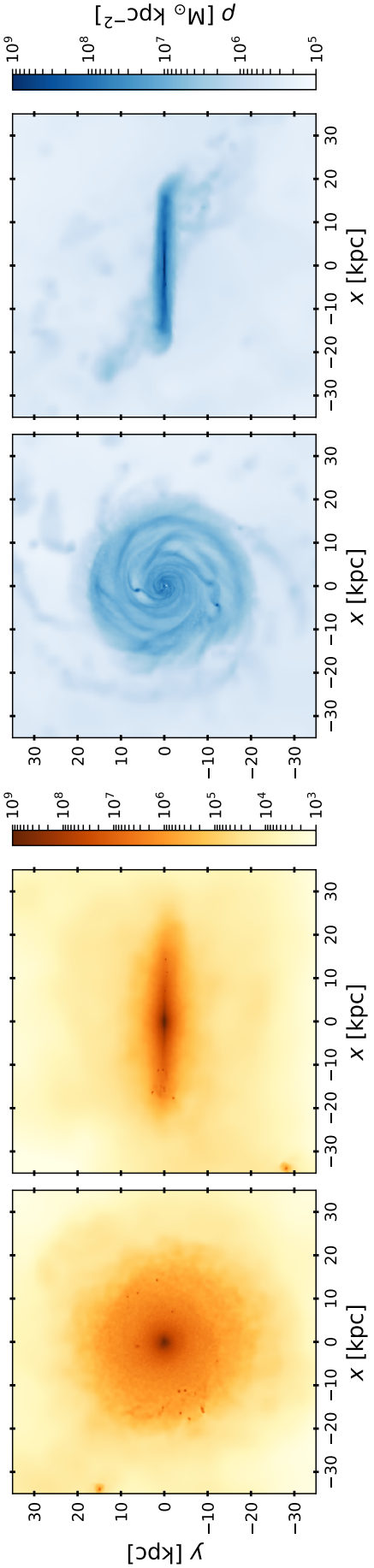

FIGURE 3.1: Stellar and gas mass densities of the simulated M33 galaxy at z=0. *Left*: stellar mass density, face-on and edge-on. *Right*: gas density, face-on and edge-on. Spiral features and a thin warped disc of gas are visible, in agreement with observational data (e.g. Corbelli and Schneider 1997; Kam et al. 2017).

TABLE 3.1: Total virial mass and stellar mass of simulated and observed M33. Observational data from Corbelli et al. (2014) and Kam et al. (2017), see text for more details.

M33	$M_{\rm vir}(10^{11}{\rm M}_\odot)$	$M_\star(10^9{\rm M}_\odot)$	$M_{\rm HI}(10^9{\rm M}_\odot)$
SIM	2.7	5.1	2.8
OBS	4.3±1.0	4.8±0.6	1.9 ±0.4

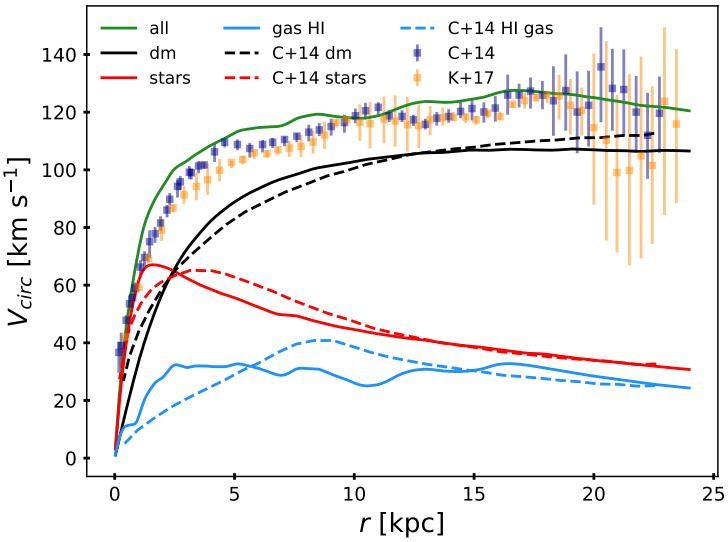

FIGURE 3.2: Circular velocity profiles of DM halo (black), stars (red) and HI gas (light blue) of the simulated M33 galaxy (solid lines) compared with observations from Corbelli et al. (2014) (dashed lines). The total velocity profile is shown in green for the simulated M33 and as blue and yellow points with error bars for the Corbelli et al. (2014) and Kam et al. (2017) data, respectively.

determined via synthesis models, and the concentration-mass relation $c(M)$ found in numerical simulations of structure formation for a ΛCDM cosmology (see Corbelli et al., 2014, for more details). Tab. 3.1 indicates that our simulated M33 is very similar, in both total and stellar mass, to the observed M33, justifying further comparisons.

In Fig. 3.2 we study the mass component distribution of the galaxy, showing the circular velocity profile of dark matter (black lines), HI gas (light blue lines), and stars (red lines), alongside observations from Corbelli et al. (2014) and Kam et al. (2017). Observations are shown as dashed lines and simulations, as solid ones. The total velocity is shown as a green solid line for the simulated M33 and as points with error bars for the observed one. The simulated velocity profiles are computed by using the gravitational potential of the particles in the galactic midplane after placing the galaxy face-on using its total angular momentum. The HI gas component was obtained directly from the simulations, which solves the Saha equation to calculate the ionisation state based on the pressure and temperature.

The total velocity curve matches the observed one quite well, reaching a maximum of $V = 127.6$ km s^{-1} at a radius of $r = 16.9$ kpc, like the real M33. However, some of the individual components have a rotation curve that rises faster in the innermost region of the galaxy, compared to the profiles derived from observational data in Corbelli et al. (2014). The HI gas component is closer to the observational data in the outer region of the galaxy ($r \gtrapprox 13$ kpc), while in the inner region it underestimates the peak velocity. Further, the slightly higher contribution from stars at the centre of the simulated galaxy reflects the contribution of its larger-than-observed bulge (see below). Nevertheless, the overall agreement between the total simulated rotation curve and the observed one is quite good, with differences of a few per cent at most, depending on the radii.

Our last comparison to observations will now go into even more details by mimicking

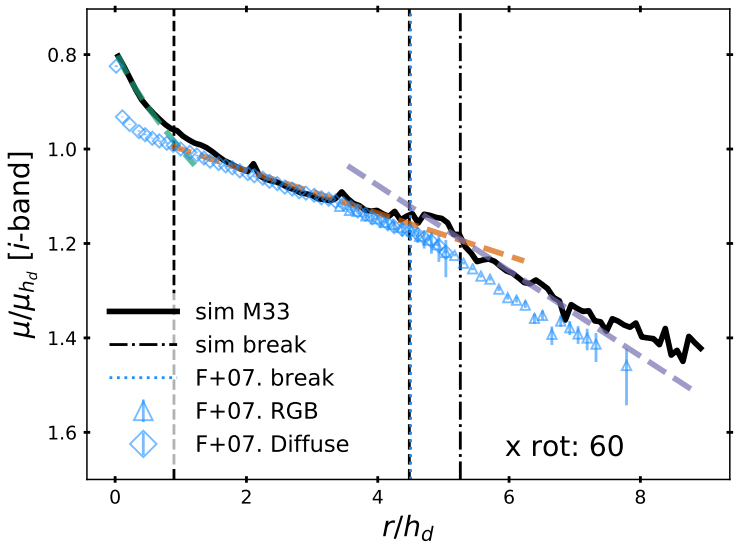

FIGURE 3.3: Surface brightness of the simulated M33 for the inclined configuration, normalised by the value at the inner disc's scale radius h_d. The best-fit values of the 3−component fit (coloured dashed lines) are presented in Tab. E.1. The vertical black dashed lines show the $r = 3$ kpc and $r = 15$ kpc regions. Observational values from Ferguson et al. (2007) are represented as blue markers, with its corresponding break at $r = 4.5h_d^{M33} = 8.1$ kpc (blue dotted line, on top of the $r = 4.5h_d = 15$ kpc dashed line). Similar to what is observed in the real M33, a break can be seen in the simulated galaxy at a similar position, $r \sim 5.3h_d = 17.6$ kpc (black dash-dotted line), as well as a truncation at $r \sim 7.6h_d = 25$ kpc.

observations as closely as possible. We therefore set the simulated M33 in a configuration which resembles the observed one. Starting from an initial face-on view, where the disc lies on the xy plane, we inclined the M33 candidate 60 degrees around the $x-$axis to reach the reported inclination of M33 to the line of sight from the Earth, $i \sim 50^\circ - 60^\circ$ (Patterson, 1940; Verley et al., 2009, e.g.). Furthermore, since observational data has been measured along the major axis of the galaxy to avoid stellar contamination from different galactic components, we select the major axis of the inclined simulated M33 in a similar fashion by applying a position cutoff in the axis perpendicular to the inclination axis, i.e. we select star particles with $|y| \leq 5$ kpc. Note that, since our galaxy is not spherically symmetric, there is a degeneracy in the initial face-on view of the galaxy; different initial face-on views (as generated by rotations about our z-axis) produce different profiles of projected quantities after inclining the galaxy. For our analysis we selected a face-on view which best reproduces the observed surface brightness profile[6], to be discussed now.

Once the simulated M33 is in its inclined configuration, we performed a bulge/disc decomposition in order to compute the galaxy's disc scale length (for a detailed description of the analysis, see App. E). We fit the $i-$band surface brightness profile of the galaxy with a 3−component model, i.e. a combined inner and outer exponential discs plus a Sersic bulge, to account for breaks in the profile. We obtain a inner disc scale-length of $h_d = 3.3 \pm 0.1$ kpc. The observed M33 has a somewhat shorter scale length for the disc, $h_d^{M33} = 1.8$ kpc (Verley et al., 2007; Ferguson et al., 2007; Verley et al., 2009; Corbelli et al., 2014). To account for this difference and in order to compare our simulated profiles with the observational data, respectively, we normalise the x-axis to the respective inner exponential disc scale length and the y-axis to the respective value at that position.

In Fig. 3.3 we show the (normalised) surface brightness profile. Along the simulated profile, we present the observed $i-$band surface brightness profile from Ferguson et al. (2007). We find the best match to observational data within the region $0.9 < r/h_d < 4.5$ (or in

[6]We studied 36 initial $z-$axis rotations of the initial face-on view, spanning 360 degrees, and found that ~ 64 per cent of the initial configurations present a strong break in the profile, while the rest show weak-to-null breaks after the 60 degree rotation.

physical units $3 < r < 15$ kpc) – as indicated by the two vertical dashed lines. In the inner region of our numerical M33 ($r \lessapprox 3$ kpc, left dashed line), we can identify an excess of light from the bulge component. From $r \gtrapprox 15$ kpc onwards (as indicated by the right dashed line), the M33 candidate follows closely the observed light distribution. Additionally, the simulated profile features a down-bending disc break at $r \sim 5.3h_d = 17.6$ kpc, which correlates with the radius at which the age reversal is found, as we discuss in the following sections. The disc break in the observational profile is found at a similar (although slightly smaller) position, at $r = 4.5h_d^{M33} = 8.1$ kpc. Following Martín-Navarro et al. (2012) and Martín-Navarro et al. (2014), at $r \sim 7.6h_{\rm d} = 25$ kpc we can also identify an up-bending in the surface brightness profile associated with the stellar halo component of the simulated galaxy, coexisting with a truncation, i.e. a sharp decline in the radial light profile, that allows the stellar halo component to outshine the disc's light distribution. We note that we obtain similar results in the stellar surface mass density profile of the simulated galaxy (not shown here): the 3−component fit leads to a comparable inner disc scale length, and we identify a break and a truncation at the same radii. The fact that we observe a break in the both profiles suggests that the reversal in the age gradient is affected by the combined effect of both the radial distribution of the star particles and their ages and metallicities.

We have just demonstrated that our numerical M33 is in fact an adequate replica of the observed M33: it is situated in the right environment, has about the correct size and mass, features comparable kinematics, and even agrees fairly well when observed from the right angle. And as we will see in the next section, it also features the observed reversal of the age gradient. This motivated us to seek its origin using the constrained simulation of the Local Group and its constituent M33. However, we like to close with the cautionary note that even though our numerical M33 appears to be a reasonable counterpart of the observed one, we need to remind the reader that it is by far a facsimile. As mentioned before, the very nature of following non-linear cosmic structure by means of numerical simulation only allows constraining scales beyond the size of the Local Group; random fluctuations will always enter scales smaller than that. For an elaborate discussion of such effects and restrictions we like to refer to the work of Carlesi et al. (2016) where the "Local Group Factory", i.e. a framework for simulating the "near field", has been presented.

3.2.3 Results and discussion

In the previous section we examined some specific properties of our M33 candidate, and we showed that, despite some unavoidable differences we are able to reproduce fairly well the morphology, luminosity, mass and velocity curve of the observed M33 galaxy. But one of the strongest arguments for studying the numerical M33 in our simulated LG is that we found a similar reversal of the age gradient in the cumulative normalised SFH of the simulated M33, as observations report (e.g. Williams et al., 2009; Barker et al., 2011). In the next sections we present our analysis of this phenomenon.

Presentation of the radial stellar age gradient

In Fig. 3.4 we show the combined observational results of the cumulative normalised SFH of M33, as reported in Williams et al. (2009) and Barker et al. (2011), referred to as W09+B11 from now on. The observations were made along the major axis of M33 using the HST/ACS in the Wide Field Channel, with field of view of $202''x202''$, at radii of $r = 0.9$, 2.5, 4.3, 6.1 kpc in Williams et al. (2009), and later extended to $r = 9.1$, 11.6 kpc by Barker et al. (2011). As we move further out from the galactic centre the intermediate-to-old star population fraction decreases while young stars start contributing more and more to the overall budget in the outer disc, compatible with an inside-out growth. Within 0.9 kpc from the galactic centre, more than 70 per cent of stars are old, having formed in the first 4 Gyrs of the galaxy assembly, while less than 10 per cent of the stars found at a radius of 6.1 kpc are old. At 9.1 kpc, more than 80 per cent of the stars are young, specifically younger than 4 Gyrs.

However, as already noted in Barker et al. (2011), once the radius $r = 11.6$ kpc is reached (in magenta), the curve shifts to lower t with respect to $r = 9.1$ kpc (in yellow), i.e. the fraction of old stars increases again. Indeed, at 11.6 kpc stars are found that are older than the oldest population at $r = 9.1$ kpc, even after considering the 1σ error (dashed lines). Such

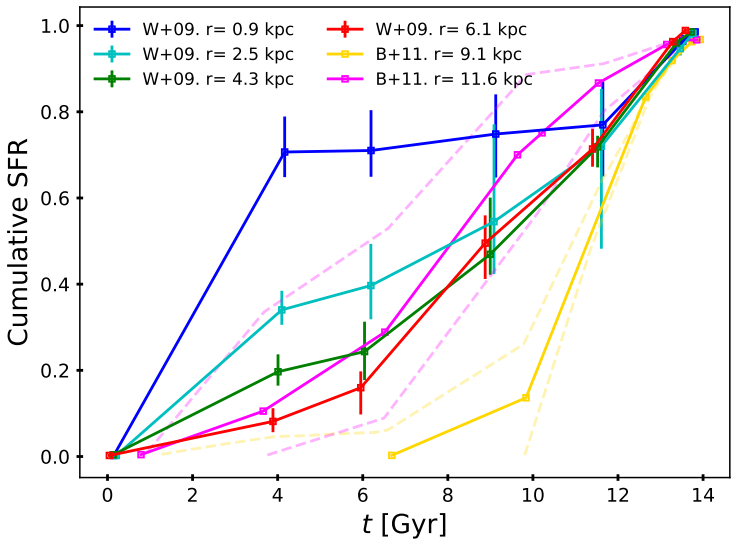

FIGURE 3.4: Cumulative normalised SFH of the M33 galaxy measured along its major axis. Data retrieved from Barker et al. (2011) with results from Williams et al. (2009), presented in a revised form for direct comparison with our simulation. The dashed lines represent the 1σ contours for the last two radial bins.

an age gradient reversal, with increasing mean stellar age with radius, thus happens for radii beyond 9 kpc.

In order to compare our galaxy to observations we analyse the star particles in our halo in a similar fashion to the measurements done in W09+B11. After positioning the simulated galaxy face-on, we choose a series of concentric annuli of thickness $\delta_{\rm ann} = 0.8$ kpc, similar to the field of view of the camera used in W09+B11, centred at the same radii of Fig. 3.4, $r_{\rm obs}$, for which observations exist. The annuli's radii will then be $r_{\rm ann} = r_{\rm obs} \pm \delta_{\rm ann}/2$, where $r_{\rm obs} = 0.9, 2.5, 4.3, 6.1, 9.1$, and 11.6 kpc. We further extend the sampling region up to $r_{\rm ann} =$ 30 kpc, in order to cover even the outer part of the disc, for which observations of the M33's SFH currently do not exist. We choose annular regions in order to avoid a definition of a major axis and to get a statistically meaningful result. In order to check that our results are insensitive to – and not driven by – the inclination of the galaxy, we repeat the same analysis for our (best) inclined configuration described in the previous section.

In Fig. 3.5 we show the annular regions used to compute the SFHs[7], superimposed on the stellar mass density of our simulated galaxy, for the face-on view (left panel), and for the inclined view (right panel). For this latter setup, instead of taking the star particles in the whole annular regions as done for the face-on analysis, we select the ones in the annular regions within the major axis ($|y| < 5$ kpc) for this configuration. The area of the annuli that we consider in this case is indicated as a bright region in the right panel of Fig. 3.5. Once the annuli are defined, the star particles inside them are selected and used to calculate the SFH at each radius[8].

In Fig. 3.6 we show the results of the SFH analysis of the simulated M33, presented analogously to the observational data in Fig. 3.4, as cumulative SFHs at different radii, for the galaxy viewed face-on (left panel) and for the 60° inclined view (right panel). Increasing radii are shown in different colours, from violet (0.9 kpc) to red (30 kpc). Moving from the inner radii to the outer ones, the mean stellar age decreases, compatible with an inside-out growth of the disc.

[7]Considering that star particles migrate from their birth position, technically we calculate the Stellar Formation Time Distribution of the M33 look-alike at $z = 0$. For clarity, we will maintain the SFH nomenclature throughout the paper.

[8]Each annular region is further subdivided in smaller regions, each subtending an arch of 0.8 kpc across as we spam the 360° angle around each annuli, to mimick the size of the HST/ACS field of view. We perform the SFH analysis for such individual regions, as well as for the total amount of stellar particles within each annuli, in order to confirm that our results are not affected by a specific position within each annuli.

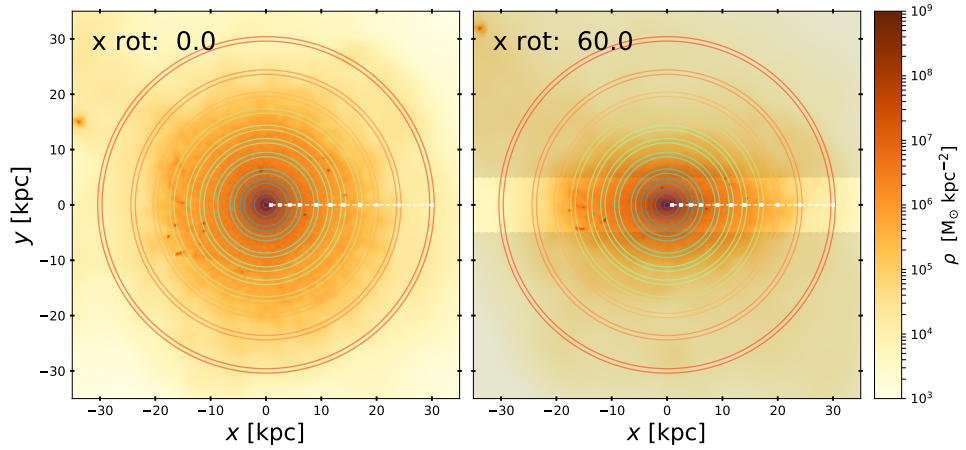

FIGURE 3.5: Concentric annuli spanning a region between 0.9 to 30 kpc from the galactic centre, chosen to select the star particles used to compute the SFH of our M33 candidate. The annuli are shown superimposed on the stellar mass density plot. The SFH at different radii will be computed for two configurations of the galaxy: face on, *left panel*, and after a rotation of 60°, *right panel*.

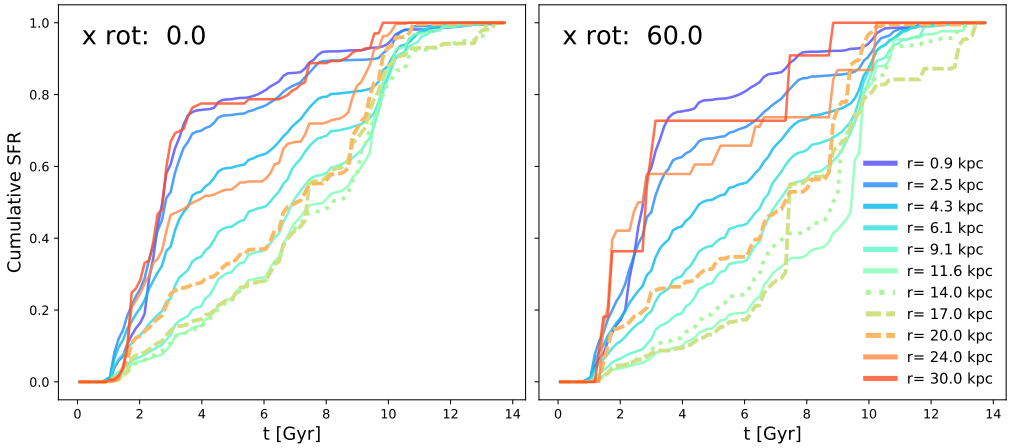

FIGURE 3.6: The cumulative normalized SFH of the simulated M33 galaxy, for several increasing radii out to a maximum radius of 30 kpc.*Left*: SFH for the galaxy positioned face-on. *Right*: SFH after a 60° rotation around the x-axis of the galaxy. In both the face-on and the inclined case, the radius at which the age reversal appears is between $r = 17$ kpc and $r = 20$ kpc (dashed lines). Projection effects may lead to a misidentification of the reversal radius, as seen from the median stellar age at $r = 14$ kpc (dotted line).

However, at radii larger than $r = 17$ kpc a reversal of the age gradient is observed in both the face-on and the inclined view, just as found in observations, with the percentage of old stars that contribute to the SFH rising again. The reversal region reported in W09+B11 ($r > 9.1$ kpc) is smaller than the one found in our simulation: this should not be surprising given the different scale-lengths of the observed and simulated M33. In terms of relative disc scale lengths, the age reversal appears at a radius of about 5.1 times the disc scale length in the observed M33, and 5.2 times in the M33 look-alike. As mentioned in the previous section, we note that a break in the surface brightness and stellar surface density profiles of our M33 candidate appears at a radius $r = 17.6$ kpc, coinciding with the radial region at which the age turnaround is found, which suggest that a correlation between the two effects could exist, similar to what has been discussed in W09+B11.

Comparing the inferred region of the reversal radius of the face-on and inclined views, we expect that projection effects in the inclined view would move the reversal radius closer to the galactic centre after rotating the galaxy. The reversal region is instead found between $r = 17$ and $r = 20$ kpc (dashed lines) for both configurations. However, analysing the surface brightness and stellar surface density profiles of the face-on view, we indeed find that the break moved to $r \sim 19$ kpc (still within $17 < r < 20$ kpc). Thus, inspecting the cumulative SFH only provides a rough estimation of the turnaround radius' location, that is, it constrains the boundary of the region in which the turnaround radius is found. The age reversal detected in observations could be similarly affected by the inclination of the galaxy itself and subsequent projection effects. Indeed, with a 60° inclination with respect to the line-of-sight, the old stars in the outer region will overlap with the young stars in the disc, causing a higher contribution of old stars at smaller radii. This effect can be seen in the median formation time of the $r = 14.0$ kpc region (dotted line), which shifted to a slightly older population after the inclination.

We conclude that a reversal in stellar age gradient appears for our M33 candidate with respect to the line-of-sight, and that the value of the reversal radius is sensitive to the particular inclination chosen, being smaller for larger inclinations. While this change is not observed directly in the SFH of the face-on and inclined views of the galaxy, considering the correlation between the reversal radius and the break radius we are able to trace the projection effects through the break radius. Therefore, the deprojected reversal radius of the observed M33 may be at a different position than the one currently reported.

Explanation of the stellar age gradient

As already touched upon before, there are several hypothesis that could explain the reversal of the stellar age gradient, such as mergers and stellar radial migration. To investigate which process determines the age turnaround in our simulation, we select the star particles that are within the M33 host at $z = 0$ and trace them back in time to their birth redshift $z_{\rm birth}$ and position $r(z_{\rm birth})$, respectively.

Then, by looking at their $r(z_{\rm birth})/R_{\rm vir}^{M33}(z_{\rm birth})$ distribution, we were able to identify a main population of stars in the inner region of the galaxy, well separated from an outer stellar population found beyond 20 per cent of M33's virial radius. Thus, we define *in-situ* star particles as those that formed within 20 per cent of the virial radius of the main progenitor of M33 at the formation redshift, that is, whose birth radius satisfies the condition $r(z_{\rm birth}) < 0.2 \times R_{\rm vir}^{M33}(z_{\rm birth})$. If, instead, the star particle has a birth radius larger than the above value it is defined as *accreted*, since it is brought into the main M33 galaxy via mergers and accretion of haloes. We performed some tests to check our selection criterion. We used a different classification of "in-situ" versus "accreted" stars by checking whether a star particle was born in the progenitor of M33, inside a subhalo, or outside the progenitor's virial radius. We also cleaned the disc from highly eccentric orbits that are not compatible with stars formed in the disc by making an eccentricity and vertical (z-component) velocity cut at $z = 0$ of $e < 0.6$ and $|v_z| < 150$ km/s, respectively. We confirm that our tests did not drastically change the results presented here and that the virial radius condition is sufficient to ensure that the star particles are formed within the disc of the progenitor of M33.

In Fig. 3.7, we show the projected (2D) median formation time for all (red solid line), in-situ (green dash-dotted line) and accreted (blue dashed line) star particles, as a function of radius (normalised by the disc scale length to correct for the size of the galaxies), for

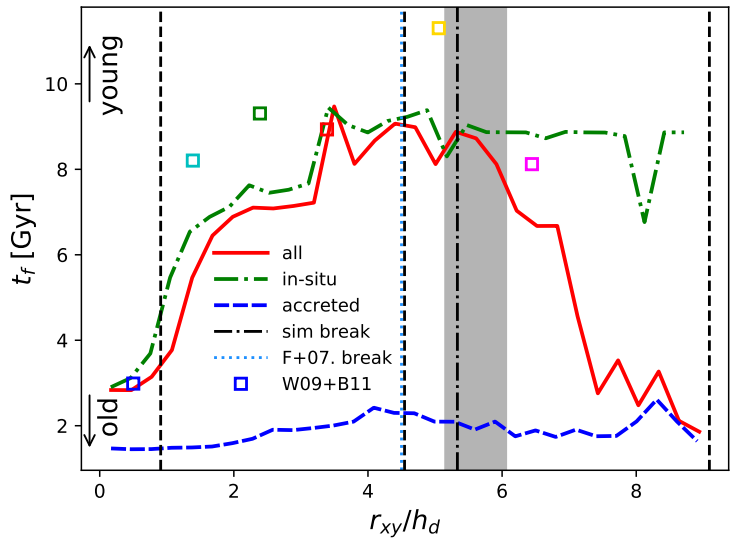

FIGURE 3.7: Projected (2D) median formation time of star particles in the inclined view, for increasing radial bins normalised by the disc scale length. The formation time profile of all star particles within M33 at $z = 0$ is shown as a red line, while in-situ and accreted stars are shown as green dash-dotted and blue dashed lines, respectively. Vertical dashed lines indicate the pre-turnaround (3-15 kpc) and the turnaround region (15-30 kpc) of the galaxy. The inferred median formation time for different radii from W09+B11 is shown as the colour-coded markers. The blue vertical dotted line shows the surface brightness break radius from Ferguson et al. (2007), whereas the black dash-dotted vertical line shows the break radius in the M33 look-alike. The inferred age turnaround radius from the SFH of the M33 candidate in Fig. 3.6 is represented by the grey shaded region.

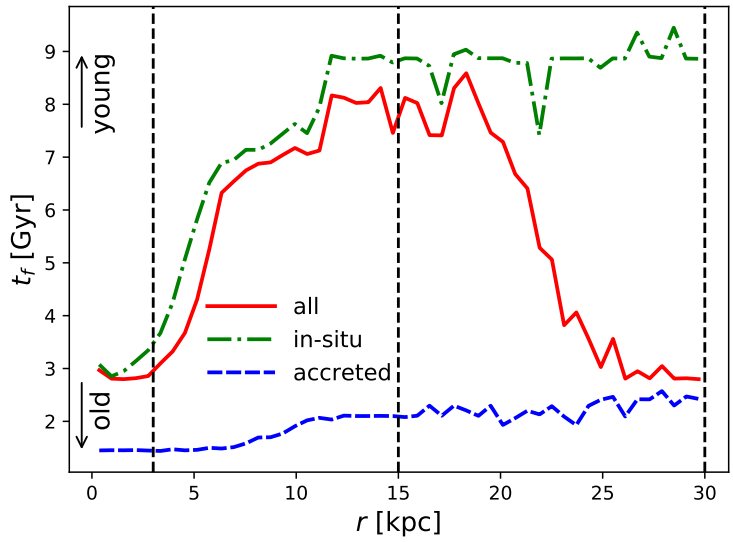

FIGURE 3.8: 3D median formation time of star particles for increasing radial bins. We can see similar trends as the ones identified in the projected (2D) median formation time profile in Fig. 3.7: a turnaround in the whole star population at $r > 15$ kpc, a formation time flattening of the in-situ population, and an old flat distribution of star particles up to $r < 30$ kpc. The fraction of in-situ stars within these regions is shown in Fig. 3.9.

the inclined view of the M33 candidate. Along the simulated results we show the inferred median formation time profile from W09+B11 (colour-coded markers), i.e. the formation time at which half of the cumulative SFR is reached at each radius. As we can see in the figure, the break radius of our simulation (dash-dotted black line) lies within the region of the turnaround radius inferred from the cumulative SFH (grey shaded region). Moreover, the maximum formation time (minimum age) of each profile is located at a similar relative projected radial positions, at $r_{\mathrm{max,t_f}} \sim 4.5h_d \sim 15$ kpc for the simulated profile, and at $r^{M33}_{\mathrm{max,t_f}} \sim 5h^{\mathrm{M33}}_d \sim 9.1$ kpc for the observed one; and at a similar projected radius to their respective break radii, at $r_{\mathrm{break}} \sim 5.3h_d \sim 17.6$ kpc for the M33 candidate, and at $r^{M33}_{\mathrm{break}} \sim 4.5h^{\mathrm{M33}}_d \sim 8.1$ kpc for the real M33.

Once we scale the radial dependence of the profile to the corresponding disc scale length, the results are in good agreement with the observational trends. However, this has been done for a particular inclined initial configuration (i.e. our best configuration as introduced in Sec. 3.2.2). Although we obtain similar trends to the observational data, we are aware of the statistical limitation of the analysis. While the age turnaround is evident when considering the full sample of stars, with a median formation time decreasing from a maximum of $t_f \sim 8$ Gyrs at $r_{\mathrm{xy}} \sim 4.5h_d$ ($r_{\mathrm{xy}} = 15$ kpc) to a minimum of $t_f \sim 3$ Gyrs at $r_{\mathrm{xy}} \sim 9.1h_d$ ($r_{\mathrm{xy}} = 30$ kpc), such a turnaround does not show up when only in-situ star particles are considered. Hence, the main driver of the reversal is not due to in-situ star particles, but rather to accreted ones.

As we move further out from the galactic centre, the in-situ stars become progressively younger until reaching a radius of $r_{xy} \sim 4h_d$ ($r_{\mathrm{xy}} \sim 13$ kpc), after which their age distribution flattens, with a median age of 4.7 Gyrs ($t_f \sim 9$ Gyrs) for radii larger than 13 kpc. Note that, in an inside-out formation scenario we expect a monotonic increase of the formation time of the in-situ star particles with increasing radii, thus, the flattening of the profile clearly demonstrates that stellar migration also plays a role in the stellar age gradient of our simulated M33 (we will return to this point later). The same trends can be seen in the (3D) median formation time profile of the galaxy, as presented in Fig. 3.8: a turnaround in the whole star population at $r > 15$ kpc, a formation time flattening of the in-situ population, and an old flat distribution of star particles up to $r < 30$ kpc; with the only difference being the actual median formation time values of each component. In light of these results, in the following section we opted for a full 3D analysis of the origin of the turnaround.

Star particles that get into the galaxy via mergers are the main drivers of the observed age turnaround. The relative fraction of in-situ and accreted star particles within radial bins are shown in Fig. 3.9: the in-situ star fraction within $3-15$ kpc is ~ 80 per cent, while it decreases sharply as we move towards the outskirt of the galaxy, with a minimum of 20 per cent star particles found at $r = 30$ kpc being in-situ. The fraction of accreted stars, correspondingly, increases with radius: in the turn-around region, the accreted star fraction move from less than 20 to almost 80 per cent. We verified that the accreted stars that end up in the age reversal region (at $r > 15$ kpc) are brought in through minor mergers. Instead, the peak of accreted stars seen in the inner radii, at $r = 3-4$ kpc, is attributable to the last major merger that occurred in the early phases of the life of the galaxy, before $z = 2$.

To investigate the role of accreted stellar particles as a function of their age, we first aim at classifying the stars by their actual formation time. To this extent we present in Fig. 3.10 the total, integrated SFH for the simulated M33 analogue at $z = 0$. We can observe several star forming bursts along its evolution. These bursts allow us to divide the stars into the following formation time bins: an old population of stars with $0 < t_f \leq 4$ Gyr, a old-to-intermediate stellar population corresponding to a small burst with $4 < t_f \leq 6$ Gyr, an intermediate-to-young stellar population with $6 < t_f \leq 8$ Gyr, and the rest of the stellar population with $t_f > 8$ Gyr corresponding to the last major stellar burst.

We then show, in Fig. 3.11, the percentage of in-situ star particles in the pre-turnaround region, $3 < r \leq 15$ kpc (top row), and in the turnaround area $15 < r \leq 30$ kpc (bottom row)[9]. From left to right, we indicate the full percentage of in-situ stars, and the relative percentages of in-situ stars once binning by formation time t_f. In-situ star particles account for ~ 85 per cent of the total stellar mass in the inner region of M33, and only for ~ 74 per cent of the total star mass in the outer region. Therefore, the total accreted star particle

[9]Since we are interested in disc-stars, we avoid the central bulge region of our simulated galaxy when computing percentages, and select star particles with $r > 3$ kpc.

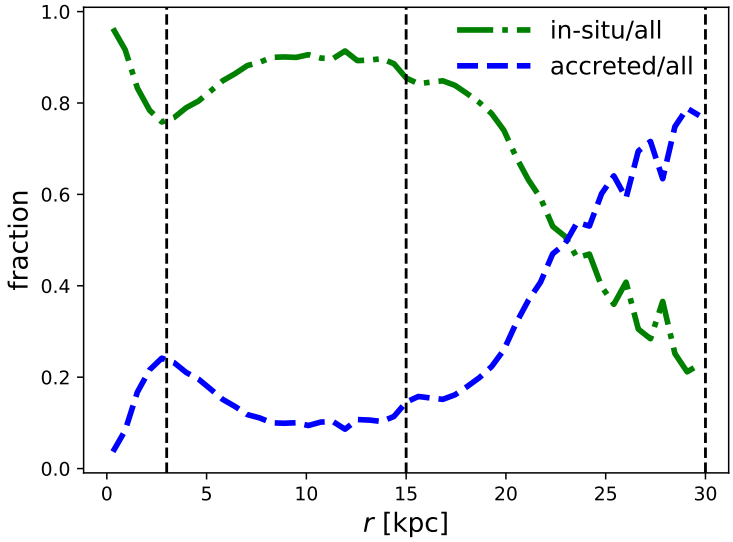

FIGURE 3.9: Fraction of in-situ and accreted stellar particles within radial bins, found in the simulated M33 at $z = 0$. The in-situ stars made up $\sim$ 85 per cent of the total stellar mass within $r = 15$ kpc, while at larger radii their fraction decreases dramatically to about $\sim$ 20 per cent for $r = 30$ kpc. Correspondingly, the fraction of stars accreted via mergers increases with radius, causing the age-reversal observed at large radii. The peak of accreted stars seen in the inner radii, at $r = 3 - 4$ kpc, is attributable to the last major merger that occurred in the early phases of the life of the galaxy, before $z = 2$.

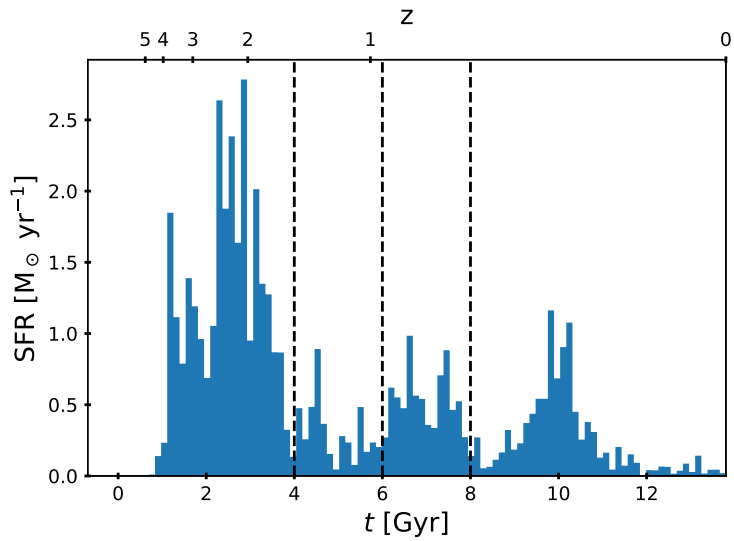

FIGURE 3.10: Integrated SFH of the simulated M33. We indicate the stellar age bins that will be later used for further analysis, selected following the main bursts of star formation.

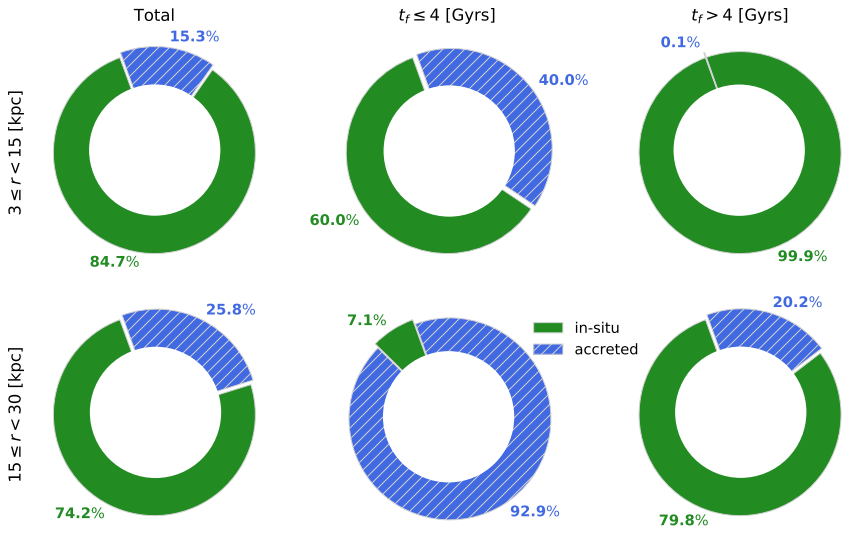

FIGURE 3.11: In-situ star particles percentages in the pre-turnaround region ($3 < r \leq 15$ kpc, top row) and in the turnaround region ($15 < r \leq 30$ kpc, bottom row).

fraction increases from $\sim$ 15 to $\sim$ 26 per cent when moving towards the outskirts of the galaxy. As expected for an inside-out growth scenario, almost all the stars with a formation time $t_f > 4$ Gyrs are born in-situ, at any radial region. While, strikingly, only about $\sim$ 7 per cent of the old stars ($t_f \leqslant 4$ Gyrs) found in the outskirt of M33 (15 to 30 kpc), where the age turnaround is observed, are in-situ star particles. In the radial region corresponding to the observed age reversal, $\sim$ 93 per cent of the stars with old formation time are accreted via mergers, being the cause for the turnaround in the formation time profile.

Next, to verify whether stellar migration also plays a role in the age reversal, we quantify the amount of radial migration that has taken place in the disc. To this extent, we need to estimate the change in angular momentum, which is equivalent to the change in guiding radius (r_g) since a star particle's formation time. We approximate r_g for each star particle as described in Minchev, Chiappini, and Martig (2014) by calculating the birth and end guiding radii as:

$$r_g = \frac{L}{v_{\rm circ}(r)} = \frac{r \cdot v_\phi}{v_{\rm circ}(r)}\,, \tag{3.1}$$

where L and v_ϕ are the angular momentum and rotational velocity of the star particle, respectively, and $v_{\rm circ}$ is the rotation curve. The guiding radius takes into account stars with high eccentricity orbits by comparing the star's tangential circular velocity, v_ϕ, with the circular velocity of the galaxy at the star's radius, $v_{\rm circ}(r)$. This allows us to know the change in the angular momentum of the star particles, which is equivalent to the change in the guiding radius at $z = 0$ ($r_{g,\rm end}$), and the guiding radius at the birth redshift of the star particle ($r_{g,\rm birth}$). By using the guiding radius we avoid mistaking stars with high eccentricity orbits as instances of radial migration.

We now present in Fig. 3.12 the guiding radius at $z = 0$ ($r_{g,\rm end}$) vs. the guiding radius at the birth redshift ($r_{g,\rm birth}$) for the star particles that were born in M33's main progenitor, i.e. in-situ ones, selected from two regions in the formation time profile, $3 < r \leq 15$ kpc (top row) and $15 < r \leq 30$ kpc (bottom row), further separating the stars using aforementioned formation time bins (from left to right, we move from old to young stars). Black dashed lines indicate the locus of stars that have not changed their position, i.e. whose guiding birth radius $r_{g,\rm birth}$ is the same as their end one $r_{g,\rm end}$.

In the inner region, most of the old, $t_f \leq 4$ Gyr, population moved to slightly greater radii ($\sim$ 70 per cent of stars moved from $r_{g,\rm birth} \sim 0.5 - 1.5$ kpc to $r_{g,\rm end} \sim 2 - 4$ kpc), whereas almost all the younger stars ($t_f > 4$ Gyr) remained close to where they were born, i.e. close to the black dashed line. Thus, radial migration is observed to some extent for the

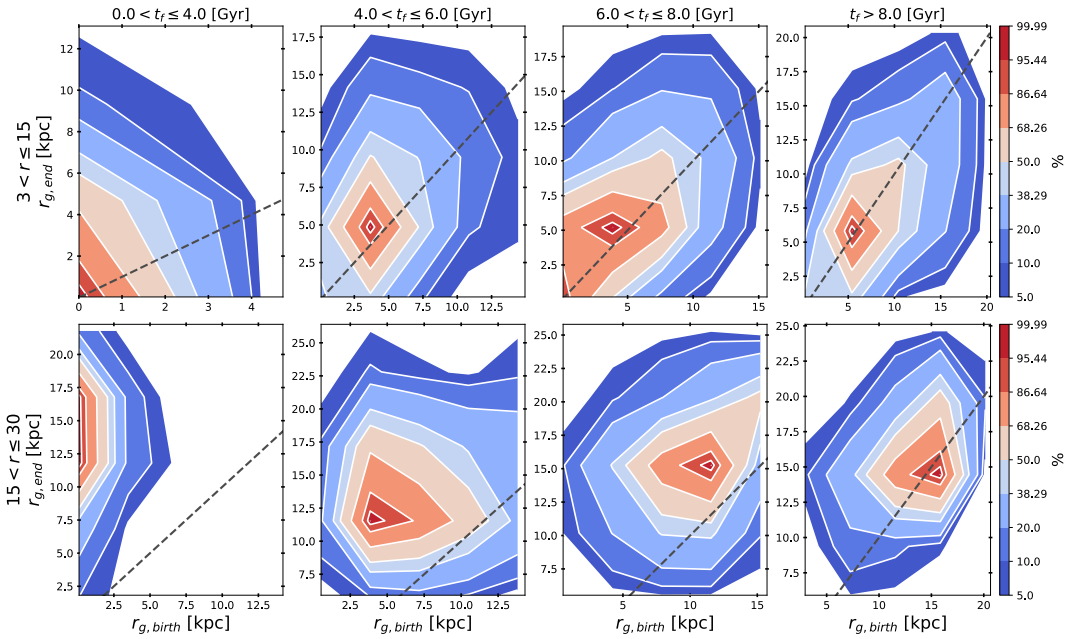

FIGURE 3.12: Stellar migration density probability, end guiding radius $r_{g,\mathrm{end}}$ versus birth guiding radius $r_{g,\mathrm{birth}}$ for in-situ star particles. *Top row:* stellar migration in the inner region, $3 < r \leq 15$ kpc. *Bottom row:* stellar migration in the outer region, $15 < r \leq 30$ kpc. The dashed line represents the locus of star particles for which no migration occurred.

old population of in-situ stars in the inner region of the galaxy: their final guiding radius, however, it is still smaller than the radius at which the age turnaround is found.[10]

In the outer region, however, we see a considerable radial migration for the old population ($t_f < 4$ Gyr), most of which migrate from $r_{\mathrm{g,birth}} \sim 0$ kpc to $r_{\mathrm{g,end}} \sim 12 - 17$ kpc, and few of them reaching as far out as $r_{\mathrm{g,end}} \sim 20$ kpc. The rest of the stellar populations present less and less radial migration the younger they are. Thus, the old in-situ stars, which made up only the 7 per cent of the old stars found in the outer region of M33, have undergone thorough radial migration, i.e. they are stars that were born close to the galaxy's disc plane centre and have migrated outwards. However, given their small number compared to the fraction of old accreted stars, migration of in-situ stars alone is not sufficient to explain the age turnaround found in Fig. 3.8: without accretion we could not observe this age reversal. Hence, we conclude that the main driver behind the reversal of the age gradient is stellar accretion and, to a lesser extent, stellar migration.

Observational predictions

In order to verify that the age turnaround is mainly driven by stellar accretion, one would need to be able to differentiate – observationally – accreted from in-situ stars. Since both groups of stars share the same location in the galaxy at $z = 0$, we must rely on their kinematics for this aim. In this section, we investigate the kinematic properties of the two populations of star particles found in the outer region of our simulated Triangulum galaxy.

Using the same (best) inclined configuration of our numerical M33, we study the line of sight velocity V_{los} of the star particles in the disc. We selected the projected star particles within a square region of 4 kpc in side, alongside the major axis of M33, centred on the age turnaround region, $16 \leqslant x \leqslant 20$ kpc and $|y| \leqslant 2$ kpc. To improve the sample of stars, and to avoid any preferential direction on the mayor axis, we performed the selection for both the

[10] Note that we initially selected the star particles by their radius $3 < r \leq 15$ kpc, and by using the guiding radius r_g we find stars with $r_{\mathrm{g,end}} < 3$ kpc, outside the originally selected region at $z = 0$. This indicates that in this region there are some star particles that are on highly eccentric orbits. Although we find them at a particular radius at $z = 0$, their guiding radius reveals they have different average radii.

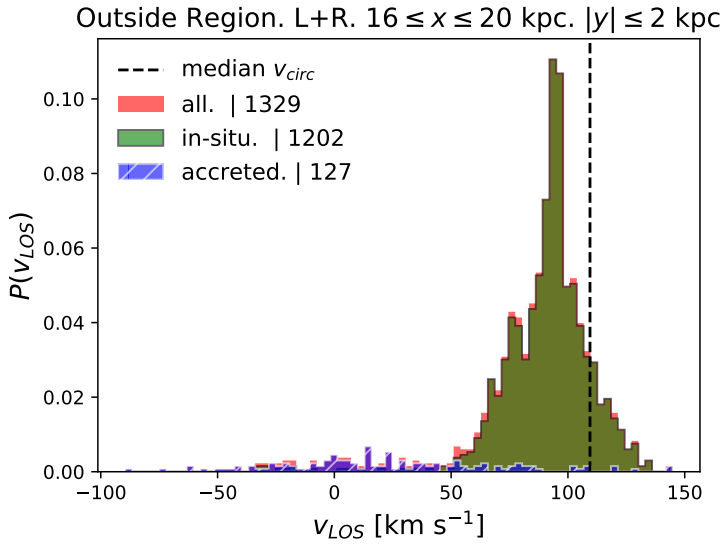

FIGURE 3.13: Line-of-sight velocity histograms of all (red), in-situ (green) and accreted (blue hatched fill) star particles, with the number of star particles in each category, within a 4×4 kpc^2 region centred at the turnaround radius, after inclining the galaxy 60°, as the observed M33. The vertical dashed line is the galaxy's circular velocity corrected for inclination. In-situ star particles co-rotate with the galactic disc, and lag with respect to the rotation curve due to the asymmetric drift effect, resulting from the non-zero stellar velocity dispersion. Accreted ones have a random distribution of their $V_{\rm los}$, with a large dispersion.

right-hand side (x>0) and the left-hand side (x<0) of the galaxy, and combined the selected stars taking into account the sign change due to the rotation of the star particles in the disc.

We then plotted a histogram of the star particles' line of sight velocity $V_{\rm los}$ (in projection, identified with the z axis-component of the star particle's velocity), in Fig. 3.13. The total, in-situ and accreted stars, are shown as red, green and blue histograms, respectively, along the number of stars in each category. The vertical dashed line at $V_{\rm los} \sim 109$ km/s is the galaxy's circular velocity corrected for inclination.

The difference between the accreted star particles and the in-situ ones is clear: while the latter are co-rotating with the disc, with a peak rotation of $V_{\rm los} \sim 94$ km/s and a relatively small velocity dispersion, $\sigma \sim 19$ km/s, the accreted stars have randomly distributed $V_{\rm los}$, averaging to 0, i.e. implying radial orbits in the absence of angular momentum, and displaying a much higher dispersion, $\sigma \sim 46$ km/s.

Future surveys will potentially be able to identify rotationally supported stars in the outskirts of M33, a signature that they are in-situ stars, and differentiate them from accreted ones. Our model predicts that the in-situ stellar population in the outskirts of the galaxy should have a flat radial age gradient as a result of accretion and stellar migration: in our particular simulation, the median stellar age of in-situ, co-rotating stars at large radii is $4-5$ Gyrs. Accreted stars, on the contrary, are expected to be uniformly old, with a median age of ∼11 Gyrs.

3.2.4 Conclusions

In this section we presented properties of a M33-analogue galaxy, simulated within the framework of Constrained Local UniversE Simulations (Gottlöber, Hoffman, and Yepes, 2010; Di Cintio et al., 2012; Carlesi et al., 2016), run with the code `GASOLINE` (Wadsley, Stadel, and Quinn, 2004) and including supernova feedback following the Stinson et al. (2006) prescription, which allows for an efficient regulation of star formation within galaxies.

The properties of the simulated M33 are in fair agreement with observational data from Ferguson et al. (2007), Corbelli et al. (2014) and Kam et al. (2017), in terms of mass, rotation velocity, and surface brightness. Our simulated M33 has a total virial mass of $2.7 \times 10^{11} M_\odot$

with a stellar mass of $5.1 \times 10^9 M_\odot$, placing the galaxy on the correct expectations from abundance matching prediction, a thin extended disc with scale length value of ~ 3.2 kpc, and a rotation curve whose maximum value of $V = 127.6$ km/s is reached at a radius of $r \sim 17$ kpc, similar to what is reported in observations. The M33 simulated candidate does, however, have a small bulge in its inner region, not observed in the Triangulum galaxy. Consequently, we have avoided the region of the galaxy $r < 3$ kpc in our analysis.

In the CLUES-M33 analogue, we observe a trend of decreasing stellar age as we move towards outer radii, a sign of an inside-out formation of the disc (e.g. Pilkington et al. 2012), in which old stars are found within the inner most regions of a galaxy and young stars in the outskirt of the disc, as a result of newly accreting gas. In order to compare the observational results with our simulations we selected stellar particles within concentric annuli regions of similar thickness as the field of view of the HST/ACS camera, that has been used to derive the cumulative star formation history (SHF) of M33 along its major axis (Williams et al., 2009; Barker et al., 2011).

Using the aforementioned criteria we studied the radial stellar age gradient of our M33 analogue. Here we summarise the main results:

- Similarly to what was found in observations, the age gradient of stars in the simulated M33 shows a turnaround at large radii, r$\geq$ 17-20 kpc, with the percentage of old stars ($t_f < 4$ Gys) increasing from ~ 20 to ~ 80 per cent, moving from radii 14 to 30 kpc.

- We demonstrate that this age reversal is mostly a result of accretion of old ($t_f \leq 4$ Gyrs) stars from merging satellite galaxies into the main host galaxy and, to a much lesser extent, of stellar migration of old in-situ stars from the central regions towards the outskirts of M33. This result is in agreement with previous work by Ruiz-Lara et al. (2016b), using more massive galaxies. Indeed, at large radii where the age turnaround is found, about 93 per cent of the old stars come from accretion events, while only a mere 7 per cent were formed within the M33 galaxy disc (i.e. are in-situ): the reversal in the stellar age gradient disappears when considering only in-situ star particles. This suggests that accretion from mergers are the origin of the turnaround in our simulated M33.

- This scenario could be verified observationally, studying the kinematic of stars in the outer fields of M33: in-situ stars should be co-rotating with the galactic disc, and should have a relatively small velocity dispersion σ, while accreted stars, which are kinematically hot, are expected to have a random distribution in their line-of-sight velocity, and to show a large velocity dispersion (in our model, more than two times higher than the σ of in-situ stars at the same radius). Moreover, the median age of the rotationally supported, in-situ stars, should indicate that this stellar population is young (median age of 4-5 Gyrs), unlike the pressure supported, accreted stars, causing the age turnaround, which should be all old (median age ~ 11 Gyrs).

- We highlight that the method used is sensitive to projection effects. While changing the inclination of the galaxy did not induce an apparent change in the turnaround radius region observed in the cumulative star formation history of the galaxy (i.e. $17 \leq r \leq 20$ kpc), since it only provides a rough estimation of the turnaround radius; considering the correlation between the age reversal radius in the median formation time profile and the break radius of the surface brightness and stellar mass density profiles we are able to trace the projection effects through the break radius. Therefore, projection effects must be thought of carefully since they might play an important role in the determination of the true age turnaround radius.

- Similar to what was found in observations (Ferguson et al., 2007), a break in the surface brightness profile of our M33 candidate in its inclined configuration appears at $r = 17.6$ kpc (5.3 times its disc scale length), coinciding with the radius at which the age turnaround is found. Moreover, following the Martín-Navarro et al. (2012) and Martín-Navarro et al. (2014) classification, we detect a truncation coexisting with an up-bending of the surface brightness profile associated with the stellar halo component of the simulated galaxy at $r = 25$ kpc. Similar results are obtained from the stellar surface mass density profile of the M33 candidate, i.e. a comparable disc scale length,

and a break and a truncation at the same radii. Thus, both the radial mass distribution of the star particles and their age/metallicity contributes to the reversal of the age gradient at the outskirts of the galaxy. Recently, Ruiz-Lara et al. (2017) showed, using simulations, that breaks are a consequence of the combined effects of outward-moving and accreted stars, in good agreement with our results.

Finally, we note that Ruiz-Lara et al. (2016b) found similar results when studying Milky Way-mass galaxies in the RADES (RAMSES *Disc Environment Study* simulations, Few et al., 2012). In those simulations, the age reversal appears due to a combination of an inside-out growth of the disc, stellar migration (both inwards and outwards) of disc stars and accretion from old satellites: interestingly, as in our model, the age reversal was still recovered after suppressing stellar radial motion, indicating the minor relevance of stellar migration in generating the age upturn observed at large radii in massive galaxies.

In the future we intend to verify if the accretion phenomenon causing the age turnaround is dependent on the specific mass accretion history of each galaxy: in order to shed light on this we would need a large statistical sample of hydrodynamically simulated halos of M33's mass. The recently developed Local Group Factory (Carlesi et al., 2016) could be used to this aim.

3.3 Pericentric passage-driven star formation bursts in satellite galaxies

Section based on Di Cintio et al. (2020) (In prep.)

The star formation histories (SFHs) of satellite galaxies show a variety of features whose origin is not yet well understood. Using a cosmological simulation performed within the Constrained Local UniversE project (CLUES) we study the SFH of satellite and isolated galaxies. The typical SFH of a satellite before infall is very similar to the one of isolated galaxies of comparable mass accretion histories. Notable differences can be instead found amongst the SFH of satellites after their infall and the SFH that they would have had if they were isolated: while in the majority of the cases the accretion onto the main host causes the satellite to lose its gas with a subsequent suppression in star formation, in about one third of the satellites we observe a clear enhancement of star formation after infall. Galaxies which enter the main host's virial radius with a high reservoir of cold gas have their star formation enhanced due to the interaction with the host itself, during which the gas is compressed and able to form new stars. Peaks in star formation clearly correlate with the satellite-host and, in one case, also with a satellite-satellite interaction. We show that suppressed versus enhanced SFHs can be discriminated based upon the fraction of cold gas mass of their satellite at infall, $M_{\rm gas}/M_{\rm halo}$. This finding should be taken into account in semi-analytic models of galaxy formation and satellite quenching.

3.3.1 Introduction

Studying dwarf galaxies and, in particular, understanding their star formation histories (SFHs) is crucial for our comprehension of their formation and evolution within a cosmological context. The Local Group (LG) of galaxies is the ideal region in the Universe to perform such study, given the vicinity of its dwarf galaxy population to our own Milky Way. Detailed SFHs can be obtained by means of accurately modelling colour-magnitude diagrams, along with the ability of resolving individual stars, thanks to the newly delivered Gaia DR2 data (Gaia Collaboration et al., 2018b). A large body of observational work suggests that LG dwarfs have notably diverse SFHs. Understanding such variety and their origin is at the very centre of current theoretical efforts (e.g. Weisz et al., 2014; Skillman et al., 2017).

Several mechanisms can affect the star formation of dwarf galaxies across cosmic times, amongst which we note the prominent role of reionisation, which is expected to evaporate gas from the haloes of dwarfs (e.g. Shapiro, Iliev, and Raga, 2004); the interactions with large-scale filaments of gas, i.e. the so-called 'cosmic web stripping' that is able to remove gas from dwarfs, thus preventing further star formation (e.g. Benítez-Llambay et al., 2013);

and the role of internal stellar feedback, that expels the gas via energetic outflows episodes (e.g. Benson et al., 2003). Additionally, we shall consider those processes that are specific to dwarf satellite galaxies, such as ram pressure stripping, as the satellites pass through the hot cloud of gas around their host, leading to a truncation or reduction of their star formation (Grebel, Gallagher, and Harbeck, 2003); and tidal stripping and 'stirring', as an alternative way of removing gas from dwarf galaxies and to lead to fundamental changes in their configuration (Mayer et al., 2006). All of these physical processes can be at work simultaneously in satellite galaxies of the LG to give rise to the current variety of SFHs that we observe in dwarf spheroidals (dSphs) around our Galaxy, as indicated by deep photometric observations of Galactic satellites with the Hubble Space Telescope (HST) (Weisz et al., 2014). While all dSphs contain an ancient stellar population, which in most cases is the dominant component (e.g., Sculptor, Draco, Ursa Minor), in other cases an intermediate age stellar component is also present (e.g., Carina, Fornax, Leo I). The existence of such multiple populations in dwarf galaxies such as Carina, Leo I or Fornax (Hurley-Keller, Mateo, and Nemec, 1998; Gallart et al., 1999; Monelli et al., 2003; Bono et al., 2010; del Pino et al., 2013) remains an open question.

Previous observational works have suggested that the close passage of a satellite galaxy near its host could be connected with a peak in its SFH (e.g. Sohn et al., 2007; Pasetto et al., 2011; Rocha, Peter, and Bullock, 2012): such early findings have been recently supported by the work of Rusakov et al. (2020), who finds a correspondence between the main intermediate-age and young SFH events of Fornax dSphs and its pericentric passages around the Milky Way. Moreover, it has been shown in a novel work (Ruiz-Lara et al., 2020) that the SFH of the host galaxy itself could be impacted by the pericentric passage of its satellites: three narrow episodes of enhanced star formation have been derived for the MW, whose timing coincides very well with proposed Sagittarius dwarf pericentric passage. In another study, Miyoshi and Chiba (2020) considered a time-varying gravitational potential for the MW to calculate the orbits of Galactic dSphs, guided with Gaia DR2 proper motions, and found that the infall time of a satellite coincides well with the time when the star formation rate (SFR) is peaked for the sample of classical dSphs. Some early theoretical work using simulations hinted to a link between the surface density profile of gas bound to the dwarfs and their pericentre passages. In such simulations the surface density gas profile of a dwarf steepens remarkably at each pericentre passage because of tidal compression and torques (Mayer et al., 2001). Other literature based on hydrodynamical cosmological simulations suggest that, for isolated galaxies, star formation can be reignited due to interactions with streams of gas in the intergalactic medium (Wright et al., 2019). Fillingham et al. (2019) used DM only simulations to infer quenching timescales for low-mass satellites around the MW, showing a rapid cessation of star formation following infall, and quenching timescales that are shorter for those dSphs having high orbital eccentricities. They further note that Carina and Fornax are on orbits with relatively large pericentres of 60 and 58 kpc, respectively. Simpson et al. (2018) used AURIGA simulations to show that ram pressure stripping appears to be the dominant quenching mechanism for satellites, with 50 per cent of quenched systems stopping their star formation within 1 Gyr of first infall; furthermore, they show a compression of gas within the satellite at pericentric passage, resulting in a small star burst. The analysis done by Genina et al. (2019) using hydrodynamical simulations showed that ram pressure acting on satellite dwarf galaxies that retained part of their gas after infall may compress the gas at the centre of the satellite, forming new stars. Sales, Helmi, and Battaglia (2010) used DM only simulations to study the effects of tidal forces on satellite dwarf galaxies, modelled by galaxies with two distinct populations: one centrally concentrated with lower velocity dispersion, representing the 'metal-rich' population; and a more extended, higher velocity population to represent the 'metal-poor' one. Their analysis showed that close pericentre passages and short orbital periods promote the tidal stripping of the satellite, which in turn erases the kinematical segregation between the two populations. Thus, there is mounting evidence that the orbital configuration plays a fundamental role in shaping SFHs of LG satellite galaxies.

Beside simulations, semi-analytic models (SAMs) have historically quenched satellites as soon as they infall into the main halo. There are a number of processes that affect SF in satellites, and different groups include all or only a few of such processes: common to all groups is that once a galaxy becomes a satellite it stops receiving primordial infall of gas. On

top of that, tidal and ram-pressure stripping acts on the hot gas of the satellite. Historically, SAMs implemented a very simple prescription, in which all the hot gas is removed once a halo/galaxy becomes a satellite, with only a few semi-analytic models accounting simultaneously for ram-pressure stripping of cold gas and a gradual stripping of hot gas (Stevens, Croton, and Mutch, 2016; Cora et al., 2018). More recent SAMs are starting to adopt to such prescriptions (e.g. Xie et al., 2020). Nevertheless, asides from the specifics, the implemented processes in SAMs tend to remove the fuel for star formation in satellites.

Motivated by previous observational and theoretical work, in particular by Miyoshi and Chiba (2020) and Rusakov et al. (2020), we investigated the origin of the diverse SFHs of satellite galaxies within hydrodynamical cosmological simulations of the Local Group from the Constrained Local UniversE (CLUES) project[11](Gottlöber, Hoffman, and Yepes, 2010; Libeskind et al., 2010; Carlesi et al., 2016; Sorce et al., 2016). The advantage of these constrained simulations is that they offer a unique opportunity to perform studies of LG satellites, since they reproduce faithfully the LG environment (e.g. Libeskind et al., 2011; Knebe et al., 2011a; Di Cintio et al., 2012; Benítez-Llambay et al., 2013; Ocvirk et al., 2013; Dixon et al., 2018). The aim of our work is to understand the role of environment, internal properties and orbits of the satellites, in quenching, or oppositely, enhancing their SF; and to investigate if a clear signature of the satellite's infall can be found. In order to do this we use a control sample of isolated galaxies in the CLUES simulations, that cover the same stellar mass range as our selected satellites, to highlight any difference between the evolution of these two groups.

This section is organised as follows. In Sec. 3.3.2 we present the simulation's properties. Sec. 3.3.3 contains the main results: we present the sample of satellite galaxies selected for the analysis, the isolated galaxies used for comparison, we discuss the role of infall in our results and the classification of our SFHs, and we discuss the impact of pericentric passages. Finally, in Sec. 3.3.4 we summarise our results.

3.3.2 The simulation

In order to explore the differences in star formation histories of satellite versus isolated galaxies, we use one of the constrained Local Group simulations from the CLUES project (Gottlöber, Hoffman, and Yepes, 2010; Libeskind et al., 2010; Carlesi et al., 2016; Sorce et al., 2016). The particular simulation used here is called 'Clues3_LGGas' and has already been extensively analysed in previous studies (e.g. Libeskind et al., 2010; Libeskind et al., 2011; Knebe et al., 2010; Knebe et al., 2011b; Di Cintio et al., 2011). The halo catalogues and merger trees are further publicly available[12]. While all the physical and technical information can be found in aforementioned papers and the database website, respectively, we nevertheless repeat the most important points here.

The CLUES simulations were run with the TreePM-SPH code GADGET2 (Springel, 2005), and their initial conditions were constrained such that the observed Local Volume, at scales larger than $\approx 5\ h^{-1}$Mpc, is reproduced. A zoom-in, higher resolution simulation was performed around a region of $2h^{-1}$ Mpc centred on the Local Group (LG) with 4096^3 effective particles within it. Within such region, it is possible to identify the three main galaxies formally corresponding to Milky Way (MW), Andromeda (M31) and Triangulum galaxy (M33). The simulations assume a WMAP3 cosmology (Spergel et al., 2007), i.e. $\Omega_m = 0.24$, $\Omega_b = 0.042$, $\Omega_\Lambda = 0.76$ and $h = 0.73$, a normalisation of $\sigma_8 = 0.75$, and a slope of the power spectrum of $n = 0.95$. The cosmological box of the simulation has a side length of $L_{\rm box} = 64h^{-1}$ Mpc, and the particle mass resolution is $m_{\rm DM} = 2.1 \times 10^5 h^{-1}{\rm M}_\odot$ for the dark matter particles, $m_{\rm gas} = 4.4 \times 10^4 h^{-1}{\rm M}_\odot$ for the gas particles and $m_{\rm star} = 2.2 \times 10^4 h^{-1}{\rm M}_\odot$ for the star particles. The gravitational softening length is $\epsilon = 150h^{-1}$kpc.

The feedback and star formation recipes are described in Springel and Hernquist (2003). Essentially, the interstellar medium (ISM) is modelled as a two phase medium composed of hot ambient gas and cold gas clouds in pressure equilibrium. The thermodynamic properties of the gas are computed in the presence of a uniform but evolving ultra-violet cosmic background switched on at $z = 6$ (Haardt and Madau, 1996). Cooling rates are calculated

[11] www.clues-project.org
[12] www.cosmosim.org

from a mixture of a primordial plasma composition and no metal dependent cooling is assumed. Star formation is treated stochastically, in order to reproduce the Kennicutt-Schmidt law for spiral galaxies (Schmidt, 1959; Kennicutt, 1998). The first time a gas particle undergoes star formation, a star particle of half the gas particle's mass is created, reducing the gas particle mass appropriately. The second episode of star formation results in the gas particle converting all its remaining mass into a star particle. Thus all star particles (first and second generations) have the same mass of $m_{\rm star} = 2.21 \times 10^4 h^{-1}{\rm M}_\odot$while gas particles have either their full original mass of $m_{\rm gas} = 4.42 \times 10^4 h^{-1}{\rm M}_\odot$, or half their original mass.

The *AMIGA Halo Finder* (AHF)[13] (Knollmann and Knebe, 2009; Gill, Knebe, and Gibson, 2004) has been used in combination with its bundled MergerTree code to identify and track in time all haloes and subhaloes in the simulation. The (virial) mass of each halo is defined as the mass of a sphere containing $\Delta = 94$ times the critical matter density of the Universe $\rho_{\rm crit} = 3H^2/8\pi G$ at $z = 0$, unless the density profiles rises before, which might be the case for subhaloes (for which the radius is then the upturn point). Nevertheless, we will refer to the (sub-)halo virial mass as $M_{\rm vir}$ (or $M_{\rm halo}$) and its virial radius as $R_{\rm vir}$.

3.3.3 Results and discussion

In this section we present the main results of our analysis. First we describe the sample selection. Next we classify the satellite sample according to their SFHs after their infall. Finally, we conclude with an in-depth discussion of the enhanced SFHs in our sample.

Satellite galaxies

We select satellites belonging to either one of the three main galaxies within the simulated LG, namely the Milky Way, Andromeda or the Triangulum galaxy. All the satellite used here are chosen in order to be more massive than $M_{\rm vir} = 10^9{\rm M}_\odot$ at their (first) infall time, defined here as the time at which a satellite entered its host halo for the first time. They are further required to contain at least 100 star particles at redshift $z = 0$: this selection criterion provides a sample of 23 objects in total. The star formation histories of satellite galaxies are inferred from the age histogram of their bound stars at $z = 0$.

In Fig. 3.14 we show the star formation history (normalised by their maximum star formation rate) of all the 23 satellites in our sample, together with their stellar, gas and halo mass at z=0, satellite's ID (unique identifier from the halo finder catalogue[14]), and the corresponding maximum star formation rate used for the normalisation of each panel. The first 12 objects are satellites of M31, the following seven are satellites of the MW and the last four are satellites of M33. The vertical dashed red line in each panel indicates the time of first infall of each of these objects into their respective host. Some of the satellites may have "backsplashed" (Gill, Knebe, and Gibson, 2005), and in that case the first infall is considered as the relevant one. Fig. 3.14 shows the large variety of SFHs of our simulated satellites, similar to what is observed in the Local Group. As found in observations (Dolphin et al., 2005), we notice that higher stellar mass galaxies show extended star formation histories, while less massive systems formed most of their stars in the first $2-3$ Gyrs. A sign of the combined effect of reionisation and infall quenching was found in Rocha, Peter, and Bullock (2012): while classical dwarfs appear to be suppressed after infall, the ultrafaint dwarfs tend to be suppressed for the most part – even long before infall. This feature is also found in our simulations: the satellites with the least stellar mass only form stars in the first few Gyrs of their evolution and by the time of their first infall SF was already suppressed (see for example ID= 1055 or ID= 310), while more luminous satellites which are suppressed show a sign of infall quenching.

Fig. 3.14 already shows the main conclusion of this study: *galaxies not necessarily shutdown star formation once becoming a satellite galaxy*. We will investigate and quantify this in more detail in the following sections.

[13] http://popia.ft.uam.es/AHF

[14] In order to obtain the *ahfId* used in the www.cosmosim.org database we add 'snapnum' $\times 10^6$ to the ID given here, with snapnum = 496, as this corresponds to redshift $z = 0$.

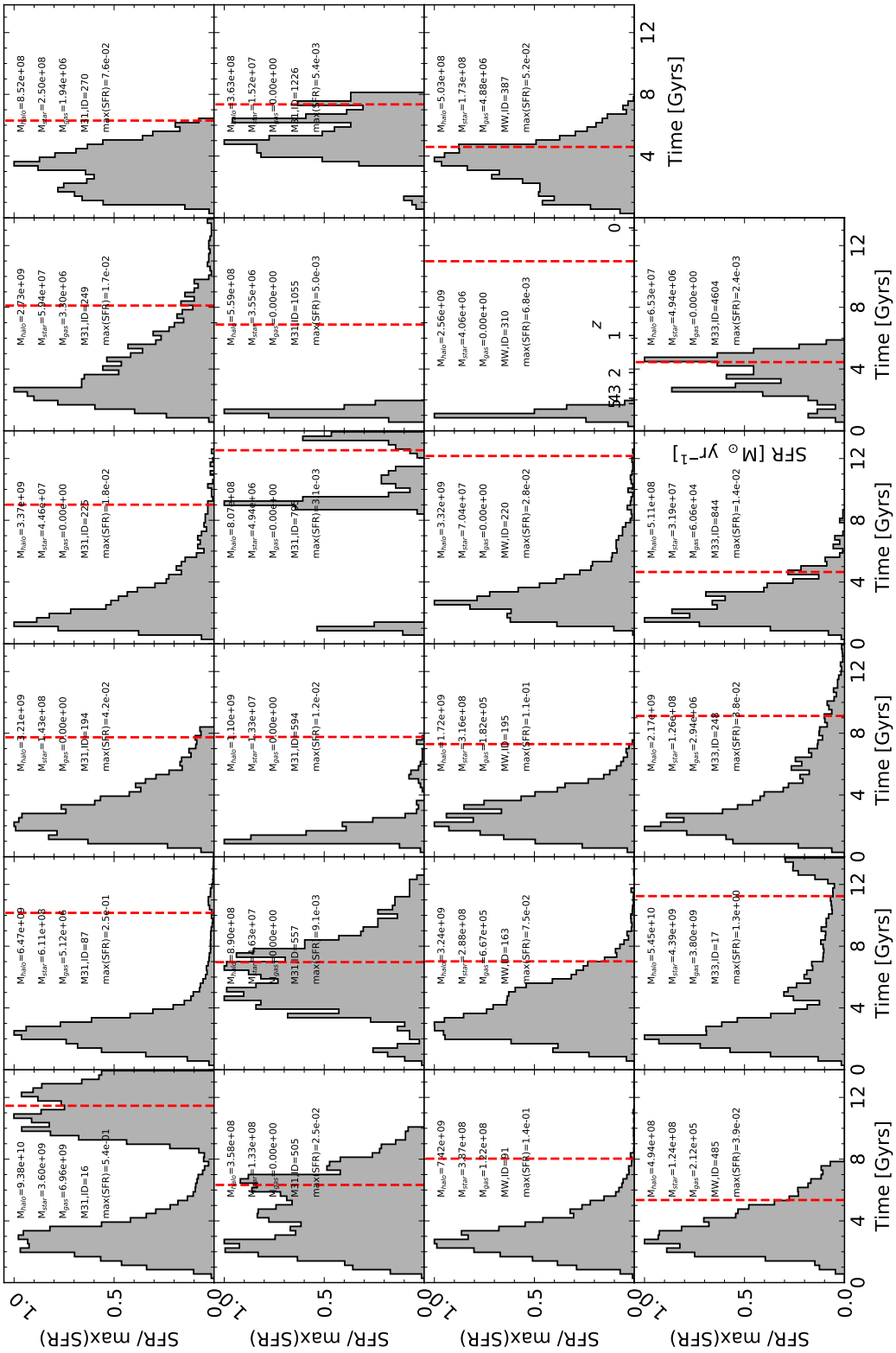

FIGURE 3.14: The (normalised) star formation histories of our mass-selected satellite galaxies of M31, MW and M33. The (first) infall time is indicated as a red dashed line. The total mass of the halo, gas and stars are shown for each satellite at $z = 0$ (measured in $M_{\odot}$), together with the satellites' IDs and the corresponding maximum star formation rate (measured in $M_{\odot}/yr$).

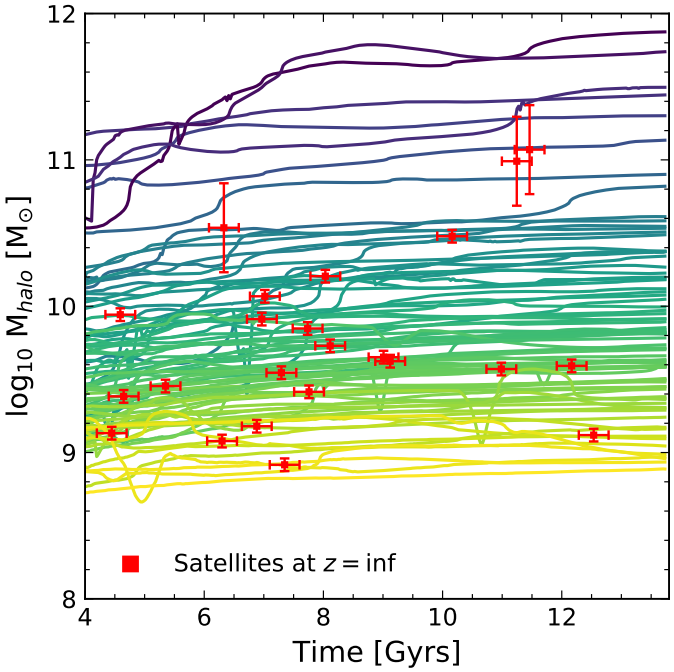

FIGURE 3.15: The mass accretion history of our isolated galaxies. The halo mass of each satellite galaxy at infall is indicated as a red square. The colour code scheme corresponds to progressively more massive galaxies as we move from yellow to dark blue. We associated isolated galaxy to each satellite by matching their infall masses, allowing a ± 10 per cent variation in infall mass and within a 250 Myrs time interval. For the three most massive satellites we connect them to the three closest isolated galaxies by extending the allowed range to that indicated by the red bars.

Comparison to isolated galaxies

We proceed to derive the star formation histories of isolated galaxies within the simulated Local Group volume, i.e. haloes containing at least 100 stellar particles and $M_{\rm vir} > 3 \times 10^8 {\rm M}_\odot$ at redshift $z = 0$. This is a comparable mass-selection criterion as used for the satellite galaxies (taking into account that satellites will have lost mass since infall) and it provides us with a sample of 83 objects. The question that we would like to address now is *what is the SFH that a satellite would have had if it had evolved in isolation, rather than infalling into its host?* In order to faithfully compare the star formation history of satellite and isolated galaxies, we have to define a way to assign the latter to the former. Associating satellites and central galaxies based upon their mass at $z = 0$ is not a good criterion, as it is well known that satellites undergo substantial mass loss due to tidal stripping (e.g. Muldrew, Pearce, and Power, 2011; van den Bosch and Ogiya, 2018). For similar reasons, using the stellar mass at $z = 0$ is not an option, as the final stellar mass in satellite galaxies will be the result of the complex interplay between start formation and infall, which is exactly the target of our study.

A more reasonable and consistent approach is to assign isolated galaxies to satellites based upon the satellites' masses at the redshift of infall. In Fig. 3.15 we show as solid lines the evolution of the halo mass as a function of time for all the isolated galaxies of our sample, with the colour code scheme corresponding to progressively more massive galaxies as we move from yellow to dark blue. Superimposed in the same figure are the halo masses for the 23 satellite galaxies at infall time, each of them indicated as a red box. For a given satellite galaxy we now compare those isolated galaxies to it that have their MAH pass through the satellite's infall mass box, allowing for a ± 10 per cent variation in infall mass and using a 250 Myrs wide time interval: the error bars around each satellite's infall mass are indicative of this range. For satellites with halo infall mass between 10^9 and $10^{10} {\rm M}_\odot$, this association results in as many as 13 isolated galaxies assigned to each satellite. The three most massive

satellites, however, would only have one isolated galaxy passing through their infall mass box, and in this case we extend the mass range (indicated as red bars in Fig. 3.15) such that at least three isolated galaxies are assigned to each of these satellites.

Once this assignment has been made, we now derive the average star formation history of each group of associated isolated galaxies, i.e. calculating the bin-wise mean values from the SFH of each object in the corresponding group of isolated galaxies. We show this in Fig. 3.16, where each box shows the average over the $N_{\rm iso}$ isolated galaxies associated to that satellite galaxy found in the corresponding box of Fig. 3.14. In Benítez-Llambay et al. (2014) the authors show that the main quantities that determine the SFH of isolated galaxies are the halo mass of each galaxy at reionisation time and their subsequent mass accretion history. The combination of these factors leads to different stellar formation times that can be summarised as continuous, old, and old plus young SFHs. Galaxies that are already massive at redshift $z = 6$ are sufficiently large to retain their gas during reionisation and continue to form stars, showing a SFH declining with time as more gas in consumed. On the contrary, galaxies with $M_{\rm halo} < 10^{8.5}{\rm M}_{\odot}$at reionisation have all their gas photo-evaporated and can only form stars before $z = 6$, ending up with a single, old stellar populations. These features are clearly visible in Fig. 3.16.

Quantifying the role of infall

To explore what is the role of infall in shaping the SFH of satellite galaxies, we now compute for each satellite the fraction of stars formed before and after infall, $f_{\rm before}$ and $f_{\rm after}$, normalising these fractions to the respective time interval $\triangle T_{\rm before} = T_{\rm infall}$ and $\triangle T_{\rm after} = T_{z=0} - T_{\rm infall}$. The quantity that we are interested in is:

$$\bar{f}_j = \frac{f_j}{\triangle T_j \times 2 \times \bar{f}} \tag{3.2}$$

where the subscript j stands for either *before* or *after* infall, and

$$\bar{f} = \left(\frac{f_{\rm before}}{\triangle T_{\rm before}} + \frac{f_{\rm after}}{\triangle T_{\rm after}} \right) / 2 \,, \tag{3.3}$$

such that $\bar{f}_{\rm before} + \bar{f}_{\rm after} = 1$. This procedure is similar to the one presented in Benítez-Llambay et al. (2014).

Calculating these fractions for all our galaxies from their bound stars at z=0, i.e. using Eq. (3.2) for each satellite galaxy and by calculating the mean of fractions for their associated isolated galaxies, we can finally proceed to compare the SFHs of isolated vs. satellite galaxies. This sheds light into our question raised earlier: what fraction of stars $\bar{f}_{\rm before}$ and $\bar{f}_{\rm after}$ would have formed if the satellite had evolved in isolation?

Suppressed vs enhanced star formation histories

In every panel of Fig. 3.17 we show, for each satellite, the ratio between the fraction of stars formed before and after its first infall, divided by the same fraction for the corresponding isolated galaxies. In the top-left panel, we show such ratio as a function of $z = 0$ stellar mass, in the top-right panel as a function of infall time, in the bottom-left panel as a function of the infall virial mass and finally in the bottom-right panel as a function of the gas fraction at infall. The ratios $\bar{f}_{\rm before,SAT_i} / \bar{f}_{\rm before,ISO}$ between the fraction of stars formed before infall in each satellites and corresponding isolated are shown as black diamonds. The ratios $\bar{f}_{\rm after,SAT_i} / \bar{f}_{\rm after,ISO}$ between the fraction of stars formed after infall in satellites versus isolated are instead shown as circles.

A value of such ratios equal to one means that the satellite has formed stars just like an isolated galaxy, within the corresponding time interval. It is immediate to note that every satellite forms stars at the same rate as their average isolated counterpart before infall, since the ratio $\bar{f}_{\rm before,SAT_i} / \bar{f}_{\rm before,ISO}$ (black diamonds) is about one for all of them. This is expected, and it is a confirmation of the fact that – before infall – there are no qualitative differences between satellite galaxies and isolated ones, in terms of their SFHs. The situation is different when looking at the fraction of stars formed after infall. Satellites that form less

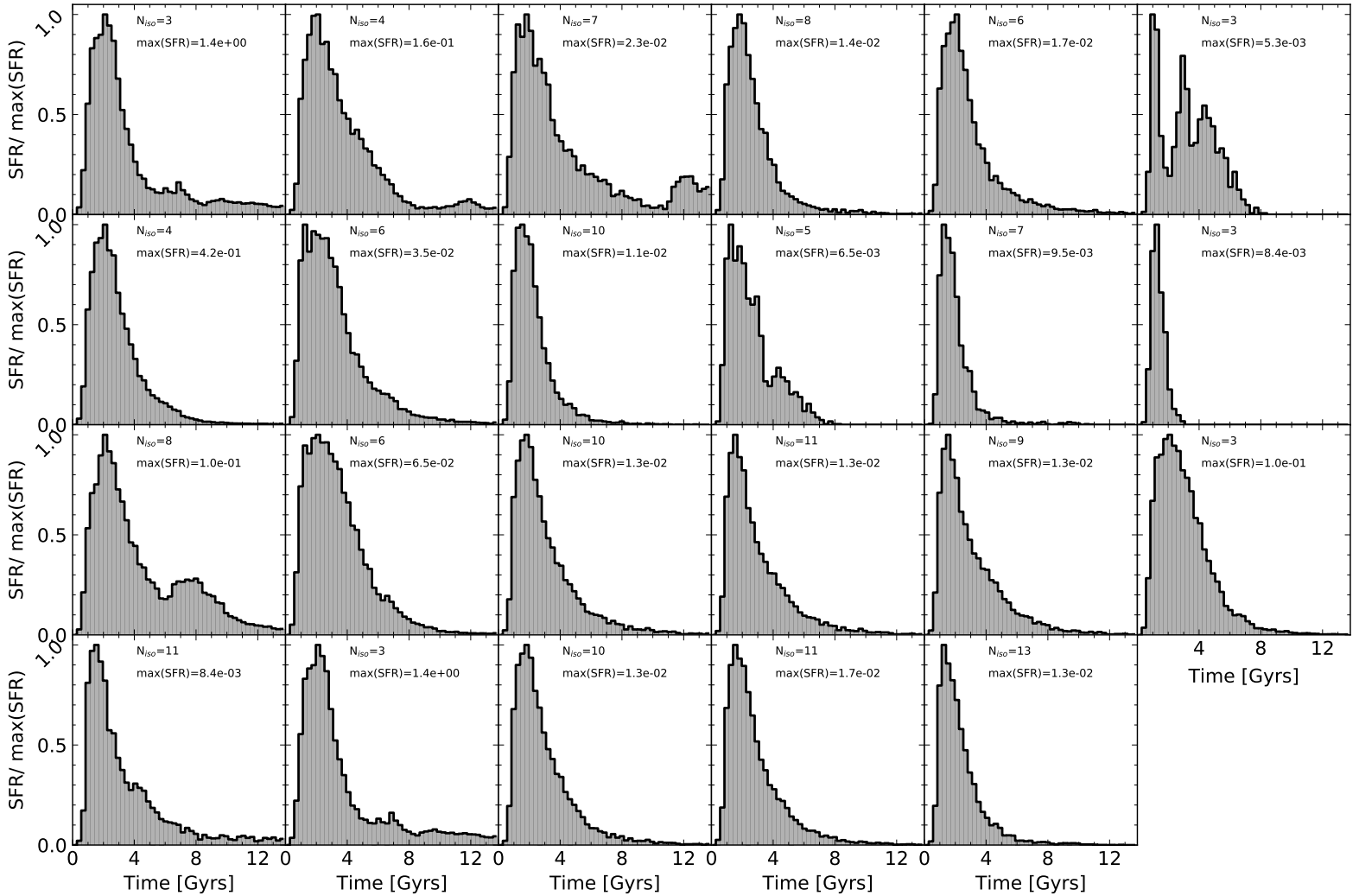

FIGURE 3.16: The mean star formation history of isolated galaxies whose mass accretion history matches the mass at infall of the corresponding satellite. Each box shows the average over the $N_{\rm iso}$ isolated galaxies associated to that satellite galaxy found in the corresponding box of Fig. 3.14.

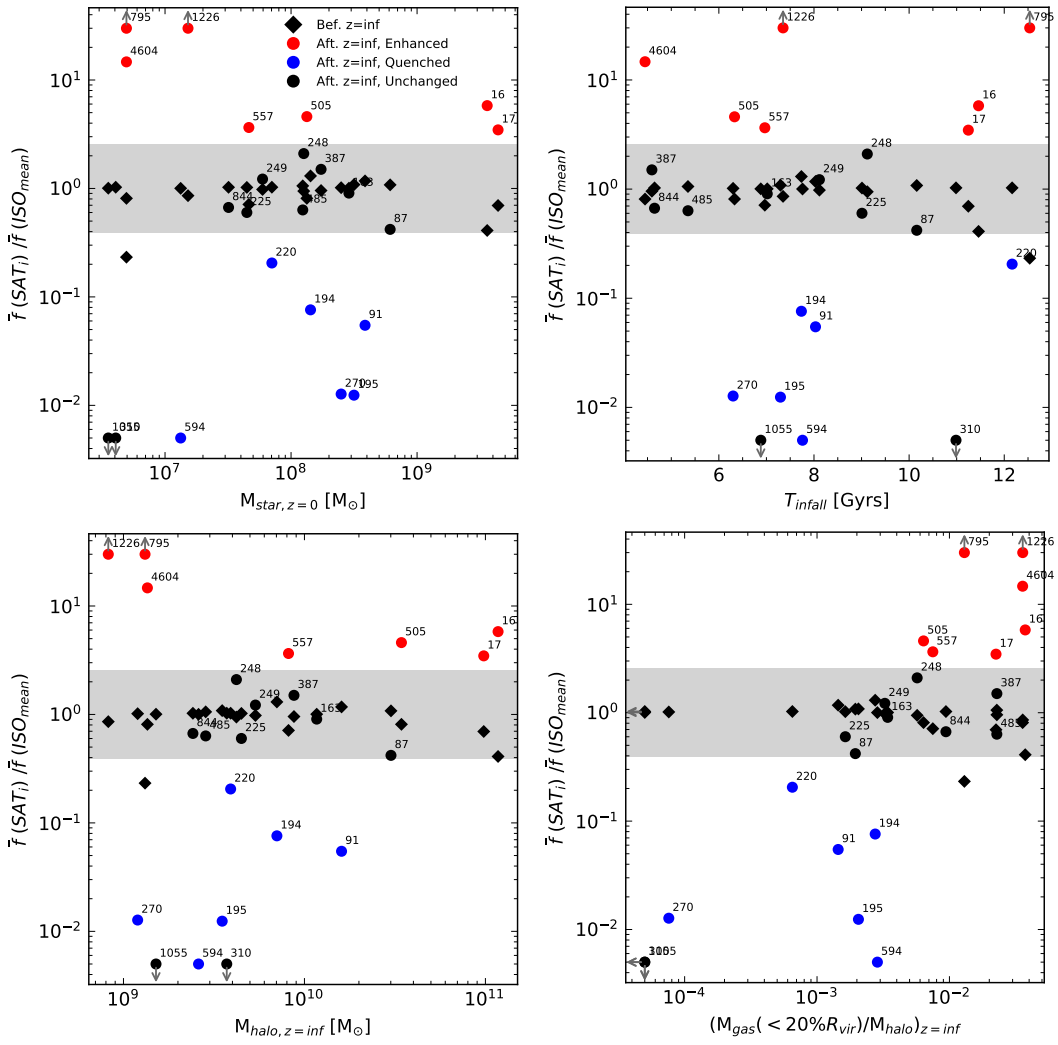

FIGURE 3.17: The normalised fraction of stars formed before ($\bar{f}_{\rm before}$, diamonds) and after infall ($\bar{f}_{\rm after}$, circles) for each satellite, divided by the same number for the average isolated galaxy group corresponding to each satellite. Top-left panel: as a function of z=0 stellar mass, top-right panel: as a function of infall time, bottom-left panel: as a function of infall virial mass, and bottom-right panel: as a function of gas fraction at infall. Satellites which have their star formation enhanced after infall are indicated as red circles, satellites whose star formation is instead suppressed are indicated as blue circles. Satellites whose SF has not changed after infall, compared to the isolated group, are indicated as black circles. Black diamonds refer to the stars formed before infall. Satellite's IDs are shown for comparison with Fig. 3.14. For visualisation purposes, satellites with properties that are either zero or too great are indicated with grey arrows pointing towards such values.

stars than their isolated counterparts have $\bar{f}_{\rm after,SAT_i}/\bar{f}_{\rm after,ISO} < 1$, and are indicated as blue circles; for them, the infall had the effect of suppressing star formation. On the other side, satellites that form more stars than their isolated equivalents have $\bar{f}_{\rm after,SAT_i}/\bar{f}_{\rm after,ISO} > 1$, and are indicated as red circles; for them, the infall had instead the effect of enhancing star formation. We define a fiducial region between $\bar{f}_{\rm SAT_i}/\bar{f}_{\rm ISO} \in \pm 0.4$ dex: satellites that lie within this interval are indicated as black circles as they behave very similarly to their isolated counterpart; we shall call them 'unchanged', referring to the fact that the infall did not have any effect on their SFH. We also consider 'unchanged' those satellites whose ratio $\bar{f}_{\rm after,SAT_i}/\bar{f}_{\rm after,ISO} = 0$ (again indicated as black circles), simply because their SFH had already finished before infall. Note that, for visualisation purposes, satellites with properties (e.g. ratio of fraction of formed stars, stellar mass, gas mass, etc.) that are either zero or too great too show in the plot are identified using grey arrows that point towards such values.

In Fig. 3.17 we observe that 7 out of 23 satellites are found to have their SFH enhanced after infall, about 1/3 of the total sample. This is a surprising result, as usually galaxy formation models shutdown SF in satellites after infall. The figure further indicates that there is no apparent correlation between the enhancement (or the suppression) in SFHs of satellites and the stellar mass at $z = 0$, infall time, or the virial mass at infall, although for increasing stellar masses the fraction of suppressed satellites diminishes, such that in the range $10^9 < M_{\rm star}/{\rm M}_\odot < 10^{10}$ none of the satellites are suppressed, similarly to what has been reported in Slater and Bell (2014)[15]. However, the bottom-right panel of Fig. 3.17 indicates a correlation between the fraction of gas at infall (defined as the gas within 20 per cent of the virial radius of the satellite divided by the satellite's virial mass, both quantities calculated at infall) and the enhancement in star formation. We verified that all the gas particles found within the 20 per cent of the satellites' radius at infall are either in a cold or star forming phase with temperatures of T$< 10^5$K and densities n$> 0.12{\rm cm}^{-3}$.

To investigate possible mechanisms that drive a different evolution in the satellite's SFH after infall, we show in the top row of Fig. 3.18 the amount of gas at infall for each satellite within 20 per cent (left panel) and 100 per cent (right panel) of its radius, as a function of infall time. The bottom row shows instead the infall gas mass within 20 per cent (left panel) and 100 per cent (right panel) of its radius, relative to the total virial mass of the halo at infall, as a function of infall time. Satellites are again colour-coded in red, if their SFH is enhanced after infall; and blue, if their SFH is suppressed. Satellites that did not experience a substantial change in their SFH after their infall are represented in black. It is evident that the SF enhanced satellites are objects infalling with a higher fraction of gas. When considering gas within the virial radius, several satellites belonging to the SF suppressed group have the same amount of gas as satellites within the SF enhanced group, reflecting the fact that both cold, star forming as well as hot, diffused gas is found within the virial radius of each galaxy. On the other side, in the satellite's inner region (20 per cent of the virial radius) only cold star forming gas is found, and the separation between the two groups in more clear. None of the satellites with less than $10^7{\rm M}_\odot$ in gas within their central region is able to form new stars after infall: they will start loosing gas after infall, with a consequent suppression in their star formation.

In terms of gas fractions we observe a similar result: only satellites with at least $\sim 0.5-1$ per cent of their virial mass in gas within their central region can potentially experience an enhancement of their SF after infall. Note that, however, in addition to the enhanced satellites, we identify objects with sufficient amounts of cold gas which nevertheless remained unchanged after their infall, e.g. ID$=$ 387, 485, 844. In light of these results, the question that we now seek to answer is *why some satellites do not have an enhanced star formation after their infall, despite their high cold gas fractions?*

Impact of pericentric passages

We have shown that satellites with enhanced SF are galaxies that infell with high fractions of bound gas (where at least $\sim 0.5-1$ per cent of their virial mass is gas). Yet the SF of some satellites with comparable amounts of cold gas remained unchanged.

In Fig. 3.19 we study the orbits and SFH of three SF-enhanced satellites (top panel, from left to right: ID$=$ 16, 17, 795) and two SF-unchanged objects (bottom panel, from left to right:

[15]Note however that such trend is less strong than what reported by the authors

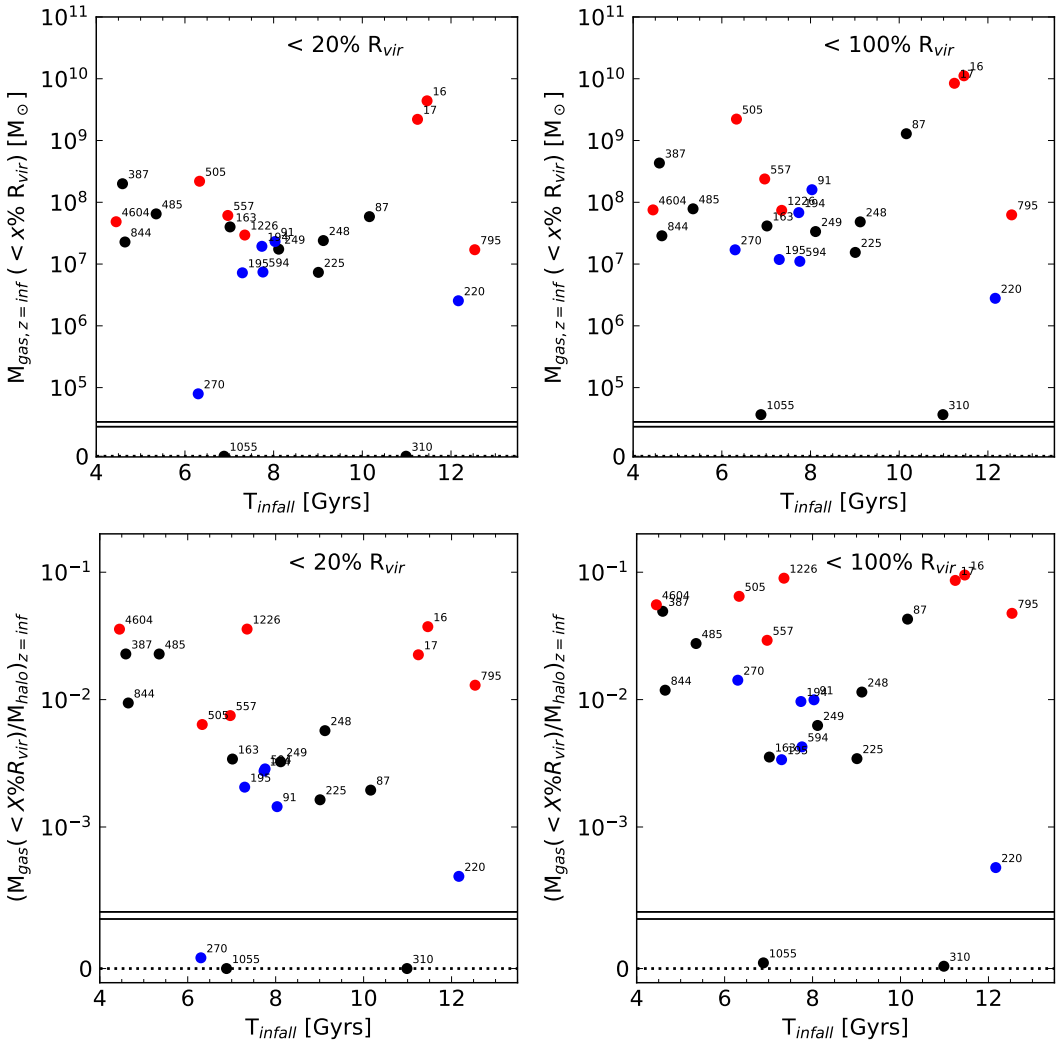

FIGURE 3.18: Top left panel (right panel): The total amount of gas at infall within 20 per cent (100 per cent) of the virial radius of each satellite, versus infall time. Bottom left panel (right panel): The total amount of gas at infall within 20 per cent (100 per cent) of the virial radius of each satellite, normalised by the virial mass of the halo, as a function of infall time. The colour code is the same as in Fig. 3.17: red = SF enhanced satellites, blue = SF suppressed, black = SF unchanged.

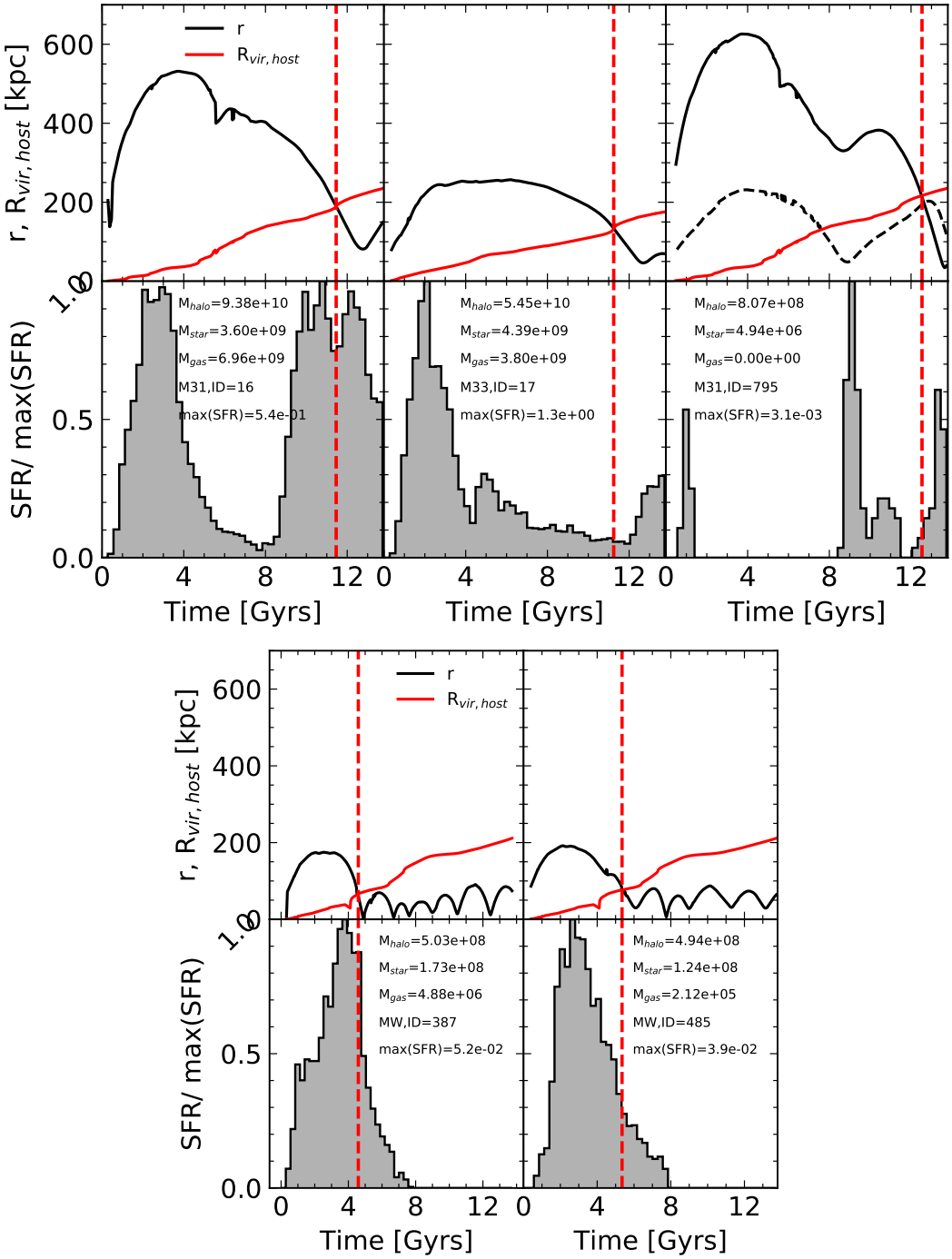

FIGURE 3.19: Examples of SF enhanced objects (top 3 panels) and SF suppressed satellites (bottom 2 panels). From left to right, satellite ID= 16, 17 and 795, in which star formation has been enhanced by the interaction between satellite-host or satellite-satellite. Last two panels, satellite ID= 387 and 485, in which start formation has been abruptly stopped due to the severe gas loss provoked by the close pericentric approaches of these satellites. For each satellite we plot, as a function of time and from top to bottom, its orbit with respect to the main galaxy (for satellite = 795 we also show the orbit with respect to subhalo= 16 as dashed line), along with the virial radius of its respective hosts (red line), and its star formation history. The red vertical dashed line shows the infall time of each satellite.

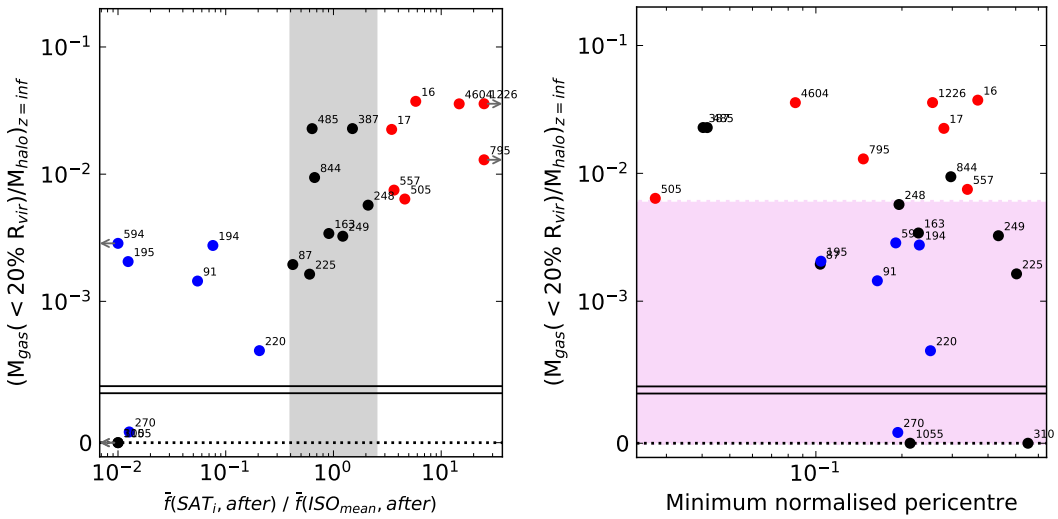

FIGURE 3.20: Left panel: Infall bound gas mass relative to the satellite's total mass as a function of the normalised fraction of stars formed after infall, divided by the same number for the corresponding average group of isolated galaxies. Right panel: as a function of minimum pericentre passage normalised by the host's virial radius at the time. To represent the normalised pericentre values which disrupt the bound gas of the satellite and the fractions of bound gas which are not sufficient to continue forming stars after the infall of a satellite we use two (arbitrarily chosen) regions, the light orange and the light violet regions, respectively. The colour code is the same as in Fig. 3.17: red = SF enhanced satellites, blue = SF suppressed, black = SF unchanged.

ID = 387, 485). For each satellite we show as a function of time and from top to bottom, its orbit with respect to its main galaxy (black lines), the virial radius of its respective host (red lines), and its star formation history. Additionally, for satellite = 795 we show its orbit with respect to a subhalo (ID= 16) as a dashed line. Their infall time is marked with a red vertical dashed line.

The orbits of the satellites presented in Fig. 3.19 show that unchanged satellites followed orbits closer to their main galaxy after their infall than enhanced satellites: whereas the minimum pericentre for the enhanced satellites is close to $\sim 30-100$ kpc ($\sim 15-30$ per cent of the host's virial radius at the time), for the unchanged satellites is $\sim 3-6$ kpc ($\sim 3-4$ per cent). Although these satellites have high amounts of bound gas at their infall, (multiple) close pericentric passages are able to disrupt their bound gas and suppress their star formation. On the other hand, the SFH of the enhanced satellites shows that a star formation burst occurred around their pericentre, suggesting that a similar mechanism might be responsible for the star formation bursts in the enhanced satellites: the tidal shocks experienced by the bound gas in infalling satellites during their pericentre passages are able to promote star formation by heating the clumped gas at the centre of the satellites. For satellite ID= 795, the close encounter with its main galaxy is additionally supported by a pericentric passage with a subhalo (ID= 16). We remark that the SFHs of the satellites are obtained from the age histogram of their bound stars at $z = 0$, i.e. the origin of the bound stars is not taken into consideration. Thus, we verified that the origin of the bound stars at $z = 0$ and the mass accretion histories of each satellite are compatible with in-situ star formation, i.e. stars that formed in the progenitors of the satellites, as opposed to stars captured in progenitors from merger events.

To further investigate the role of pericentre passages in the SF of infalling satellites with high ratios of cold gas we show in Fig. 3.20 the infall cold gas mass fraction as a function of the normalised fraction of stars formed after infall, divided by the same number for the corresponding average group of isolated galaxies (left panel); and as a function of the minimum pericentre normalised by the host's virial radius at the time, i.e. $\min r_{\rm peri}/R_{\rm vir}(z = \min$

$r_{\rm peri}$) (right panel), following the same colour code as in Fig. 3.17. The left panel confirms the general correlation we found so far: the more bound (cold) gas a satellite retains at their infall time, the more likely it is that its star formation is enhanced after its infall. As anticipated in the previous section, this is not an absolute relation, since for a number of satellites with comparable bound gas fractions (e.g. ID= 485, 387), their star formation remained unchanged after their infall. In the right panel we identify these unchanged satellites as objects with close pericentric approaches to their main galaxies, i.e. within 5 per cent of their host's radius. Comparing the fractions of cold gas with the minimum normalised pericentre and the SF classification of the satellites we can validate the mechanism inferred from Fig. 3.19: infalling satellites with high amounts of (cold) bound gas (e.g. $\gtrapprox 7 \times 10^{-3}$) are able to form stars after their infall if their pericentre passage is not too close to their main galaxy (e.g. $\gtrapprox 5$ per cent of the host's virial radius). Such satellites undergo star formation bursts which correlate with the pericentric encounters with their corresponding main galaxy. Satellites with closer pericentric distances to their main galaxy experience strong tidal interactions which are able to disrupt the bound gas in the satellite and suppress further star formation. We represent these two conditions by two (arbitrarily chosen) regions. The light orange region marks the < 5 per cent minimum normalised pericentre values, and the light violet region the $< 7 \times 10^{-3}$ gas fractions at infall values.

Note that there are two satellites that deviate from the picture described here: satellite ID $= 505$, which has the closest minimum pericentric approach of all the satellites yet it is classified as an enhanced satellite; and ID $= 844$, which, despite having enough bound gas and a typical minimum pericentric distance, its SF remained unchanged. The evolution of satellite 505 shows that, during its infall, the object has experienced tidal stripping which removed, among dark matter and gas, a considerable amount of old stars (stellar age > 10 Gyrs) residing in the halo component of the object. Since we classify the SF of satellites after their infall by their stellar fraction ratios (i.e. using Eq. (3.2) and their bound stars at $z = 0$), they would inevitably be affected by such processes. In particular, for satellite 505 this leads to a higher than expected ratio, since the average stellar fraction term $\bar{f}$ (i.e. Eq. (3.2), and more precisely, its term $f_{\rm before}$) is lower for a halo stripped of part of its old stars than for a halo with a higher amount of old stars, which produces a higher $\bar{f}_{\rm after}$. For satellite 844, we identified two aspects that contribute to its unchanged star formation after infall. The first one is its virial mass. At $z = 0$, satellite 844 has a total mass of $5.11 \times 10^8 {\rm M}_\odot$. Being in the lower end of the mass distribution of satellites, the high amount of bound gas at infall that the satellite acquired during its evolution is completely lost after ~ 4 Gyrs since its infall at 4.6 Gyrs. The second aspect is its orbital history. Following its evolution we find that its orbit with respect to the main galaxy shows a series of sudden bumps past $t \sim 11$ Gyrs, which can be attributed to temporary misidentifications from the (spherical overdensity) `AHF` halo finder. Such misidentifications are likely to occur whenever close density peaks must be individually classified, e.g. during mergers events or close encounters with other haloes (e.g. Behroozi et al., 2015). We verified the trajectory of the progenitors of the satellite and the distances to other close haloes and found that, indeed, a series of close encounters with other objects around $\sim 11 - 12$ Gyrs disrupted the halo and prevented the subsequent accretion of gas. As the satellite was already stripped of all its gas by the time it underwent the close encounters (i.e. by $t \sim 9$ Gyrs there was no gas left in the satellite), there was not enough time for the satellite to acquire gas and form stars.

To finalise this section we remark that so far we have analysed the effect of pericentric passages on the SF of infalling satellites, without taking into account possible effects on the main galaxies. In Fig. 3.21 we present the SFHs of the three main galaxies of the sample, i.e. M31, MW, and M33, together with the orbits of their corresponding satellites with respect to them (black solid lines). The evolution of the virial radius of the host halo of each central galaxy is represented by the red solid line. For each panel we mark the minimum pericentre of each satellite with a red vertical dashed line. Surprisingly, similar to the results presented in Ruiz-Lara et al. (2020), we identify a correlation between the minimum pericentres of the satellites and the SFH peaks of each main galaxy: for M31, at around ~ 8 Gyrs and ~ 12 Gyrs; for MW, at ~ 8 Gyrs; and for M33, at ~ 5 Gyrs and ~ 12 Gyrs. Consequently, we infer that satellites are able to induce star formation bursts in their central galaxy in the same way main galaxies are able to tidally-shock the bound gas in the centre of their satellites to trigger star formation events.

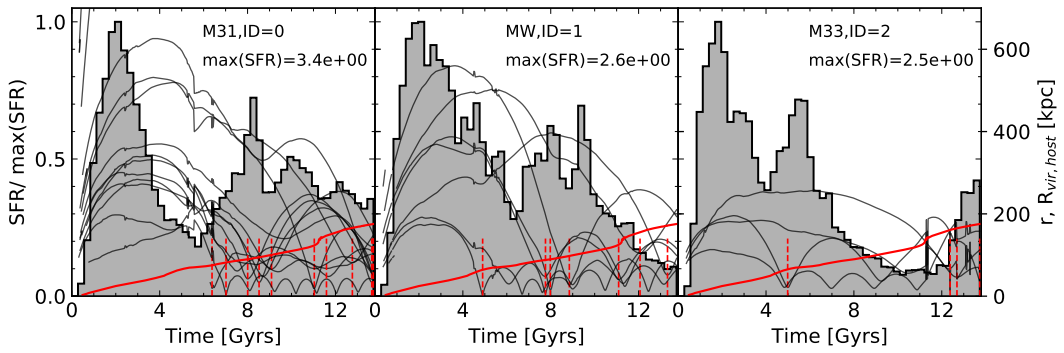

FIGURE 3.21: Normalised star formation histories of the three main galaxies in the simulation, along with the orbits of their satellites (black lines) as a function of time. The evolution of the virial radius of the host halo of each main galaxy is represented by the red line. We use red vertical dashed lines to mark the time at which each satellite achieve their minimum pericentre during their orbit.

Overall, we can conclude that the relatively simple mechanism presented here is able to illustrate why some satellites are capable of forming stars after their infall while others are unable to. Nevertheless, some further analysis is required in order to solidify our results. As of the writing of this Section, we are working on an in-depth analysis of the orbital motions of the satellites, characterising their trajectories in terms of parameters such as their eccentricity, or their tangential and radial velocities; and on comparisons with the peculiar motion data of galaxies from the GAIA project (Fritz et al., 2018). Additionally, we aim to analyse the evolution of the mix of unchanged and quenched satellites in the region below the enhanced satellites, i.e. $(M_{gas}(< 20\%R_{vir})/M_{halo})_{z=inf} < 7 \times 10^{-3}$, in order to find a better gas fraction threshold and to determine the origin of such mix. Finally, we intend to quantify the effect of the aforementioned processes, i.e. mergers and close encounters, that led to deviations from the gas fraction at infall—minimum normalised pericentre assignment, in order to obtain confidence levels for the SF classification of our satellites.

3.3.4 Conclusions

We used cosmological simulations of the Local Group of galaxies from the CLUES project to study the differences in the star formation history (SFH) of the satellite galaxies of the three most massive centrals, namely Milky Way, Andromeda and Triangulum galaxy. Motivated by previous work, such as Miyoshi and Chiba (2020) and Rusakov et al. (2020), we investigate the physical effects that lead to such differences and search for signatures of infall. The variety of star formation histories in satellite galaxies is due to the complex interplay between the satellite's evolution before its infall into the main galaxy and the after infall evolution. Before infall, and in analogy to the isolated galaxy case, the main ingredients that shape the SFH of a satellite are its halo mass at reionisation epoch and its subsequent mass accretion history. As discusses in detailed in Benítez-Llambay et al. (2014), a combination of these effects can lead to well defined typologies of SFHs in isolated galaxies: a continuous SFH, an old ($< 2-3$ Gyrs) stellar populations and an old plus young SFH. After infall, the SFH of satellites becomes more complex. Here we summarise the main results:

- The SFH of satellites after infall is essentially determined by two factors: the amount of cold (bound) gas that a satellite has at infall time and the type of orbit with which it enters within the host. We found that the $\sim$ 70 per cent of the satellites in our sample suffer from a quenching in SF, while as much as the $\sim$ 30 have their SF enhanced after infall. To determine whether SF has been suppressed or enhanced after infall, we assign each satellite galaxy to the corresponding isolated galaxy group according to their mass accretion history and compare the SFH of satellites after infall with the SFH that they would have had if they would have kept evolving in isolation.

- We found, in agreement with previous studies (e.g. Rocha, Peter, and Bullock, 2012), that the least luminous satellites stop forming stars well before infall and in this case the infall does not play any role in shaping their SFH. More massive galaxies can instead have their SF suppressed by the close pericentric passage near by the host, which captures all the gas.

- A necessary, but not sufficient, condition to have enhancement of SF after infall is that the satellite enters the host's virial radius with a large amount of gas. Those satellites that enter the virial radius of their host with small amount of gas have all their gas stripped during infall. None of the satellites that infall with $M_{\rm gas} < 7 \times 10^{-3} M_{\rm halo}$ within the inner region (20 per cent of the $R_{\rm vir}$) will form stars after infall.

- We found some interesting features amongst the SF enhanced group: whenever a new, strong peak is generated, it is clearly correlated with the pericentric passage of the satellite within the central galaxy, which is nevertheless not too extreme. Perhaps more important than the quantity of gas at infall is the type of orbit that a satellite follows after infall: for orbits in which their minimum pericentric approach is $r_{\rm peri} < 0.05 R_{\rm vir,host}$, tidal interactions are strong enough to disrupt the bound gas of satellite, regardless of their gas fraction at infall.

- The pericentric passages of infalling satellites likewise correlate with the peaks of SF in their main galaxy, suggesting that the same mechanism that is able to induce SF in satellites at their pericentres affects the SF of central galaxies too, in agreement with Ruiz-Lara et al. (2020).

The results presented in this Section show that the SF of infalling satellites depends on the amount of (bound) gas per halo mass at infall and how close their pericentric passage with respect to their central galaxy. A satellite with high amounts of gas with a close pericentre is stripped of its gas by the tidal interactions with its central galaxy, otherwise the satellite is able to keep forming stars after its infall via star formation burst which correlate with pericentric passages for both satellites and central galaxies. Nevertheless, a more detailed analysis is required in order to properly characterise the SF of the satellites according to their normalised stellar fractions, so that the classification takes into account processes during their infall that deviate from this model, e.g. tidal stripping of the old stellar component in haloes or close encounters with other haloes for low mass satellites.

Our satellites resemble galaxies with large pericentres and SF peaks such as Carina and Fornax (I) (e.g. Fritz et al., 2018; Fillingham et al., 2019, with pericentres of 60 and 58 kpc, respectively). The fact that we observe that small pericentres lead to removal of gas and thus, suppression in SF, is compatible with the analysis done in Miyoshi and Chiba (2020), who found a remarkable correlation between a smaller pericentric radius and a reduction of star formation after its peak.

For future work we aim to characterise the orbits of the satellites in the simulation. Obtaining orbital parameters, such as eccentricity of radial and tangential velocities, would allow us to compare our sample with the proper motion data from the GAIA project (Fritz et al., 2018). Additionally, we are in the process of obtaining new simulations which include black hole feedback, known to regulate the star formation of the host halo. The addition of such simulations to our analysis would greatly improve the robustness of our results, allowing us to determine the role of the feedback (if any) in tidally-induced star formation events.

4 Conclusions and future prospects

4.1 Conclusions

A complete theory of cosmology needs to be matched by an accurate model of galaxy formation. To build such model we use numerical simulations that aim to, first, reproduce the distribution and properties of the galaxies observed in our Universe, and second, predict features that could potentially be searched for in future observational analysis. Considering that they are the only method that allows us to experiment with our Universe's initial conditions and evolution, great effort is put into building simulations that are able to reproduce and predict observational constrains.

As the quality of the observational data improves, so do the numerical models. However, the sheer amount of complex galactic interactions inferred from observations accentuates the degeneracy in our models: different recipes for galaxy formation are able to produce similar results (e.g. Fig. 10 in Sembolini et al., 2016b), which further feeds the feedback loop between observational constrains and numerical results.

This Thesis follows the same goals: we aim to understand aspects of galaxy formation throughout simulations. For this reason, we used hydrodynamical simulations to study the complex interactions that shaped galaxies during their evolution. The analysis was done using two complementary approaches: we used simulations of clusters of galaxies to obtain statistical results about the evolution of cluster galaxies and infalling objects into their environment (Ch. 2), and constrained simulations to understand observed properties of galaxies in our local Universe and provide potential observational properties which could confirm our models (Ch. 3).

In this section we summarise the main results of the Thesis, and we discuss the implications of the work presented here. In the following section, we provide future projects that can further expand the results presented here.

4.1.1 Clusters of galaxies

We used the THE THREE HUNDRED dataset to study how cluster environments affect infalling galaxies. The dataset is comprised of 324 synthetic galaxy clusters with mass $M_{200} > 6 \times 10^{14} h^{-1} \mathrm{M}_{\odot}$, modelled in a cosmological volume of side length $1 h^{-1}$Gpc with all the relevant baryonic physics, which not only allows to perform a statistically significant study of the formation and evolution of a mass-complete sample, but also probe their environments and the pre-processing of material entering the galaxy cluster.

How well can we model the properties of massive galaxy clusters?

Naturally, before we can start any kind of analysis on the objects in the dataset first we must understand the general properties of the sample. Thus, the first part of this study aimed to validate the dataset by comparing the simulated clusters with common observational constrains in order to find which are the strengths (and limitations) of our sample. We found the following results:

- THE THREE HUNDRED dataset is a fair representation of realistic clusters that is able to reproduce properties such as baryonic fractions and gas scaling relations. We found that baryonic processes have a weak influence on gas scaling relations, in agreement with Hahn et al. (2007).
- Stellar fractions differ from observations in codes without AGN feedback. Thus, AGN feedback (such as the one in `GADGET-X`) is necessary for obtaining realistic baryonic

fractions, as codes that lack it overproduce stars (i.e. GADGET-MUSIC). The AGN implementation in GADGET-X alleviates this issue. However, there is room for improvement, as we find that massive clusters ($M_{500} \gtrsim 10^{14} h^{-1} \mathrm{M}_{\odot}$) slightly overproduce stars, whereas in low mass haloes ($M_{500} \lesssim 10^{14} h^{-1} \mathrm{M}_{\odot}$) is too suppressed.

- The theoretical modelled galaxies in the sample present similar results and match observations. Nevertheless, identifying the massive central galaxies in each cluster (i.e. BCG) and the intra-cluster light of the halo are difficult tasks, which obfuscates observational comparisons.

- In terms of luminosity, the sample shows a linear luminosity-mass relation consistent with observations. On the other hand, their colours are bluer than in observations.

These results reveal the main challenge of building an accurate model of galaxy formation from numerical simulations. Subgrid physics are needed due to technological limitations, yet generally they cover degenerate properties. As a consequence, some results resemble observations (i.e. baryonic fractions, luminosity-mass relations, etc.) while others slightly deviate from the observational constrains (i.e. stellar fractions, colours, etc.), despite being properties that are tightly related. Overall, we find that THE THREE HUNDRED dataset contains objects in reasonable agreement with observational counterparts, which can be used to understand how galaxy clusters influence the evolution of their galaxies.

How do massive galaxy clusters accrete their mass and how stable is the process in the presence of baryons?

Once validated the dataset, we investigated the growth of the main galaxy clusters in the sample. Previous studies have analysed the evolution of the gas mass density profiles of clusters of galaxies and found that, despite the diversity shown in individual cluster profiles, statistically they all follow the same self-similar evolution, even up to redshift $z \sim 2$ (McDonald et al., 2017). An akin self-similar evolution was also found in dark-matter-only simulations, even when the sample is dominated by unrelaxed objects (Le Brun et al., 2018). We extended the analysis to full hydrodynamical simulations to find how the baryonic component – already dominating the inner cluster region — affects the self-similar evolution of clusters, especially in the presence of an AGN feedback. However, instead of selecting the most massive objects at each target time as previous studies, we considered the temporal evolution of a mass-complete sample of massive galaxy clusters selected at $z = 0$. This allowed us to find how their $z = 0$ dynamical state and their formation time classification influence the sample evolution. We found the following results:

- The theoretical self-similar evolution of their total mass density profiles holds in the presence of baryonic interactions. We found that their median profiles are already in place at $z \geq 2$, i.e. way before they accreted half of their $z = 0$ total mass, in agreement with the dark-matter-only results from Le Brun et al. (2018).

- Separating the sample by their formation time and dynamical state at $z = 0$ shows that dynamically relaxed clusters at $z = 0$ (which generally are early-formed clusters, i.e. $z_{\mathrm{form}} \geq 0.6$) break the self-similar evolution as they show a shift in their median scaled density profiles, which can be understood from the two-phase accretion model of halo formation, i.e. haloes that entered their slow-phase mode of accretion accrete material that is deposited in the outermost parts of the halo, thus their radius grows while their scale radius (which generally denotes the boundary between the core and the outskirts of a NFW-like halo; Navarro, Frenk, and White, 1996) remains approximately constant.

- Gas profiles follow essentially the same trends. At $z \sim 2.5$ we observe a deviation from self-similarity, which we attribute to the combined effect of the merger activity and star formation rate at the time, and numerical effects from the SPH implementation in the simulation. The AGN feedback in GADGET-X can only be seen up to distances $r \gtrsim 0.1 r_{500}$, and naturally increases the scatter in the inner regions of the cluster, $r/r_{500} < 0.01 - 0.1$, depending on the redshift.

Our results support previous observational results (e.g. McDonald et al., 2017; Ghirardini et al., 2018), since the gas component is a biased tracer of the underlying gravitational potential in the cluster. However, the shift found in the dynamically relaxed/early-formed subsample is not detected in observational studies due to the implicit selection of the sample in every observation, i.e. observations pick the most-massive objects at a given redshift interval and are unable of following the evolution of the population. We found that relaxed clusters, i.e. the objects traditionally selected for evolution and growth studies along theoretical lines because of their lower scatter in their properties, are the ones which may not actually evolve self-similarly. Certainly such conundrum is irrelevant in observations due to the fact that the selected samples are mass-limited, as the ones used in Le Brun et al. (2018) to avoid this issue. However, such a choice may obscure certain theoretical ideas about cluster growth.

Do cluster environments affect the stellar kinematics of infalling objects?

Next we studied the influence of cluster environments on the stellar kinematics of infalling haloes. Previous studies have shown that tidal interactions are able to disrupt infalling haloes in different environments (e.g. Hayashi et al., 2003; Bullock and Johnston, 2005; Peñarrubia, Navarro, and McConnachie, 2008; Łokas, 2020). However, their primary goal was to determine mass-loss estimations from infalling haloes, without considering the kinematical properties of the stellar component in full-physics simulations. Thus, following previous studies, we analysed the evolution of the fraction of co-rotation of the star particles contained within an aperture of each infalling halo, and the specific stellar angular momentum – stellar mass relation of the population. We found that, while the mass of infalling haloes can be considerably stripped since their infall, their stellar angular momentum hardly changes. Here we summarise the main results:

- The internal dynamics of the infalling galaxies remains mostly unchanged for most of the galaxies after they entered the galaxy cluster environment, even when they were mostly depleted of all their gas and stripped off their dark matter halo by the time they reach $z = 0$.
- Numerical effects reduce the fraction of ordered rotation close to the pericentre passage of the infalling galaxies. Along this effect, we found that stellar mergers of infalling haloes (in agreement with Lagos et al., 2018b; Schulze et al., 2018), and transient encounters with the stellar remnants of haloes that have lost their dark matter component during their own passage through the cluster, entering within the aperture we used for defining the properties of our galaxies, are able to "spin-up" galaxies.
- Similar to the κ evolution of our galaxies, the specific angular momentum-stellar mass relation for the galaxies in the sample showed no substantial change in their location on the $j - M$ plane from their infall redshift until $z = 0$.

Our analysis suggests that, given that the disruption of the stellar specific angular momentum of a galaxy since its infall is mostly negligible, the different kinematical mix between cluster environments and field galaxies may not be caused by environmental effects transforming galaxies in clusters, as the stellar specific angular momentum disruption we observe in the infalling haloes in our sample only affects a small percentage of the total population.

The statistical analysis done in Ch. 2 shows the importance of a studying large sample of massive clusters. Individual profiles are diverse, but median trends show the underlying properties of the population. Moreover, we found that environmental effects are not that relevant for stellar kinematics of infalling objects, and that most of their influence concerns their collisional (i.e. gas) component (e.g. Arthur et al., 2019; Mostoghiu et al., 2020b).

4.1.2 Constrained simulations of the local Universe

The second part of the Thesis used constrained simulations to understand and predict observational results from our Local Universe. Constrained simulations, unlike "regular" numerical simulations, aim to reproduce our local Universe. This allows us to directly compare observations with their simulated counterpart object to understand aspects of galaxy formation and provide predictions that could disentangle the unknown processes. The results

from this chapter were derived from constrained simulations within the CLUES project and we focused mainly on star formation processes of individual galaxies.

How can we attain a reversed galactic stellar age gradient?

The Triangulum galaxy (also known as M33) is a nearby bulge-less galaxy ($\sim$ 800 kpc) with an (almost) face-on disc component. Recent high-resolution observational studies of the M33 stellar component show that its radial stellar distribution is compatible with an inside-out growth of the disc, i.e. old stars found in the central region, young stars found in the outskirts of the disc. However, at around $\sim$ 9 kpc, the stellar age gradient reverses, i.e. we start to find old stars again. To study this peculiar stellar age profile, we used a M33 analogue to find if such age gradient reversal could be found in the simulation. We found that the M33 analogue resembles the observational counterpart in terms of mass, rotational velocity and surface brightness, and it features a similar stellar age profile. This motivated us to seek its origin. Here we summarise the main results:

- The turnaround in the radial age profile of the simulated M33 galaxy is a result of primarily accretion of old stars from merging satellite galaxies into the main host galaxy and, to a much lesser extent, of stellar migration of old in-situ stars from the central regions towards its outskirts.
- The simulation allowed us to further investigate projection effects on these observations and to estimate how much they influence the results. By following a procedure similar to observations, we studied the M33 analogue in different projections and found that the observed correlation between breaks in the surface brightness profile and the age turnaround radius region also holds in our simulation when studied in a projection similar to the one that the Triangulum galaxy shows, in agreement with other studies in simulations (Ruiz-Lara et al., 2017).
- To verify this scenario observationally we provided an estimation for the line-of-sight velocity dispersion of the stars in the M33 analogue. In-situ stars co-rotate with the galactic disc and have a small velocity dispersion, while accreted stars are kinematically hot and are expected to have a random line-of-sight velocity distribution, with approximately twice the velocity dispersion of the in-situ stars at the same radius.
- The median age of the rotationally supported, in-situ stars, of the analogue indicate that this stellar population is young (median age of 4-5 Gyrs), whereas the pressure supported, accreted stars, causing the age turnaround, should be all old (median age $\sim$ 11 Gyrs).

Our results point to a formation scenario in which M33 followed a traditional inside-out growth of its galactic disc and, due to its mass accretion history, old stars were deposited at the outskirts of its galactic disc through subsequent mergers, creating the particular stellar age profile we observe today. Moreover, we show that the correlation observed in the surface brightness and the age reversal radius is sensitive to projection effects. Yet, the question of the likelihood of forming such stellar age profiles, i.e. if the stellar age reversal in the age profile in M33 is a consequence of its particular merger history or if is it a common occurrence, remains unsolved. To obtain a statistical significant answer we need to analyse a bigger sample of simulated counterparts, as so far our results were derived from a single constrained realisation of M33.

Can satellite galaxies experience a star formation burst after their infall?

Motivated by previous works on the star formation histories (SFHs) of dwarf galaxies, and especially by the results from Miyoshi and Chiba (2020) and Rusakov et al. (2020), we investigate the different SFHs of satellite galaxies of the three most massive central galaxies from a Local Group simulation from the CLUES project: the Milky Way, Andromeda, and Triangulum. We studied physical effects that lead to such differences and searched for possible signatures of infall. Here we summarise the main results:

- The SFH of satellites after infall is determined by two factors: the amount of cold (bound) gas that a satellite has at infall time and the type of orbit with which it enters within the host.
- In agreement with previous studies (e.g. Rocha, Peter, and Bullock, 2012), the least luminous satellites stop forming stars well before infall and in this case the infall does not play any role in shaping their SFH. More massive galaxies, on the other hand, can instead have their SF suppressed by the close pericentric passage near by the host, which captures all the gas.
- A necessary, but not sufficient, condition to have enhancement of SF after infall is that the satellite enters the host's virial radius with a large amount of gas. We find that the SF enhanced group shows a correlation between their SF peaks and their pericentric passages, indicating that the tidal shock experienced at their pericentres are able to trigger SF events in the satellite. However, if their orbits have a close pericentric approach to their central galaxy, the tidal interactions are strong enough to disrupt the bound gas of satellite, regardless of their gas fraction at infall.
- The pericentric passages of infalling satellites likewise correlate with the peaks of SF in their main galaxy, suggesting that the same mechanism that is able to induce SF in satellites at their pericentres affects the SF of central galaxies too, in agreement with Ruiz-Lara et al. (2020).

We have shown that the two main conditions that determine the SF of infalling satellites are the amount of (bound) gas per halo mass in the satellite at their infall and how close they approach their central galaxy during their evolution after infall. Satellites with enough gas form stars at intervals which correlate with their pericentric passage. However, if their pericentre is too close to their central galaxy, they are depleted of their gas instead. For central galaxies, we found that the multiple close pericentric passages of their respective satellites correlates with their peaks in SF. Nevertheless, this simple picture requires a more detailed analysis of the orbits of the satellites in the sample. As of the writing of this Thesis, this is an ongoing project.

The results from constrained simulations provide a unique opportunity of testing proposed mechanisms from simulations in observational studies, as we can provide limits on results that should be comparable to the observed analysis. Moreover, they allows us to perform comparisons in a more straightforward way with observable objects, as their simulated counterparts are chosen to resemble the observational data.

4.2 Future prospects

Thorough this Thesis we have outlined some potential paths for future work. Here we describe some of the possible future studies from each method that we can follow up.

For the cluster analysis, we aim to refine the mock images available in the dataset by performing a detailed analysis of their luminosity and morphological properties, and compare them with observations using software such as `ProFound` (Robotham et al., 2018) and `ProFit` (Robotham et al., 2017) (see Fig. 4.1 for an example analysis using the software). A preliminary analysis has been already done on the objects from THE THREE HUNDRED, and it proved to be a promising project as we were able to successfully recover projected luminosity properties for most of the objects after a luminosity cut. Yet the limited resolution of the simulations only provided a rough estimation of the morphological properties of the stellar component of the haloes in the sample. To overcome this, we need data with enough resolution to accommodate the analysis, but also in a comparable volume in order to study cluster environmental effects. Such data could be obtained from the next generation of simulations already running within the THE THREE HUNDRED collaboration.

Recent studies showed that machine learning techniques like Convolutional Neural Networks (CNN) can accurately estimate cluster properties from mock catalogues (Baron, 2019; Yan et al., 2020). As our dataset is comprised of many objects, we aim to introduce such machine learning techniques in the parameter estimation part of the analysis, reducing the amount of parameter tuning workload needed for a sample of such magnitude.

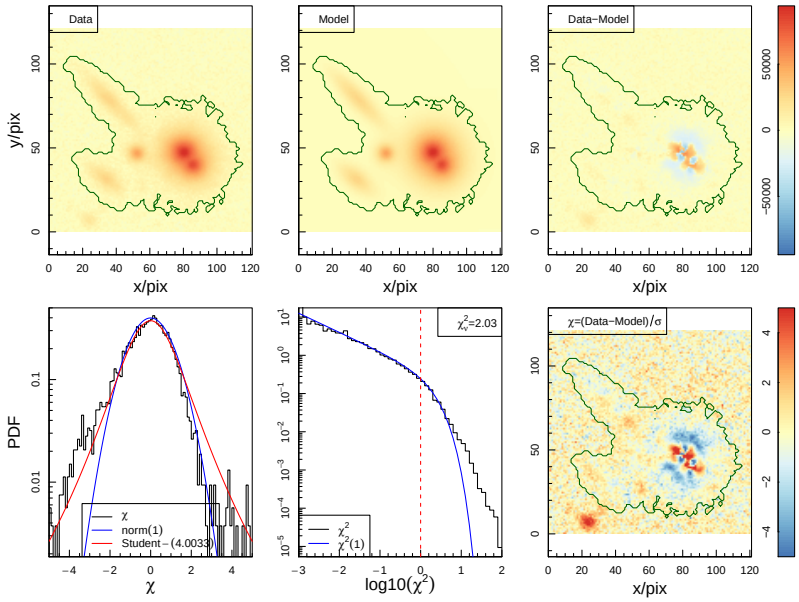

FIGURE 4.1: Fitting of a group of sources extracted using `ProFound` and fitted with `ProFit`. The top row shows the segmentation map from `ProFound`, the model obtained from `ProFit`, and the residual. The bottom row contains a series of statistics for the fit. The objects extracted using `ProFound` are analysed in `ProFit` to obtain, among other properties, an accurate multi-fit decomposition of its 1-dimensional surface brightness radial profile by modelling sky subtraction, a sigma map for the root-mean-square of the sky, and an adequate segmentation map for extended sources. (Image credit: Robotham et al., 2018)

In this regard, we additionally plan to extend the environmental study done for the stellar angular momentum of infalling galaxies in Sec. 2.4 to consider the large scale structure in the cluster region, i.e. if objects are subjected to group infall through filaments, or preferential directions of infall, akin to what was presented for the gas component in Kuchner et al. (2020) and Mostoghiu et al. (2020b). Following the aforementioned discussion, obtaining data with better resolution would also allow us to extend the (purely) kinematic analysis to also consider morphological properties, and to perform a kinematical classification based on luminosity that follow observational techniques, as presented in previous works (e.g. Veale et al., 2017; Correa et al., 2017; Lagos et al., 2018a; Lagos et al., 2018b).

From the constrained simulations part, we intend to expand on the analysis of the M33 candidate by analysing more simulated counterparts to find how likely is to obtain a reversed radial age gradients in galaxies, its connection with breaks in their surface brightness profiles, if mergers of old stars are always the primary mechanism of such feature (as our current results suggest), and how projection effects enhance (or diminish) this effect. Such questions would allow us to, not only understand the formation of the observed M33, but also galaxies with similar formation histories. The aforementioned questions can only be reliably answered by performing a systematic analysis of a statistically significant sample of M33-like galaxies.

The study of the star formation of infalling satellites in a Local Group environment is an ongoing project. Besides the short-term goals that we aim to reach, i.e. characterising the orbits of the satellites, comparisons with observational data, etc., we expect to obtain new constrained simulations which include, among other improvements, black hole feedback that regulates star formation in host environments. Such simulations would allow us to study in detail if the tidally-induced star formation mechanism that we identified in the current simulation is influenced by the feedback. Moreover, the sample would also increase, which is always a great improvement for the statistics of the results.

The future of cosmological simulations is promising. As our technology (inevitably)

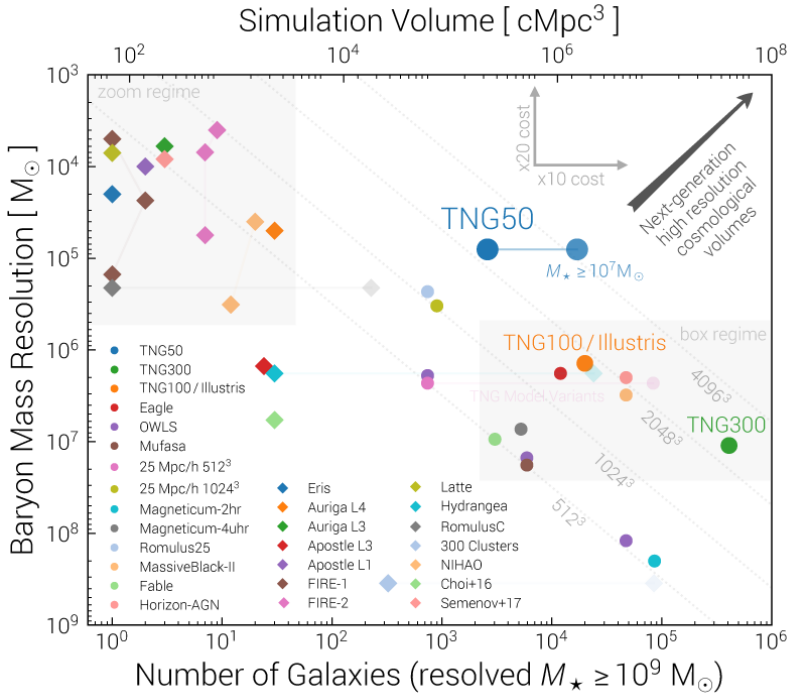

FIGURE 4.2: Summary of state-of-the-art simulations. The quoted effective volume and baryon mass resolution are at z=0. Zoom simulations push towards higher baryon mass resolutions (diamonds), whereas cosmological simulations seek higher volumes (circles). The trade-off between higher volumes and higher mass resolutions is reflected in the distribution of simulations in the figure. Ideally, we aim towards the region in the top-right corner, where high cosmological volumes and high mass resolution would allows us to capture at the same time both the large scale structure of the Universe and complex galaxy formation interactions. However, the technological limitations of the greatest supercomputers (as estimated by the inset axis) constrain the simulations achievable today. (Image credit: `Illustris-TNG` project, `https://www.tng-project.org/about/`)

grows, our computational power increases, and as such, we are able to produce more ambitious cosmological simulations. More than 30 years ago, numerical simulations described the evolution of the universe with 32^3 (collisionless) particles in a $64^3 h^{-1}$Mpc volume (Davis et al., 1985). Nowadays, state-of-the-art simulations are able to resolve objects with halo masses of $\sim 10^{10}$M$_\odot$ with more than 20 000 particles (e.g. NIHAO, Wang et al., 2015); or for galactic scale simulations, structures with $\sim 10^7$M$_\odot$ with up to 2500 particles (e.g. ILLUSTRIS-TNG, Nelson et al., 2019). A diagram showing the current state-of-the-art simulations can be seen in Fig. 4.2.

However, gaining more computational power is not sufficient for achieving scientific progress. New data coming from surveys such as DESI (DESI Collaboration et al., 2016) and EUCLID (Euclid Collaboration et al., 2019) will provide cosmological data of distant galaxies at much higher quality, surveys such as SAMI (Owers et al., 2017), XXL (Pierre et al., 2016), X-COP (Eckert et al., 2017) or MANGA (Graham et al., 2019) have been providing valuable information about clusters and their infalling objects, and on smaller scales, the proper motions of dwarf galaxies from GAIA (Gaia Collaboration et al., 2018a) further constrained the properties of the local universe. Therefore, ultimately, thanks to the combined effort of new high resolution observations of greater samples of objects, and more powerful and sophisticated state-of-the-art simulations, reaching a complete model galaxy formation is a matter of time.

5 Conclusiones y planes futuros

5.1 Conclusiones

Una teoría cosmológica completa requiere un modelo de formación de galaxias preciso. Para construir dicho modelo hacemos uso de simulaciones numéricas cuyos objetivos son, en primer lugar, reproducir la distribución y propiedades de las galaxias que observamos en nuestro Universo, y en segundo lugar, predecir características que potencialmente podrían ser detectadas en futuros estudios observacionales. Ya que esta metodología es la única a nuestro alcance que nos permite experimentar con las condiciones iniciales y la evolución de nuestro Universo, gran parte del esfuerzo colectivo se emplea en construir simulaciones que sean capaces de reproducir y predecir constreñimientos observacionales.

A medida que la calidad de los datos observacionales mejora, asimismo lo hacen los modelos numéricos. No obstante, la enorme cantidad de complejas interacciones entre galaxias inferidas gracias a las observaciones acentúan la degeneración presente en nuestros modelos numéricos: diferentes prescripciones de formación de galaxias pueden dar lugar a resultados similares (p. ej. Fig. 10 en Sembolini et al., 2016b), lo que retroalimenta el bucle entre los constreñimientos observacionales y los resultados numéricos.

Esta Tesis persigue los mismos objetivos: buscamos entender aspectos de la formación de galaxias a través de simulaciones numéricas. Debido a esto, hemos hecho uso de simulaciones hidrodinámicas con el fin de estudiar las complejas interacciones que moldearon las galaxias durante su evolución. El análisis fue realizado usando dos métodos complementarios: empleamos simulaciones de cúmulos de galaxias y objetos que caen en sus entornos (Ch. 2), y simulaciones constreñidas para entender las propiedades observacionales de las galaxias en nuestro Universo local y proporcionar propiedades potencialmente observables que nos permitirían confirmar nuestros modelos (Ch. 3).

En esta sección resumimos los principales resultados de la Tesis y discutimos las implicaciones de éste trabajo. En la siguiente sección, proporcionamos ideas para futuros proyectos que pueden expandir los resultados presentados aquí.

5.1.1 Cúmulos de galaxias

Hemos usado datos del proyecto THE THREE HUNDRED con el fin de estudiar cómo los entornos de los cúmulos de galaxias afectan a las galaxias que inciden en ellos. El conjunto de datos está formado por 324 cúmulos de galaxias sintéticos con masas $M_{200} > 6 \times 10^{14} h^{-1} \mathrm{M}_{\odot}$, modelizados en un volumen cosmológico de lado $1 h^{-1}$Gpc incluyendo toda la física bariónica relevante, lo que no solo nos permite realizar un estudio estadísticamente representativo de la formación y evolución de una muestra de cúmulos de galaxias completa en términos de masa, sino que además nos permite investigar sus entornos y el preprocesamiento del material que entra en el cúmulo de galaxias.

¿Cómo de bien podemos modelizar las propiedades de los cúmulos de galaxias masivos?

Naturalmente, antes de comenzar cualquier estudio de los objetos del conjunto de datos, primero tenemos que entender sus propiedades generales. Así pues, la primera parte de este estudio tuvo por objetivo el validar los datos mediante una comparación de los cúmulos de galaxias simulados con propiedades observacionales típicas, con el propósito de discernir las fortalezas (y debilidades) de nuestra muestra. Hemos hallado los siguientes resultados:

- El conjunto de datos del proyecto THE THREE HUNDRED es una representación razonable de cúmulos realistas que es capaz de reproducir propiedades tales como fracciones bariónicas y relaciones de escala gaseosas. Encontramos que los procesos bariónicos

tienen una influencia débil sobre las relaciones de escala gaseosas, de acuerdo con los resultados de Hahn et al. (2007).

- Las fracciones estelares difieren de los resultados observacionales para los códigos que no contienen retroalimentación a través de Núcleos Galácticos Activos (NGA). Por tanto, la retroalimentación NGA (tal como la presente en `GADGET-X`) es necesaria para obtener fracciones bariónicas realistas, ya que los códigos que no la implementan sobreproducen estrellas (p. ej. `GADGET-MUSIC`). La implementación NGA de `GADGET-X` mitiga este problema. Sin embargo, aún hay posibilidad de mejora, puesto que encontramos que los cúmulos masivos ($M_{500} \gtrsim 10^{14} h^{-1}\mathrm{M}_{\odot}$) de nuestra muestra tienen una ligera sobreproducción de estrellas, mientras que en los halos menos masivos $M_{500} \lesssim 10^{14} h^{-1}\mathrm{M}_{\odot}$) está demasiado mitigada.

- Las galaxias modelizadas teóricamente de la muestra presentan resultados similares a las simuladas hidrodinámicamente y se adecuan a las observaciones. Sin embargo, el identificar las galaxias centrales masivas de cada cúmulo (es decir, la Galaxia más Brillante del Cúmulo, GBC) y la luz intracúmulo del halo son tareas complicadas, lo que dificultan las comparaciones con resultados observacionales.

- En términos de luminosidad, la muestra exhibe una dependencia luminosidad-masa linear consistente con las observaciones. Por otro lado, sus colores son más azulados que en los resultados observacionales.

Estos resultados revelan el principal desafío de construir un modelo preciso de formación de galaxias a partir de simulaciones numéricas. Las simulaciones requieren física de subresolución debido a las limitaciones tecnológicas actuales, pese a que engloban propiedades degeneradas. Como consecuencia de esto, algunos resultados se asemejan a los resultados observacionales (p. ej. fracciones bariónicas, relación luminosidad-masa, etc.) mientras que otras se alejan ligeramente de los constreñimientos observacionales (p. ej. fracciones estelares, colores, etc.), a pesar de que estas propiedades están fuertemente correlacionadas. En general, encontramos que los datos del proyecto THE THREE HUNDRED contienen objetos razonablemente similares a sus homólogos observacionales, lo que nos permite usarlos para entender cómo los cúmulos galácticos influencian la evolución de sus galaxias.

¿Cómo acretan los cúmulos de galaxias masivos su masa y cómo de estable es el proceso en presencia de bariones?

Una vez hemos validado el conjunto de datos, hemos investigado el crecimiento de los principales cúmulos galácticos de la muestra. Estudios anteriores analizaron la evolución de los perfiles de masa gaseosa de cúmulos de galaxias y encontraron que, a pesar de la diversidad de perfiles obtenida, estadísticamente todos siguen la misma evolución autosimilar, incluso a redshift $z \sim 2$ (McDonald et al., 2017). Una evolución autosimilar parecida se encontró en simulaciones de materia oscura, incluso cuando la muestra estaba dominada por objectos no relajados (Le Brun et al., 2018). Hemos extendido el análisis a simulaciones hidrodinámicas completas para hallar cómo la componente bariónica – que domina la región central del cúmulo – afecta a la evolución autosimilar de los cúmulos, especialmente en presencia de retroalimentación NGA. No obstante, en vez de seleccionar los objetos más masivos para cada tiempo como en los estudios anteriores, nosotros consideramos la evolución temporal de una muestra completa en términos de masa de cúmulos masivos de galaxias seleccionados a $z = 0$. Esto nos permite determinar cómo su clasificación dinámica a $z = 0$ y su tiempo de formación influencian la evolución de la muestra. Hallamos los siguientes resultados:

- La evolución teórica autosimilar de sus perfiles de densidad de masa total se mantiene en presencia de interacciones bariónicas. Encontramos que sus perfiles medianos se encuentran ya establecidos a $z \geq 2$, i.e. mucho antes de haber acretado la mitad de su masa total a $z = 0$, de acuerdo con los resultados obtenidos a partir de simulaciones de materia oscura de Le Brun et al. (2018).

- Separando la muestra según su tiempo de formación y su estado dinámico a $z = 0$ se observa que los cúmulos dinámicamente relajados a $z = 0$ (que generalmente se

formaron temprano, es decir $z_{\rm form} \geq 0.6$) quebrantan la evolución autosimilar puesto que muestran un desplazamiento en sus perfiles escalados de densidad medianos, que se puede entender gracias al modelo de acreción en dos fases de formación de halos, esto es, halos que entraron en su fase lenta de acreción acretan material que se deposita en las partes más externas del halo, por lo tanto su radio crece mientras que su radio de escala (que generalmente denota la frontera entra la región central y las afueras de un halo tipo NFW; Navarro, Frenk, and White, 1996) se mantiene aproximadamente constante.

- Los perfiles de gas siguen esencialmente el mismo comportamiento. A $z \sim 2.5$ detectamos una desviación de la evolución autosimilar que atribuimos tanto a eventos de coalescencia y a la tasa de formación estelar a esos tiempos, como a efectos numéricos de la implementación de la Hidrodinámica de Partículas Suavizadas (HPS) en la simulación. La influencia de la retroalimentación NGA en `GADGET-X` solo puede ser observada hasta distancias $r \gtrsim 0.1 r_{500}$, y naturalmente incrementa la dispersión en las regiones interiores del cúmulos, $r/r_{500} < 0.01 - 0.1$, en función del redshift.

Nuestro análisis concuerda con los resultados observacionales anteriores (e.g. McDonald et al., 2017; Ghirardini et al., 2018), dado que la componente gaseosa es un trazador parcial del potencial gravitatorio subyacente al cúmulo. Sin embargo, la desviación observada en las submuestras dinámicamente relajadas/formadas temprano no se detecta observacionalmente debido a la selección implícita realizada en los estudios observacionales, esto es, las observaciones seleccionan los objectos más masivos a cierto intervalo de redshift y son incapaces de seguir la evolución de dicha población. Encontramos que los cúmulos relajados, objetos que tradicionalmente son seleccionados en estudios de evolución y crecimiento de cúmulos junto a resultados teóricos debido a su pequeña dispersión en sus propiedades, son los que no necesariamente evolucionan de manera autosimilar. Indudablemente este detalle es irrelevante en estudios observacionales ya que las muestras seleccionadas están limitadas en términos de masa, como el empleado en Le Brun et al. (2018), para evitar este problema. Aun así, dicha selección puede dificultar ciertos aspectos teóricos sobre el crecimiento de los cúmulos.

¿Afectan los entornos de los cúmulos a la cinemática estelar de los objectos incidentes?

A continuación, estudiamos cómo los entornos de los cúmulos galácticos alteran la cinemática estelar de los halos incidentes. Estudios anteriores han demostrado que las interacciones de marea alteran los halos incidentes en diversos entornos (p. ej. Hayashi et al., 2003; Bullock and Johnston, 2005; Peñarrubia, Navarro, and McConnachie, 2008; Łokas, 2020). No obstante, el principal objetivo de estos estudios fue el determinar estimaciones de pérdida de masa a partir de los halos incidentes, sin considerar las propiedades cinemáticas de la componente estelar en simulaciones de física completa. Por lo tanto, siguiendo estudios anteriores, analizamos la evolución de la fracción de co-rotación de las partículas estelares contenidas en una apertura para cada halo incidente, y la relación momento angular específico estelar – masa estelar de la población. Encontramos que, mientras que la masa de los halos incidentes es considerablemente despojada desde su incidencia, su momento angular estelar apenas cambia. Aquí resumimos los principales resultados:

- La dinámica interna de las galaxias incidentes se mantiene mayoritariamente invariable para las galaxias que entraron en el entorno del cúmulo galáctico, incluso cuando han sido despojadas en su mayor parte de su gas y su halo de materia oscura para cuando alcanzan $z = 0$.

- Los efectos numéricos reducen la fracción de rotación coherente cerca del pericentro de las galaxias incidentes. Además de este efecto, encontramos que eventos de coalescencia de halos incidentes (de acuerdo con Lagos et al., 2018b; Schulze et al., 2018), y encuentro transitorios con remanentes estelares de halos que perdieron su componente de materia oscura durante su propia trayectoria a través del cúmulo, que entran dentro de la apertura que usamos para definir las propiedades de nuestras galaxias, son capaces de "incrementar" el grado de giro de las galaxias.

- De manera similar a la evolución del parámetro κ de nuestras galaxias, la relación momento angular específico-masa estelar de nuestras galaxias no muestra ningún cambio sustancial en su distribución en el plano $j - M$ desde su redshift de incidencia hasta $z = 0$.

Nuestro análisis sugiere que, dado que las variaciones en el momento angular específico de una galaxia desde su incidencia en el cúmulo galáctico son despreciables, la diferencia cinemática entre los entornos de los cúmulos y las galaxias de campo podría no deberse a efectos de entorno que transforman las galaxias en cúmulos, ya que los cambios que observamos en el momento angular específico estelar de nuestra muestra solo se manifiestan en un pequeño porcentaje de la población total.

El análisis estadístico presentado en Ch. 2 muestra la importancia de realizar estudios sobre grandes muestras de cúmulos masivos. Los perfiles individuales de los cúmulos galácticos son diversos, pero sus tendencias medianas manifiestan las propiedades subyacentes de la población. Adicionalmente, encontramos que los efectos de entorno de cúmulos no son tan relevantes para la cinemática estelar de los objectos incidentes, y que gran parte de su influencia concierne la componente colisional (es decir, gas. P. ej. Arthur et al., 2019; Mostoghiu et al., 2020b).

5.1.2 Simulaciones constreñidas del Universo local

La segunda parte de esta Tesis empleó simulaciones constreñidas con el fin de entender y predecir resultados sobre nuestro Universo local. Las simulaciones constreñidas, a diferencia de las simulaciones numéricas "tradicionales", tienen como objetivo reproducir nuestro Universo local. Esto nos permite comparar de manera directa observaciones con resultados simulados homólogos para comprender aspectos de la formación de galaxias y proporcionar predicciones que permitan dilucidar procesos desconocidos. Los resultados de Ch. 3 fueron derivados de simulaciones constreñidas del proyecto CLUES y se centraron principalmente en procesos de formación estelar en galaxias individuales.

¿Cómo podemos lograr un gradiente invertido de edad estelar galáctico?

La galaxia Triangulum (también conocida como M33) es una galaxia cercana ($\sim$ 800 kpc) sin bulbo, con un componente de disco (prácticamente) de cara. Estudios observacionales recientes de alta resolución de la componente estelar de M33 muestran que su distribución radial estelar es compatible con un escenario en el que el crecimiento del disco se da desde dentro hacia afuera, esto es, las estrellas más antiguas se encuentran en la región central de la galaxia y las jóvenes en las afueras del disco. No obstante, a aproximadamente $\sim$ 9 kpc, el gradiente de edad estelar se revierte, o en otras palabras, volvemos a encontrar estrellas antiguas. Para estudiar este peculiar perfil de edad estelar usamos un análogo de M33 para encontrar si dicha característica se encuentra en la simulación. Encontramos que el análogo simulado de M33 se asemeja a la galaxia observacional en términos de masa, velocidad rotacional y brillo superficial, y posee un perfil de edad estelar similar. Esto nos motiva a analizar el origen de sus características. Aquí resumimos los principales resultados:

- La inversión en el perfil radial de edad estelar de la galaxia M33 simulada es el resultado de principalmente acreción de estrellas antiguas de coalescencias de galaxias satélite en la galaxia anfitrión principal y, en menor medida, migración estelar de estrellas in-situ antiguas desde la región central de la galaxias a sus afueras.

- La simulación nos permitió extender la investigación a los efectos de proyección en estas observaciones y estimar su importancia en los resultados. Siguiendo un procedimiento similar al empleado en observaciones, estudiamos el análogo de M33 en distintas proyecciones y encontramos que la correlación observada entre las roturas en el perfil de brillo superficial y la región del radio de inversión de edad estelar también se aprecia en la simulación cuando la estudiamos en una configuración similar a la que Triangulum muestra, de acuerdo con otros estudios en simulaciones (Ruiz-Lara et al., 2017)

- Para verificar este escenario observacionalmente proporcionamos una estimación de la dispersión de la velocidad en línea de visión de las estrellas del análogo de M33. Las estrellas in-situ co-rotan con el disco galáctico y tienen poca dispersión de velocidad, mientras que las acretadas son cinemáticamente calientes y se espera que tengan una distribución de dispersión de velocidades en línea de visión aleatoria, con aproximadamente el doble de velocidad de dispersión que las estrellas in-situ situadas al mismo radio.

- La edad mediana de las estrellas in-situ, soportadas por rotación, del análogo de M33 indican que esta población es joven (edad mediana de 4-5 Gyrs), mientras que las estrellas soportadas por presión, acretadas, causantes de la inversión del perfil de edad estelar, deberían ser antiguas (edad mediana de $\sim$ 11 Gyrs).

Nuestros resultados sugieren un escenario de formación en el cual el disco de M33 siguió un crecimiento tradicional desde dentro hacia afuera y, debido a su historia de acreción de masa, las estrellas antiguas fueron depositadas a las afueras del disco galáctico a través de subsiguientes coalescencias, dando lugar al particular perfil de edad estelar que observamos a día de hoy. Asimismo, mostramos cómo la correlación que se observa en el brillo superficial y el radio de inversión del perfil de edad estelar es sensible a efectos de proyección. No obstante, la pregunta sobre la verosimilitud de formar dichos perfiles estelares, es decir, de si la inversión del perfil de edad estelar en M33 es una consecuencia de su particular historia de coalescencias o si es un fenómeno común, sigue abierta. Para obtener una respuesta estadísticamente significativa necesitamos analizar una muestra más grande de análogos simulados, ya que nuestros resultados fueron derivados de una sola realización constreñida de M33.

¿Pueden las galaxias satélite experimentar brotes de formación estelar tras su incidencia?

Motivados por estudios anteriores sobre historias de formación estelar (HFE) de galaxias enanas, y en especial por los resultados de Miyoshi and Chiba (2020) y Rusakov et al. (2020), investigamos las diferentes HFE de las galaxias satélite de las tres galaxias centrales más masivas de una simulación del Grupo Local del proyecto CLUES: la Vía Láctea, Andrómeda y la Galaxia del Triángulo. Estudiamos los efectos físicos que llevan a tales diferencias y buscamos posibles señales de incidencia en dichas historias. Aquí resumimos los principales resultados:

- Las HFS de los satélites después de su incidencia son determinadas por dos factores: la cantidad de gas frío (y ligado) que un satélite tiene en su momento de incidencia y el tipo de órbita con el que entra dentro de su anfitrión.

- De acuerdo con resultados previos (p. ej. Rocha, Peter, and Bullock, 2012), los satélites menos luminosos dejan de formar estrellar mucho antes de su incidencia y en este caso su incidencia no juega ningún papel en la forma de su HFE. Por otra parte, las galaxias más masivas pueden suprimir su formación estelar mediante pasajes pericéntricos cercanos al anfitrión, que capturan todo el gas.

- Una condición necesaria, pero no suficiente, para el crecimiento de la formación estelar de un satélite después de su incidencia es que entre dentro del radio virial del anfitrión con una gran cantidad de gas. Encontramos que el grupo de satélites con formación estelar aumentada presenta una correlación entre sus picos de formación estelar y sus pasajes pericéntricos, indicando que los shocks de marea que experimenta en sus pericentros son capaces de desencadenar eventos de formación estelar en el satélite. Sin embargo, si sus órbitas tienen pasajes pericéntricos cercanos a la galaxia central, las interacciones de marea son lo suficientemente fuertes como para alterar el gas ligados de los satélites, independientemente de las fracciones de gas que tenían en su tiempo de incidencia.

- Los pasajes de pericentro de los satélites incidentes también están correlacionados con los picos de formación estelar de sus galaxias principales, lo que sugiere que el mismo mecanismo que permite inducir formación estelar en los satélites en sus pericentros

afecta también la formación estelar de las galaxias centrales, de acuerdo con Ruiz-Lara et al. (2020).

Hemos demostrado que las dos condiciones principales para determinar la formación estelar de un satélite incidente son la cantidad de gas (ligado) por masa de halo en su tiempo de incidencia y lo cerca que se acercan de su galaxia central durante su evolución tras su incidencia. Los satélites con suficiente gas forman estrellas en intervalos que correlacionan con pasajes pericéntricos. No obstante, si su pericentro es demasiado cercano a la galaxia central, son vaciados de su gas. Para las galaxias centrales, hemos encontrado que los múltiples pasajes pericéntricos cercanos de sus satélites respectivos correlacionan con sus picos de formación estelar. Sin embargo, este simple mecanismo requiere un análisis más detallado de las órbitas de los satélites de la muestra. A la fecha de redacción de esta Tesis, éste es un proyecto en curso.

Los resultados de simulaciones constreñidas proporcionan una oportunidad única de poner a prueba mecanismos propuestos en simulaciones en estudios observacionales, ya que podemos proveer límites a resultados que pueden ser comparables a un análisis observacional. Por otra parte, nos permite realizar comparaciones de una manera más directa con los objetos observados, ya que sus homólogos simulados son elegidos para que se asemejen a los datos observacionales.

5.2 Planes futuros

A lo largo de esta Tesis hemos esbozado algunos proyectos para el futuro. Aquí describimos algunos posibles futuros trabajos para cada método.

Para el análisis de cúmulos, nuestro objetivo es mejorar las imágenes sintéticas que ya se encuentran disponibles en nuestro set de datos realizando un análisis detallado de sus propiedades lumínicas y morfológicas, y compararlas con observaciones haciendo uso de software como `ProFound` (Robotham et al., 2018) y `ProFit` (Robotham et al., 2017) (en Fig. 5.1 podemos ver un ejemplo del análisis realizado por el software). Se ha realizado un estudio preliminar de los objetos de THE THREE HUNDRED y se han obtenido resultados prometedores que nos permitieron recuperar propiedades lumínicas en proyección para la mayoría de objectos, tras realizar un corte de luminosidad. No obstante, la resolución limitada de las simulaciones solo posibilita la obtención de una estimación aproximada de las propiedades morfológicas de la componente estelar de los halos en la muestra. Para superar esta limitación necesitamos datos con mejor resolución, pero también un volumen comparable para poder analizar los efectos de los entornos de los cúmulos galácticos. Estos datos se pueden obtener de la siguiente generación de simulaciones que ya están siendo ejecutadas en la colaboración THE THREE HUNDRED.

Estudios recientes han mostrado cómo técnicas de aprendizaje de máquinas como las Redes Neuronales Convolucionales (RNC) pueden estimar con precisión las propiedades de los cúmulos a partir de imágenes sintéticas (Baron, 2019; Yan et al., 2020). Como nuestro set de datos está formado por muchos objetos, nuestro objetivo es incluir tales técnicas de aprendizaje de máquinas a la hora de estimar parámetros en nuestro análisis, reduciendo la cantidad de trabajo a la hora de ajustar parámetros para una muestra de tal envergadura.

En líneas similares, adicionalmente planeamos ampliar el análisis sobre entornos de cúmulos realizado para el momento angular de la componente estelar de las galaxias incidentes presentado en Sec. 2.4 para que incluya la estructura a gran escala de las regiones de cúmulos, es decir, por ejemplo, si los objetos incidentes están sometidos a una incidencia en grupo a través de filamentos, o direcciones preferenciales de incidencia, similar al trabajo presentado sobre la componente gaseosa en Kuchner et al. (2020) and Mostoghiu et al. (2020b). Siguiendo la discusión anterior, la obtención de datos con mejor resolución nos permitiría extender el análisis (puramente) cinemático a propiedades morfológicas, y a realizar una clasificación cinemática basándonos en luminosidades siguiendo técnicas observacionales, tal como se ha presentado en trabajos anteriores (p. ej. Veale et al., 2017; Correa et al., 2017; Lagos et al., 2018a; Lagos et al., 2018b).

En cuanto a la parte de simulaciones constreñidas, planeamos ampliar el estudio del análogo de M33 analizando un número mayor de análogos simulados, con el fin de entender lo

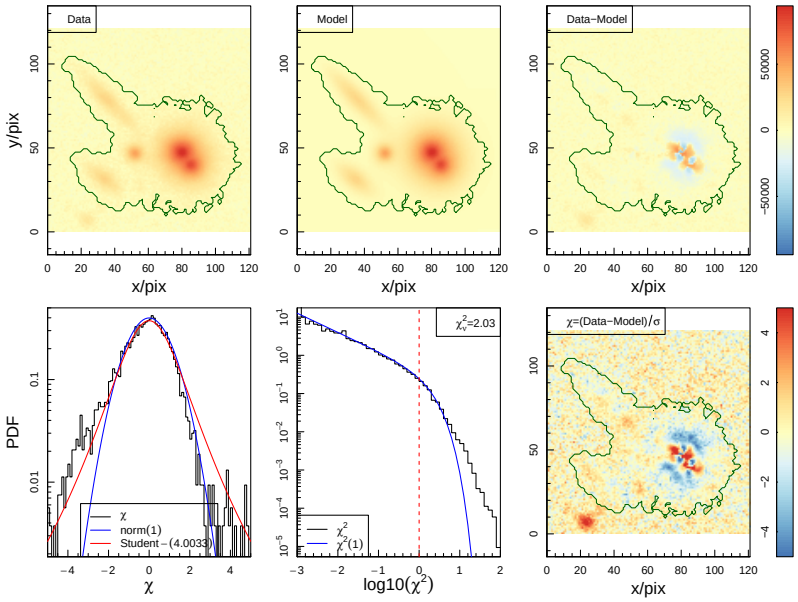

FIGURE 5.1: Ajuste de un grupo de fuentes extraídas con `ProFound` y ajustadas con `ProFit`. La fila superior muestra el mapa de segmentación de `ProFound`, el modelo obtenido de `ProFit`, y el residual. La fila inferior contiene una serie de estadísticas del ajuste. Los objetos extraídos mediante `ProFound` son analizados con `ProFit` para obtener, entre otras propiedades, un preciso multi-ajuste de su brillo superfial radial 1-dimensional mediante la modelización de una extracción de cielo, un mapa de dispersión para la raíz media cuadrática del cielo, y una segmentación adecuada de fuentes extensas. (Crédito de la imagen: Robotham et al., 2018)

frecuente que es obtener un gradiente radial invertido de edad estelar en galaxias, su conexión con las quebraduras en los perfiles de brillo superficial, si las coalescencias de estrellas antiguas siempre son el mecanismo principal de tal característica (tal como indican nuestros resultados actuales), y si los efectos de proyección aumentan (o disminuye) este efecto. Tales cuestiones nos permitirán no solo entender cómo se formó M33, sino que además las galaxias que tengan historias de formación similares. Estas preguntas solo pueden ser abordadas de manera certera si se realiza un estudio estadísticamente significativo de una muestra de galaxias análogas a M33.

El estudio de la formación de estrellas en satélites incidentes en un entorno del Grupo Local es un proyecto en curso. Además de los objetivos a corto plazo que esperamos alcanzar, p. ej. caracterizar las órbitas de los satélites, comparaciones con datos observacionales, etc., esperamos obtener nuevas simulaciones constreñidas que incluyan, entre otras mejoras, una retroalimentación de agujero negro que regule la formación de estrellas en entornos anfitrión. Dichas simulaciones nos permitirían estudiar en detalle si el mecanismo de formación estelar inducido por fuerzas de marea que hemos identificado en la simulación actual se ve influenciado por dicha retroalimentación. Además, la muestra incrementaría, lo que siempre es una mejora excelente para la estadística de los resultados.

El futuro de las simulaciones cosmológicas es prometedor. A medida que nuestra tecnología (inevitablemente) mejora, nuestra capacidad computacional incrementa y, por tanto, somos capaces de producir simulaciones cosmológicas más ambiciosas. Hace más de 30 años, las simulaciones numéricas describían la evolución de un universo constituido de 32^3 partículas (acolisionales) en un volumen de $64^3 h^{-1}$Mpc (Davis et al., 1985). Actualmente, las simulaciones más avanzadas son capaces de resolver objetos con masas totales de $\sim 10^{10}$M$_\odot$ formadas por más de 20 000 partículas (p. ej. NIHAO, Wang et al., 2015); o a escalas galácticas, estructuras con $\sim 10^7$M$_\odot$ y hasta 2500 partículas (p. ej. ILLUSTRIS-TNG, Nelson et al., 2019). Un diagrama del panorama de las simulaciones actuales puede apreciarse en Fig. 5.2.

Sin embargo, un incremento de la capacidad computacional no es suficiente si lo que deseamos es progresar científicamente. Los nuevos datos procedentes de estudios tales como

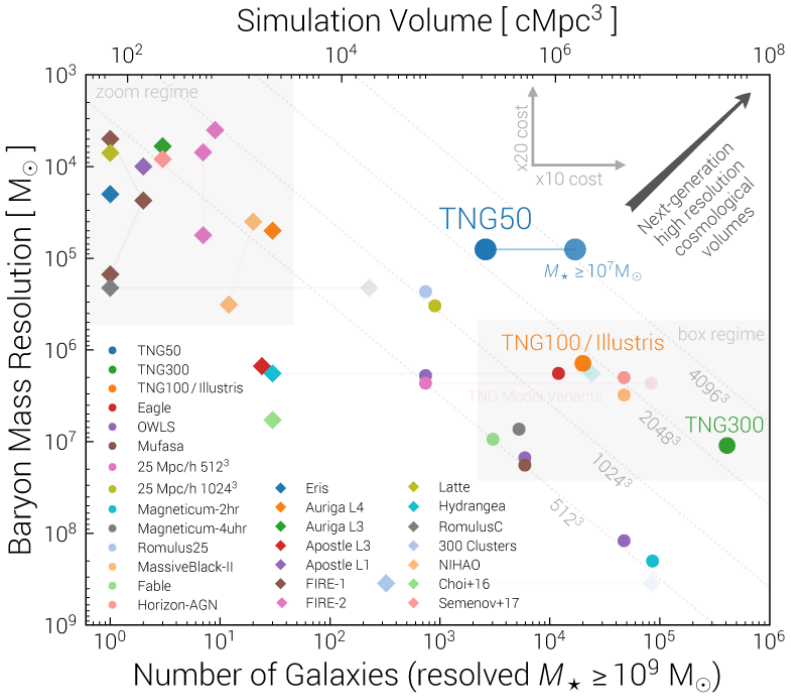

FIGURE 5.2: Resumen de las simulaciones más modernas. El volumen efectivo y la resolución de la masa bariónica señalados corresponden a los valores a $z = 0$. Las simulaciones "zoom" tienden a mayores resoluciones en la masa bariónica (diamantes), mientras que las simulaciones cosmológicas buscan abarcar mayores volúmenes (círculos). La concesión entre mayor volúmenes y mayores masas bariónicas se ve reflejada en la distribución de las simulaciones en la figura. Idealmente, buscamos alcanzar la región de la esquina superior derecha, donde la gran resolución bariónica y los grandes volúmenes nos permitirían capturar simultáneamente tanto la estructura a gran escala del Universo como las complejas interacciones que intervienen en la formación de galaxias. No obstante, las limitaciones tecnológicas de los mayores superordenadores (estimada por la figura en el recuadro) limitan las simulaciones alcanzables a día de hoy. (Crédito de la imagen: `Illustris-TNG` project, https://www.tng-project.org/about/)

DESI (DESI Collaboration et al., 2016) y EUCLID (Euclid Collaboration et al., 2019) proporcionarán datos sobre galaxias lejanas con mucha mayor calidad, estudios como SAMI (Owers et al., 2017), XXL (Pierre et al., 2016), X-COP (Eckert et al., 2017) o MANGA (Graham et al., 2019) han proporcionado información valiosa sobre cúmulos de galaxias y sus objetos incidentes, y a escalas más pequeñas, las trayectorias peculiares de las galaxias enanas provenientes de GAIA (Gaia Collaboration et al., 2018a) restringen aún más las propiedades del universo local. Por tanto, en última instancia, gracias al esfuerzo combinado de las nuevas observaciones de alta resolución de grandes muestras de objectos, y de las simulaciones avanzadas más potentes y sofisticadas, alcanzar un modelo de formación de galaxias completo es cuestión de tiempo.

A Sec. 2.2 - Evolution of the halo mass function

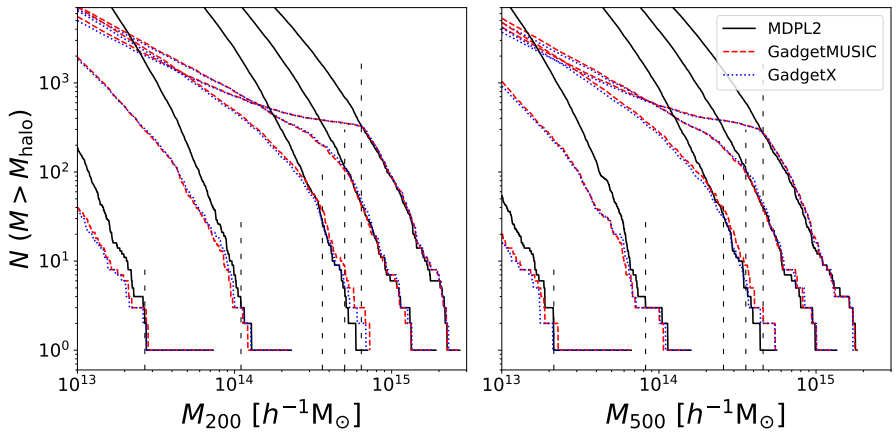

FIGURE A.1: The cumulative halo mass function from different simulation runs for M_{200} (left panel) and M_{500} (right panel). Different colour and line styles represent different simulations: solid black lines are for the DM-only MDPL2; red dashed lines are for `GADGET-MUSIC` and blue dotted lines are for `GADGET-X` . From left to right, we show the halo mass function at redshifts $z = 4.0, 2.3, 1.0, 0.5$, and 0.0 respectively. The dashed vertical lines indicate the mass to which we are complete (i.e. our simulation dataset contains all the haloes above this mass in the full simulation volume). Tab. A.1 lists the exact values.

Our 30 h^{-1}Mpc diameter re-simulated regions contain many more objects in addition to the central clusters. While there are lots of haloes in the region that surrounds the central cluster, there would be many more similar haloes in the full volume. It is therefore important to understand the completeness of our comprehensive sample. Here, completeness refers to the total number of haloes above a given mass within a certain cosmological volume. The mass-complete sample in our hydrodynamic simulations is given by $N_{\rm hydro}(> M_{\rm X}) \geq N_{\rm MDPL2}(> M_{\rm X})$, where N is the total number of haloes above a certain mass $M_{\rm X}$ and X is the chosen mass overdensity e.g. 200. This is the mass above which our sample contains every cluster in the full volume. Below this mass some haloes have not been captured by our re-simulation procedure.

In Fig. A.1, we show the cumulative halo mass functions for the two mass definitions M_{200} (left panel) and M_{500} (right panel) as derived from MDPL2 (solid black lines), `GADGET-X` (blue dot-dash lines), and `GADGET-MUSIC` (red dashed lines). There are five families of lines inside each panel, which, from left to right, show the results at $z = 4.0, 2.3, 1.0, 0.5$, and 0.0. The mass function of the full halo catalogue from the MDPL2 is used here as a reference line. The vertical dashed lines indicates the mass down to which our sample is complete, determined by the crossing point between the `GADGET-X` and MDPL2 lines. The mass limit will slightly decrease at some redshifts if `GADGET-MUSIC` were to be used instead of `GADGET-X` . This is caused by the baryon effects, as `GADGET-MUSIC` forms more stars. In order to make sure the complete sample is chosen to be conservative, we use `GADGET-X` which returns a higher mass limit. We especially note here that the complete sample is based on the MDPL2 halo mass function. This matching ignores any baryon effects on the halo mass function.

TABLE A.1: The mass-complete sample limits of the Three Hundred cluster catalogues at different redshifts. The first column shows the redshift. The second is the M_{200} mass limit and the third column gives the values for M_{500}.

Redshift	M_{200} $[10^{14}h^{-1}\mathrm{M}_{\odot}]$	M_{500} $[10^{14}h^{-1}\mathrm{M}_{\odot}]$
0.0	6.42	4.60
0.5	5.02	3.57
1.0	3.62	2.57
2.3	1.10	0.82
4.0	0.27	0.21

However, this could only affect a small number of them near the mass limitation (see Fig. A.1 for the mass difference). The precise values for these limits for our mass-complete sample are presented in Tab. A.1.

Below the mass-complete limits, the completeness fraction, which will be used later to weight the fitting of the scaling relations, is calculated by the ratio of these lines. It is interesting to note that even at $z = 1$ the number of clusters in the complete sample has fallen dramatically. This is due to the fact that there is significant shuffling in the rank order of the most massive objects in the sample. The set of the largest objects at $z = 4$ bears little relation to the largest objects at $z = 0$ and one set does not evolve uniquely into the other. On the other hand, the largest objects identified at $z = 0$ are not all the largest objects at higher redshift and modelling them alone does not produce a large mass-complete sample at earlier times. We further note here that there is only a few mass-complete clusters at $z \geq 2.3$. The mass limits are more useful for indicating the boundary of the in-complete sample than for selecting the complete sample for statistical studies.

B Sec. 2.3 - Median profiles properties

TABLE B.1: Properties of the median profiles of the whole sample: the median r_{500}, the validation radius $r_{\rm valid}$ (which is equal to the maximum convergence radius in the MDPL2 simulation $r_{\rm conv}^{MDPL2}$), the inner and outer limits of the region where at least 50 per cent of the sample contributes to the median $[r_{\rm in}^{50\%}, r_{\rm in}^{50\%}]$, and the inner and outer limits of the region where *all* the clusters contribute to the median $[r_{\rm in}^{100\%}, r_{\rm out}^{100\%}]$. All the values are in units of (comoving) h^{-1} kpc.

Redshift	r_{500}		$r_{\rm valid}$	$r_{\rm in}^{50\%}$		$r_{\rm out}^{50\%}$		$r_{\rm in}^{100\%}$		$r_{\rm out}^{100\%}$	
	G-X	G-MUSIC		G-X	G-MUSIC	G-X	G-MUSIC	G-X	G-MUSIC	G-X	G-MUSIC
$z = 0$	1005.9	1009.5	28	6.2	5.9	1279.0	1268.4	16.6	10.4	861.5	1046.8
$z = 0.5$	979.2	980.6	37	10.2	8.8	1243.0	1245.3	26.7	26.5	846.4	1036.8
$z = 1$	807.3	824.9	44	12.3	11.1	889.9	983.0	31.1	37.2	889.8	696.4
$z = 2.5$	398.5	409.7	55	15.1	14.7	477.5	484.2	71.6	97.7	338.2	361.9

In Tab. B.1 we present the properties of the median profiles: the median r_{500}, the validation radius $r_{\rm valid}$ (which is equal to the maximum convergence radius in the MDPL2 simulation $r_{\rm conv}^{\rm MDPL2}$), the inner and outer limits of the region where at least 50 per cent of the sample contributes to the median $[r_{\rm in}^{50\%}, r_{\rm in}^{50\%}]$ (i.e. the threshold used for our analysis), and the inner and outer limits of the region where *all* the clusters contribute to the median $[r_{\rm in}^{100\%}, r_{\rm out}^{100\%}]$. Note that the range of interest (i.e. about the peak position) always resides inside the region where *all* clusters contribute to the median ($x_{\rm peak} \sim 0.3 - 0.8 \in [r_{\rm in}^{100\%}, r_{\rm out}^{100\%}]/r_{500}$ for every redshift). Moreover, up to $z < 2.5$ our "50 per cent criterion" only affects the outer median profile and *not* the inner one due to the validation radius we employed (i.e. $r_{\rm valid} > r_{\rm in}^{100\%}$). At higher redshift ($z \geq 2.5$) the validation radius does affect the inner limit. Since AHF uses adaptive binning based on the number of particles of a halo, at higher redshift the $[r_{\rm in}^{100\%}, r_{\rm out}^{100\%}]$ region becomes smaller. Nevertheless, the peak position $x_{\rm peak}$ is always well inside the 100 per cent region, thus, its determination is *insensitive* to the choice of the inner and outer limits threshold.

C Sec. 2.3 - Most massive haloes at each redshift

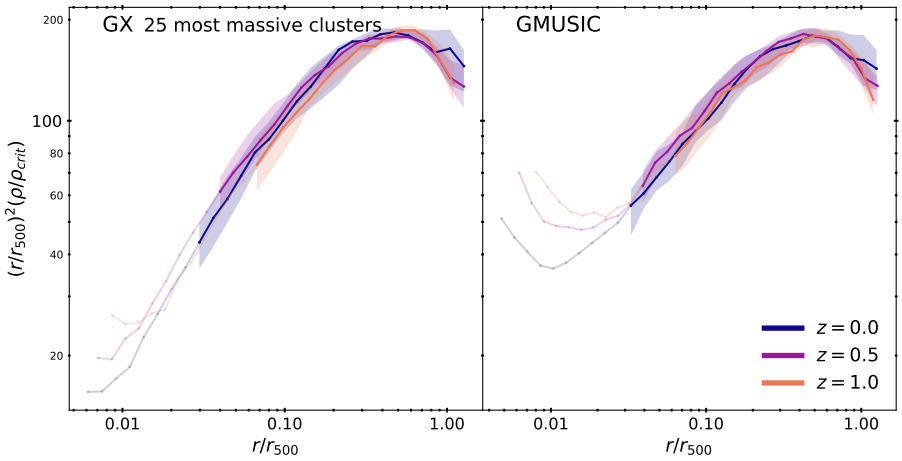

FIGURE C.1: Median scaled mass density profiles for the 25 most massive galaxy clusters at redshift $z = 0$, 0.5, and 1 for the two hydrodynamical simulations in the sample, `GADGET-X` (left) and `GADGET-MUSIC` (right). The shaded region shows the 30-70 percentiles. Unvalidated values are shown in lighter colours. The baryonic component of the clusters is reflected as a turnaround in the innermost region, at $r/r_{500} \sim 0.02$ and $r/r_{500} \sim 0.03$ at $z = 1$ for `GADGET-X` and `GADGET-MUSIC` , respectively. Although `GADGET-X` has implemented a model for AGN feedback, the self-similarity evolution is preserved.

The analysis presented in Sec. 2.3 traced a mass-complete sample, i.e. the central haloes of the 324 simulated $15h^{-1}$ Mpc regions, from redshift $z = 0$ backwards in time. While this allows us to directly measure and quantify the *evolution* of density profiles, the progenitors identified at any higher redshift certainly do not form a mass-complete sample anymore. This is why, for instance, LB+18 have chosen the alternative approach of always using the most massive clusters at each redshift studied. In order to test any differences entering the analysis due to these varying strategies, we have also restricted our analysis to the 25 most massive clusters at $z = 0$,0.5, and 1.0; we confirm that they do in fact form a mass-complete sample at each of these redshifts (see Sec. 2.2). In this way we extract a sample similar to that studied by LB+18.

TABLE C.1: Minimum, median, and maximum mass values of the 25 most massive haloes at each redshift (see Sec. 2.3 for further details). In each row, the left value corresponds to the GADGET-X simulation, the right one to GADGET-MUSIC . All values are in units of $10^{14}h^{-1}\mathrm{M}_{\odot}$.

Redshift	min(M_{200})		med(M_{200})		max(M_{200})	
	G-X	G-MUSIC	G-X	G-MUSIC	G-X	G-MUSIC
$z = 0$	13.57	13.81	15.76	15.68	26.21	26.22
$z = 0.5$	7.43	7.06	8.44	8.30	18.93	18.95
$z = 1$	3.68	3.78	4.16	4.23	6.90	6.89

In Tab. C.1 we show the minimum, median, and maximum M_{200} values for the 25 most massive cluster sample for both GADGET-X and GADGET-MUSIC . In Fig. C.1 we show the median scaled mass density profiles for the 25 most massive galaxy clusters at redshift $z = 0$, 0.5, and $z = 1$. In agreement with the results of LB+18, the mass distribution of massive galaxy clusters is in place at $z > 1$, despite the presence of non-gravitational radiative baryonic processes. Note that the baryonic turnaround in the profiles is more pronounced for GADGET-MUSIC . This is mainly attributed to an over-production of stars due to the lack of AGN feedback in the code. However, as we can see from the GADGET-X results, the AGN feedback is not strong enough to disrupt the total mass distribution considerably, thus the self-similarity of the profiles is preserved down to $r/r_{500} \approx 0.03$.

D Sec. 2.3 - Dark matter only simulation

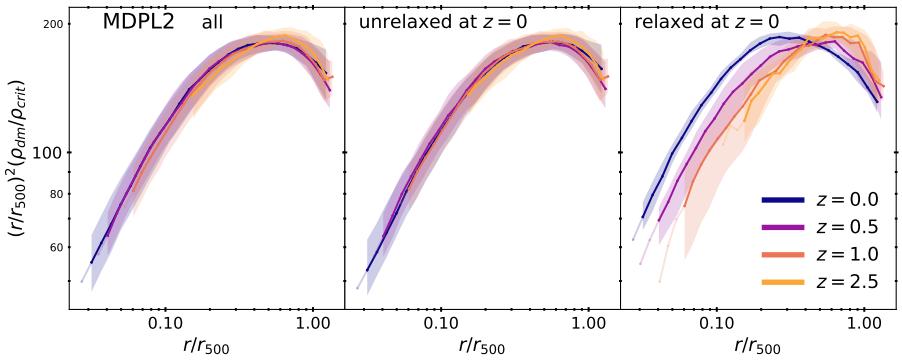

FIGURE D.1: Median scaled mass density profiles for 324 dark-matter-only central haloes from the MDPL2 simulation at redshift $z = 0$, 0.5, 1 and 2.5. Once classified by their dynamical state at $z = 0$, the relaxed subsample (~ 11 per cent of the total sample, right column) presents the same r_s evolution as the results from the hydrodynamical simulations.

In order to directly quantify any influence on our results stemming from the modelled baryonic physics, we have repeated all our analysis for the analogues of our clusters as found in the dark matter only MDPL2 simulation. Proceeding in a similar fashion, once classified by their dynamical state at $z = 0$, a similar shift is observed for the relaxed subsample (~ 11 per cent of the total sample) when tracking their progenitor's evolution– as can be verified in Fig. D.1. Thus, the baryonic influence can be safely attributed to the innermost region of the cluster; and therefore, it does not affect the results presented here and the conclusions drawn.

E Sec. 3.2 - Determination of the disc scale length of the M33 candidate

To obtain luminosities from the simulation we used the routines available from PYNBODY. The code uses the Padova simple stellar populations (SSPs) isochrones and evolutionary tracks (Marigo et al., 2008; Girardi et al., 2010), with no dust extinction, to create a table which returns, for a set of ages and metallicities, a magnitude in the desired photometric system[1] for an overview of the different settings available for the table). PYNBODY reads the star particle's ages and metallicities returned from the simulation and interpolates the aforementioned table to associate magnitudes/luminosities to each star particle, and consequently, to the M33 candidate.

The $i-$band surface brightness profile has been fitted to a Sersic bulge and two exponential discs components corresponding to the inner and outer discs. Consequently, we used the following intensity profiles:

$$\begin{aligned} I_{\rm bulge}(r) &= B_e \exp\left\{-b_n\left[(r/r_e)^{1/n}-1\right]\right\}, \\ I_{\rm disc,in}(r) &= D_{0,\rm in}\exp\left\{-r/h_{\rm d,in}\right\}, \text{ and} \\ I_{\rm disc,out}(r) &= D_{0,\rm out}\exp\left\{-r/h_{\rm d,out}\right\}, \end{aligned} \tag{E.1}$$

where n is the Sersic index, $b_n \approx 1.9992n - 0.3271$ (Capaccioli, 1989), r_e the effective radius, h_d the disc scale length, and B_e, D_0 the intensity at the effective radius and at $r = 0$, respectively. Thus, for the $i-$band, the surface brightness profile is:

$$\mu_i(r) = 25.73 - 2.5\log_{10} I_i(r) \text{ mag arcs}^{-2}, \tag{E.2}$$

where $I(r)$ is expressed in $L_\odot$ pc^{-2}.

TABLE E.1: Best-fit values for the surface brightness profile of the simulated M33 in the inclined configuration.

M33	$\mu_e(\mu_0)$[mag arcs^{-2}]	$r_e(h_d)$[kpc]	n
Bulge	21.2 ± 0.2	1.3 ± 0.1	1.3 ± 0.2
Inner disc	22.9 ± 0.2	3.3 ± 0.1	-
Outer disc	17.1 ± 0.7	1.68 ± 0.09	-

The fitting has been done in the following regions: the bulge, $r \leq 2$ kpc; inner disc, $5 \leq r \leq 14$ kpc; and outer disc, $16.5 \leq r \leq 23$ kpc. These regions were chosen in order to avoid radial ranges where we see an overlap of galactic components, and to minimise contamination from old stars at the outskirts of the galaxy $r \sim 30$ kpc. The same regions were used for the fit of the face-on view. The best-fit values for the inclined configuration are shown in Tab. E.1.

To obtain the y-axis normalisation value for the simulated profiles we used the inner disc fit models and best-fit parameters from Tab. E.1, and linearly interpolated the curves at the desired radial value $r = h_{\rm d}$. This has been done in order to avoid the contribution of

[1] see http://stev.oapd.inaf.it/cgi-bin/cmd

the bulge when determining the normalisation. On the other hand, since the observed M33 has no bulge component, we linearly interpolated the observational values directly at the (observational) disc scale length $h_d^{\mathrm{M33}} = 1.8$ kpc.

Bibliography

Aarseth, S. J., III Gott J. R., and E. L. Turner (Mar. 1979). "N-body simulations of galaxy clustering. I. Initial conditions and galaxy collapse times." In: *ApJ* 228, pp. 664–683. DOI: 10.1086/156892.

Abadi, M. G., B. Moore, and R. G. Bower (Oct. 1999). "Ram pressure stripping of spiral galaxies in clusters". In: *MNRAS* 308, pp. 947–954. DOI: 10.1046/j.1365-8711.1999.02715.x. eprint: astro-ph/9903436.

Abbott, T. M. C. et al. (Feb. 2019). "First Cosmology Results using Type Ia Supernovae from the Dark Energy Survey: Constraints on Cosmological Parameters". In: *ApJ* 872.2, L30, p. L30. DOI: 10.3847/2041-8213/ab04fa. arXiv: 1811.02374 [astro-ph.CO].

Addison, G. E. et al. (Feb. 2018). "Elucidating ΛCDM: Impact of Baryon Acoustic Oscillation Measurements on the Hubble Constant Discrepancy". In: *ApJ* 853.2, 119, p. 119. DOI: 10.3847/1538-4357/aaa1ed. arXiv: 1707.06547 [astro-ph.CO].

Agertz, Oscar, Romain Teyssier, and Ben Moore (Jan. 2011). "The formation of disc galaxies in a ΛCDM universe". In: *MNRAS* 410.2, pp. 1391–1408. DOI: 10.1111/j.1365-2966.2010.17530.x. arXiv: 1004.0005 [astro-ph.CO].

Allen, Steven W., August E. Evrard, and Adam B. Mantz (Sept. 2011). "Cosmological Parameters from Observations of Galaxy Clusters". In: *ARA&A* 49.1, pp. 409–470. DOI: 10.1146/annurev-astro-081710-102514. arXiv: 1103.4829 [astro-ph.CO].

Andersson, K. et al. (Sept. 2011). "X-Ray Properties of the First Sunyaev-Zel'dovich Effect Selected Galaxy Cluster Sample from the South Pole Telescope". In: *ApJ* 738.1, 48, p. 48. DOI: 10.1088/0004-637X/738/1/48. arXiv: 1006.3068 [astro-ph.CO].

Ansarifard, S. et al. (Feb. 2020). "The Three Hundred Project: Correcting for the hydrostatic-equilibrium mass bias in X-ray and SZ surveys". In: *A&A* 634, A113, A113. DOI: 10.1051/0004-6361/201936742. arXiv: 1911.07878 [astro-ph.CO].

Appel, A. W. (Jan. 1985). "An Efficient Program for Many-Body Simulation". In: *SIAM Journal on Scientific and Statistical Computing* 6.1, pp. 85–103.

Arthur, Jake et al. (2017). "nIFTy galaxy cluster simulations - V. Investigation of the cluster infall region". In: *MNRAS* 464.2, pp. 2027–2038. DOI: 10.1093/mnras/stw2424. arXiv: 1609.07311 [astro-ph.GA].

Arthur, Jake et al. (2019). "THETHREEHUNDRED Project: ram pressure and gas content of haloes and subhaloes in the phase-space plane". In: *MNRAS* 484.3, pp. 3968–3983. DOI: 10.1093/mnras/stz212. arXiv: 1901.05969 [astro-ph.GA].

Ascasibar, Y., Y. Hoffman, and S. Gottlöber (Mar. 2007). "Secondary infall and dark matter haloes". In: *MNRAS* 376, pp. 393–404. DOI: 10.1111/j.1365-2966.2007.11439.x. eprint: astro-ph/0609713.

Ascasibar, Y. et al. (Aug. 2004). "On the physical origin of dark matter density profiles". In: *MNRAS* 352, pp. 1109–1120. DOI: 10.1111/j.1365-2966.2004.08005.x. eprint: astro-ph/0312221.

Athanassoula, E. et al. (May 2000). "Optimal softening for force calculations in collisionless N-body simulations". In: *MNRAS* 314.3, pp. 475–488. DOI: 10.1046/j.1365-8711.2000.03316.x. arXiv: astro-ph/9912467 [astro-ph].

Bahé, Yannick M. and Ian G. McCarthy (Feb. 2015). "Star formation quenching in simulated group and cluster galaxies: when, how, and why?" In: *MNRAS* 447.1, pp. 969–992. DOI: 10.1093/mnras/stu2293. arXiv: 1410.8161 [astro-ph.GA].

Bahé, Yannick M. et al. (2017). "The Hydrangea simulations: galaxy formation in and around massive clusters". In: *MNRAS* 470.4, pp. 4186–4208. DOI: 10.1093/mnras/stx1403. arXiv: 1703.10610 [astro-ph.GA].

Bailin, J. and M. Steinmetz (July 2005). "Internal and External Alignment of the Shapes and Angular Momenta of ΛCDM Halos". In: *ApJ* 627, pp. 647–665. DOI: 10.1086/430397. eprint: arXiv:astro-ph/0408163.

Bakos, J., I. Trujillo, and M. Pohlen (Aug. 2008). "Color Profiles of Spiral Galaxies: Clues on Outer-Disk Formation Scenarios". In: *ApJ* 683, L103, p. L103. DOI: 10.1086/591671. arXiv: 0807.2776.

Baldry, I. K., K. Glazebrook, and S. P. Driver (Aug. 2008). "On the galaxy stellar mass function, the mass-metallicity relation and the implied baryonic mass function". In: *MNRAS* 388, pp. 945–959. DOI: 10.1111/j.1365-2966.2008.13348.x. arXiv: 0804.2892.

Baldry, Ivan K. et al. (Jan. 2004). "Quantifying the Bimodal Color-Magnitude Distribution of Galaxies". In: *ApJ* 600.2, pp. 681–694. DOI: 10.1086/380092. arXiv: astro-ph/0309710 [astro-ph].

Balogh, Michael L., Julio F. Navarro, and Simon L. Morris (Sept. 2000). "The Origin of Star Formation Gradients in Rich Galaxy Clusters". In: *ApJ* 540.1, pp. 113–121. DOI: 10.1086/309323. arXiv: astro-ph/0004078 [astro-ph].

Barker, M. K. et al. (Jan. 2011). "The star formation history in the far outer disc of M33". In: *MNRAS* 410, pp. 504–516. DOI: 10.1111/j.1365-2966.2010.17458.x. arXiv: 1008.0760.

Barnes, David J. et al. (2017a). "The Cluster-EAGLE project: global properties of simulated clusters with resolved galaxies". In: *MNRAS* 471.1, pp. 1088–1106. DOI: 10.1093/mnras/stx1647. arXiv: 1703.10907 [astro-ph.GA].

Barnes, David J. et al. (Feb. 2017b). "The redshift evolution of massive galaxy clusters in the MACSIS simulations". In: *MNRAS* 465.1, pp. 213–233. DOI: 10.1093/mnras/stw2722. arXiv: 1607.04569 [astro-ph.CO].

Barnes, J. and P. Hut (Dec. 1986). "A Hierarchical O(NlogN) Force-Calculation Algorithm". In: *Nature* 324, pp. 446–449.

Baron, Dalya (Apr. 2019). "Machine Learning in Astronomy: a practical overview". In: *arXiv e-prints*, arXiv:1904.07248, arXiv:1904.07248. arXiv: 1904.07248 [astro-ph.IM].

Bartalucci, I. et al. (Dec. 2017a). "Recovering galaxy cluster gas density profiles with XMM-Newton and Chandra". In: *A&A* 608, A88, A88. DOI: 10.1051/0004-6361/201731689.

Bartalucci, I. et al. (Feb. 2017b). "Resolving galaxy cluster gas properties at z ?? 1 with XMM-Newton and Chandra". In: *A&A* 598, A61, A61. DOI: 10.1051/0004-6361/201629509.

Baumann, Daniel (July 2009). "TASI Lectures on Inflation". In: *arXiv e-prints*, arXiv:0907.5424, arXiv:0907.5424. arXiv: 0907.5424 [hep-th].

Beck, A. M. et al. (Jan. 2016). "An improved SPH scheme for cosmological simulations". In: *MNRAS* 455, pp. 2110–2130. DOI: 10.1093/mnras/stv2443. arXiv: 1502.07358.

Behroozi, P. et al. (Dec. 2015). "Major mergers going Notts: challenges for modern halo finders". In: *MNRAS* 454, pp. 3020–3029. DOI: 10.1093/mnras/stv2046. arXiv: 1506.01405.

Behroozi, P. S., R. H. Wechsler, and H.-Y. Wu (Jan. 2013). "The ROCKSTAR Phase-space Temporal Halo Finder and the Velocity Offsets of Cluster Cores". In: *ApJ* 762, 109, p. 109. DOI: 10.1088/0004-637X/762/2/109. arXiv: 1110.4372 [astro-ph.CO].

Behroozi, Peter S. et al. (2014). "Mergers and Mass Accretion for Infalling Halos Both End Well Outside Cluster Virial Radii". In: *ApJ* 787.2, 156, p. 156. DOI: 10.1088/0004-637X/787/2/156. arXiv: 1310.2239 [astro-ph.CO].

Bell, Eric F. et al. (June 2004). "Nearly 5000 Distant Early-Type Galaxies in COMBO-17: A Red Sequence and Its Evolution since z∼1". In: *ApJ* 608.2, pp. 752–767. DOI: 10.1086/420778. arXiv: astro-ph/0303394 [astro-ph].

Benítez-Llambay, A. et al. (May 2014). "The Imprint of Reionization on the Star Formation Histories of Dwarf Galaxies". In: *ArXiv e-prints*. arXiv: 1405.5540.

Benitez-Llambay, Alejandro (July 2015). *py-sphviewer: Py-SPHViewer v1.0.0*. DOI: 10.5281/zenodo.21703. URL: http://dx.doi.org/10.5281/zenodo.21703.

Benítez-Llambay, Alejandro et al. (Feb. 2013). "Dwarf Galaxies and the Cosmic Web". In: *ApJ* 763.2, L41, p. L41. DOI: 10.1088/2041-8205/763/2/L41. arXiv: 1211.0536 [astro-ph.CO].

Bensby, T., S. Feltzing, and M. S. Oey (Feb. 2014). "Exploring the Milky Way stellar disk. A detailed elemental abundance study of 714 F and G dwarf stars in the solar neighbourhood". In: *A&A* 562, A71, A71. DOI: 10.1051/0004-6361/201322631. arXiv: 1309.2631.

Benson, A. J. (Oct. 2010). "Galaxy formation theory". In: *Phys. Rep.* 495, pp. 33–86. DOI: 10.1016/j.physrep.2010.06.001. arXiv: 1006.5394.

Benson, A. J. et al. (Dec. 2003). "What Shapes the Luminosity Function of Galaxies?" In: *ApJ* 599, pp. 38–49.

Benson, Andrew J. (Feb. 2012). "G ALACTICUS: A semi-analytic model of galaxy formation". In: *New Astron.* 17.2, pp. 175–197. DOI: 10.1016/j.newast.2011.07.004. arXiv: 1008.1786 [astro-ph.CO].

Berger, M. J. and P. Colella (May 1989). "Local Adaptive Mesh Refinement for Shock Hydrodynamics". In: *Journal of Computational Physics* 82.1, pp. 64–84. DOI: 10.1016/0021-9991(89)90035-1.

Bernyk, M. et al. (Mar. 2016). "The Theoretical Astrophysical Observatory: Cloud-based Mock Galaxy Catalogs". In: *ApJS* 223, 9, p. 9. DOI: 10.3847/0067-0049/223/1/9. arXiv: 1403.5270 [astro-ph.GA].

Biffi, V. et al. (Aug. 2016). "On the Nature of Hydrostatic Equilibrium in Galaxy Clusters". In: *ApJ* 827.2, 112, p. 112. DOI: 10.3847/0004-637X/827/2/112. arXiv: 1606.02293 [astro-ph.CO].

Bird, J. C. et al. (Aug. 2013). "Inside out and Upside down: Tracing the Assembly of a Simulated Disk Galaxy Using Mono-age Stellar Populations". In: *ApJ* 773, 43, p. 43. DOI: 10.1088/0004-637X/773/1/43. arXiv: 1301.0620.

Biviano, A. et al. (Nov. 2017). "The concentration-mass relation of clusters of galaxies from the OmegaWINGS survey". In: *A&A* 607, A81, A81. DOI: 10.1051/0004-6361/201731289. arXiv: 1708.07349 [astro-ph.CO].

Bluck, Asa F. L. et al. (2014). "Bulge mass is king: the dominant role of the bulge in determining the fraction of passive galaxies in the Sloan Digital Sky Survey". In: *MNRAS* 441.1, pp. 599–629. DOI: 10.1093/mnras/stu594. arXiv: 1403.5269 [astro-ph.GA].

Bluck, Asa F. L. et al. (2019). "What shapes a galaxy? - unraveling the role of mass, environment, and star formation in forming galactic structure". In: *MNRAS* 485.1, pp. 666–696. DOI: 10.1093/mnras/stz363. arXiv: 1902.01665 [astro-ph.GA].

Blumenthal, G. R. et al. (Oct. 1984). "Formation of galaxies and large-scale structure with cold dark matter." In: *Nature* 311, pp. 517–525. DOI: 10.1038/311517a0.

Blumenthal, G. R. et al. (Feb. 1986). "Contraction of dark matter galactic halos due to baryonic infall". In: *ApJ* 301, pp. 27–34. DOI: 10.1086/163867.

Bocquet, Sebastian et al. (Mar. 2016). "Halo mass function: baryon impact, fitting formulae, and implications for cluster cosmology". In: *MNRAS* 456.3, pp. 2361–2373. DOI: 10.1093/mnras/stv2657. arXiv: 1502.07357 [astro-ph.CO].

Bonamente, Massimiliano et al. (Mar. 2008). "Scaling Relations from Sunyaev-Zel'dovich Effect and Chandra X-Ray Measurements of High-Redshift Galaxy Clusters". In: *ApJ* 675.1, pp. 106–114. DOI: 10.1086/525517. arXiv: 0708.0815 [astro-ph].

Bond, J. R. et al. (Jan. 1984). "Dark matter and shocked pancakes". In: *NATO Advanced Science Institutes (ASI) Series C*. Ed. by J. Audouze and J. Tran Thanh Van. Vol. 117. NATO Advanced Science Institutes (ASI) Series C, p. 87.

Bono, G. et al. (June 2010). "On the Stellar Content of the Carina Dwarf Spheroidal Galaxy". In: *PASP* 122.892, p. 651. DOI: 10.1086/653590. arXiv: 1004.2559 [astro-ph.GA].

Bower, R. G. (June 1997). "The Entropy-Driven X-ray Evolution of Galaxy Clusters". In: *MNRAS* 288, pp. 355–364. DOI: 10.1093/mnras/288.2.355. eprint: astro-ph/9701014.

Bower, R. G. et al. (Oct. 2010). "The parameter space of galaxy formation". In: *MNRAS* 407.4, pp. 2017–2045. DOI: 10.1111/j.1365-2966.2010.16991.x. arXiv: 1004.0711 [astro-ph.CO].

Brackbill, J. U. and D. C. Barnes (May 1980). "The Effect of Nonzero $\nabla \cdot$ B on the numerical solution of the magnetohydrodynamic equations". In: *Journal of Computational Physics* 35.3, pp. 426–430. DOI: 10.1016/0021-9991(80)90079-0.

Bromm, Volker and Naoki Yoshida (Sept. 2011). "The First Galaxies". In: *ARA&A* 49.1, pp. 373–407. DOI: 10.1146/annurev-astro-081710-102608. arXiv: 1102.4638 [astro-ph.CO].

Brook, C. B. et al. (Sept. 2004). "The Emergence of the Thick Disk in a Cold Dark Matter Universe". In: *ApJ* 612, pp. 894–899. DOI: 10.1086/422709. eprint: astro-ph/0405306.

Brook, C. B. et al. (Oct. 2012). "Thin disc, thick disc and halo in a simulated galaxy". In: *MNRAS* 426, pp. 690–700. DOI: 10.1111/j.1365-2966.2012.21738.x. arXiv: 1206.0740.

Brough, Sarah et al. (2017). "The SAMI Galaxy Survey: Mass as the Driver of the Kinematic Morphology-Density Relation in Clusters". In: *ApJ* 844.1, 59, p. 59. DOI: 10.3847/1538-4357/aa7a11. arXiv: 1704.01169 [astro-ph.GA].

Bryan, G. L. and M. L. Norman (Mar. 1998). "Statistical Properties of X-Ray Clusters: Analytic and Numerical Comparisons". In: *ApJ* 495, pp. 80–+. DOI: 10.1086/305262. eprint: arXiv:astro-ph/9710107.

Bullock, J. S. et al. (Mar. 2001). "Profiles of dark haloes: evolution, scatter and environment". In: *MNRAS* 321, pp. 559–575. eprint: arXiv:astro-ph/9908159.

Bullock, James S. and Kathryn V. Johnston (Dec. 2005). "Tracing Galaxy Formation with Stellar Halos. I. Methods". In: *ApJ* 635.2, pp. 931–949. DOI: 10.1086/497422. arXiv: astro-ph/0506467 [astro-ph].

Burke, C. and C. A. Collins (Oct. 2013). "Growth of brightest cluster galaxies via mergers since z=1". In: *MNRAS* 434, pp. 2856–2865. DOI: 10.1093/mnras/stt1192. arXiv: 1307.1702.

Burkert, A. et al. (2016). "The Angular Momentum Distribution and Baryon Content of Star-forming Galaxies at z 1-3". In: *ApJ* 826.2, 214, p. 214. DOI: 10.3847/0004-637X/826/2/214. arXiv: 1510.03262 [astro-ph.GA].

Burstein, D. (Dec. 1979). "Structure and origin of S0 galaxies. III - The luminosity distribution perpendicular to the plane of the disks in S0's". In: *ApJ* 234, pp. 829–836. DOI: 10.1086/157563.

Capaccioli, M. (1989). "Photometry of early-type galaxies and the R exp 1/4 law". In: *World of Galaxies (Le Monde des Galaxies)*. Ed. by H. G. Corwin Jr. and L. Bottinelli, pp. 208–227.

Cappellari, Michele et al. (2011). "The ATLAS^{3D} project - VII. A new look at the morphology of nearby galaxies: the kinematic morphology-density relation". In: *MNRAS* 416.3, pp. 1680–1696. DOI: 10.1111/j.1365-2966.2011.18600.x. arXiv: 1104.3545 [astro-ph.CO].

Carlesi, E. et al. (July 2012). "N-body simulations with a cosmic vector for dark energy". In: *MNRAS* 424, pp. 699–715. DOI: 10.1111/j.1365-2966.2012.21258.x. arXiv: 1205.1695 [astro-ph.CO].

Carlesi, E. et al. (May 2016). "Constrained Local UniversE Simulations: a Local Group factory". In: *MNRAS* 458, pp. 900–911. DOI: 10.1093/mnras/stw357. arXiv: 1602.03919.

Chabrier, G. (July 2003). "Galactic Stellar and Substellar Initial Mass Function". In: *PASP* 115, pp. 763–795. DOI: 10.1086/376392. eprint: astro-ph/0304382.

Chiappini, C., F. Matteucci, and R. Gratton (Mar. 1997). "The Chemical Evolution of the Galaxy: The Two-Infall Model". In: *ApJ* 477, pp. 765–780. DOI: 10.1086/303726. eprint: astro-ph/9609199.

Chiu, I. et al. (Aug. 2018). "Baryon content in a sample of 91 galaxy clusters selected by the South Pole Telescope at 0.2 <z < 1.25". In: *MNRAS* 478.3, pp. 3072–3099. DOI: 10.1093/mnras/sty1284. arXiv: 1711.00917 [astro-ph.CO].

Colella, P. and Paul R. Woodward (Sept. 1984). "The Piecewise Parabolic Method (PPM) for Gas-Dynamical Simulations". In: *Journal of Computational Physics* 54, pp. 174–201. DOI: 10.1016/0021-9991(84)90143-8.

Comerford, Julia M. and Priyamvada Natarajan (July 2007). "The observed concentration-mass relation for galaxy clusters". In: *MNRAS* 379.1, pp. 190–200. DOI: 10.1111/j.1365-2966.2007.11934.x. arXiv: astro-ph/0703126 [astro-ph].

Cora, Sofía A. et al. (Sept. 2018). "Semi-analytic galaxies - I. Synthesis of environmental and star-forming regulation mechanisms". In: *MNRAS* 479.1, pp. 2–24. DOI: 10.1093/mnras/sty1131. arXiv: 1801.03883 [astro-ph.GA].

Corbelli, E. and S. E. Schneider (Apr. 1997). "A Warped Disk Model for M33 and the 21 Centimeter Line Width in Spiral Galaxies". In: *ApJ* 479, pp. 244–257. DOI: 10.1086/303849. eprint: astro-ph/9610087.

Corbelli, E. et al. (Dec. 2014). "Dynamical signatures of a ΛCDM-halo and the distribution of the baryons in M 33". In: *A&A* 572, A23, A23. DOI: 10.1051/0004-6361/201424033. arXiv: 1409.2665.

Corbelli, Edvige and Paolo Salucci (Jan. 2000). "The extended rotation curve and the dark matter halo of M33". In: *MNRAS* 311.2, pp. 441–447. DOI: 10.1046/j.1365-8711.2000.03075.x. arXiv: astro-ph/9909252 [astro-ph].

Correa, Camila A. et al. (2017). "The relation between galaxy morphology and colour in the EAGLE simulation". In: *MNRAS* 472.1, pp. L45–L49. DOI: 10.1093/mnrasl/slx133. arXiv: 1704.06283 [astro-ph.GA].

Cortese, L. et al. (2016). "The SAMI Galaxy Survey: the link between angular momentum and optical morphology". In: *MNRAS* 463.1, pp. 170–184. DOI: 10.1093/mnras/stw1891. arXiv: 1608.00291 [astro-ph.GA].

Cortese, L. et al. (2019). "The SAMI Galaxy Survey: satellite galaxies undergo little structural change during their quenching phase". In: *MNRAS* 485.2, pp. 2656–2665. DOI: 10.1093/mnras/stz485. arXiv: 1902.05652 [astro-ph.GA].

Crain, Robert A. et al. (2015). "The EAGLE simulations of galaxy formation: calibration of subgrid physics and model variations". In: *MNRAS* 450.2, pp. 1937–1961. DOI: 10.1093/mnras/stv725. arXiv: 1501.01311 [astro-ph.GA].

Croton, D. J. et al. (Feb. 2016). "Semi-Analytic Galaxy Evolution (SAGE): Model Calibration and Basic Results". In: *ApJS* 222, 22, p. 22. DOI: 10.3847/0067-0049/222/2/22. arXiv: 1601.04709.

Cui, W. et al. (Jan. 2017). "On the dynamical state of galaxy clusters: insights from cosmological simulations - II." In: *MNRAS* 464, pp. 2502–2510. DOI: 10.1093/mnras/stw2567. arXiv: 1605.07617.

Cui, W. et al. (Nov. 2018). "The Three Hundred project: a large catalogue of theoretically modelled galaxy clusters for cosmological and astrophysical applications". In: *MNRAS* 480, pp. 2898–2915. DOI: 10.1093/mnras/sty2111. arXiv: 1809.04622.

Cui, Weiguang, Stefano Borgani, and Giuseppe Murante (June 2014). "The effect of active galactic nuclei feedback on the halo mass function". In: *MNRAS* 441.2, pp. 1769–1782. DOI: 10.1093/mnras/stu673. arXiv: 1402.1493 [astro-ph.CO].

Cui, Weiguang and Youcai Zhang (2017). "The Impact of Baryons on the Large-Scale Structure of the Universe". In: *Trends in Modern Cosmology*, p. 7. DOI: 10.5772/68116.

Cui, Weiguang et al. (Oct. 2011). "Properties of fossil groups in cosmological simulations and galaxy formation models". In: *MNRAS* 416.4, pp. 2997–3008. DOI: 10.1111/j.1365-2966.2011.19248.x. arXiv: 1102.4269 [astro-ph.CO].

Cui, Weiguang et al. (July 2012). "The effects of baryons on the halo mass function". In: *MNRAS* 423.3, pp. 2279–2287. DOI: 10.1111/j.1365-2966.2012.21037.x. arXiv: 1111.3066 [astro-ph.CO].

Cui, Weiguang et al. (Jan. 2014). "Characterizing diffused stellar light in simulated galaxy clusters". In: *MNRAS* 437.1, pp. 816–830. DOI: 10.1093/mnras/stt1940. arXiv: 1310.1396 [astro-ph.CO].

Cui, Weiguang et al. (Mar. 2016a). "How does our choice of observable influence our estimation of the centre of a galaxy cluster? Insights from cosmological simulations". In: *MNRAS* 456.3, pp. 2566–2575. DOI: 10.1093/mnras/stv2839. arXiv: 1512.01253 [astro-ph.GA].

Cui, Weiguang et al. (2016b). "nIFTy galaxy cluster simulations - IV. Quantifying the influence of baryons on halo properties". In: *MNRAS* 458.4, pp. 4052–4073. DOI: 10.1093/mnras/stw603. arXiv: 1602.06668 [astro-ph.GA].

da Silva, Antonio C. et al. (Sept. 2000). "Hydrodynamical simulations of the Sunyaev-Zel'dovich effect". In: *MNRAS* 317.1, pp. 37–44. DOI: 10.1046/j.1365-8711.2000.03553.x. arXiv: astro-ph/9907224 [astro-ph].

Dalla Vecchia, Claudio and Joop Schaye (Oct. 2012). "Simulating galactic outflows with thermal supernova feedback". In: *MNRAS* 426.1, pp. 140–158. DOI: 10.1111/j.1365-2966.2012.21704.x. arXiv: 1203.5667 [astro-ph.GA].

Davis, M. et al. (May 1985). "The evolution of large-scale structure in a universe dominated by cold dark matter". In: *ApJ* 292, pp. 371–394. DOI: 10.1086/163168.

del Pino, Andrés et al. (Aug. 2013). "Spatial dependence of the star formation history in the central regions of the Fornax dwarf spheroidal galaxy". In: *MNRAS* 433.2, pp. 1505–1516. DOI: 10.1093/mnras/stt833. arXiv: 1305.2166 [astro-ph.CO].

DESI Collaboration et al. (Oct. 2016). "The DESI Experiment Part I: Science,Targeting, and Survey Design". In: *arXiv e-prints*, arXiv:1611.00036, arXiv:1611.00036. arXiv: 1611.00036 [astro-ph.IM].

Devriendt, J. E. G., B. Guiderdoni, and R. Sadat (Oct. 1999). "Galaxy modelling. I. Spectral energy distributions from far-UV to sub-mm wavelengths". In: *A&A* 350, pp. 381–398. eprint: arXiv:astro-ph/9906332.

Di Cintio, A. et al. (Oct. 2011). "Too small to succeed? Lighting up massive dark matter subhaloes of the Milky Way". In: *MNRAS* 417, pp. L74–L78. DOI: 10.1111/j.1745-3933.2011.01123.x. arXiv: 1107.5045 [astro-ph.CO].

Di Cintio, A. et al. (June 2012). "Applying scale-free mass estimators to the Local Group in Constrained Local Universe Simulations". In: *MNRAS* 423, pp. 1883–1895. DOI: 10.1111/j.1365-2966.2012.21013.x. arXiv: 1204.0005.

Di Cintio, Arianna et al. (2020). "Pericentric passage-driven star formation bursts in satellite galaxies and their hosts in hydrodynamical simulations of the Local Group".

Diemand, J., M. Kuhlen, and P. Madau (Sept. 2006). "Early Supersymmetric Cold Dark Matter Substructure". In: *ApJ* 649, pp. 1–13. DOI: 10.1086/506377. eprint: arXiv:astro-ph/0603250.

Diemer, B. and A. V. Kravtsov (July 2014). "Dependence of the Outer Density Profiles of Halos on Their Mass Accretion Rate". In: *ApJ* 789, 1, p. 1. DOI: 10.1088/0004-637X/789/1/1. arXiv: 1401.1216.

Diemer, B., S. More, and A. V. Kravtsov (Mar. 2013). "The Pseudo-evolution of Halo Mass". In: *ApJ* 766, 25, p. 25. DOI: 10.1088/0004-637X/766/1/25. arXiv: 1207.0816 [astro-ph.CO].

Dixon, Keri L. et al. (June 2018). "Reionization of the Milky Way, M31, and their satellites - I. Reionization history and star formation". In: *MNRAS* 477.1, pp. 867–881. DOI: 10.1093/mnras/sty494. arXiv: 1703.06140 [astro-ph.GA].

Dolag, K., A. M. Bykov, and A. Diaferio (Feb. 2008). "Non-Thermal Processes in Cosmological Simulations". In: *Space Sci. Rev.* 134.1-4, pp. 311–335. DOI: 10.1007/s11214-008-9319-2. arXiv: 0801.1048 [astro-ph].

Dolag, K., E. Komatsu, and R. Sunyaev (Dec. 2016). "SZ effects in the Magneticum Pathfinder simulation: comparison with the Planck, SPT, and ACT results". In: *MNRAS* 463.2, pp. 1797–1811. DOI: 10.1093/mnras/stw2035. arXiv: 1509.05134 [astro-ph.CO].

Dolag, K. et al. (Mar. 2004). "Numerical study of halo concentrations in dark-energy cosmologies". In: *A&A* 416, pp. 853–864. DOI: 10.1051/0004-6361:20031757. arXiv: astro-ph/0309771 [astro-ph].

Dolag, K. et al. (Feb. 2008). "Simulation Techniques for Cosmological Simulations". In: *Space Sci. Rev.* 134.1-4, pp. 229–268. DOI: 10.1007/s11214-008-9316-5. arXiv: 0801.1023 [astro-ph].

Dolphin, A. E. (Oct. 2000). "WFPC2 Stellar Photometry with HSTPHOT". In: *PASP* 112, pp. 1383–1396. DOI: 10.1086/316630. eprint: astro-ph/0006217.

Dolphin, Andrew E. et al. (June 2005). "Star Formation Histories of Local Group Dwarf Galaxies". In: *arXiv e-prints*, astro-ph/0506430, astro–ph/0506430. arXiv: astro-ph/0506430 [astro-ph].

Doroshkevich, A. G. (1970). "The space structure of perturbations and the origin of rotation of galaxies in the theory of fluctuation." In: *Astrofizika* 6, pp. 581–600.

Dressler, A. (Mar. 1980). "Galaxy morphology in rich clusters: implications for the formation and evolution of galaxies." In: *ApJ* 236, pp. 351–365. DOI: 10.1086/157753.

Dutton, Aaron A. and Frank C. van den Bosch (2012). "The angular momentum of disc galaxies: implications for gas accretion, outflows, and dynamical friction". In: *MNRAS* 421.1, pp. 608–620. DOI: 10.1111/j.1365-2966.2011.20339.x. arXiv: 1108.0663 [astro-ph.CO].

Eckert, D. et al. (May 2012). "The gas distribution in the outer regions of galaxy clusters". In: *A&A* 541, A57, A57. DOI: 10.1051/0004-6361/201118281. arXiv: 1111.0020.

Eckert, D. et al. (June 2016). "The XXL Survey. XIII. Baryon content of the bright cluster sample". In: *A&A* 592, A12, A12. DOI: 10.1051/0004-6361/201527293. arXiv: 1512.03814 [astro-ph.CO].

Eckert, D. et al. (Mar. 2017). "The XMM cluster outskirts project (X-COP)". In: *Astronomische Nachrichten* 338.293, pp. 293–298. DOI: 10.1002/asna.201713345. arXiv: 1611.05051 [astro-ph.CO].

Efstathiou, George (Jan. 2001). "CMB Anisotropies and the Determination of Cosmological Parameters". In: *NATO ASIC Proc. 565: Structure Formation in the Universe*. Ed. by Robert G. Crittenden and Neil G. Turok. Vol. 565, p. 179. arXiv: astro-ph/0002249 [astro-ph].

Efstathiou, George and Steven Gratton (May 2020). "The evidence for a spatially flat Universe". In: *MNRAS* 496.1, pp. L91–L95. DOI: 10.1093/mnrasl/slaa093. arXiv: 2002.06892 [astro-ph.CO].

Elahi, Pascal J. et al. (2016). "nIFTY galaxy cluster simulations - III. The similarity and diversity of galaxies and subhaloes". In: *MNRAS* 458.1, pp. 1096–1116. DOI: 10.1093/mnras/stw338. arXiv: 1511.08255 [astro-ph.GA].

Elahi, Pascal J. et al. (May 2019). "Hunting for galaxies and halos in simulations with VELOCIraptor". In: *Publ. Astron. Soc. Australia* 36, e021, e021. DOI: 10.1017/pasa.2019.12. arXiv: 1902.01010 [astro-ph.CO].

Emsellem, Eric et al. (2007). "The SAURON project - IX. A kinematic classification for early-type galaxies". In: *MNRAS* 379.2, pp. 401–417. DOI: 10.1111/j.1365-2966.2007.11752.x. arXiv: astro-ph/0703531 [astro-ph].

Errani, Raphaël and Jorge Peñarrubia (Feb. 2020). "Can tides disrupt cold dark matter subhaloes?" In: *MNRAS* 491.4, pp. 4591–4601. DOI: 10.1093/mnras/stz3349. arXiv: 1906.01642 [astro-ph.GA].

Euclid Collaboration et al. (Oct. 2019). "Euclid preparation: VII. Forecast validation for Euclid cosmological probes". In: *arXiv e-prints*, arXiv:1910.09273, arXiv:1910.09273. arXiv: 1910.09273 [astro-ph.CO].

Evrard, August E., Christopher A. Metzler, and Julio F. Navarro (Oct. 1996). "Mass Estimates of X-Ray Clusters". In: *ApJ* 469, p. 494. DOI: 10.1086/177798. arXiv: astro-ph/9510058 [astro-ph].

Fakhouri, Onsi, Chung-Pei Ma, and Michael Boylan-Kolchin (Aug. 2010). "The merger rates and mass assembly histories of dark matter haloes in the two Millennium simulations". In: *MNRAS* 406.4, pp. 2267–2278. DOI: 10.1111/j.1365-2966.2010.16859.x. arXiv: 1001.2304 [astro-ph.CO].

Fall, S. M. (1983). "Galaxy formation - Some comparisons between theory and observation". In: *Internal Kinematics and Dynamics of Galaxies*. Ed. by E. Athanassoula. Vol. 100. IAU Symposium, pp. 391–398.

Fall, S. M. and G. Efstathiou (1980). "Formation and rotation of disc galaxies with haloes." In: *MNRAS* 193, pp. 189–206. DOI: 10.1093/mnras/193.2.189.

Fall, S. Michael and Aaron J. Romanowsky (2018). "Angular Momentum and Galaxy Formation Revisited: Scaling Relations for Disks and Bulges". In: *ApJ* 868.2, 133, p. 133. DOI: 10.3847/1538-4357/aaeb27. arXiv: 1808.02525 [astro-ph.GA].

Feng, Jonathan L. (Sept. 2010). "Dark Matter Candidates from Particle Physics and Methods of Detection". In: *ARA&A* 48, pp. 495–545. DOI: 10.1146/annurev-astro-082708-101659. arXiv: 1003.0904 [astro-ph.CO].

Ferguson, A. et al. (2007). "Resolving the Stellar Outskirts of M31 and M33". In: *Astrophysics and Space Science Proceedings* 3, p. 239. DOI: 10.1007/978-1-4020-5573-7_39. eprint: astro-ph/0601121.

Few, C. G. et al. (Nov. 2012). "Properties of simulated Milky Way-mass galaxies in loose group and field environments". In: *A&A* 547, A63, A63. DOI: 10.1051/0004-6361/201219649. arXiv: 1210.1030.

Fillingham, Sean P. et al. (June 2019). "Characterizing the Infall Times and Quenching Timescales of Milky Way Satellites with *Gaia* Proper Motions". In: *arXiv e-prints*, arXiv:1906.04180, arXiv:1906.04180. arXiv: 1906.04180 [astro-ph.GA].

Fixsen, D. J. (Dec. 2009). "The Temperature of the Cosmic Microwave Background". In: *ApJ* 707.2, pp. 916–920. DOI: 10.1088/0004-637X/707/2/916. arXiv: 0911.1955 [astro-ph.CO].

Freedman, Wendy L. and Barry F. Madore (Sept. 2010). "The Hubble Constant". In: *ARA&A* 48, pp. 673–710. DOI: 10.1146/annurev-astro-082708-101829. arXiv: 1004.1856 [astro-ph.CO].

Fritz, T. K. et al. (Nov. 2018). "Gaia DR2 proper motions of dwarf galaxies within 420 kpc. Orbits, Milky Way mass, tidal influences, planar alignments, and group infall". In: *A&A* 619, A103, A103. DOI: 10.1051/0004-6361/201833343. arXiv: 1805.00908 [astro-ph.GA].

Fuhrmann, K. (Feb. 2008). "Nearby stars of the Galactic disc and halo - IV". In: *MNRAS* 384, pp. 173–224. DOI: 10.1111/j.1365-2966.2007.12671.x.

Fujii, Michiko, Yoko Funato, and Junichiro Makino (Aug. 2006). "Dynamical Friction on Satellite Galaxies". In: *PASJ* 58, pp. 743–752. DOI: 10.1093/pasj/58.4.743. arXiv: astro-ph/0511651 [astro-ph].

Fujita, Y. (Apr. 2001). "Ram-Pressure Stripping of Galaxies in High-Redshift Clusters and the Influence of Intracluster Medium Heating". In: *ApJ* 550, pp. 612–621. DOI: 10.1086/319811. eprint: astro-ph/0012252.

— (Feb. 2004). "Pre-Processing of Galaxies before Entering a Cluster". In: *PASJ* 56, pp. 29–43. DOI: 10.1093/pasj/56.1.29. eprint: astro-ph/0311193.

Fujita, Yutaka (Dec. 1998). "Quantitative Estimates of Environmental Effects on the Star Formation Rate of Disk Galaxies in Clusters of Galaxies". In: *ApJ* 509.2, pp. 587–594. DOI: 10.1086/306518. arXiv: astro-ph/9807120 [astro-ph].

Gaia Collaboration et al. (Aug. 2018a). "Gaia Data Release 2. Kinematics of globular clusters and dwarf galaxies around the Milky Way". In: *A&A* 616, A12, A12. DOI: 10.1051/0004-6361/201832698. arXiv: 1804.09381 [astro-ph.GA].

Gaia Collaboration et al. (Aug. 2018b). "Gaia Data Release 2. Summary of the contents and survey properties". In: *A&A* 616, A1, A1. DOI: 10.1051/0004-6361/201833051. arXiv: 1804.09365 [astro-ph.GA].

Gallart, Carme et al. (Nov. 1999). "The Star Formation History of the Local Group Dwarf Galaxy Leo I". In: *AJ* 118.5, pp. 2245–2261. DOI: 10.1086/301078. arXiv: astro-ph/9906121 [astro-ph].

Genina, Anna et al. (Sept. 2019). "The distinct stellar metallicity populations of simulated Local Group dwarfs". In: *MNRAS* 488.2, pp. 2312–2331. DOI: 10.1093/mnras/stz1852. arXiv: 1812.04839 [astro-ph.GA].

Ghirardini, V. et al. (Apr. 2018). "The universal thermodynamic properties of the intracluster medium over two decades in radius in the X-COP sample". In: *ArXiv e-prints*. arXiv: 1805.00042.

Gill, S. P. D., A. Knebe, and B. K. Gibson (June 2004). "The evolution of substructure - I. A new identification method". In: *MNRAS* 351, pp. 399–409. DOI: 10.1111/j.1365-2966.2004.07786.x. eprint: arXiv:astro-ph/0404258.

— (Feb. 2005). "The evolution of substructure - III. The outskirts of clusters". In: *MNRAS* 356, pp. 1327–1332. DOI: 10.1111/j.1365-2966.2004.08562.x. eprint: arXiv:astro-ph/0404427.

Gill, S. P. D. et al. (June 2004). "The evolution of substructure - II. Linking dynamics to environment". In: *MNRAS* 351, pp. 410–422. DOI: 10.1111/j.1365-2966.2004.07913.x. eprint: arXiv:astro-ph/0404255.

Gilmore, G. and N. Reid (Mar. 1983). "New light on faint stars. III - Galactic structure towards the South Pole and the Galactic thick disc". In: *MNRAS* 202, pp. 1025–1047. DOI: 10.1093/mnras/202.4.1025.

Gingold, R. A. and J. J. Monaghan (Nov. 1977). "Smoothed particle hydrodynamics - Theory and application to non-spherical stars". In: *MNRAS* 181, pp. 375–389.

Girardi, L. et al. (Dec. 2010). "The ACS Nearby Galaxy Survey Treasury. IX. Constraining Asymptotic Giant Branch Evolution with Old Metal-poor Galaxies". In: *ApJ* 724, pp. 1030–1043. DOI: 10.1088/0004-637X/724/2/1030. arXiv: 1009.4618 [astro-ph.SR].

Gnedin, Nickolay Y. (Apr. 1995). "Softened Lagrangian Hydrodynamics for Cosmology". In: *ApJS* 97, p. 231. DOI: 10.1086/192141.

Gnedin, O. Y. et al. (Nov. 2004). "Response of Dark Matter Halos to Condensation of Baryons: Cosmological Simulations and Improved Adiabatic Contraction Model". In: *ApJ* 616, pp. 16–26. DOI: 10.1086/424914. eprint: arXiv:astro-ph/0406247.

Godunov, Sergei K. (1959). "A difference method for numerical calculation of discontinuous solutions of the equations of hydrodynamics". In: *Mat. Sb. (N.S.)* 47(89).3, pp. 271–306.

Gonzalez, Anthony H., Dennis Zaritsky, and Ann I. Zabludoff (Sept. 2007). "A Census of Baryons in Galaxy Clusters and Groups". In: *ApJ* 666.1, pp. 147–155. DOI: 10.1086/519729. arXiv: 0705.1726 [astro-ph].

Gonzalez, Anthony H. et al. (Nov. 2013). "Galaxy Cluster Baryon Fractions Revisited". In: *ApJ* 778.1, 14, p. 14. DOI: 10.1088/0004-637X/778/1/14. arXiv: 1309.3565 [astro-ph.CO].

Gott III, J. R. and M. J. Rees (Dec. 1975). "A theory of galaxy formation and clustering". In: *A&A* 45, pp. 365–376.

Gottlöber, Stefan, Yehuda Hoffman, and Gustavo Yepes (2010). "Constrained Local UniversE Simulations (CLUES)". In: *High Performance Computing in Science and Engineering, Garching/Munich 2009: Transactions of the Fourth Joint HLRB and KONWIHR Review and Results Workshop, Dec. 8-9, 2009, Leibniz Supercomputing Centre, Garching/Munich, Germany*. Ed. by Siegfried Wagner et al. Berlin, Heidelberg: Springer Berlin Heidelberg, pp. 309–322. ISBN: 978-3-642-13872-0. DOI: 10.1007/978-3-642-13872-0_26. URL: http://dx.doi.org/10.1007/978-3-642-13872-0_26.

Graham, Mark T. et al. (2019). "SDSS-IV MaNGA: New benchmark for the connection between stellar angular momentum and environment: a study of about 900 groups/clusters". In: *arXiv e-prints*, arXiv:1910.05139, arXiv:1910.05139. arXiv: 1910.05139 [astro-ph.GA].

Grebel, Eva K., III Gallagher John S., and Daniel Harbeck (Apr. 2003). "The Progenitors of Dwarf Spheroidal Galaxies". In: *AJ* 125.4, pp. 1926–1939. DOI: 10.1086/368363. arXiv: astro-ph/0301025 [astro-ph].

Groener, A. M., D. M. Goldberg, and M. Sereno (Jan. 2016). "The galaxy cluster concentration-mass scaling relation". In: *MNRAS* 455.1, pp. 892–919. DOI: 10.1093/mnras/stv2341. arXiv: 1510.01961 [astro-ph.CO].

Gunn, J. E. (Dec. 1977). "Massive galactic halos. I - Formation and evolution". In: *ApJ* 218, pp. 592–598. DOI: 10.1086/155715.

Gunn, J. E. and J. R. Gott III (Aug. 1972). "On the Infall of Matter Into Clusters of Galaxies and Some Effects on Their Evolution". In: *ApJ* 176, p. 1. DOI: 10.1086/151605.

Guo, Q. et al. (May 2010). "How do galaxies populate dark matter haloes?" In: *MNRAS* 404, pp. 1111–1120. DOI: 10.1111/j.1365-2966.2010.16341.x. arXiv: 0909.4305 [astro-ph.CO].

Guo, Q. et al. (Oct. 2016). "Galaxies in the EAGLE hydrodynamical simulation and in the Durham and Munich semi-analytical models". In: *MNRAS* 461, pp. 3457–3482. DOI: 10.1093/mnras/stw1525. arXiv: 1512.00015.

Haardt, F. and P. Madau (Apr. 1996). "Radiative Transfer in a Clumpy Universe. II. The Ultraviolet Extragalactic Background". In: *ApJ* 461, pp. 20–+. DOI: 10.1086/177035. eprint: arXiv:astro-ph/9509093.

— (2001). "Modelling the UV/X-ray cosmic background with CUBA". In: *Clusters of Galaxies and the High Redshift Universe Observed in X-rays*. Ed. by D. M. Neumann and J. T. V. Tran, #64. eprint: astro-ph/0106018.

Haggar, Roan et al. (2020). "The Three Hundred Project: Backsplash galaxies in simulations of clusters". In: *MNRAS*. Submitted to MNRAS.

Hahn, O. et al. (Oct. 2007). "The evolution of dark matter halo properties in clusters, filaments, sheets and voids". In: *MNRAS* 381, pp. 41–51. DOI: 10.1111/j.1365-2966.2007.12249.x. arXiv: 0704.2595.

Hahn, Oliver et al. (Sept. 2017). "rhapsody-g simulations - I. The cool cores, hot gas and stellar content of massive galaxy clusters". In: *MNRAS* 470.1, pp. 166–186. DOI: 10.1093/mnras/stx001. arXiv: 1509.04289 [astro-ph.CO].

Harrison, C. M. et al. (2017). "The KMOS Redshift One Spectroscopic Survey (KROSS): rotational velocities and angular momentum of $z \approx 0.9$ galaxies". In: *MNRAS* 467.2, pp. 1965–1983. DOI: 10.1093/mnras/stx217. arXiv: 1701.05561 [astro-ph.GA].

Hashimoto, Yasuhiro and Jr. Oemler Augustus (2000). "The Effect of Environment on Galaxy Interactions". In: *ApJ* 530.2, pp. 652–659. DOI: 10.1086/308383.

Hayashi, E. et al. (Feb. 2003). "The Structural Evolution of Substructure". In: *ApJ* 584, pp. 541–558. DOI: 10.1086/345788. eprint: arXiv:astro-ph/0203004.

Haywood, M. et al. (2013). "The age structure of stellar populations in the solar vicinity. Clues of a two-phase formation history of the Milky Way disk". In: *A&A* 560, A109. eprint: 1305.4663.

Henden, Nicholas A. et al. (Oct. 2018). "The FABLE simulations: a feedback model for galaxies, groups, and clusters". In: *MNRAS* 479.4, pp. 5385–5412. DOI: 10.1093/mnras/sty1780. arXiv: 1804.05064 [astro-ph.GA].

Hobbs, A. et al. (Sept. 2013). "Thermal instabilities in cooling galactic coronae: fuelling star formation in galactic discs". In: *MNRAS* 434, pp. 1849–1868. DOI: 10.1093/mnras/stt977. arXiv: 1207.3814.

Hockney, R. W., S. P. Goel, and J. W. Eastwood (Feb. 1974). "Quiet High-Resolution Computer Models of a Plasma". In: *Journal of Computational Physics* 14.2, pp. 148–158. DOI: 10.1016/0021-9991(74)90010-2.

Hoffman, Yehuda and Erez Ribak (Oct. 1991). "Constrained Realizations of Gaussian Fields: A Simple Algorithm". In: *ApJ* 380, p. L5. DOI: 10.1086/186160.

Hopkins, Philip F. (Feb. 2013). "A general class of Lagrangian smoothed particle hydrodynamics methods and implications for fluid mixing problems". In: *MNRAS* 428.4, pp. 2840–2856. DOI: 10.1093/mnras/sts210. arXiv: 1206.5006 [astro-ph.IM].

Hubble, E. P. (1926). "Extragalactic nebulae." In: *ApJ* 64, pp. 321–369. DOI: 10.1086/143018.

Hurley-Keller, Denise, Mario Mateo, and James Nemec (May 1998). "The Star Formation History of the Carina Dwarf Galaxy". In: *AJ* 115.5, pp. 1840–1855. DOI: 10.1086/300326. arXiv: astro-ph/9804058 [astro-ph].

Jiang, Ing-Guey and James Binney (May 2000). "The orbit and mass of the Sagittarius dwarf galaxy". In: *MNRAS* 314.3, pp. 468–474. DOI: 10.1046/j.1365-8711.2000.03311.x. arXiv: astro-ph/9908025 [astro-ph].

Kaiser, N. (Sept. 1986). "Evolution and clustering of rich clusters". In: *MNRAS* 222, pp. 323–345. DOI: 10.1093/mnras/222.2.323.

Kam, S. Z. et al. (Aug. 2017). "H i Kinematics and Mass Distribution of Messier 33". In: *AJ* 154, 41, p. 41. DOI: 10.3847/1538-3881/aa79f3.

Karachentsev, I. D. et al. (Apr. 2004). "A Catalog of Neighboring Galaxies". In: *AJ* 127, pp. 2031–2068. DOI: 10.1086/382905.

Katz, N. et al. (Oct. 1994). "Formation of Quasars at High Redshift". In: *MNRAS* 270, p. L71. DOI: 10.1093/mnras/270.1.L71.

Katz, Neal and Simon D. M. White (Aug. 1993). "Hierarchical Galaxy Formation: Overmerging and the Formation of an X-Ray Cluster". In: *ApJ* 412, p. 455. DOI: 10.1086/172935.

Kennicutt Jr., R. C. (1998). "Overview: The Initial Mass Function in Galaxies". In: *The Stellar Initial Mass Function (38th Herstmonceux Conference)*. Ed. by G. Gilmore & D. Howell. Vol. 142. Astronomical Society of the Pacific Conference Series, pp. 1–+.

Klimentowski, J. et al. (Mar. 2010). "The grouping, merging and survival of subhaloes in the simulated Local Group". In: *MNRAS* 402, pp. 1899–1910. DOI: 10.1111/j.1365-2966.2009.16024.x. arXiv: 0909.1916.

Klypin, A. et al. (June 2001). "Resolving the Structure of Cold Dark Matter Halos". In: *ApJ* 554, pp. 903–915. DOI: 10.1086/321400. eprint: arXiv:astro-ph/0006343.

Klypin, A. et al. (Oct. 2003). "Constrained Simulations of the Real Universe: The Local Supercluster". In: *ApJ* 596, pp. 19–33. DOI: 10.1086/377574. eprint: arXiv:astro-ph/0107104.

Klypin, A. et al. (Apr. 2016). "MultiDark simulations: the story of dark matter halo concentrations and density profiles". In: *MNRAS* 457, pp. 4340–4359. DOI: 10.1093/mnras/stw248. arXiv: 1411.4001.

Klypin, A. A. and S. F. Shandarin (Sept. 1983). "Three-dimensional numerical model of the formation of large-scale structure in the Universe". In: *MNRAS* 204, pp. 891–907.

Knebe, A. and A. Domínguez (2003). "On the Reliability of Initial Conditions for Dissipationless Cosmological Simulations". In: *Publications of the Astronomical Society of Australia* 20, pp. 173–183. DOI: 10.1071/AS02039. eprint: arXiv:astro-ph/0201490.

Knebe, A. et al. (May 2008). "On the relation between the radial alignment of dark matter subhaloes and host mass in cosmological simulations". In: *MNRAS* 386, pp. L52–L56. DOI: 10.1111/j.1745-3933.2008.00459.x. eprint: arXiv:0802.1917.

Knebe, A. et al. (June 2010). "The impact of baryonic physics on the shape and radial alignment of substructures in cosmological dark matter haloes". In: *MNRAS* 405, pp. 1119–1128. DOI: 10.1111/j.1365-2966.2010.16514.x. arXiv: 1002.2853 [astro-ph.CO].

Knebe, A. et al. (Aug. 2011a). "Haloes gone MAD: The Halo-Finder Comparison Project". In: *MNRAS* 415, pp. 2293–2318. DOI: 10.1111/j.1365-2966.2011.18858.x. arXiv: 1104.0949 [astro-ph.CO].

Knebe, A. et al. (Mar. 2011b). "The luminosities of backsplash galaxies in constrained simulations of the Local Group". In: *MNRAS* 412, pp. 529–536. DOI: 10.1111/j.1365-2966.2010.17924.x. arXiv: 1010.5670 [astro-ph.CO].

Knebe, A. et al. (Jan. 2013a). "Galaxies going MAD: the Galaxy-Finder Comparison Project". In: *MNRAS* 428, pp. 2039–2052. DOI: 10.1093/mnras/sts173. arXiv: 1210.2578 [astro-ph.CO].

Knebe, A. et al. (Oct. 2013b). "Structure finding in cosmological simulations: the state of affairs". In: *MNRAS* 435, pp. 1618–1658. DOI: 10.1093/mnras/stt1403. arXiv: 1304.0585.

Knebe, A. et al. (Aug. 2015). "nIFTy cosmology: comparison of galaxy formation models". In: *MNRAS* 451, pp. 4029–4059. DOI: 10.1093/mnras/stv1149. arXiv: 1505.04607.

Knebe, Alexander et al. (May 2006). "The importance of interactions for mass loss from satellite galaxies in cold dark matter haloes". In: *MNRAS* 368.2, pp. 741–750. DOI: 10.1111/j.1365-2966.2006.10161.x. arXiv: astro-ph/0507380 [astro-ph].

Knebe, Alexander et al. (Apr. 2018). "Cosmic CARNage I: on the calibration of galaxy formation models". In: *MNRAS* 475.3, pp. 2936–2954. DOI: 10.1093/mnras/stx3274. arXiv: 1712.06420 [astro-ph.GA].

Knebe, Alexander et al. (May 2020). "The Three Hundred project: shapes and radial alignment of satellite, infalling, and backsplash galaxies". In: *MNRAS*. DOI: 10.1093/mnras/staa1407. arXiv: 2005.09896 [astro-ph.GA].

Knollmann, S. R. and A. Knebe (June 2009). "AHF: Amiga's Halo Finder". In: *ApJS* 182, pp. 608–624. DOI: 10.1088/0067-0049/182/2/608. arXiv: 0904.3662.

Kolatt, Tsafrir and Avishai Dekel (Apr. 1997). "Large-Scale Power Spectrum from Peculiar Velocities". In: *ApJ* 479.2, pp. 592–605. DOI: 10.1086/303894.

Kormendy, John and Ralf Bender (Jan. 2012). "A Revised Parallel-sequence Morphological Classification of Galaxies: Structure and Formation of S0 and Spheroidal Galaxies". In: *ApJS* 198.1, 2, p. 2. DOI: 10.1088/0067-0049/198/1/2. arXiv: 1110.4384 [astro-ph.CO].

Krajnović, Davor et al. (2013). "The ATLAS^{3D} project - XVII. Linking photometric and kinematic signatures of stellar discs in early-type galaxies". In: *MNRAS* 432.3, pp. 1768–1795. DOI: 10.1093/mnras/sts315. arXiv: 1210.8167 [astro-ph.CO].

Kravtsov, A. V., A. A. Klypin, and A. M. Khokhlov (July 1997). "Adaptive Refinement Tree: A New High-Resolution N-Body Code for Cosmological Simulations". In: *ApJS* 111, pp. 73–+. DOI: 10.1086/313015. eprint: arXiv:astro-ph/9701195.

Kravtsov, A. V., A. Vikhlinin, and D. Nagai (Oct. 2006). "A New Robust Low-Scatter X-Ray Mass Indicator for Clusters of Galaxies". In: *ApJ* 650, pp. 128–136. DOI: 10.1086/506319. eprint: astro-ph/0603205.

Kravtsov, A. V., A. A. Vikhlinin, and A. V. Meshcheryakov (Jan. 2018). "Stellar Mass—Halo Mass Relation and Star Formation Efficiency in High-Mass Halos". In: *Astronomy Letters* 44.1, pp. 8–34. DOI: 10.1134/S1063773717120015. arXiv: 1401.7329 [astro-ph.CO].

Kravtsov, Andrey V., Anatoly Klypin, and Yehuda Hoffman (June 2002). "Constrained Simulations of the Real Universe. II. Observational Signatures of Intergalactic Gas in the Local Supercluster Region". In: *ApJ* 571.2, pp. 563–575. DOI: 10.1086/340046. arXiv: astro-ph/0109077 [astro-ph].

Kuchner, Ulrike et al. (Apr. 2020). "Mapping and characterization of cosmic filaments in galaxy cluster outskirts: strategies and forecasts for observations from simulations". In: *MNRAS* 494.4, pp. 5473–5491. DOI: 10.1093/mnras/staa1083. arXiv: 2004.08408 [astro-ph.GA].

Lacey, C. and S. Cole (Dec. 1994). "Merger Rates in Hierarchical Models of Galaxy Formation - Part Two - Comparison with N-Body Simulations". In: *MNRAS* 271, pp. 676–+. eprint: arXiv:astro-ph/9402069.

Laganá, T. F. et al. (July 2013). "A comprehensive picture of baryons in groups and clusters of galaxies". In: *A&A* 555, A66, A66. DOI: 10.1051/0004-6361/201220423. arXiv: 1304.6061 [astro-ph.CO].

Lagos, Claudia del P. et al. (2017). "Angular momentum evolution of galaxies in EAGLE". In: *MNRAS* 464.4, pp. 3850–3870. DOI: 10.1093/mnras/stw2610. arXiv: 1609.01739 [astro-ph.GA].

Lagos, Claudia del P. et al. (2018a). "Quantifying the impact of mergers on the angular momentum of simulated galaxies". In: *MNRAS* 473.4, pp. 4956–4974. DOI: 10.1093/mnras/stx2667. arXiv: 1701.04407 [astro-ph.GA].

Lagos, Claudia del P. et al. (2018b). "The connection between mass, environment, and slow rotation in simulated galaxies". In: *MNRAS* 476.4, pp. 4327–4345. DOI: 10.1093/mnras/sty489. arXiv: 1712.01398 [astro-ph.GA].

Lavaux, G. (Aug. 2010). "Precision constrained simulation of the local Universe". In: *MNRAS* 406.2, pp. 1007–1013. DOI: 10.1111/j.1365-2966.2010.16719.x. arXiv: 0912.3525 [astro-ph.CO].

Le Brun, A. M. C. et al. (Jan. 2018). "Internal dark matter structure of the most massive galaxy clusters". In: *MNRAS* 473, pp. L69–L73. DOI: 10.1093/mnrasl/slx150. arXiv: 1709.07457.

Le Brun, Amandine M. C., Ian G. McCarthy, and Jean-Baptiste Melin (Aug. 2015). "Testing Sunyaev-Zel'dovich measurements of the hot gas content of dark matter haloes using synthetic skies". In: *MNRAS* 451.4, pp. 3868–3881. DOI: 10.1093/mnras/stv1172. arXiv: 1501.05666 [astro-ph.CO].

Le Brun, Amandine M. C. et al. (June 2014). "Towards a realistic population of simulated galaxy groups and clusters". In: *MNRAS* 441.2, pp. 1270–1290. DOI: 10.1093/mnras/stu608. arXiv: 1312.5462 [astro-ph.CO].

LeVeque, Randall J. (1992). *Numerical Methods for Conservation Laws*. Birkhäuser Basel, p. 220. DOI: 10.1007/978-3-0348-8629-1.

Li, Qingyang et al. (May 2020). "The Three Hundred Project: the stellar and gas profiles". In: *MNRAS*. DOI: 10.1093/mnras/staa1385. arXiv: 2005.06135 [astro-ph.GA].

Libeskind, N. I. et al. (Jan. 2010). "Constrained simulations of the Local Group: on the radial distribution of substructures". In: *MNRAS* 401, pp. 1889–1897. DOI: 10.1111/j.1365-2966.2009.15766.x. arXiv: 0909.4423.

Libeskind, N. I. et al. (Mar. 2011). "The preferred direction of infalling satellite galaxies in the Local Group". In: *MNRAS* 411, pp. 1525–1535. DOI: 10.1111/j.1365-2966.2010.17786.x. arXiv: 1010.1531 [astro-ph.CO].

Libeskind, N. I. et al. (Sept. 2015). "Planes of satellite galaxies and the cosmic web". In: *MNRAS* 452, pp. 1052–1059. DOI: 10.1093/mnras/stv1302. arXiv: 1503.05915.

Lin, Lihwai et al. (July 2008). "The Redshift Evolution of Wet, Dry, and Mixed Galaxy Mergers from Close Galaxy Pairs in the DEEP2 Galaxy Redshift Survey". In: *ApJ* 681.1, pp. 232–243. DOI: 10.1086/587928. arXiv: 0802.3004 [astro-ph].

Lin, Tongyan (Apr. 2019). "TASI lectures on dark matter models and direct detection". In: *arXiv e-prints*, arXiv:1904.07915, arXiv:1904.07915. arXiv: 1904.07915 [hep-ph].

Lin, Yen-Ting, Joseph J. Mohr, and S. Adam Stanford (Aug. 2004). "K-Band Properties of Galaxy Clusters and Groups: Luminosity Function, Radial Distribution, and Halo Occupation Number". In: *ApJ* 610.2, pp. 745–761. DOI: 10.1086/421714. arXiv: astro-ph/0402308 [astro-ph].

Lithwick, Y. and N. Dalal (June 2011). "Self-similar Solutions of Triaxial Dark Matter Halos". In: *ApJ* 734, 100, p. 100. DOI: 10.1088/0004-637X/734/2/100. arXiv: 1010.3723 [astro-ph.CO].

Łokas, E. L. and Y. Hoffman (Oct. 2000). "Formation of Cuspy Density Profiles: A Generic Feature of Collisionless Gravitational Collapse". In: *ApJ* 542, pp. L139–L142. DOI: 10.1086/312928. eprint: astro-ph/0005566.

Łokas, E. L. and G. A. Mamon (Feb. 2001). "Properties of spherical galaxies and clusters with an NFW density profile". In: *MNRAS* 321, pp. 155–166. DOI: 10.1046/j.1365-8711.2001.04007.x. eprint: arXiv:astro-ph/0002395.

Łokas, Ewa L. (June 2020). "Tidal evolution of galaxies in the most massive cluster of IllustrisTNG-100". In: *A&A* 638, A133, A133. DOI: 10.1051/0004-6361/202037643. arXiv: 2002.00610 [astro-ph.GA].

Lovisari, L., T. H. Reiprich, and G. Schellenberger (Jan. 2015). "Scaling properties of a complete X-ray selected galaxy group sample". In: *A&A* 573, A118, A118. DOI: 10.1051/0004-6361/201423954. arXiv: 1409.3845 [astro-ph.CO].

Malmquist, K. G. (Mar. 1922). "On some relations in stellar statistics". In: *Meddelanden fran Lunds Astronomiska Observatorium Serie I* 100, pp. 1–52.

— (Feb. 1925). "A contribution to the problem of determining the distribution in space of the stars". In: *Meddelanden fran Lunds Astronomiska Observatorium Serie I* 106, pp. 1–12.

Mantz, A. B., S. W. Allen, and R. G. Morris (Oct. 2016). "Cosmology and astrophysics from relaxed galaxy clusters - V. Consistency with cold dark matter structure formation". In: *MNRAS* 462.1, pp. 681–688. DOI: 10.1093/mnras/stw1707. arXiv: 1607.04686 [astro-ph.CO].

Mantz, A. B. et al. (May 2014). "Cosmology and astrophysics from relaxed galaxy clusters - II. Cosmological constraints". In: *MNRAS* 440.3, pp. 2077–2098. DOI: 10.1093/mnras/stu368. arXiv: 1402.6212 [astro-ph.CO].

Mantz, A. B. et al. (May 2015). "Cosmology and astrophysics from relaxed galaxy clusters - I. Sample selection". In: *MNRAS* 449, pp. 199–219. DOI: 10.1093/mnras/stv219. arXiv: 1502.06020.

Marigo, P. et al. (May 2008). "Evolution of asymptotic giant branch stars. II. Optical to far-infrared isochrones with improved TP-AGB models". In: *A&A* 482, pp. 883–905. DOI: 10.1051/0004-6361:20078467. arXiv: 0711.4922.

Marriage, Tobias A. et al. (Aug. 2011). "The Atacama Cosmology Telescope: Sunyaev-Zel'dovich-Selected Galaxy Clusters at 148 GHz in the 2008 Survey". In: *ApJ* 737.2, 61, p. 61. DOI: 10.1088/0004-637X/737/2/61. arXiv: 1010.1065 [astro-ph.CO].

Martín-Navarro, I. et al. (Dec. 2012). "A unified picture of breaks and truncations in spiral galaxies from SDSS and S^4G imaging". In: *MNRAS* 427, pp. 1102–1134. DOI: 10.1111/j.1365-2966.2012.21929.x. arXiv: 1208.2893 [astro-ph.CO].

Martín-Navarro, I. et al. (July 2014). "Stellar haloes outshine disc truncations in low-inclined spirals". In: *MNRAS* 441, pp. 2809–2814. DOI: 10.1093/mnras/stu767. arXiv: 1401.3749.

Martínez-Serrano, F. J. et al. (Nov. 2009). "Disk Galaxies with Broken Luminosity Profiles from Cosmological Simulations". In: *ApJ* 705, pp. L133–L137. DOI: 10.1088/0004-637X/705/2/L133. arXiv: 0906.1118 [astro-ph.GA].

Martinez-Vaquero, Luis A., Gustavo Yepes, and Yehuda Hoffman (July 2007). "Constrained simulations of the local universe - I. Mass and motion in the local volume". In: *MNRAS* 378.4, pp. 1601–1608. DOI: 10.1111/j.1365-2966.2007.11907.x. arXiv: 0704.3385 [astro-ph].

Mathis, H. et al. (July 2002). "Simulating the formation of the local galaxy population". In: *MNRAS* 333.4, pp. 739–762. DOI: 10.1046/j.1365-8711.2002.05447.x. arXiv: astro-ph/0111099 [astro-ph].

Maughan, B. J. et al. (Apr. 2012). "Self-similar scaling and evolution in the galaxy cluster X-ray luminosity-temperature relation". In: *MNRAS* 421, pp. 1583–1602. DOI: 10.1111/j.1365-2966.2012.20419.x. arXiv: 1108.1200.

Mayer, L. et al. (July 2006). "Simultaneous ram pressure and tidal stripping; how dwarf spheroidals lost their gas". In: *MNRAS* 369, pp. 1021–1038. DOI: 10.1111/j.1365-2966.2006.10403.x. eprint: arXiv:astro-ph/0504277.

Mayer, Lucio et al. (Oct. 2001). "The Metamorphosis of Tidally Stirred Dwarf Galaxies". In: *ApJ* 559.2, pp. 754–784. DOI: 10.1086/322356. arXiv: astro-ph/0103430 [astro-ph].

Mazzarini, Matteo et al. (Apr. 2020). "Simulations of satellite tidal debris in the Milky Way halo". In: *A&A* 636, A106, A106. DOI: 10.1051/0004-6361/202037558. arXiv: 2003.09464 [astro-ph.GA].

McCarthy, Ian G. et al. (Mar. 2017). "The BAHAMAS project: calibrated hydrodynamical simulations for large-scale structure cosmology". In: *MNRAS* 465.3, pp. 2936–2965. DOI: 10.1093/mnras/stw2792. arXiv: 1603.02702 [astro-ph.CO].

McDonald, M. et al. (July 2017). "The Remarkable Similarity of Massive Galaxy Clusters from z0 to z1.9". In: *ApJ* 843.1, 28, p. 28. DOI: 10.3847/1538-4357/aa7740. arXiv: 1702.05094 [astro-ph.CO].

Merten, J. et al. (June 2015). "CLASH: The Concentration-Mass Relation of Galaxy Clusters". In: *ApJ* 806.1, 4, p. 4. DOI: 10.1088/0004-637X/806/1/4. arXiv: 1404.1376 [astro-ph.CO].

Meszaros, P. (Dec. 1974). "The behaviour of point masses in an expanding cosmological substratum." In: *A&A* 37.2, pp. 225–228.

Miller, Tim B. et al. (2020). "Dynamical self-friction: how mass loss slows you down". In: *arXiv e-prints*, arXiv:2001.06489, arXiv:2001.06489. arXiv: 2001.06489 [astro-ph.GA].

Minchev, I., C. Chiappini, and M. Martig (Dec. 2014). "Chemodynamical evolution of the Milky Way disk. II. Variations with Galactic radius and height above the disk plane". In: *A&A* 572, A92, A92. DOI: 10.1051/0004-6361/201423487. arXiv: 1401.5796.

Minchev, I. et al. (May 2015). "On the Formation of Galactic Thick Disks". In: *ApJ* 804, L9, p. L9. DOI: 10.1088/2041-8205/804/1/L9. arXiv: 1502.06606.

Miyoshi, Takahiro and Masashi Chiba (Mar. 2020). "Long-term orbital evolution of Galactic satellites and the effects on their star formation histories". In: *arXiv e-prints*, arXiv:2003.07006, arXiv:2003.07006. arXiv: 2003.07006 [astro-ph.GA].

Mo, H. J., S. Mao, and S. D. M. White (Apr. 1998). "The formation of galactic discs". In: *MNRAS* 295, pp. 319–336. DOI: 10.1046/j.1365-8711.1998.01227.x. eprint: arXiv:astro-ph/9707093.

Monaco, P. et al. (July 2014). "A semi-analytic model comparison: testing cooling models against hydrodynamical simulations". In: *MNRAS* 441, pp. 2058–2077. DOI: 10.1093/mnras/stu655. arXiv: 1404.0811.

Monelli, M. et al. (July 2003). "The Carina Project. II. Stellar Populations". In: *AJ* 126.1, pp. 218–236. DOI: 10.1086/375457. arXiv: astro-ph/0303493 [astro-ph].

Moore, B. et al. (Feb. 1996). "Galaxy harassment and the evolution of clusters of galaxies". In: *Nature* 379, pp. 613–616. DOI: 10.1038/379613a0. eprint: arXiv:astro-ph/9510034.

Moore, B. et al. (May 2006). "Globular clusters, satellite galaxies and stellar haloes from early dark matter peaks". In: *MNRAS* 368, pp. 563–570. DOI: 10.1111/j.1365-2966.2006.10116.x. eprint: arXiv:astro-ph/0510370.

Moore, Ben, George Lake, and Neal Katz (Mar. 1998). "Morphological Transformation from Galaxy Harassment". In: *ApJ* 495.1, pp. 139–151. DOI: 10.1086/305264. arXiv: astro-ph/9701211 [astro-ph].

Moster, B. P. et al. (Feb. 2010). "Constraints on the Relationship between Stellar Mass and Halo Mass at Low and High Redshift". In: *ApJ* 710, pp. 903–923. DOI: 10.1088/0004-637X/710/2/903. arXiv: 0903.4682 [astro-ph.CO].

Moster, Benjamin P., Thorsten Naab, and Simon D. M. White (Feb. 2013). "Galactic star formation and accretion histories from matching galaxies to dark matter haloes". In: *MNRAS* 428.4, pp. 3121–3138. DOI: 10.1093/mnras/sts261. arXiv: 1205.5807 [astro-ph.CO].

Mostoghiu, R. et al. (2020a). "The Three Hundred Project: The stellar angular momentum evolution of cluster galaxies".

Mostoghiu, Robert et al. (2018). "CLUES about M33: the reversed radial stellar age gradient in the outskirts of Triangulum galaxy". In: *MNRAS* 480.4, pp. 4455–4467. DOI: 10.1093/mnras/sty2161. arXiv: 1808.03286 [astro-ph.GA].

Mostoghiu, Robert et al. (2019). "The Three Hundred Project: The evolution of galaxy cluster density profiles". In: *MNRAS* 483.3, pp. 3390–3403. DOI: 10.1093/mnras/sty3306. arXiv: 1812.04009 [astro-ph.GA].

Mostoghiu, Robert et al. (2020b). "The Three Hundred Project: The gas disruption of infalling objects in cluster environments".

Muldrew, S. I., F. R. Pearce, and C. Power (Feb. 2011). "The accuracy of subhalo detection". In: *MNRAS* 410, pp. 2617–2624. DOI: 10.1111/j.1365-2966.2010.17636.x. arXiv: 1008.2903 [astro-ph.CO].

Naab, Thorsten and Jeremiah P. Ostriker (Aug. 2017). "Theoretical Challenges in Galaxy Formation". In: *ARA&A* 55.1, pp. 59–109. DOI: 10.1146/annurev-astro-081913-040019. arXiv: 1612.06891 [astro-ph.GA].

Nagarajan, A. et al. (Sept. 2019). "Weak-lensing mass calibration of the Sunyaev-Zel'dovich effect using APEX-SZ galaxy clusters". In: *MNRAS* 488.2, pp. 1728–1759. DOI: 10.1093/mnras/sty1904. arXiv: 1804.03671 [astro-ph.CO].

Navarro, J. F., C. S. Frenk, and S. D. M. White (May 1996). "The Structure of Cold Dark Matter Halos". In: *ApJ* 462, p. 563. DOI: 10.1086/177173. eprint: arXiv:astro-ph/9508025.

— (Dec. 1997). "A Universal Density Profile from Hierarchical Clustering". In: *ApJ* 490, pp. 493–+. DOI: 10.1086/304888. eprint: arXiv:astro-ph/9611107.

Navarro, J. F. and S. D. M. White (Mar. 1994). "Simulations of dissipative galaxy formation in hierarchically clustering universes-2. Dynamics of the baryonic component in galactic haloes". In: *MNRAS* 267, pp. 401–412. DOI: 10.1093/mnras/267.2.401.

Neistein, Eyal and Simone M. Weinmann (July 2010). "The degeneracy of galaxy formation models". In: *MNRAS* 405.4, pp. 2717–2736. DOI: 10.1111/j.1365-2966.2010.16656.x. arXiv: 0911.3147 [astro-ph.CO].

Nelson, Dylan et al. (May 2019). "The IllustrisTNG simulations: public data release". In: *Computational Astrophysics and Cosmology* 6.1, 2, p. 2. DOI: 10.1186/s40668-019-0028-x. arXiv: 1812.05609 [astro-ph.GA].

Neto, A. F. et al. (Nov. 2007). "The statistics of Λ CDM halo concentrations". In: *MNRAS* 381, pp. 1450–1462. DOI: 10.1111/j.1365-2966.2007.12381.x. arXiv: 0706.2919.

Oñorbe, Jose et al. (Jan. 2014). "How to zoom: bias, contamination and Lagrange volumes in multimass cosmological simulations". In: *MNRAS* 437.2, pp. 1894–1908. DOI: 10.1093/mnras/stt2020. arXiv: 1305.6923 [astro-ph.CO].

Obreja, Aura et al. (2019). "NIHAO XVI: the properties and evolution of kinematically selected discs, bulges, and stellar haloes". In: *MNRAS* 487.3, pp. 4424–4456. DOI: 10.1093/mnras/stz1563. arXiv: 1804.06635 [astro-ph.GA].

Obreschkow, D. and K. Glazebrook (2014). "Fundamental Mass-Spin-Morphology Relation Of Spiral Galaxies". In: *ApJ* 784.1, 26, p. 26. DOI: 10.1088/0004-637X/784/1/26. arXiv: 1312.4543 [astro-ph.GA].

Ocvirk, P. et al. (Nov. 2013). "High-resolution Simulations of the Reionization of an Isolated Milky Way-M31 Galaxy Pair". In: *ApJ* 777.1, 51, p. 51. DOI: 10.1088/0004-637X/777/1/51. arXiv: 1310.0009 [astro-ph.CO].

Okabe, Nobuhiro and Graham P. Smith (Oct. 2016). "LoCuSS: weak-lensing mass calibration of galaxy clusters". In: *MNRAS* 461.4, pp. 3794–3821. DOI: 10.1093/mnras/stw1539. arXiv: 1507.04493 [astro-ph.CO].

Onions, J. et al. (Apr. 2012). "Subhaloes going Notts: the subhalo-finder comparison project". In: *MNRAS*, p. 2881. DOI: 10.1111/j.1365-2966.2012.20947.x. arXiv: 1203.3695 [astro-ph.CO].

Owers, M. S. et al. (June 2017). "The SAMI Galaxy Survey: the cluster redshift survey, target selection and cluster properties". In: *MNRAS* 468.2, pp. 1824–1849. DOI: 10.1093/mnras/stx562. arXiv: 1703.00997 [astro-ph.GA].

Park, Changbom et al. (2007). "Environmental Dependence of Properties of Galaxies in the Sloan Digital Sky Survey". In: *ApJ* 658.2, pp. 898–916. DOI: 10.1086/511059. arXiv: astro-ph/0611610 [astro-ph].

Pasetto, S. et al. (Jan. 2011). "Orbital evolution of the Carina dwarf galaxy and self-consistent determination of star formation history". In: *A&A* 525, A99, A99. DOI: 10.1051/0004-6361/200913415. arXiv: 1009.2758 [astro-ph.CO].

Patterson, F. S. (Dec. 1940). "The Luminosity Gradient of Messier 33". In: *Harvard College Observatory Bulletin* 914, pp. 9–10.

Peñarrubia, Jorge, Julio F. Navarro, and Alan W. McConnachie (Jan. 2008). "The Tidal Evolution of Local Group Dwarf Spheroidals". In: *ApJ* 673.1, pp. 226–240. DOI: 10.1086/523686. arXiv: 0708.3087 [astro-ph].

Pearce, F. R. et al. (Oct. 2000). "The effect of radiative cooling on the X-ray properties of galaxy clusters". In: *MNRAS* 317, pp. 1029–1040. DOI: 10.1046/j.1365-8711.2000.03773.x. eprint: astro-ph/9908062.

Peebles, P. J. E. (Feb. 1969). "Origin of the Angular Momentum of Galaxies". In: *ApJ* 155, pp. 393–+.

— (Feb. 1970). "Structure of the Coma Cluster of Galaxies". In: *AJ* 75, pp. 13–+.

— (1980). *The large-scale structure of the universe*.

Penzias, A. A. and R. W. Wilson (July 1965). "A Measurement of Excess Antenna Temperature at 4080 Mc/s." In: *ApJ* 142, pp. 419–421.

Pérez, E. et al. (Feb. 2013). "The Evolution of Galaxies Resolved in Space and Time: A View of Inside-out Growth from the CALIFA Survey". In: *ApJ* 764, L1, p. L1. DOI: 10.1088/2041-8205/764/1/L1. arXiv: 1301.1679 [astro-ph.CO].

Perlmutter, S. et al. (June 1999). "Measurements of Ω and Λ from 42 High-Redshift Supernovae". In: *ApJ* 517.2, pp. 565–586. DOI: 10.1086/307221. arXiv: astro-ph/9812133 [astro-ph].

Pierre, M. et al. (June 2016). "The XXL Survey. I. Scientific motivations - XMM-Newton observing plan - Follow-up observations and simulation programme". In: *A&A* 592, A1, A1. DOI: 10.1051/0004-6361/201526766. arXiv: 1512.04317 [astro-ph.CO].

Pilkington, K. et al. (Apr. 2012). "Metallicity gradients in disks. Do galaxies form inside-out?" In: *A&A* 540, A56, A56. DOI: 10.1051/0004-6361/201117466. arXiv: 1201.6359.

Pillepich, Annalisa et al. (Mar. 2018). "First results from the IllustrisTNG simulations: the stellar mass content of groups and clusters of galaxies". In: *MNRAS* 475.1, pp. 648–675. DOI: 10.1093/mnras/stx3112. arXiv: 1707.03406 [astro-ph.GA].

Planck Collaboration et al. (Nov. 2014). "Planck 2013 results. XVI. Cosmological parameters". In: *A&A* 571, A16, A16. DOI: 10.1051/0004-6361/201321591. arXiv: 1303.5076.

Planck Collaboration et al. (2016). "Planck 2015 results. XIII. Cosmological parameters". In: *A&A* 594, A13, A13. DOI: 10.1051/0004-6361/201525830. arXiv: 1502.01589 [astro-ph.CO].

Planck Collaboration et al. (July 2018a). "Planck 2018 results. I. Overview and the cosmological legacy of Planck". In: *arXiv e-prints*, arXiv:1807.06205, arXiv:1807.06205. arXiv: 1807.06205 [astro-ph.CO].

Planck Collaboration et al. (July 2018b). "Planck 2018 results. VI. Cosmological parameters". In: *arXiv e-prints*, arXiv:1807.06209, arXiv:1807.06209. arXiv: 1807.06209 [astro-ph.CO].

Planelles, S. et al. (May 2013). "Baryon census in hydrodynamical simulations of galaxy clusters". In: *MNRAS* 431.2, pp. 1487–1502. DOI: 10.1093/mnras/stt265. arXiv: 1209.5058 [astro-ph.CO].

Planelles, S. et al. (2017). "Pressure of the hot gas in simulations of galaxy clusters". In: *MNRAS* 467.4, pp. 3827–3847. DOI: 10.1093/mnras/stx318. arXiv: 1612.07260 [astro-ph.CO].

Plummer, H. C. (Mar. 1911). "On the Problem of Distribution in Globular Star Clusters". In: *MNRAS* 71, pp. 460–470.

Pontzen, A. et al. (May 2013). *pynbody: N-Body/SPH analysis for python*. Astrophysics Source Code Library. ascl: 1305.002.

Power, C. and A. Knebe (Aug. 2006). "The impact of box size on the properties of dark matter haloes in cosmological simulations". In: *MNRAS* 370, pp. 691–701. DOI: 10.1111/j.1365-2966.2006.10562.x. eprint: arXiv:astro-ph/0512281.

Power, C., A. Knebe, and S. R. Knollmann (Jan. 2012). "The dynamical state of dark matter haloes in cosmological simulations - I. Correlations with mass assembly history". In: *MNRAS* 419, pp. 1576–1587. DOI: 10.1111/j.1365-2966.2011.19820.x. arXiv: 1109.2671.

Power, C. et al. (Jan. 2003). "The inner structure of ΛCDM haloes - I. A numerical convergence study". In: *MNRAS* 338, pp. 14–34. DOI: 10.1046/j.1365-8711.2003.05925.x. eprint: arXiv:astro-ph/0201544.

Power, C. et al. (2018). "nIFTy Galaxy Cluster simulations VI: The gaseous outskirts of galaxy cluster". In: *arXiv e-prints*, arXiv:1810.00534, arXiv:1810.00534. arXiv: 1810.00534 [astro-ph.CO].

Price, Daniel J. (Feb. 2012). "Smoothed particle hydrodynamics and magnetohydrodynamics". In: *Journal of Computational Physics* 231.3, pp. 759–794. DOI: 10.1016/j.jcp.2010.12.011. arXiv: 1012.1885 [astro-ph.IM].

Puchwein, Ewald et al. (Aug. 2010). "Intracluster stars in simulations with active galactic nucleus feedback". In: *MNRAS* 406.2, pp. 936–951. DOI: 10.1111/j.1365-2966.2010.16786.x. arXiv: 1001.3018 [astro-ph.CO].

Pujol, A. et al. (Feb. 2017). "nIFTy Cosmology: the clustering consistency of galaxy formation models". In: *ArXiv e-prints*. arXiv: 1702.02620.

Ragone-Figueroa, C. et al. (Sept. 2018). "BCG mass evolution in cosmological hydro-simulations". In: *MNRAS* 479.1, pp. 1125–1136. DOI: 10.1093/mnras/sty1639. arXiv: 1803.08049 [astro-ph.GA].

Ragone-Figueroa, Cinthia et al. (Dec. 2013). "Brightest cluster galaxies in cosmological simulations: achievements and limitations of active galactic nuclei feedback models". In: *MNRAS* 436.2, pp. 1750–1764. DOI: 10.1093/mnras/stt1693. arXiv: 1308.3246 [astro-ph.CO].

Rasia, E. et al. (Oct. 2013). "On the Discrepancy between Theoretical and X-Ray Concentration-Mass Relations for Galaxy Clusters". In: *ApJ* 776.1, 39, p. 39. DOI: 10.1088/0004-637X/776/1/39. arXiv: 1301.7476 [astro-ph.CO].

Rasia, E. et al. (2015). "Cool Core Clusters from Cosmological Simulations". In: *ApJ* 813.1, L17, p. L17. DOI: 10.1088/2041-8205/813/1/L17. arXiv: 1509.04247 [astro-ph.CO].

Read, J. I. and T. Hayfield (June 2012). "SPHS: smoothed particle hydrodynamics with a higher order dissipation switch". In: *MNRAS* 422.4, pp. 3037–3055. DOI: 10.1111/j.1365-2966.2012.20819.x. arXiv: 1111.6985 [astro-ph.CO].

Recchi, Simone (Jan. 2014). "Chemodynamical Simulations of Dwarf Galaxy Evolution". In: *Advances in Astronomy* 2014, 750754, p. 750754. DOI: 10.1155/2014/750754. arXiv: 1310.4932 [astro-ph.CO].

Refregier, A. (2003). "Weak Gravitational Lensing by Large-Scale Structure". In: *ARA&A* 41, pp. 645–668. DOI: 10.1146/annurev.astro.41.111302.102207. eprint: arXiv:astro-ph/0307212.

Reiprich, T. H. and H. Böhringer (Mar. 2002). "The Mass Function of an X-Ray Flux-limited Sample of Galaxy Clusters". In: *ApJ* 567, pp. 716–740. DOI: 10.1086/338753. eprint: astro-ph/0111285.

Reiprich, T. H. et al. (Aug. 2013). "Outskirts of Galaxy Clusters". In: *Space Sci. Rev.* 177, pp. 195–245. DOI: 10.1007/s11214-013-9983-8. arXiv: 1303.3286.

Riess, Adam G. et al. (Sept. 1998). "Observational Evidence from Supernovae for an Accelerating Universe and a Cosmological Constant". In: *AJ* 116.3, pp. 1009–1038. DOI: 10.1086/300499. arXiv: astro-ph/9805201 [astro-ph].

Robotham, A. S. G. et al. (Apr. 2017). "PROFIT: Bayesian profile fitting of galaxy images". In: *MNRAS* 466.2, pp. 1513–1541. DOI: 10.1093/mnras/stw3039. arXiv: 1611.08586 [astro-ph.IM].

Robotham, A. S. G. et al. (May 2018). "ProFound: Source Extraction and Application to Modern Survey Data". In: *MNRAS* 476.3, pp. 3137–3159. DOI: 10.1093/mnras/sty440. arXiv: 1802.00937 [astro-ph.IM].

Rocha, Miguel, Annika H. G. Peter, and James Bullock (Sept. 2012). "Infall times for Milky Way satellites from their present-day kinematics". In: *MNRAS* 425.1, pp. 231–244. DOI: 10.1111/j.1365-2966.2012.21432.x. arXiv: 1110.0464 [astro-ph.CO].

Rodríguez-Puebla, Aldo et al. (Sept. 2017). "Constraining the galaxy-halo connection over the last 13.3 Gyr: star formation histories, galaxy mergers and structural properties". In: *MNRAS* 470.1, pp. 651–687. DOI: 10.1093/mnras/stx1172. arXiv: 1703.04542 [astro-ph.GA].

Romanowsky, Aaron J. and S. Michael Fall (2012). "Angular Momentum and Galaxy Formation Revisited". In: *ApJS* 203.2, 17, p. 17. DOI: 10.1088/0067-0049/203/2/17. arXiv: 1207.4189 [astro-ph.CO].

Roškar, R. et al. (Mar. 2008a). "Beyond Inside-Out Growth: Formation and Evolution of Disk Outskirts". In: *ApJ* 675, L65, p. L65. DOI: 10.1086/586734. arXiv: 0710.5523.

Roškar, R. et al. (Sept. 2008b). "Riding the Spiral Waves: Implications of Stellar Migration for the Properties of Galactic Disks". In: *ApJ* 684, L79, p. L79. DOI: 10.1086/592231. arXiv: 0808.0206.

Rubin, Vera C. and Jr. Ford W. Kent (Feb. 1970). "Rotation of the Andromeda Nebula from a Spectroscopic Survey of Emission Regions". In: *ApJ* 159, p. 379. DOI: 10.1086/150317.

Ruiz-Lara, T. et al. (Feb. 2016a). "No direct coupling between bending of galaxy disc stellar age and light profiles". In: *MNRAS* 456, pp. L35–L39. DOI: 10.1093/mnrasl/slv174. arXiv: 1511.03499.

Ruiz-Lara, T. et al. (Feb. 2016b). "The imprint of satellite accretion on the chemical and dynamical properties of disc galaxies". In: *A&A* 586, A112, A112. DOI: 10.1051/0004-6361/201526470. arXiv: 1512.00625.

Ruiz-Lara, T. et al. (Dec. 2017). "The role of stellar radial motions in shaping galaxy surface brightness profiles". In: *A&A* 608, A126, A126. DOI: 10.1051/0004-6361/201731485. arXiv: 1709.06968 [astro-ph.GA].

Ruiz-Lara, Tomás et al. (May 2020). "The recurrent impact of the Sagittarius dwarf on the star formation history of the Milky Way". In: *Nature Astronomy*. DOI: 10.1038/s41550-020-1097-0. arXiv: 2003.12577 [astro-ph.GA].

Ruppin, F. et al. (Dec. 2017). "First Sunyaev-Zel'dovich mapping with the NIKA2 camera: Implication of cluster substructures for the pressure profile and mass estimate". In: *ArXiv e-prints*, arXiv:1712.09587, arXiv:1712.09587. arXiv: 1712.09587.

Rusakov, V. et al. (Feb. 2020). "The bursty star formation history of the Fornax dwarf spheroidal galaxy revealed with the HST". In: *arXiv e-prints*, arXiv:2002.09714, arXiv:2002.09714. arXiv: 2002.09714 [astro-ph.GA].

Saad, Michel A. (1993). *Compressible Fluid Flow*. Pearson, p. 704. ISBN: 978-0131613737.

Sales, L. V. et al. (Aug. 2007). "Cosmic ménage à trois: the origin of satellite galaxies on extreme orbits". In: *MNRAS* 379, pp. 1475–1483. DOI: 10.1111/j.1365-2966.2007.12026.x. arXiv: 0704.1773.

Sales, Laura V., Amina Helmi, and Giuseppina Battaglia (Jan. 2010). "The Effect of Tidal Stripping on Composite Stellar Populations in Dwarf Spheroidal Galaxies". In: *Advances in Astronomy* 2010, 194345, p. 194345. DOI: 10.1155/2010/194345. arXiv: 0910.0471 [astro-ph.GA].

Sales, Laura V. et al. (2010). "Feedback and the structure of simulated galaxies at redshift z= 2". In: *MNRAS* 409.4, pp. 1541–1556. DOI: 10.1111/j.1365-2966.2010.17391.x. arXiv: 1004.5386 [astro-ph.CO].

Salpeter, E. E. (Jan. 1955). "The Luminosity Function and Stellar Evolution." In: *ApJ* 121, p. 161. DOI: 10.1086/145971.

Sánchez-Blázquez, P. et al. (Sept. 2009). "The origin of the light distribution in spiral galaxies". In: *MNRAS* 398, pp. 591–606. DOI: 10.1111/j.1365-2966.2009.15133.x. arXiv: 0905.4579.

Sánchez-Blázquez, P. et al. (Oct. 2014). "Stellar population gradients in galaxy discs from the CALIFA survey. The influence of bars". In: *A&A* 570, A6, A6. DOI: 10.1051/0004-6361/201423635. arXiv: 1407.0002.

Santos-Santos, I. M. et al. (Jan. 2016). "The distribution of mass components in simulated disc galaxies". In: *MNRAS* 455, pp. 476–483. DOI: 10.1093/mnras/stv2335. arXiv: 1510.02474.

Santos-Santos, I. M. E. et al. (June 2017). "Diversity of dwarf galaxy IR-submm emission patterns: CLUES from hydrodynamical simulations". In: *A&A* 603, A4, A4. DOI: 10.1051/0004-6361/201629426. arXiv: 1703.03419.

Saro, A. et al. (Aug. 2010). "Gas cooling in semi-analytic models and smoothed particle hydrodynamics simulations: are results consistent?" In: *MNRAS* 406, pp. 729–743. DOI: 10.1111/j.1365-2966.2010.16737.x. arXiv: 1001.3115 [astro-ph.CO].

Sartoris, B. et al. (June 2016). "Next generation cosmology: constraints from the Euclid galaxy cluster survey". In: *MNRAS* 459.2, pp. 1764–1780. DOI: 10.1093/mnras/stw630. arXiv: 1505.02165 [astro-ph.CO].

Savitzky, A. and M. J. E. Golay (1964). "Smoothing and differentiation of data by simplified least squares procedures". In: *Analytical Chemistry* 36, pp. 1627–1639.

Scannapieco, C. et al. (June 2012). "The Aquila comparison project: the effects of feedback and numerical methods on simulations of galaxy formation". In: *MNRAS* 423, pp. 1726–1749. DOI: 10.1111/j.1365-2966.2012.20993.x. arXiv: 1112.0315 [astro-ph.GA].

Schaller, Matthieu et al. (Aug. 2015a). "Baryon effects on the internal structure of ΛCDM haloes in the EAGLE simulations". In: *MNRAS* 451.2, pp. 1247–1267. DOI: 10.1093/mnras/stv1067. arXiv: 1409.8617 [astro-ph.CO].

Schaller, Matthieu et al. (Sept. 2015b). "The effect of baryons on the inner density profiles of rich clusters". In: *MNRAS* 452.1, pp. 343–355. DOI: 10.1093/mnras/stv1341. arXiv: 1409.8297 [astro-ph.CO].

Schmidt, Maarten (Mar. 1959). "The Rate of Star Formation." In: *ApJ* 129, p. 243. DOI: 10.1086/146614.

Schuecker, P. et al. (Feb. 2003). "The REFLEX galaxy cluster survey. VII. Omega$_m$ and sigma$_8$ from cluster abundance and large-scale clustering". In: *A&A* 398, pp. 867–877. DOI: 10.1051/0004-6361:20021715. arXiv: astro-ph/0208251 [astro-ph].

Schulze, Felix et al. (2018). "Kinematics of simulated galaxies - I. Connecting dynamical and morphological properties of early-type galaxies at different redshifts". In: *MNRAS* 480.4, pp. 4636–4658. DOI: 10.1093/mnras/sty2090. arXiv: 1802.01583 [astro-ph.GA].

Sembolini, Federico et al. (Feb. 2013). "The MUSIC of galaxy clusters - I. Baryon properties and scaling relations of the thermal Sunyaev-Zel'dovich effect". In: *MNRAS* 429.1, pp. 323–343. DOI: 10.1093/mnras/sts339. arXiv: 1207.4438 [astro-ph.CO].

Sembolini, Federico et al. (2016a). "nIFTy galaxy cluster simulations - I. Dark matter and non-radiative models". In: *MNRAS* 457.4, pp. 4063–4080. DOI: 10.1093/mnras/stw250. arXiv: 1503.06065 [astro-ph.CO].

Sembolini, Federico et al. (2016b). "nIFTy galaxy cluster simulations - II. Radiative models". In: *MNRAS* 459.3, pp. 2973–2991. DOI: 10.1093/mnras/stw800. arXiv: 1511.03731 [astro-ph.CO].

Shapiro, Paul R., Ilian T. Iliev, and Alejandro C. Raga (Mar. 2004). "Photoevaporation of cosmological minihaloes during reionization". In: *MNRAS* 348.3, pp. 753–782. DOI: 10.1111/j.1365-2966.2004.07364.x. arXiv: astro-ph/0307266 [astro-ph].

Simpson, Christine M. et al. (July 2018). "Quenching and ram pressure stripping of simulated Milky Way satellite galaxies". In: *MNRAS* 478.1, pp. 548–567. DOI: 10.1093/mnras/sty774. arXiv: 1705.03018 [astro-ph.GA].

Skillman, Evan D. et al. (Mar. 2017). "The ISLAndS Project. II. The Lifetime Star Formation Histories of Six Andromeda dSphS". In: *ApJ* 837.2, 102, p. 102. DOI: 10.3847/1538-4357/aa60c5. arXiv: 1606.01207 [astro-ph.GA].

Slater, C. T. and E. F. Bell (Sept. 2014). "The Mass Dependence of Dwarf Satellite Galaxy Quenching". In: *ApJ* 792, 141, p. 141. DOI: 10.1088/0004-637X/792/2/141. arXiv: 1407.6006.

Smith, R., J. I. Davies, and A. H. Nelson (July 2010). "How effective is harassment on infalling late-type dwarfs?" In: *MNRAS* 405.3, pp. 1723–1735. DOI: 10.1111/j.1365-2966.2010.16545.x. arXiv: 1004.4602 [astro-ph.CO].

Smith, R. et al. (Dec. 2015). "The sensitivity of harassment to orbit: mass loss from early-type dwarfs in galaxy clusters". In: *MNRAS* 454.3, pp. 2502–2516. DOI: 10.1093/mnras/stv2082. arXiv: 1509.02537 [astro-ph.GA].

Smith, Rory et al. (2016). "The Preferential Tidal Stripping of Dark Matter versus Stars in Galaxies". In: *ApJ* 833.1, 109, p. 109. DOI: 10.3847/1538-4357/833/1/109. arXiv: 1610.04264 [astro-ph.GA].

Sofue, Yoshiaki and Vera Rubin (Jan. 2001). "Rotation Curves of Spiral Galaxies". In: *ARA&A* 39, pp. 137–174. DOI: 10.1146/annurev.astro.39.1.137. arXiv: astro-ph/0010594 [astro-ph].

Sohn, Sangmo Tony et al. (July 2007). "Exploring Halo Substructure with Giant Stars. X. Extended Dark Matter or Tidal Disruption?: The Case for the Leo I Dwarf Spheroidal Galaxy". In: *ApJ* 663.2, pp. 960–989. DOI: 10.1086/518302. arXiv: astro-ph/0608151 [astro-ph].

Sorce, J. G. et al. (Jan. 2016). "Cosmicflows Constrained Local UniversE Simulations". In: *MNRAS* 455, pp. 2078–2090. DOI: 10.1093/mnras/stv2407. arXiv: 1510.04900.

Spergel et al., D. N. (June 2007). "Three-Year Wilkinson Microwave Anisotropy Probe (WMAP) Observations: Implications for Cosmology". In: *ApJS* 170, pp. 377–408. DOI: 10.1086/513700. eprint: arXiv:astro-ph/0603449.

Springel, V. (Jan. 2010). "E pur si muove: Galilean-invariant cosmological hydrodynamical simulations on a moving mesh". In: *MNRAS* 401, pp. 791–851. DOI: 10.1111/j.1365-2966.2009.15715.x. arXiv: 0901.4107.

Springel, V. and L. Hernquist (Feb. 2003). "Cosmological smoothed particle hydrodynamics simulations: a hybrid multiphase model for star formation". In: *MNRAS* 339, pp. 289–311. DOI: 10.1046/j.1365-8711.2003.06206.x. eprint: arXiv:astro-ph/0206393.

Springel, Volker (Dec. 2005). "The cosmological simulation code GADGET-2". In: *MNRAS* 364.4, pp. 1105–1134. DOI: 10.1111/j.1365-2966.2005.09655.x. arXiv: astro-ph/0505010 [astro-ph].

Springel, Volker, Tiziana Di Matteo, and Lars Hernquist (Aug. 2005). "Modelling feedback from stars and black holes in galaxy mergers". In: *MNRAS* 361.3, pp. 776–794. DOI: 10.1111/j.1365-2966.2005.09238.x. arXiv: astro-ph/0411108 [astro-ph].

Springel, Volker, Carlos S. Frenk, and Simon D. M. White (Apr. 2006). "The large-scale structure of the Universe". In: *Nature* 440.7088, pp. 1137–1144. DOI: 10.1038/nature04805. arXiv: astro-ph/0604561 [astro-ph].

Springel, Volker et al. (Dec. 2001). "Populating a cluster of galaxies - I. Results at [formmu2]z=0". In: *MNRAS* 328.3, pp. 726–750. DOI: 10.1046/j.1365-8711.2001.04912.x. arXiv: astro-ph/0012055 [astro-ph].

Srisawat, C. et al. (Nov. 2013). "Sussing Merger Trees: The Merger Trees Comparison Project". In: *MNRAS* 436, pp. 150–162. DOI: 10.1093/mnras/stt1545. arXiv: 1307.3577 [astro-ph.CO].

Staniszewski, Z. et al. (Aug. 2009). "Galaxy Clusters Discovered with a Sunyaev-Zel'dovich Effect Survey". In: *ApJ* 701.1, pp. 32–41. DOI: 10.1088/0004-637X/701/1/32. arXiv: 0810.1578 [astro-ph].

Steinborn, L. K. et al. (Apr. 2015). "A refined sub-grid model for black hole accretion and AGN feedback in large cosmological simulations". In: *MNRAS* 448, pp. 1504–1525. DOI: 10.1093/mnras/stv072. arXiv: 1409.3221.

Stevens, A. R. H., D. J. Croton, and S. J. Mutch (Sept. 2016). "Building disc structure and galaxy properties through angular momentum: the DARK SAGE semi-analytic model". In: *MNRAS* 461, pp. 859–876. DOI: 10.1093/mnras/stw1332. arXiv: 1605.00647.

Stinson, G. et al. (Dec. 2006). "Star formation and feedback in smoothed particle hydrodynamic simulations - I. Isolated galaxies". In: *MNRAS* 373, pp. 1074–1090. DOI: 10.1111/j.1365-2966.2006.11097.x. eprint: astro-ph/0602350.

Strateva, Iskra et al. (Oct. 2001). "Color Separation of Galaxy Types in the Sloan Digital Sky Survey Imaging Data". In: *AJ* 122.4, pp. 1861–1874. DOI: 10.1086/323301. arXiv: astro-ph/0107201 [astro-ph].

Sugimoto, Daiichiro et al. (May 1990). "A special-purpose computer for gravitational many-body problems". In: *Nature* 345.6270, pp. 33–35. DOI: 10.1038/345033a0.

Sunyaev, R. A. and Ya. B. Zeldovich (Apr. 1970). "Small-Scale Fluctuations of Relic Radiation". In: *Ap&SS* 7.1, pp. 3–19. DOI: 10.1007/BF00653471.

Tacchella, S. et al. (Apr. 2015). "Evidence for mature bulges and an inside-out quenching phase 3 billion years after the Big Bang". In: *Science* 348, pp. 314–317. DOI: 10.1126/science.1261094. arXiv: 1504.04021.

Teklu, Adelheid F. et al. (2015). "Connecting Angular Momentum and Galactic Dynamics: The Complex Interplay between Spin, Mass, and Morphology". In: *ApJ* 812.1, 29, p. 29. DOI: 10.1088/0004-637X/812/1/29. arXiv: 1503.03501 [astro-ph.GA].

Thomas, P. A. et al. (June 2001). "A simulated τCDM cosmology cluster catalogue: the NFW profile and the temperature-mass scaling relations". In: *MNRAS* 324.2, pp. 450–462. DOI: 10.1046/j.1365-8711.2001.04330.x. arXiv: astro-ph/0007348 [astro-ph].

Tong, David (2019). "Lectures on Cosmology". In: Department of Applied Mathematics and Theoretical Physics, Cambridge University. Chap. 3: Structure Formation.

Tonry, J. L. et al. (Jan. 2001). "The SBF Survey of Galaxy Distances. IV. SBF Magnitudes, Colors, and Distances". In: *ApJ* 546, pp. 681–693. DOI: 10.1086/318301. eprint: astro-ph/0011223.

Tornatore, L. et al. (Dec. 2007). "Chemical enrichment of galaxy clusters from hydrodynamical simulations". In: *MNRAS* 382, pp. 1050–1072. DOI: 10.1111/j.1365-2966.2007.12070.x. arXiv: 0705.1921.

Truong, N. et al. (Mar. 2018). "Cosmological hydrodynamical simulations of galaxy clusters: X-ray scaling relations and their evolution". In: *MNRAS* 474.3, pp. 4089–4111. DOI: 10.1093/mnras/stx2927. arXiv: 1607.00019 [astro-ph.CO].

Tully, R. Brent, Hélène M. Courtois, and Jenny G. Sorce (Aug. 2016). "Cosmicflows-3". In: *AJ* 152.2, 50, p. 50. DOI: 10.3847/0004-6256/152/2/50. arXiv: 1605.01765 [astro-ph.CO].

Valtonen, M. J. et al. (June 1990). "Dynamical Friction on a Satellite of a Disk Galaxy - the Circular Orbit". In: *Celestial Mechanics and Dynamical Astronomy* 48.2, pp. 95–113. DOI: 10.1007/BF00049508.

van den Bosch, Frank C. (2017). "Dissecting the evolution of dark matter subhaloes in the Bolshoi simulation". In: *MNRAS* 468.1, pp. 885–909. DOI: 10.1093/mnras/stx520. arXiv: 1611.02657 [astro-ph.GA].

van den Bosch, Frank C. and Fangzhou Jiang (May 2016). "Statistics of dark matter substructure - II. Comparison of model with simulation results". In: *MNRAS* 458.3, pp. 2870–2884. DOI: 10.1093/mnras/stw440.

van den Bosch, Frank C. and Go Ogiya (Apr. 2018). "Dark matter substructure in numerical simulations: a tale of discreteness noise, runaway instabilities, and artificial disruption". In: *MNRAS* 475.3, pp. 4066–4087. DOI: 10.1093/mnras/sty084. arXiv: 1801.05427 [astro-ph.GA].

van Dokkum, Pieter G. and Marijn Franx (May 2001). "Morphological Evolution and the Ages of Early-Type Galaxies in Clusters". In: *ApJ* 553.1, pp. 90–102. DOI: 10.1086/320645. arXiv: astro-ph/0501236 [astro-ph].

Veale, Melanie et al. (2017). "The MASSIVE Survey - VII. The relationship of angular momentum, stellar mass and environment of early-type galaxies". In: *MNRAS* 471.2, pp. 1428–1445. DOI: 10.1093/mnras/stx1639. arXiv: 1703.08573 [astro-ph.GA].

Verley, S. et al. (Dec. 2007). "Star formation in M 33: Spitzer photometry of discrete sources". In: *A&A* 476, pp. 1161–1178. DOI: 10.1051/0004-6361:20078179. arXiv: 0709.2601.

Verley, S. et al. (Jan. 2009). "Star formation in M 33: multiwavelength signatures across the disk". In: *A&A* 493, pp. 453–466. DOI: 10.1051/0004-6361:200810566. arXiv: 0810.0473.

Vikhlinin, A. et al. (Apr. 2006). "Chandra Sample of Nearby Relaxed Galaxy Clusters: Mass, Gas Fraction, and Mass-Temperature Relation". In: *ApJ* 640.2, pp. 691–709. DOI: 10.1086/500288. arXiv: astro-ph/0507092 [astro-ph].

Vikhlinin, A. et al. (Feb. 2009). "Chandra Cluster Cosmology Project. II. Samples and X-Ray Data Reduction". In: *ApJ* 692.2, pp. 1033–1059. DOI: 10.1088/0004-637X/692/2/1033. arXiv: 0805.2207 [astro-ph].

Villalobos, Á. and A. Helmi (Dec. 2008). "Simulations of minor mergers - I. General properties of thick discs". In: *MNRAS* 391, pp. 1806–1827. DOI: 10.1111/j.1365-2966.2008.13979.x.

Vogelsberger, Mark et al. (Jan. 2020). "Cosmological simulations of galaxy formation". In: *Nature Reviews Physics* 2.1, pp. 42–66. DOI: 10.1038/s42254-019-0127-2. arXiv: 1909.07976 [astro-ph.GA].

Voit, G. M. and T. J. Ponman (Sept. 2003). "Signatures of Galaxy Formation in the Intracluster Medium". In: *ApJ* 594, pp. L75–L78. DOI: 10.1086/378627. eprint: astro-ph/0308475.

Wadsley, J. W., J. Stadel, and T. Quinn (Feb. 2004). "Gasoline: a flexible, parallel implementation of TreeSPH". In: *New Astron.* 9, pp. 137–158. DOI: 10.1016/j.newast.2003.08.004. eprint: astro-ph/0303521.

Wang, L. et al. (Nov. 2015). "NIHAO project - I. Reproducing the inefficiency of galaxy formation across cosmic time with a large sample of cosmological hydrodynamical simulations". In: *MNRAS* 454, pp. 83–94. DOI: 10.1093/mnras/stv1937. arXiv: 1503.04818.

Wang, Y. et al. (June 2016). "Sussing merger trees: stability and convergence". In: *MNRAS* 459, pp. 1554–1568. DOI: 10.1093/mnras/stw726. arXiv: 1604.01463.

Wang, Yang et al. (2018). "The Three Hundred Project: The Influence of Environment on Simulated Galaxy Properties". In: *ApJ* 868.2, 130, p. 130. DOI: 10.3847/1538-4357/aae52e. arXiv: 1809.05244 [astro-ph.GA].

Wang, Yi (July 2014). "Inflation, Cosmic Perturbations and Non-Gaussianities". In: *Communications in Theoretical Physics* 62.1, 109-166, pp. 109–166. DOI: 10.1088/0253-6102/62/1/19. arXiv: 1303.1523 [hep-th].

Wechsler, R. H. et al. (Mar. 2002). "Concentrations of Dark Halos from Their Assembly Histories". In: *ApJ* 568, pp. 52–70. DOI: 10.1086/338765. eprint: arXiv:astro-ph/0108151.

Weinberg, David H. et al. (Sept. 2013). "Observational probes of cosmic acceleration". In: *Phys. Rep.* 530.2, pp. 87–255. DOI: 10.1016/j.physrep.2013.05.001. arXiv: 1201.2434 [astro-ph.CO].

Weisz, Daniel R. et al. (July 2014). "The Star Formation Histories of Local Group Dwarf Galaxies. II. Searching For Signatures of Reionization". In: *ApJ* 789.2, 148, p. 148. DOI: 10.1088/0004-637X/789/2/148. arXiv: 1405.3281 [astro-ph.GA].

White, Martin (Apr. 2014). "The Zel'dovich approximation". In: *MNRAS* 439.4, pp. 3630–3640. DOI: 10.1093/mnras/stu209. arXiv: 1401.5466 [astro-ph.CO].

White, S. D. M. (1984). "Angular momentum growth in protogalaxies". In: *ApJ* 286, pp. 38–41. DOI: 10.1086/162573.

White, S. D. M., C. S. Frenk, and M. Davis (Nov. 1983). "Clustering in a neutrino-dominated universe". In: *ApJ* 274, pp. L1–L5. DOI: 10.1086/184139.

White, S. D. M. and M. J. Rees (May 1978). "Core condensation in heavy halos - A two-stage theory for galaxy formation and clustering". In: *MNRAS* 183, pp. 341–358.

Wiersma, R. P. C. et al. (Oct. 2009). "Chemical enrichment in cosmological, smoothed particle hydrodynamics simulations". In: *MNRAS* 399, pp. 574–600. DOI: 10.1111/j.1365-2966.2009.15331.x. arXiv: 0902.1535 [astro-ph.CO].

Williams, B. F. et al. (Apr. 2009). "The Detection of Inside-Out Disk Growth in M33". In: *ApJ* 695, pp. L15–L19. DOI: 10.1088/0004-637X/695/1/L15. arXiv: 0902.3460 [astro-ph.CO].

Willick, J. A. et al. (Apr. 1997). "Homogeneous Velocity-Distance Data for Peculiar Velocity Analysis. III. The Mark III Catalog of Galaxy Peculiar Velocities". In: *ApJS* 109, pp. 333–366. DOI: 10.1086/312983. eprint: astro-ph/9610202.

Wong, A. W. C. and J. E. Taylor (Sept. 2012). "What Do Dark Matter Halo Properties Tell Us about Their Mass Assembly Histories?" In: *ApJ* 757, 102, p. 102. DOI: 10.1088/0004-637X/757/1/102. arXiv: 1112.4229 [astro-ph.CO].

Wright, Anna C. et al. (Jan. 2019). "Reignition of star formation in dwarf galaxies". In: *MNRAS* 482.1, pp. 1176–1189. DOI: 10.1093/mnras/sty2759. arXiv: 1802.03019 [astro-ph.GA].

Wu, Hao-Yi et al. (Sept. 2015). "RHAPSODY-G simulations: galaxy clusters as baryonic closed boxes and the covariance between hot gas and galaxies". In: *MNRAS* 452.2, pp. 1982–1991. DOI: 10.1093/mnras/stv1434. arXiv: 1503.03924 [astro-ph.CO].

Wu, Xiang-Ping et al. (Dec. 1998). "A comparison of different cluster mass estimates: consistency or discrepancy?" In: *MNRAS* 301.3, pp. 861–871. DOI: 10.1046/j.1365-8711.1998.02055.x. arXiv: astro-ph/9808179 [astro-ph].

Xie, Lizhi et al. (Aug. 2020). "The influence of environment on satellite galaxies in the GAEA semi-analytic model". In: *MNRAS*. DOI: 10.1093/mnras/staa2370. arXiv: 2003.12757 [astro-ph.GA].

Xu, Guohong (May 1995). "A New Parallel N-Body Gravity Solver: TPM". In: *ApJS* 98, p. 355. DOI: 10.1086/192166. arXiv: astro-ph/9409021 [astro-ph].

Yadav, Jaswant et al. (Dec. 2005). "Testing homogeneity on large scales in the Sloan Digital Sky Survey Data Release One". In: *MNRAS* 364.2, pp. 601–606. DOI: 10.1111/j.1365-2966.2005.09578.x. arXiv: astro-ph/0504315 [astro-ph].

Yan, Z. et al. (May 2020). "Galaxy cluster mass estimation with deep learning and hydrodynamical simulations". In: *arXiv e-prints*, arXiv:2005.11819, arXiv:2005.11819. arXiv: 2005.11819 [astro-ph.CO].

Yang, X., H. J. Mo, and F. C. van den Bosch (Apr. 2009). "Galaxy Groups in the SDSS DR4. III. The Luminosity and Stellar Mass Functions". In: *ApJ* 695, pp. 900–916. DOI: 10.1088/0004-637X/695/2/900. arXiv: 0808.0539.

Yang, X. et al. (June 2012). "Evolution of the Galaxy-Dark Matter Connection and the Assembly of Galaxies in Dark Matter Halos". In: *ApJ* 752, 41, p. 41. DOI: 10.1088/0004-637X/752/1/41. arXiv: 1110.1420 [astro-ph.CO].

Yang, Xiaohu et al. (June 2018). "ELUCID. V. Lighting Dark Matter Halos with Galaxies". In: *ApJ* 860.1, 30, p. 30. DOI: 10.3847/1538-4357/aac2ce. arXiv: 1712.00883 [astro-ph.GA].

Yepes, G. et al. (Jan. 1997). "Hydrodynamical simulations of galaxy formation: effects of supernova feedback". In: *MNRAS* 284.1, pp. 235–256. DOI: 10.1093/mnras/284.1.235. arXiv: astro-ph/9605182 [astro-ph].

Yoachim, P. and J. J. Dalcanton (Jan. 2006). "Structural Parameters of Thin and Thick Disks in Edge-on Disk Galaxies". In: *AJ* 131, pp. 226–249. DOI: 10.1086/497970. eprint: astro-ph/0508460.

Yoachim, P., R. Roškar, and V. P. Debattista (June 2012). "Spatially Resolved Spectroscopic Star Formation Histories of nearby Disks: Hints of Stellar Migration". In: *ApJ* 752, 97, p. 97. DOI: 10.1088/0004-637X/752/2/97. arXiv: 1204.0026.

Zel'dovich, Y. B. (Mar. 1970). "Gravitational instability: An approximate theory for large density perturbations." In: *A&A* 5, pp. 84–89.

Zhang, Y. Y. et al. (Nov. 2011). "Star-formation efficiency and metal enrichment of the intracluster medium in local massive clusters of galaxies". In: *A&A* 535, A78, A78. DOI: 10.1051/0004-6361/201116803. arXiv: 1109.0390 [astro-ph.CO].

Zhao, D. H. et al. (Nov. 2003a). "Mass and Redshift Dependence of Dark Halo Structure". In: *ApJ* 597.1, pp. L9–L12. DOI: 10.1086/379734. arXiv: astro-ph/0309375 [astro-ph].

Zhao, D. H. et al. (Feb. 2003b). "The growth and structure of dark matter haloes". In: *MNRAS* 339, pp. 12–24. DOI: 10.1046/j.1365-8711.2003.06135.x. eprint: astro-ph/0204108.

Zheng, Z. et al. (Feb. 2015). "The Structure and Stellar Content of the Outer Disks of Galaxies: A New View from the Pan-STARRS1 Medium Deep Survey". In: *ApJ* 800, 120, p. 120. DOI: 10.1088/0004-637X/800/2/120. arXiv: 1412.3209.

Zibetti, Stefano et al. (Apr. 2005). "Intergalactic stars in z$\sim$0.25 galaxy clusters: systematic properties from stacking of Sloan Digital Sky Survey imaging data". In: *MNRAS* 358.3, pp. 949–967. DOI: 10.1111/j.1365-2966.2005.08817.x. arXiv: astro-ph/0501194 [astro-ph].

Zwicky, F. (Jan. 1933). "Die Rotverschiebung von extragalaktischen Nebeln". In: *Helvetica Physica Acta* 6, pp. 110–127.